

INFORMATION TO USERS

This manuscript has been reproduced from the microfilm master. UMI films the text directly from the original or copy submitted. Thus, some thesis and dissertation copies are in typewriter face, while others may be from any type of computer printer.

The quality of this reproduction is dependent upon the quality of the copy submitted. Broken or indistinct print, colored or poor quality illustrations and photographs, print bleedthrough, substandard margins, and improper alignment can adversely affect reproduction.

In the unlikely event that the author did not send UMI a complete manuscript and there are missing pages, these will be noted. Also, if unauthorized copyright material had to be removed, a note will indicate the deletion.

Oversize materials (e.g., maps, drawings, charts) are reproduced by sectioning the original, beginning at the upper left-hand corner and continuing from left to right in equal sections with small overlaps. Each original is also photographed in one exposure and is included in reduced form at the back of the book.

Photographs included in the original manuscript have been reproduced xerographically in this copy. Higher quality 6" x 9" black and white photographic prints are available for any photographs or illustrations appearing in this copy for an additional charge. Contact UMI directly to order.

UMI

A Bell & Howell Information Company
300 North Zeeb Road, Ann Arbor MI 48106-1346 USA
313/761-4700 800/521-0600

MIGRATION OF CROSS-WELL SEISMIC AND VSP DATA

**A DISSERTATION
SUBMITTED TO THE DEPARTMENT OF GEOPHYSICS
AND THE COMMITTEE ON GRADUATE STUDIES
OF STANFORD UNIVERSITY
IN PARTIAL FULFILLMENT OF THE REQUIREMENTS
FOR THE DEGREE OF
DOCTOR OF PHILOSOPHY**

**By
Le-Wei Lihui Mo
October, 1997**

UMI Number: 9901558

**Copyright 1997 by
Mo, Le-Wei Lihui**

All rights reserved.

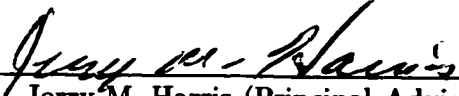
**UMI Microform 9901558
Copyright 1998, by UMI Company. All rights reserved.**

**This microform edition is protected against unauthorized
copying under Title 17, United States Code.**

UMI
300 North Zeeb Road
Ann Arbor, MI 48103

© Copyright by Le-Wei Lihui Mo 1997
All Rights Reserved

I certify that I have read this thesis and that in my opinion it is fully adequate, in scope and in quality, as a dissertation for the degree of Doctor of Philosophy.



Jerry M. Harris (Principal Advisor)

I certify that I have read this thesis and that in my opinion it is fully adequate, in scope and in quality, as a dissertation for the degree of Doctor of Philosophy.



Jon Claerbout

I certify that I have read this thesis and that in my opinion it is fully adequate, in scope and in quality, as a dissertation for the degree of Doctor of Philosophy.



Francis Muir

I certify that I have read this thesis and that in my opinion it is fully adequate, in scope and in quality, as a dissertation for the degree of Doctor of Philosophy.



Greg Beroza

Approved for the University Committee on Graduate Studies:



Migration of cross-well seismic and VSP data

Le-Wei Lihui Mo, Ph.D.

Stanford University, 1997

ABSTRACT

Cross-well seismic survey, has been proven to be a promising method of imaging the subsurface. It can provide high resolution images between wells. However, the conventional imaging method – VSP-CDP mapping can only image simple structures correctly. Correct imaging of complex structures calls for the application of prestack migration. The conventional full-aperture Kirchhoff migration has the potential of correctly imaging reflectors of dips up to 90-degrees. But the long impulse response of this algorithm can severely spread noise. Thus, in processing noisy field data one need to make a balance between correct imaging of dipping reflectors and spreading of noise. An aperture-limited Kirchhoff migration algorithm is presented in this thesis for processing cross-well seismic data. By limiting the aperture of the Kirchhoff migration integral, noises in the data are not spread to a large area, and the accuracy of imaging is good up to the user-defined dip limits.

Efficient implementation of prestack Kirchhoff migration requires fast calculation of direct arrival traveltimes on a uniform grid. The travelttime calculation scheme presented in this thesis calculates the traveltimes of direct arrivals from a point source by solving the Eikonal equation using the finite-difference method. Physical wave phenomena are incorporated in the travelttime computation. Travelttime computation at critical incidence is carefully handled, so that the method is stable even in situations of large velocity contrast.

The new algorithms presented in this thesis, namely finite-difference Eikonal equation travelttime solver, tube wave attenuation and aperture-limited Kirchhoff migration are applied to process a field cross-well data set where the geology is fairly complicated. The data preprocessing consists of tube wave attenuation, amplitude correction, and attenuation of the direct arrivals. The velocity model used in migration is the tomogram obtained from transmission travelttime tomography. Two elastic wave modes, namely $P - P$ and

$S - S$ are each used in migration. The resulting images clearly show geological structures, flat and dipping beds, an unconformity and reef of thickness less than 200 ft.

Cross-well processing can be thought of as imaging multiple offset VSPs. In VSP, a source is located on the Earth surface and a string of receivers are placed in the borehole to record both the downgoing direct arrival and the upgoing reflections. VSP can provide high-resolution image of the earth subsurface, in the vicinity of the borehole. The most popular imaging method used in VSP is the CDP mapping, whose strength is not spreading noise. The VSP-CDP migration method presented in this thesis corrects the mispositioning errors in the image produced by CDP mapping. VSP-CDP maps reflections from a dipping reflector into a third-order polynomial in unmigrated VSP-CDP image (offset-depth) space. A point in the $\tau - p$ space of the migrated image is obtained by stacking the VSP-CDP image along the image trajectory calculated by modeling the VSP-CDP mapping process. Inverse transformation on the resulting $\tau - p$ data gives the migration image. This migration algorithm assumes a constant velocity medium. In contrast, the VSP-CDP mapping can handle a general velocity medium. Thus, this algorithm can perhaps best be used to help estimating the dip of the reflector in interactive VSP-CDP mapping.

Acknowledgments

Above all, I would like to thank my advisor, Prof Jerry Harris, for giving me the chance to work and study in the Seismic Tomography Project (STP), an outstanding research environment and the cradle for cross-well survey seismology. Through the course of this study, Jerry has always been a source of encouragement and advice. He allowed me the freedom to experiment and follow my interest, while providing me the right amount of guidance at the right moment. I would like to thank Prof Robert Langan of Chevron for editing the chapter of attenuating tube waves in cross-well seismic survey and offering insightful suggestions. I would like to thank Prof Jon Claerbout for supporting me for two years at Stanford Exploration Project. I also thank Prof Francis Muir. Francis helped me get started in my first year at SEP. I also thank Dave Nichols, Martin Karrenbach, Stew Levin for helping to install SEPlib in the DEC alpha workstation that I use.

All my fellow students in the STP research group (Ann, Feng, Guan, Jesse, Mark, Nick, Ricardo, Youli) made my graduate study and research an enjoyable experience. I would like to thank all of them for assistance and support. Mark van Schaack provided the tomogram of the King Mountain data set.

I would like to thank the sponsors of the Seismic Tomography Project for their continuous support and interest in this research, and especially Chevron Petroleum Technology Company and Exxon Production Research Company for providing the field data.

I would like to thank my parents, my wife, and my son. Their love, support and understanding gave me the strength to complete this work.

Contents

Abstract	v
Acknowledgments	vii
1 Introduction	1
1.1 Thesis overview	1
1.1.1 Computation of the direct arrival travel times by the eikonal equation and its application (Chapter 2)	1
1.1.2 Analysis and attenuation of tube waves for cross-well seismic survey (Chapter 3)	2
1.1.3 Finite-difference reverse-time migration of cross-well data (Chapter 4)	2
1.1.4 Kirchhoff migration of cross-well data (Chapter 5)	3
1.1.5 Noise-tolerant and aperture-limited Kirchhoff migration (Chapter 6)	3
1.1.6 Prestack migration of cross-well field data in bigger doses (Chapter 7)	3
1.1.7 Post-CDP-mapped migration in vertical seismic profile (Chapter 8) .	4
1.2 Assumptions	4
2 Computation of direct arrival travel times by the eikonal equation and its applications	5
2.1 Introduction	5
2.2 Why direct arrival travel times	7
2.3 Ray tracing	8
2.4 Solving the eikonal equation	9
2.4.1 Computation order	12
2.5 Travel time examples	14

2.6	A posteriori ray tracing	16
2.7	Discussion	19
2.8	Conclusions	21
3	Analysis and attenuation of tube waves for cross-well seismic survey	22
3.1	Introduction	23
3.2	Analysis of cross-well tube waves	23
3.3	Attenuation of cross-well tube waves	24
3.4	Data examples	28
3.5	Conclusions	30
4	Finite-difference reverse-time migration of cross-well data	35
4.1	Introduction	36
4.2	Theory	37
4.2.1	Conjugate modeling and migration	37
4.2.2	Implementation of reverse-time migration	40
4.2.3	Stacking images of upgoing/downgoing source wavefields	41
4.3	Application in field data	41
4.3.1	Description of field data	41
4.3.2	Preprocessing of field data	42
4.3.3	Background velocity model	45
4.3.4	<i>P-P</i> wave migration	46
4.3.5	<i>S-S</i> wave migration	51
4.3.6	<i>P-S</i> wave migration	56
4.3.7	<i>S-P</i> wave migration	63
4.4	Conclusions	63
5	Kirchhoff migration of cross-well data	69
5.1	Introduction	70
5.2	Theory	71
5.2.1	Kirchhoff migration	71
5.2.2	Implementation of Kirchhoff migration	77
5.3	Application in field data	78
5.3.1	Description of field data	78

5.3.2	Preprocessing of field data	78
5.3.3	Background velocity model	79
5.3.4	<i>P-P</i> wave migration	79
5.3.5	<i>S-S</i> wave migration	81
5.3.6	<i>P-S</i> wave migration	84
5.3.7	<i>S-P</i> wave migration	84
5.4	Comparison with finite-difference reverse-time migration	91
5.5	Conclusions	95
6	Noise-tolerant and aperture-limited Kirchhoff migration	97
6.1	Introduction	97
6.2	Theory	99
6.2.1	Kirchhoff migration	99
6.2.2	Aperture-limited Kirchhoff migration	104
6.2.3	Implementation	105
6.3	Synthetic data examples	106
6.4	Conclusions	107
7	Prestack migration of cross-well field data in bigger doses	112
7.1	The processing sequence	113
7.2	The field data	114
7.3	Preprocessing	114
7.3.1	Attenuation of tube waves	114
7.3.2	Amplitude corrections	114
7.3.3	Attenuation of direct arrivals	116
7.4	Velocity model used in migration	116
7.5	Kirchhoff migration	120
7.5.1	90-degree full-aperture <i>P-P</i> wave migration	120
7.5.2	45-degree limited-aperture <i>P-P</i> wave migration	122
7.5.3	45-degree limited-aperture <i>S-S</i> wave migration	125
7.6	Interpretation of results	125
7.7	Conclusions	136

8 Post-CDP-mapped migration in vertical seismic profile	137
8.1 Introduction	137
8.2 VSP reflection travel time from a dipping interface	139
8.3 VSP reflection CDP depth mapping	140
8.4 Analysis of VSP-CDP mispositioning caused by dip	142
8.5 Analysis of VSP-CDP mispositioning caused by velocity inaccuracy	144
8.6 Post-CDP-mapped migration	149
8.7 Synthetic data	150
8.7.1 Dipping reflectors	150
8.7.2 Curvilinear reflectors	150
8.8 Field data – Exxon Friendswood	153
8.9 Conclusions	156
 Bibliography	 162

List of Tables

List of Figures

2.1	Comparing the direct arrival travel times and the wave forms	8
2.2	Comparing the first arrival travel times and the wave forms	9
2.3	A field common shot gather	10
2.4	Ray tracing in a medium with two velocity layers	10
2.5	Wave propagation in a square cell with constant slowness	11
2.6	Computation of creeping wave travel times at an interface	13
2.7	Ordering travel time computation sequence	15
2.8	Locating the points with local minimum travel times	15
2.9	Three loops are used to compute travel times at an edge	16
2.10	Direct arrival travel times in a 1-D medium	17
2.11	Comparing the direct arrival travel times and wave forms in a 1-D medium	17
2.12	Direct arrival travel times in a 2-D medium	18
2.13	Comparing the direct arrival travel times and wave forms in a 2-D medium	18
2.14	Direction of rays in a cell	20
2.15	Direct arrival ray paths in a 1-D medium	20
3.1	Generation of source well tube waves	25
3.2	A synthetic common shot gather	25
3.3	Generation of receiver well tube waves	26
3.4	A synthetic common receiver gather	26
3.5	Relationships of source well tube waves between neighboring CSGs	29
3.6	An unprocessed field common shot gather	31
3.7	An unprocessed field common receiver gather	31
3.8	Estimated source well tube wave	32
3.9	Common shot gather after removal of source well tube wave	32

34.10	Common receiver gather after removal of source well tube wave	33
3.11	Estimated receiver well tube wave	33
3.12	Common receiver gather after removal of source and receiver well tube wave	34
3.13	Common shot gather after removal of source and receiver well tube wave . .	34
4.1	Cross-well survey geometry and travel time curves	38
4.2	Orginal and preprocessed common receiver gather	43
4.3	Radiation patterns of down-hole source	44
4.4	Common receiver gather after attenuation of direct arrivals	45
4.5	<i>P</i> -wave tomogram	46
4.6	<i>P-P</i> wave migration image	48
4.7	<i>P-P</i> wave migration image	49
4.8	<i>P-P</i> wave migration image	50
4.9	A volume of images after migration	51
4.10	Common surface location image gather	52
4.11	Common surface location image gather	53
4.12	<i>P-P</i> wave stacked migration image	54
4.13	<i>P-P</i> wave migration image and VSP-CDP mapping images	55
4.14	<i>S-S</i> wave migration image	57
4.15	Common surface location image gather	58
4.16	<i>S-S</i> wave migration image and VSP-CDP mapping images	59
4.17	<i>P-S</i> wave migration image	60
4.18	<i>P-S</i> wave migration image	61
4.19	Common surface location image gather	62
4.20	<i>P-S</i> wave stacked migration imag	64
4.21	<i>S-P</i> wave migration imag	65
4.22	Common surface location image gather	66
4.23	<i>S-P</i> wave stacked migration imag	67
5.1	Wave field extrapolation in Kirchhoff migration	72
5.2	Cross-well survey geometry and travel time curves	74
5.3	Travel time maps from the source and the receiver, and migration ellipse . .	75
5.4	Impulse responses of 90-degree migration algorithms	76
5.5	Preprocessed common receiver gather	78

5.6	<i>P-P</i> wave migration image	80
5.7	A volume of images after migration	81
5.8	Common surface location image gather	82
5.9	<i>P-P</i> wave stacked migration image	83
5.10	<i>S-S</i> wave migration image	85
5.11	Common surface location image gather	86
5.12	<i>S-S</i> wave stacked migration image	87
5.13	<i>P-S</i> wave migration image	88
5.14	Common surface location image gather	89
5.15	<i>P-S</i> wave stacked migration image	90
5.16	<i>S-P</i> wave migration image	92
5.17	Common surface location image gather	93
5.18	<i>S-P</i> wave stacked migration image	94
6.1	Wave field extrapolation in Kirchhoff migration	100
6.2	Travel times from a source or receiver	102
6.3	Impulse responses of 90-degree and 5-degree migration	103
6.4	Aperture of the Kirchhoff integral can be computed from dip requirement	105
6.5	Reflector model and synthetic common shot gather with Gaussian noise	108
6.6	Migration images of the 90-degree and 15-degree migration algorithms	109
6.7	Images of the 15-degree migration algorithm and true reflector locations	110
6.8	Limited-aperture migration mispositions dipping reflector	111
6.9	Limited-aperture migration mispositions dipping reflector	111
7.1	Cross-well migration data processing flow chart	113
7.2	Common receiver gather after attenuation of tube waves	115
7.3	Common receiver gather after correction of amplitude	117
7.4	Common receiver gather after attenuation of direct arrivals	118
7.5	Common source gather after attenuation of direct arrivals	119
7.6	<i>P</i> -wave velocity tomogram	121
7.7	Full-aperture <i>P-P</i> wave migration image	123
7.8	Full-aperture stacked <i>P-P</i> wave migration image	124
7.9	45-degree <i>P-P</i> wave migration image	126
7.10	45-degree <i>P-P</i> wave migration image	127

7.11	<i>P-P</i> wave common surface location image gather	128
7.12	<i>P-P</i> wave common surface location image gather	129
7.13	45-degree stacked <i>P-P</i> wave migration image	130
7.14	45-degree <i>S-S</i> wave migration image	131
7.15	45-degree <i>S-S</i> wave migration image	132
7.16	<i>S-S</i> wave common surface location image gather	133
7.17	<i>S-S</i> wave common surface location image gather	134
7.18	45-degree stacked <i>S-S</i> wave migration image	135
8.1	Layout of VSP survey. Travel time of reflection	139
8.2	VSP-CDP mapping assumes the reflectors are flat	142
8.3	VSP-CDP mispositions a dipping reflector	145
8.4	VSP-CDP mispositions a dipping reflector	145
8.5	Difference between the lateral coordinates of reflection and image point	146
8.6	Difference between the depth coordinates of reflection and image point	146
8.7	Difference between the lateral coordinates of reflection and image point	147
8.8	Difference between the depth coordinates of reflection and image point	147
8.9	Comparing a dipping reflector and its VSP-CDP image	148
8.10	Comparing a dipping reflector and its VSP-CDP image	148
8.11	Three steps are involved to process VSP data to obtain	151
8.12	A VSP common shot gather data	152
8.13	Image produced by the conventional VSP-CDP mapping	152
8.14	VSP-CDP migration image	153
8.15	A VSP common shot gather data	154
8.16	Upgoing reflection data obtained by f-k filtering	154
8.17	Image produced by the conventional VSP-CDP mapping	155
8.18	VSP-CDP migration image	155
8.19	Original field common shot gather	156
8.20	Common shot gather VSP data after filtering	157
8.21	Upgoing wavefiled obtained by f-k filtering	157
8.22	VSP-CDP image	158
8.23	Constructed $\tau - p$ image obtained by scanning the VSP-CDP image	159
8.24	VSP-CDP migration image	160

Chapter 1

Introduction

As oil fields in the world undergo more and more development, there are more and more wells drilled. One can foresee there will be more and more seismic surveys involving boreholes for EOR purposes. The two major survey configurations that involve boreholes are vertical seismic profiling (VSP) and cross-well seismic profiling. In VSP, a source is located on the Earth surface and a string of receivers are placed in the borehole to record both the downgoing wave fields and the upgoing reflection wave fields. VSP can provide high-resolution images in the vicinity of the borehole. In cross-well seismic profiling, sources are fired in one borehole, and a string of receivers are placed in a nearby borehole to record the seismic wave fields. The frequency contents of the cross-well seismic data can be an order of magnitude higher than those of the VSP and surface seismic survey. Thus, cross-well seismic survey can provide images between two boreholes in the resolution scale of several feet. The goals of this thesis are to develop the migration imaging methodologies for the two types of borehole seismic surveys described above and for the efficient and robust implementation of the migration algorithms.

1.1 Thesis overview

1.1.1 Computation of the direct arrival travel times by the eikonal equation and its application (Chapter 2)

Reflectivity imaging algorithms operate on the reflections and diffractions generated by the direct arrivals from the source. And travel time tomography for inversion of velocity model operates on the travel times of direct arrivals. Thus, efficient and accurate prestack depth

migration and travel time tomography requires fast calculation of direct arrival travel times and ray paths on a uniform grid. Former finite-difference Eikonal equation travel time solvers (Vidale, 1988, 1990; van Trier et al, 1991; Zhang 1993) attempted solving for the travel times of first arrivals. In velocity models with large contrasts, these methods can encounter stability problems of calculating the square root of a negative number; and some of the computed travel times (travel times of head wave and diffraction) are not what are needed in migration imaging and tomography. In this chapter, I present a new finite-difference method of solving the Eikonal equation. Physical wave phenomena are incorporated in the travel time computation. Travel time computation at post-critical incidence is carefully handled to avoid calculating the square root of a negative number, so that the method is stable even in situations of large velocity contrast. The travel time field is used to compute direct arrival ray paths by following the steepest descent gradient from the receiver back to the source (Aldridge et al, 1993).

1.1.2 Analysis and attenuation of tube waves for cross-well seismic survey (Chapter 3)

Seismic data collected in a crosswell survey often contain strong tube waves that have parts of their travel paths along wells where the sources and receivers are positioned. Because of the slow propagation velocity of the tube waves in the fluid, they are usually spatially aliased in field recorded data, in common shot gathers (CSG) and common receiver gathers (CRG). Previous methods (Cai et al, 1993) of attenuating tube waves requires picking the travel times of the tube wave events. In this chapter, I analyze the generation and propagation of the tube waves. I show that the source (receiver) well tube waves are well sampled and can be predicted and attenuated in CSGs (CRGs).

1.1.3 Finite-difference reverse-time migration of cross-well data (Chapter 4)

In this chapter, I implement and apply the finite-difference reverse-time migration to process a cross-well field data set recorded in the Permian Basin, West Texas. The quality of the data is good and recording aperture is wide and the geological structure is simple. Migration images of four elastic wave modes, P - P , S - S , P - S , S - P are obtained. The geological structures as suggested by these images are consistent with each other and with those obtained by VSP-CDP mapping.

1.1.4 Kirchhoff migration of cross-well data (Chapter 5)

In this chapter, I implement and apply the Kirchhoff migration to process the cross-well field data set also used in Chapter 4. Images of four elastic wave modes, P - P , S - S , P - S , S - P are obtained. The geological structures as suggested by these images are consistent with each other and with those obtained by finite-difference reverse-time migration and VSP-CDP mapping.

1.1.5 Noise-tolerant and aperture-limited Kirchhoff migration (Chapter 6)

The conventional full-aperture Kirchhoff migration algorithm has the potential of correctly imaging reflectors with dips up to 90-degrees. But the long impulse response of this algorithm can severely spread noise in not-ideal field data. Qin et al (1993) presented a cross-well constrained migration algorithm that removed events of large dips in the image. In this chapter, I present an aperture-limited Kirchhoff migration algorithm whose integral aperture depends on the maximum dip to be imaged correctly. By limiting the aperture of the Kirchhoff migration integral, noises in the data are not spread to a large area. And the migration smiles due to ill-conditioned data are weaker than in the full-aperture algorithm.

1.1.6 Prestack migration of cross-well field data in bigger doses (Chapter 7)

In this chapter, I apply the new algorithms presented in this thesis, namely finite-difference Eikonal equation travel time solver, tube wave attenuation and limited-aperture Kirchhoff migration to process a field cross-well data set recorded in the Permian Basin, West Texas. The data preprocessing consists of tube wave attenuation, amplitude correction, and attenuation of the direct arrivals. The velocity model used in migration is the tomogram obtained from transmission travel time tomography. Two elastic wave modes, namely $P - P$ and $S - S$ are each used in migration. Migration is performed in the domains of both common shot gathers and common receiver gathers. Image events at common surface location gathers show generally good flat alignment suggesting the velocity model used in migration is correct. The resulting images clearly show geological structures, flat and dipping beds, an unconformity and reef of thickness less than 200 ft.

1.1.7 Post-CDP-mapped migration in vertical seismic profile (Chapter 8)

In VSP surveys, there are usually only a few common shot gathers recorded. And in each common shot gather, there are usually less than 100 receiver traces. This means the VSP surveying aperture is very narrow. Imaging of VSP data calls for the application of an algorithm that can tolerate low signal-to-noise ratio in the data. VSP-CDP mapping (Wyatt et al, 1981) is the algorithm for this purpose. However, there are mispositioning errors in the images generated by VSP-CDP mapping. Interactive data processing techniques (Lazaratos, 1993; Smalley, 1997) have been developed to correct the mispositioning errors in the VSP-CDP images. These interactive methods are flexible but time consuming. In this chapter, I develop an automatic method to correct the mispositioning errors in the VSP-CDP image. Like surface seismic data processing, the VSP data are first CDP mapped into the image space under the assumption of flat reflectors. Then the CDP image is corrected for dip errors by the migration process. This migration algorithm assumes a constant velocity medium.

1.2 Assumptions

Throughout this thesis, I assume that the seismic wave fields in the earth propagate through a 2-D, isotropic, elastic medium. In an elastic medium, in the forward problem the propagations of compressional waves (P -waves) and shear waves (S -waves) are fully coupled in the elastic wave equation. But in migration processing of the four elastic wave modes, P - P , S - S , P - S and S - P , I use the scalar wave equation to perform the forward propagation of waves from the sources and also to perform the backpropagation of waves from the receivers.

Chapter 2

Computation of direct arrival travel times by the eikonal equation and its applications

In this chapter, I present a traveltimes calculation scheme based on the eikonal equation that calculates the traveltimes of direct arrivals from a point source. In typical earth models, critical refractions, diffractions and reflections are weak. Most of the energy radiated by the source is contained in the direct arrivals. Direct arrivals are thus generally the most energetic events in a time evolving wavefield. This scheme successfully computes the traveltimes of direct arrivals on a uniform grid and is computationally efficient. I use the travel time field to compute direct arrival ray paths, which can be further applied to travel time tomography and attenuation tomography. The method is presented in two dimensions.

2.1 Introduction

Wave propagation in heterogeneous media, in high frequency asymptotics, can be described by the WKBJ Green's function, which consists of traveltimes and amplitudes. The traveltimes satisfy the eikonal equation that relates the gradient of the traveltimes to the slowness of the medium. The amplitudes satisfy the transport equations. In this chapter, I will address the problem of solving the eikonal equation for direct arrival traveltimes. One method of solving the eikonal equation is the method of characteristics (Cerveny et

al., 1977). The ray equations are derived from the eikonal equation, whose solutions are raypaths or the characteristic curves of the eikonal equation. However, ray tracing has its limitations and disadvantages as pointed out by some authors (Vidale, 1988). Seismic depth migration, and many other applications require traveltimes on a uniform grid. If these traveltimes are computed by ray tracing, computation cost is immense. It is more efficient to solve the eikonal equation directly for traveltimes on a uniform grid.

Reshef and Kosloff (1986) formulated finite-difference scheme to solve the eikonal equation for traveltimes on a uniform grid by extrapolating the depth gradient of traveltimes. Vidale (1988, 1990) formulated a finite-difference scheme in Cartesian coordinates that solves the eikonal equation progressing outward from an "expanding square" for traveltimes of first arriving waves from a point source. His scheme quickly fills in traveltimes in a uniform grid, and is by far the fastest method of computing traveltime. However, Vidale's scheme encounters stability problems, e.g., calculating the square root of a negative number. Qin et al. (1992) proposed an alternate to Vidale's scheme, by progressing outward from an "expanding wavefront." Qin et al.'s scheme solves only some of the stability problems of Vidale's algorithm. But searching for the global minimum to start computation at each step makes their scheme computational costly. Podvin and Lecomte (1991) dissected wave propagation in a cell into all possible modes of transmission, diffraction and head waves, resulting in a stable scheme of traveltime calculation. Van Trier and Symes (1991) formulated traveltime calculation in polar coordinates by extrapolating the gradients of traveltimes. In their scheme, traveltime computation has the disadvantage of dense sampling near the source and coarse sampling far away from the source. And mapping the slowness and traveltime fields between Cartesian and polar coordinates requires additional computation cost. As a matter of fact, efficiency of a traveltime computation scheme also depends on the computer architecture, but Vidale's scheme has the advantage of requiring the least number of algebraic operations.

The common shortcoming of the above finite-difference traveltime calculation schemes is that they all explicitly or implicitly calculate traveltime of first arriving waves, which may carry very little energy and are very weak, e.g., head waves and diffractions. In this chapter, I propose a traveltime calculation scheme that aims to calculate the traveltimes of direct arrivals from a point source. In typical earth models, diffraction and reflection events are weak; therefore, most of the energy radiated by the source is contained in the direct arrivals. Direct arrivals are thus generally the most energetic events in a time

evolving wavefield. First, I describe why I prefer direct arrival traveltimes to first arrival traveltimes in tomography and migration imaging. Then, I analyse ray tracing and finite difference method of solving the eikonal equation. Then I present a scheme of calculating direct arrival traveltimes. Finally, I show several numerical examples of calculating direct arrival traveltimes. This scheme successfully computes the traveltimes of direct arrivals and is computationally efficient. The method is presented in two dimensions.

2.2 Why direct arrival travel times

Figure 2.1(a) shows the depth profile of a one-dimensional two layer velocity structure. Figure 2.1(b) shows the snapshot wavefield at 0.16 seconds. The wavefield is simulated by the finite-difference solution to the scalar wave equation. The source is located at the upper left corner. The source wavelet is the first derivative of the Gaussian function. For this model, a head wave is generated and part of its travel path is the boundary separating the slow and the fast medium. The head wave is a boundary wave, which carries very little energy. Figure 2.1(c) is the common shot gather or seismograms recorded by receivers located at the right edge of Figure 2.1(b). From Figure 2.1(b) and (c), one can see that the first arrival - head wave, travels ahead of the direct arrival and is much weaker than the direct arrival. If the traveltimes of the head wave in the slow medium were used for transmission traveltime tomography, the slow velocity medium would be inverted as an erroneous high velocity medium. And reflections that are used by migration to image velocity discontinuities are not generated by the first arrival head wave. But if the traveltimes of the head wave in the slow medium were used in migration, the velocity boundary would be mispositioned in the resulting image. Thus traveltimes of the first arrival - head wave, are not suitable as inputs for transmission traveltime tomography and migration imaging. Instead, the traveltimes of direct arrivals should be used. The overlay on Figure 2.1(b) and (c) are the direct arrival traveltimes computed by this finite-difference scheme of solving the eikonal equation. The direct arrival traveltimes closely match the first breaks of the direct arrivals computed by finite-difference wave equation modeling.

Figure 2.2 compares the travel times computed using Vidale's scheme (1988) on the same velocity model and computational parameters as in Figure 2.1. One can see Vidale's scheme computes the first arrival travel times. And the travel time wavefront tends to go

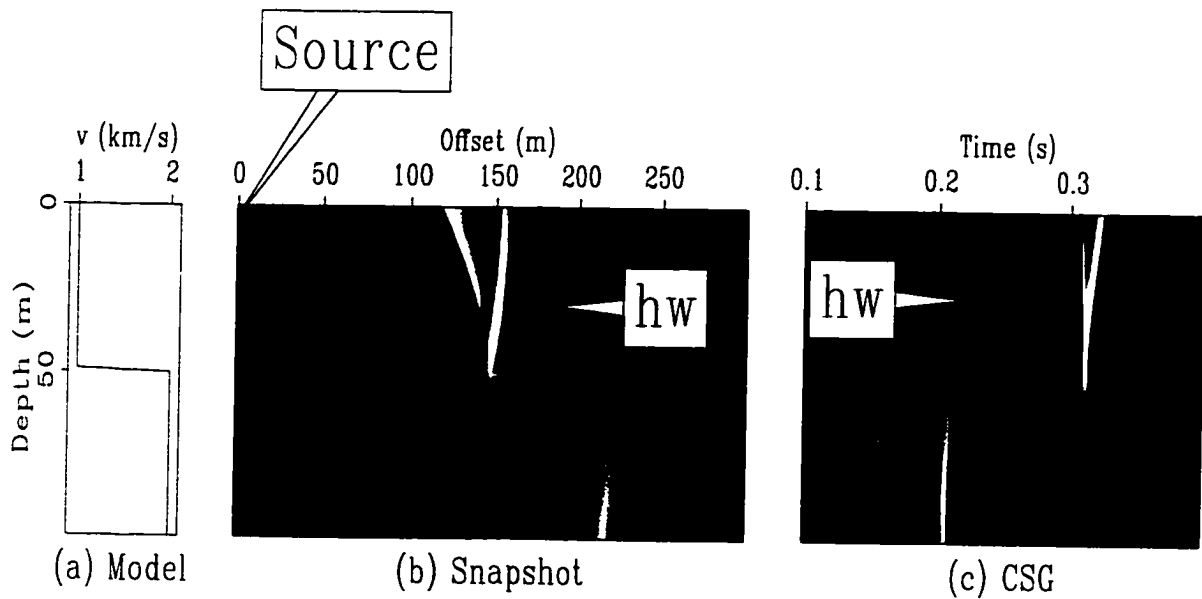


Figure 2.1: (a) shows the one-dimensional velocity depth profile. (b) shows a modeling snapshot wavefield at 0.16 second, the source is located at the upper left corner. (c) shows the common shot gather with the receivers at the right edge of (b). Overlaid on (b) and (c) are the travel times of direct arrival computed using this scheme of solving the eikonal equation.

ahead of the wavefront of the wavefield when post-critical incidence occurs.

Figure 2.3 shows a common shot gather from a cross-well field survey. The source is located in a low velocity zone. It shows similar wave phenomena as in the above synthetic data, that the first arrival – head wave, arrives at the receivers earlier than the direct arrival body wave, and is weaker than the latter.

2.3 Ray tracing

Figure 2.4 is a two layer velocity model. The lower medium has higher velocity. In ray tracing, the incident ray at point *C* is at critical incidence and generates a creeping ray along the boundary. The incident rays to the left of point *C*, e.g., at point *A*, are pre-critical and generate refracted waves in the lower medium. The incident rays to the right of point *C*, e.g., at point *B*, are post-critical, where total reflection occurs. For post-critical incident rays, the sine of the refraction angle is greater than 1 and the incident wavefront in the slow medium and the creeping wavefront in the fast medium are discontinuous across the interface. Transmission ray tracing can be performed for pre-critical incident

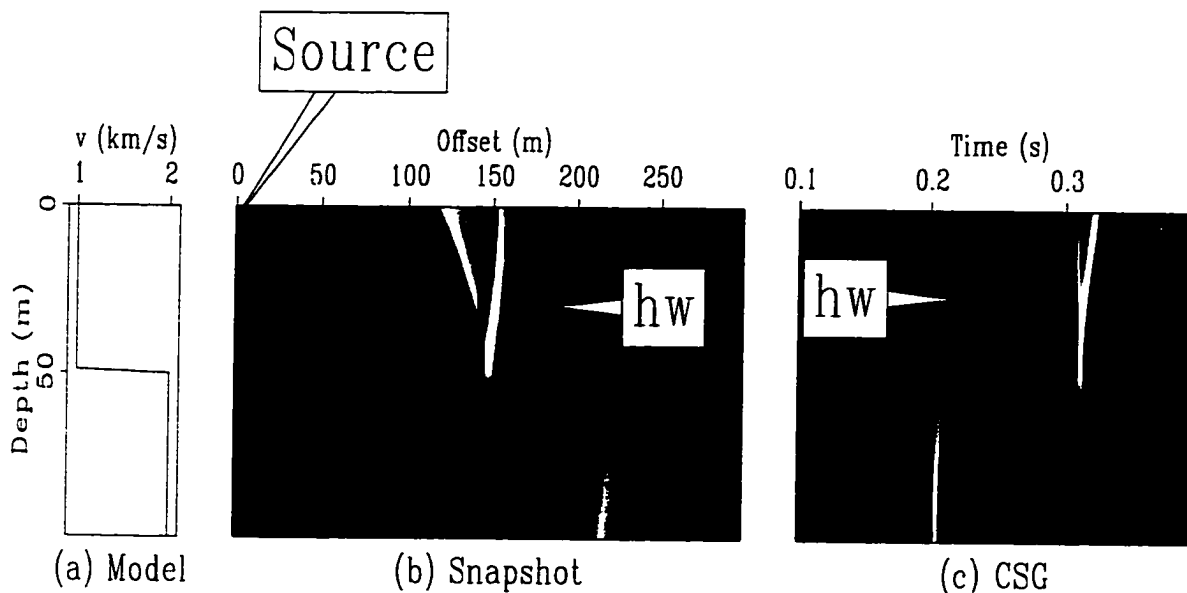


Figure 2.2: (a) shows the one-dimensional velocity depth profile. (b) shows a modeling snapshot wavefield at 0.16 second, the source is located at the upper left corner. (c) shows the common shot gather with the receivers at the right edge of (b). Overlaid on (b) and (c) are the travel times of first arrival computed using Vidale's scheme of solving the eikonal equation.

rays to the left of point C . However, transmission ray tracing can not be performed for post-critical incident rays to the right of point C . That is, transmission ray tracing is performed only until total reflection occurs, or until the sine of the refraction angle is equal to 1.

2.4 Solving the eikonal equation

In a two dimensional medium, the traveltme of wave propagation is described by the eikonal equation, which relates the gradient of traveltimes to the slowness of the medium,

$$\left(\frac{\partial t}{\partial x}\right)^2 + \left(\frac{\partial t}{\partial z}\right)^2 = s^2(x, z) \quad (2.1)$$

where (x, z) is the spatial coordinate, t is traveltme, and $s(x, z)$ is slowness. I parameterize the medium using square cells, with mesh spacing h , Figure 2.5. In a localized cell of Figure 2.5, when traveltimes at three corners a , b and c are known, the traveltme at the fourth corner — d can be computed by a finite-difference method based on the assumption of local plane wave propagation. I use the centered finite-difference (Vidale, 1988) to approximate

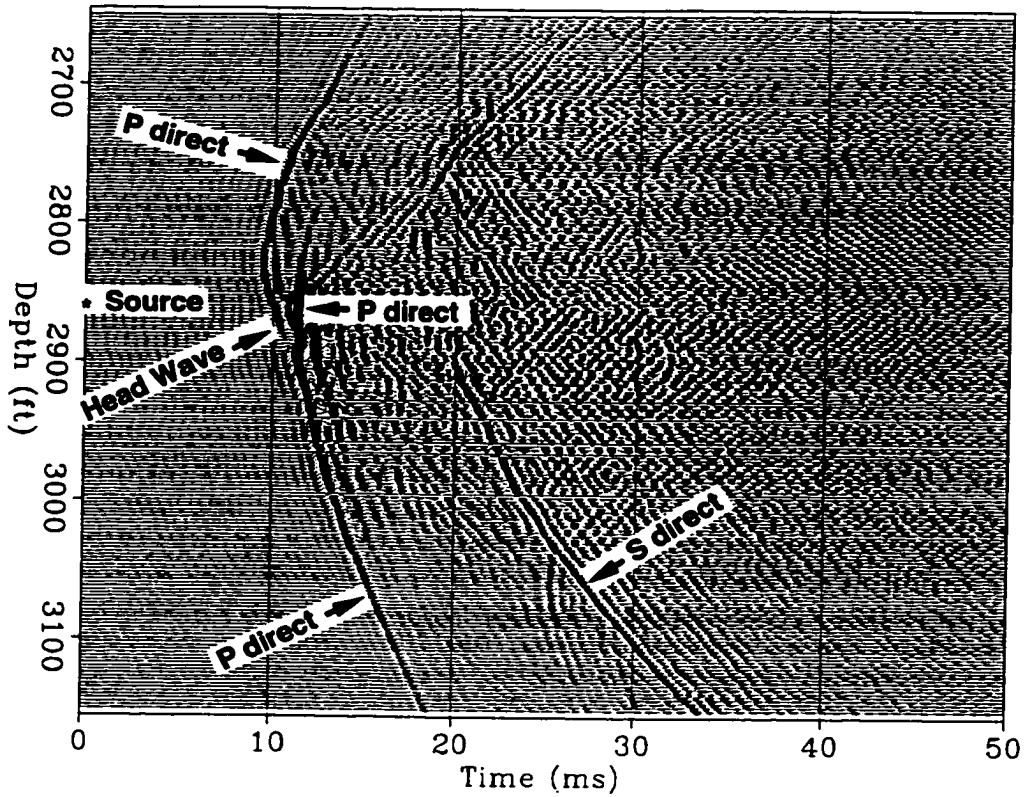


Figure 2.3: A field cross-well common shot gather. The source is at the depth of 2860 ft, and is in a low velocity zone. The first arrival - head wave, arrives at the receivers ahead of the direct arrival body wave, and is weaker than the latter.

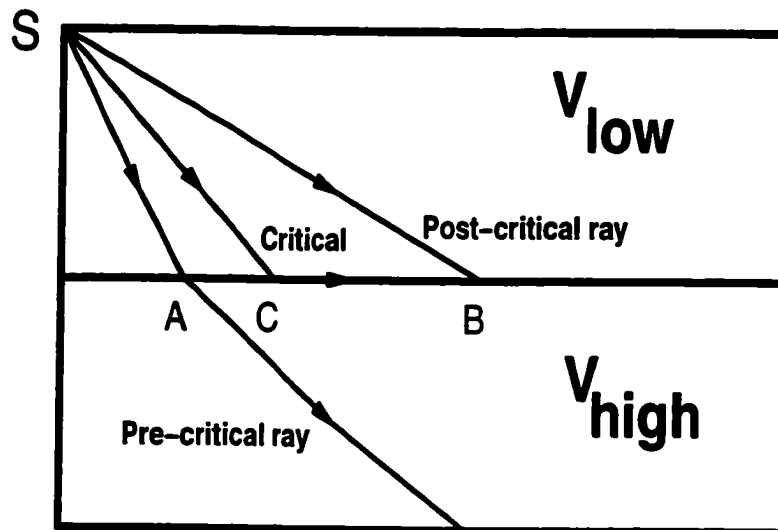


Figure 2.4: Incident ray at point C is in critical incidence, it generates a creeping boundary ray along the interface. Incident ray at A (B) is in pre-critical (post-critical) incidence.

the two differential terms in equation (2.1) based on the assumption of local plane wave

$$\frac{\partial t}{\partial x} = \frac{1}{2h}(t_b + t_d - t_a - t_c), \quad (2.2)$$

and

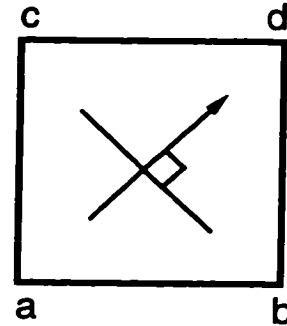
$$\frac{\partial t}{\partial z} = \frac{1}{2h}(t_c + t_d - t_a - t_b). \quad (2.3)$$

Substituting equations (2.2) and (2.3) into equation (2.1) gives

$$t_d = t_a + \sqrt{2(hs)^2 - (t_b - t_c)^2}, \quad (2.4)$$

where h is mesh spacing, s is the slowness inside the cell with the grid index of corner d , t_a , t_b , t_c and t_d are the traveltimes at the corners a , b , c and d . Finite-differences in equations (2.2) and (2.3) have first order numerical accuracy.

Figure 2.5: In a square cell with constant slowness s , wave propagates from corner a to corner d through corners b and c . Traveltimes are larger at corner b than at corner a .



Equation (3.4) can only be used for traveltimes calculation at pre-critical incidence. At post-critical incidence, the problem is to compute the square root of a negative number. Setting the negative number inside the square root to zero (Vidale, 1988, 1990) does not conform to the physical phenomena. When geometrical ray theory is valid and the direct arrival wavefronts are continuous across an interface, the time difference between diagonal nodes of a square cell is at most $\sqrt{2}hs$, where h is the mesh spacing of the cell and s is the slowness inside the cell. Thus there are three equivalent indications of post-critical incidence, the sine of the refraction angle being greater than 1, the direct arrival wavefronts being discontinuous across an interface and the time difference between diagonal nodes of a square cell being greater than $\sqrt{2}hs$. Thus in solving the eikonal equation, the term inside the square root of equation (2.4) is negative at post-critical incidence. When at post-critical incidence, I use creeping wave (which is a direct arrival)

to compute traveltimes along the velocity boundary. In a discrete velocity model, dipping interfaces are represented by stairways. I assume the dips of velocity interfaces to be less than 45 degrees, so that I can use the horizontal parts of the stairways to approximate a dipping interface.

Depending on whether at the left/right or top/bottom side of the expanding computational ring (to be discussed below), the corners a , b , c and d are oriented differently (Figure 2.6). But edge ab is always at the interior and edge cd at the exterior of the computation front. When edge ab lies in a horizontal direction and wave travels from a to b , at post-critical incidence corners a and b are in the slow velocity medium, and corners c and d are in the high velocity medium. In geometric ray theory, the direct arrival to corner d is a creeping ray from corner c . The traveltime at corner d is then computed as

$$t_d = t_c + hs. \quad (2.5)$$

On the other hand, if edge ab lies in a vertical direction and wave travels from a to c , at post-critical incidence the direct arrival to corner d is a creeping ray from corner b . The traveltime at corner d is then computed as

$$t_d = t_b + hs. \quad (2.6)$$

Slowness value s is the slowness inside the cell with the grid index of corner d .

I have described the traveltime computation at a localized cell. Next, I describe the arrangement of computation orders.

2.4.1 Computation order

Traveltime computation is initialized by assuming straight ray paths in a constant velocity square surrounding the source point. The square with the length of a side $5h$ is a generally good choice for the initialization. Traveltime computations are then carried out by expanding squares around the source point, as the computation layout in Figure 2.7 shows. The filled circles indicate grid points that have had their traveltimes calculated. I use the traveltimes at the boundary ring of grid points, large filled circles, to compute traveltimes of grid points at an outer ring, the hollow circles. The inductive scheme for calculating a new ring of traveltimes is now described. Computations proceed sequentially on the four sides, as shown in Figure 2.7. To initialize computation at an edge, the points in the inner edge are examined in a loop from one end to the other to locate the points

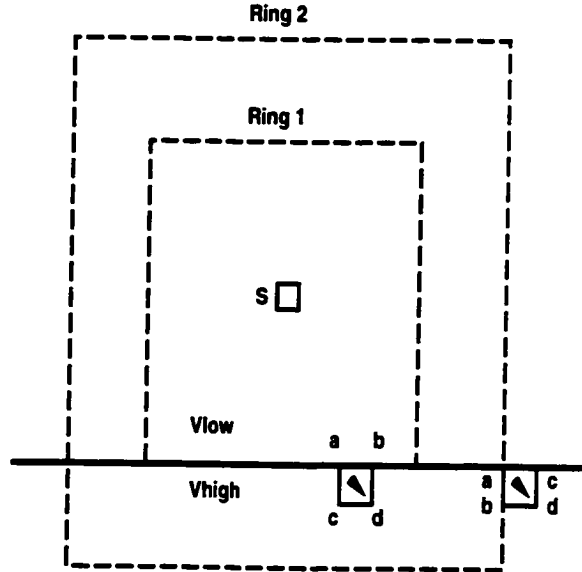


Figure 2.6: At a velocity interface separating V_{low} from V_{high} , depending on the orientation of the cell with the expanding computational ring, the traveltime of direct arrival creeping wave to corner d is computed from either corner c or b .

with local minimum traveltimes, Figure 2.8. I use the following finite-differences and plug them in the eikonal equation (2.1)

$$\frac{\partial t}{\partial x} = \frac{1}{2h}(t_b - t_c), \quad (2.7)$$

and

$$\frac{\partial t}{\partial z} = \frac{1}{h}(t_d - t_a). \quad (2.8)$$

The traveltime of the point outside the point with local minimum traveltime is computed as

$$t_d = t_a + \sqrt{(hs)^2 - 0.25(t_b - t_c)^2}, \quad (2.9)$$

where t_d is the time to be found, t_a is the local minimum traveltime in the inside row, t_b and t_c are the traveltimes of the two neighboring grid points, s is the slowness with index of node d . However, if the term inside the square root of equation (2.9) is negative, the traveltime at node d is computed as

$$t_d = t_a + hs. \quad (2.10)$$

At the next stage, equations (2.4), (2.5), and (2.6) are applied to compute traveltimes sequentially on the four edges.

In application of equation (2.4), the propagation direction of local plane wave does not come in play. The traveltimes at the three corners a , b and d can also be used to compute the traveltime at corner c based on the assumption of a local plane wave. Equations (2.5) and (2.6) are then changed by computing the right hand side unknown traveltime from the left hand side known traveltime. However, it is easier to program calculation from small traveltimes to large traveltimes, i.e., in a upwind format.

Consider calculating traveltimes at edge 1 (top) of Figure 2.9. Application of equation (2.4) is carried out in three loops. The first loop progresses from the left end to the lateral location of the source. Then the second loop progresses from the right end to the left end. Finally the third loop progresses from the lateral location of the source to the right end. During each loop, calculation starts at each point of local minimum traveltime and progresses until a point of local maximum traveltime is reached. Similar traveltime calculations are carried out sequentially for the other three sides. In physical models, one can expect the direct arrival waves to be out-going from the source. On both sides of the source in Figure 2.9, travel times of the out-going waves have the chance to wipe out the earlier computed travel times of possible in-coming waves. In this computation layout, travel times at the relative maxima are computed from both sides, the travel time of the outgoing wave (computed later) replaces that of the incoming wave (computed in an earlier loop).

As shown in Figure 2.7, the start and end point indices of the computation layouts are not the same for the four edge (Podvin and Lecomte, 1991). Thus, the computed travel times can have artificial anisotropy even for isotropic velocity models at the 45-degree diagonal directions from the source. To alleviate the artificial anisotropy, I rotate the first of the four edges to start computation. For example, in Figure 2.7 I perform computation sequentially at the top, right, bottom and left edges, then at the next ring I perform computation sequentially at the right, bottom, left and top edges, and so on.

2.5 Travel time examples

Figure 2.10 shows in the grey-scale background a complicated 1-D velocity model. It also shows the traveltime contours of direct arrivals with the source at the upper left corner. All the possible direct arrivals in 1-D medium are correctly modeled. It has transmission from high velocity medium to low velocity medium, transmission and creeping boundary wave

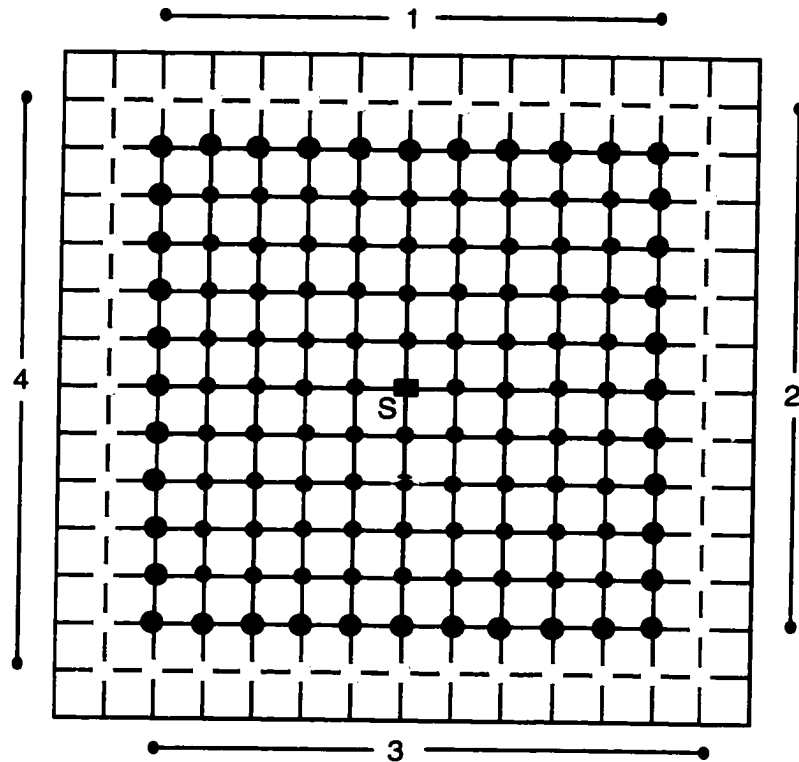


Figure 2.7: S is the source grid point. Traveltime computations proceed sequentially on the four sides, first the top, then the right, then the bottom, and finally the left side. For the line outside the frame, e.g., the one at the top of the figure, the two end dots designate the left/right ends of the top computation edge.

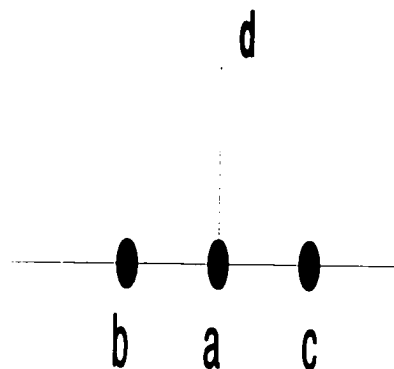


Figure 2.8: The first step in computing travel times at an edge is to loop over the edge to locate points with local minimum travel times. In this case, $t_b > t_a$ and $t_c > t_a$, t_a is a local minimum. Travel times at local minimums are computed first.

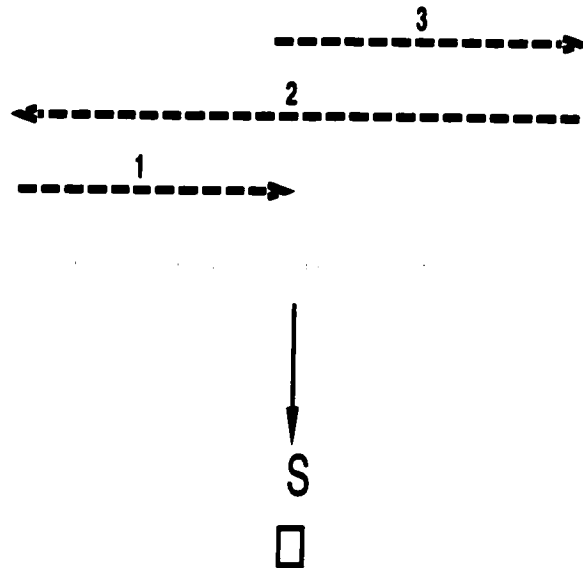


Figure 2.9: Computation of travel times at an edge is carried out in three sequential loops. The hollow circles represent nodes of a slowness model. S is the lateral/vertical position of the source. Travel times of waves diverging from the source replace possible previously computed travel times of waves converging toward the source.

from low velocity medium to high velocity medium, and overturning waves in medium with linear increasing velocities. Figure 2.11 overlays a snap-shot wavefield computed by finite-difference wave equation modeling with the corresponding direct arrival traveltimes computed by this eikonal equation solver. There is a close match between the traveltimes and the waveforms.

Figure 2.12 shows a 2-D velocity model and the traveltime contours of direct arrivals. Figure 2.13 shows a wave equation modeling snap-shot wavefield and the corresponding direct arrival traveltime contour. The transmissions from high velocity medium to low velocity medium, and from low velocity medium to high velocity medium are correctly described. However, there are some jitters on the traveltime contours along the 45-degree direction from the source, which is owing to the numerical inaccuracy incurred by the stairway approximation of dipping interface.

2.6 A posteriori ray tracing

After travel times have been computed for all the grid nodes, ray path from any receiver grid point back to the source can be traced by following the steepest descent direction

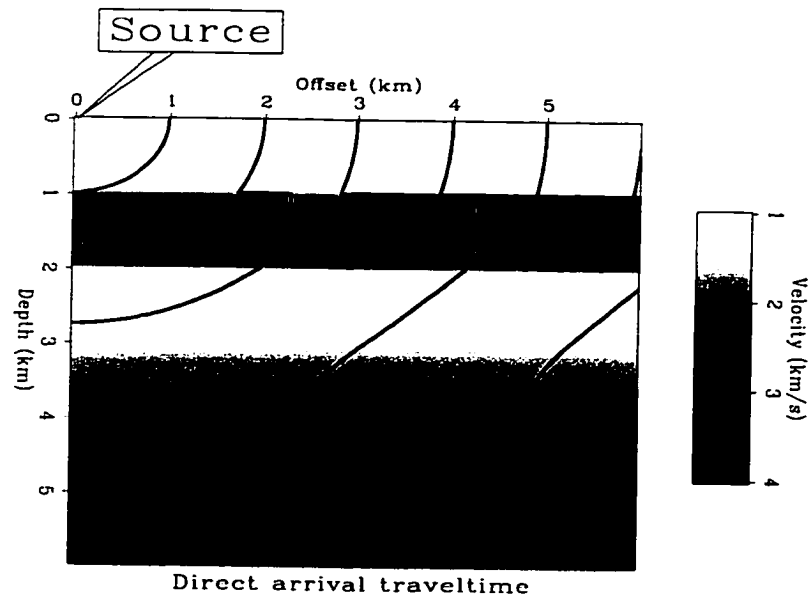


Figure 2.10: Shown at the grey-scale background is a 1-D velocity model. The contours show the direct arrival traveltimes from a source located at the upper left corner.

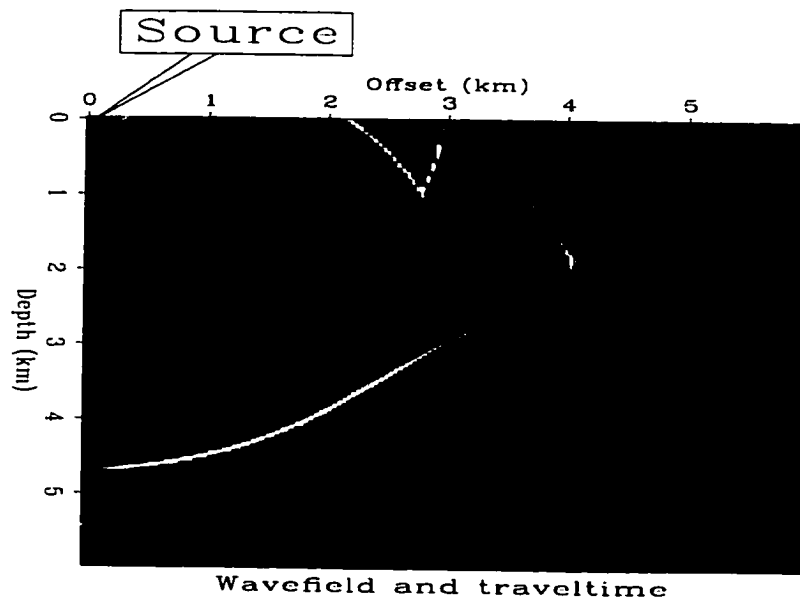


Figure 2.11: Comparison of the calculated direct arrival traveltimes and the snapshot wavefields calculated by finite-difference wave equation modeling at 3 seconds.

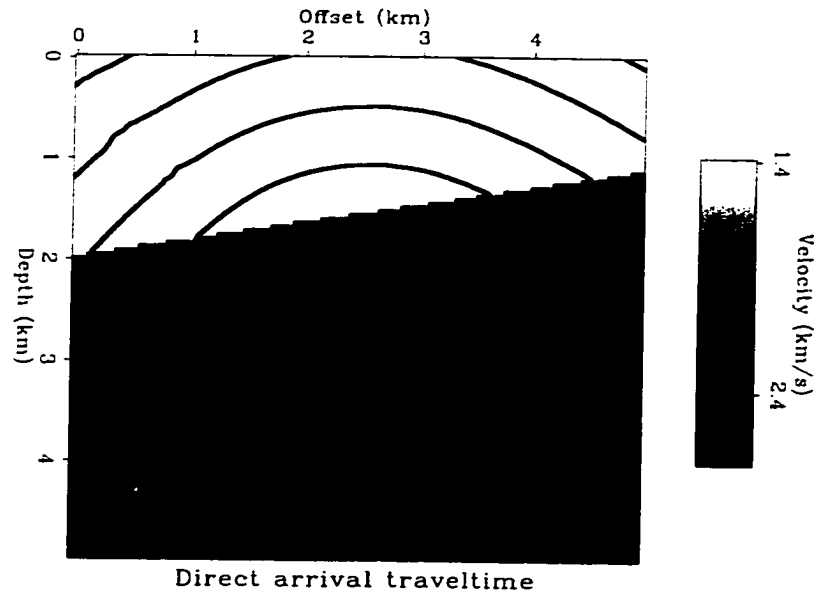


Figure 2.12: Shown at the grey-scale background is a 2-D velocity model with dipping velocity interfaces. The contours show the direct arrival traveltimes from a source located at the center of the model.

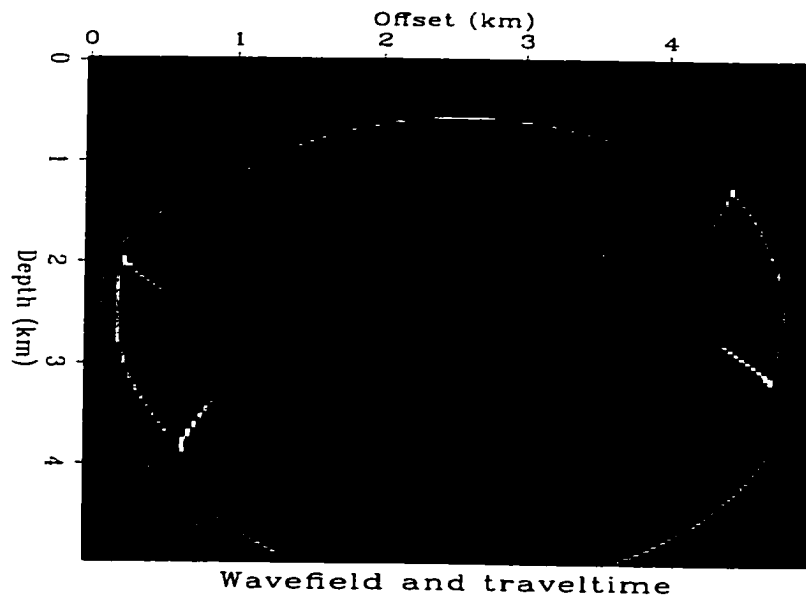


Figure 2.13: Comparison of the calculated direct arrival traveltimes and the snap-shot wavefields calculated by finite-difference wave equation modeling.

through the travel time field (Aldridge and Oldenburg, 1993). I adapt the method for cross-well direct arrival ray tracing that can compute ray paths of critical incidence wave. The ray paths are guaranteed to end at the source as the source point has the smallest travel time, zero. The derivatives of the travel time gradient direction in a cell are computed by using the following finite-difference equations, Figure 2.14.

$$\frac{\partial t}{\partial x} = -\frac{1}{2h}(t_b + t_d - t_a - t_c) \quad (2.11)$$

and

$$\frac{\partial t}{\partial z} = \sqrt{\max(0, s^2 - \left(\frac{\partial t}{\partial x}\right)^2)} \text{signum}(t_c + t_d - t_a - t_b) \quad (2.12)$$

Equation (3.11) is different from equation (2.2), because ray tracing follows the steepest descent direction of the travel time field. The z derivative computed in the above equation (2.12) guarantees that pre-critical and critical ray paths are correctly handled. Ray path in a cell is modeled as a straight line segment, being consistent with travel time computation, which assumes local plane wave.

In cross-well ray tracing with the source located at the left well and the receivers at the right well, a ray path crossing a slowness cell can enter the cell on the right, top, and bottom boundaries of the cell, and can leave the cell on the left, top, and bottom boundaries. The lengths of the ray path segment within the cell ranges from zero to a maximum of $\sqrt{2}h$. For a fixed source, all ray paths that cross a specified cell have the same direction in the cell. Ray segment in a cell is computed by using geometrical theory.

Figure 2.15 shows the direct arrival ray paths calculated on the velocity model and travel time map of Figures 2.10 and 2.11. It shows straight ray paths in constant velocity medium, transmission ray paths from low (high) to high (low) velocity layers, and over-turning ray paths in medium with linearly increasing velocity gradient. In this model, 500 ray paths can be computed in one minute. I only display 10 of them for presentation purpose.

2.7 Discussion

In this traveltimes calculation scheme, the velocity model is parameterized as constant velocity cells. The finite difference scheme has first order of numerical accuracy. As seen in Figures 2.1, 2.11 and 2.13, the calculated direct arrival traveltimes closely match the

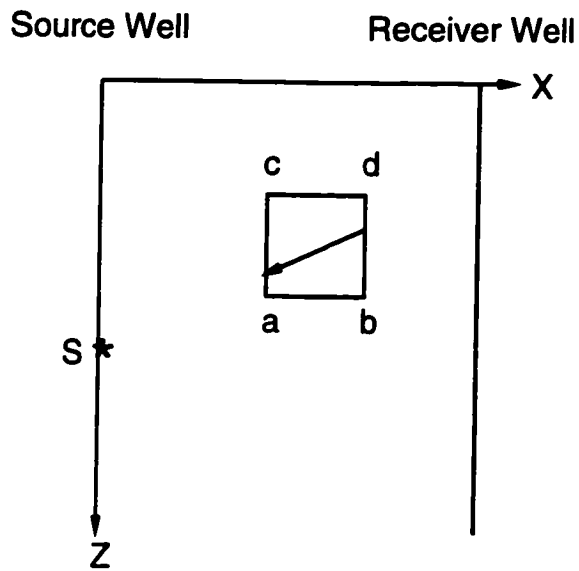


Figure 2.14: Ray direction in a cell is computed following the steepest descent direction of the travel time map.

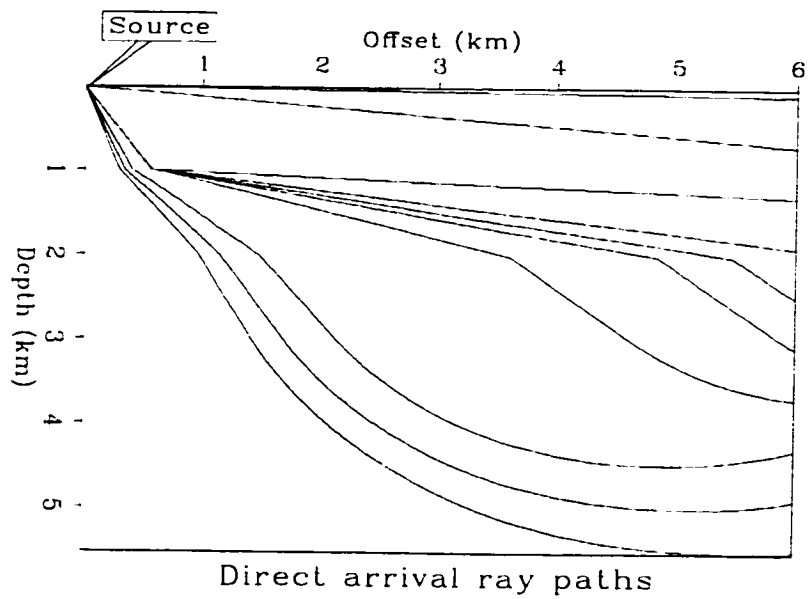


Figure 2.15: Direct arrival ray paths calculated on the velocity model and geometry of Figures 2.10 and 2.11.

arrival times of the direct arrival waveforms of wave equation modeling. The direct arrival traveltimes calculated by this scheme are accurate up to the spatial and temporal sampling requirements in traveltime tomography and seismic migration.

The computational cost of this scheme at each grid point is to evaluate equation (2.4). For a model of realistic size, say 250,000 grid points, computational time is just a few seconds at a modern workstation with computation speed of Mflops/s, e.g., IBM RS6000. Thus, this method promises to be very useful in computing traveltime tables for tomography and migration imaging.

2.8 Conclusions

Direct arrivals are usually the most energetic events in a time evolving wavefield. Travel-times of direct arrivals are needed in transmission traveltime tomography and migration imaging. This new scheme of finite-difference solves the eikonal equation successfully and computes the traveltimes of direct arriving waves. The computed traveltimes closely match the arrival times of the direct arrival waveforms computed by finite-difference wave equation modeling. By incorporating physical wave phenomena in travel time computation and carefully handling travel time computation at critical incidence, computing the square root of a negative number is avoided and the method is guaranteed to be stable.

Chapter 3

Analysis and attenuation of tube waves for cross-well seismic survey

Seismic data collected in a crosswell survey often contain strong tube waves that have parts of their travel paths along wells where the sources and receivers are positioned. Tube wave can be excited by the source and propagates along the source well. This tube wave radiates as body wave at the impedance discontinuities of the source well, propagating to the receiver well to be recorded. This is called the source well tube wave. Tube wave can also be excited by passing body waves at the impedance discontinuities of the receiver well, propagating along the receiver well to be recorded. This is called the receiver well tube wave. By the principle of reciprocity, source and receiver well tube waves have similar characteristics and can be attenuated by the same method. Because of the slow propagation velocity of the tube waves in the fluid, they are usually spatially aliased in field recorded data, in either common shot gathers (CSG) or common receiver gathers (CRG). While receiver well tube waves are aliased in CSG, they are well sampled and predictable in CRG, and vice versa for source well tube waves. Tube waves that have travel paths in both the source and receiver wells are also predictable. I predict and attenuate source well tube waves in CSG, and predict and attenuate receiver well tube waves in CRG.

3.1 Introduction

Seismic data recorded in a crosswell survey often contain strong tube waves. These tube waves can be stronger than any useful body waves being recorded. Most geophysicists view the tube waves as undesirable coherent noise because they are superimposed on reflection signals and prevent optimum imaging of stratigraphic and structural targets in the subsurface. Thus, attenuation of tube waves has been the topic of extensive current research. One method to attenuate tube waves is to apply special equipment in field data recording (Pham et al., 1993). Even though tube waves are attenuated in field data recording, they are still recorded. Then one has to resort to numerical processing techniques. Cai and Schuster (1993) aligned tube waves along their travel time picks in common shot gathers and common receiver gathers and applied a median filter to predict tube waves. Finally, the predicted tube waves are subtracted from the field data. In this method, tube wave travel times must be picked and upgoing and downgoing tube waves are processed separately. Another problem with this method is the difficulty handling the data in a polygonal area when the tube waves are aligned. When the wells are not straight, the travel time trajectories of the tube waves are not straight, then the travel times of the tube waves are difficult to pick.

In this paper, I first analyze the generation and propagation of tube waves in a crosswell experiment. Then I show how to predict and attenuate source well tube waves in CSG, and predict and attenuate receiver well tube waves in CRG. The method is shown to be effective in attenuating tube waves in a field data set.

3.2 Analysis of cross-well tube waves

In crosswell seismic surveying using a downhole source, the source excites body waves, and it also excites a tube wave propagating in the borehole fluid called the source well tube wave. When the tube wave encounters an impedance discontinuity in the source well, it excites body waves that propagate to the receiver well to be recorded. Common impedance discontinuities in a borehole are changes of borehole diameters, junction points between casing and noncasing, perforation, and the top and bottom of the borehole. And according to numerical calculations and field data, body waves excited by tube waves at these impedance discontinuities can often be stronger than the body waves directly excited by the source (Balch and Lee, 1984).

When body waves from the source well impinge the receiver well, they are recorded by the receivers. And at the same time, strong tube waves are excited at impedance discontinuities and propagate along the receiver well. The excitation and propagation of body waves and tube waves in a crosswell experiment are schematically illustrated in Figure 3.1 for the recording of a common shot gather. Squares in the two wells represent the locations where tube waves are generated. Figure 3.2 is a synthetic CSG obtained by ray tracing with the experimental geometry of Figure 3.1(a) assuming constant velocity.

Figure 3.3 schematically illustrates the wave propagation and the travel time trajectories in a common receiver gather. By the principle of reciprocity, a common receiver gather can be considered as a common shot gather. And this can be realized by reversing the wave propagation directions (the directions the arrows point) in Figure 3.3(a). Thus, source and receiver well tube waves have similar characteristics and can be analyzed by the same method. Figure 3.4 is a synthetic CRG with the experiment geometry of Figure 3.3(a). Notice how the aliasing and dealiasing of the events change between CSG and CRG, Figure 3.2 and Figure 3.4.

Because of the slow propagation velocity of the tube waves, the receiver (source) well tube waves have steep slopes in the common shot (receiver) gathers. In discretely sampled field data, these steep events are usually spatially aliased. However, in the other domain, they are well sampled and predictable. For the source (receiver) well tube waves in a CSG (CRG), they are well sampled and predictable. For those tube waves that have propagation paths in both the source and receiver wells, even though they are aliased, they are also predictable.

In neighboring CSG's, the source well tube waves 2 and 22 in Figure 1 and Figure 2 vary by a static time delay, the time that the source well tube wave propagates between neighboring source positions. Likewise, in neighboring CRGs, the receiver well tube waves 12 and 22 in Figure 3 and Figure 3 vary by a static time delay, the time that the receiver well tube wave propagates between neighboring receiver positions. I apply this observation to predict and estimate tube waves.

3.3 Attenuation of cross-well tube waves

When the source is at a location that excites source well tube wave, the source direct arrival and source well tube wave are time coincident; this is demonstrated as the source

Common Shot Gather

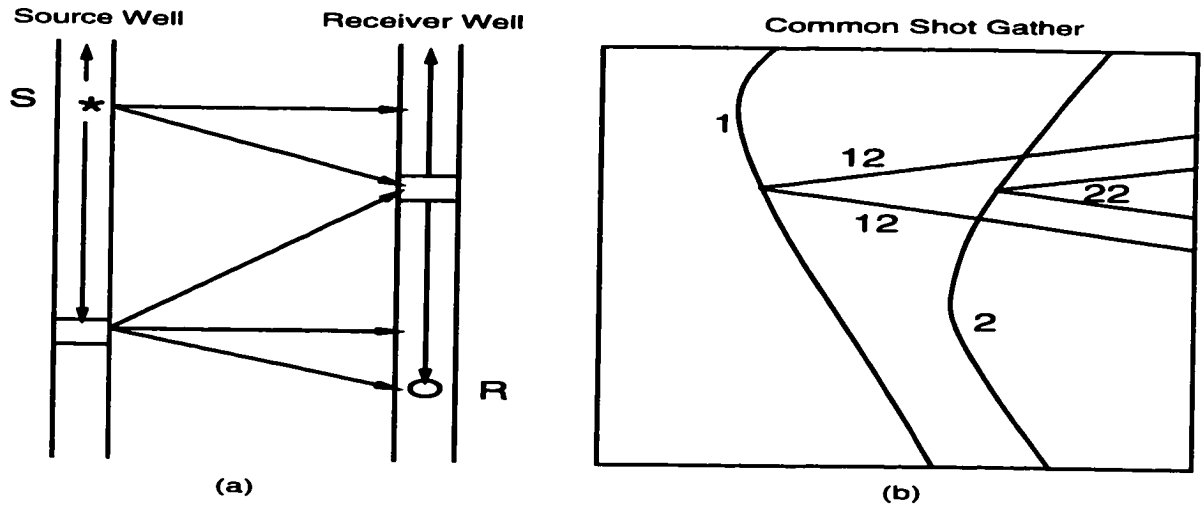


Figure 3.1: (a) is the crosswell experiment setup. (b) is the travel time trajectory of a common shot gather. In (b), 1 is the direct arrival, 2 is the body wave excited by the source well tube wave, 12 (22) is the receiver well tube wave excited by 1 (2).

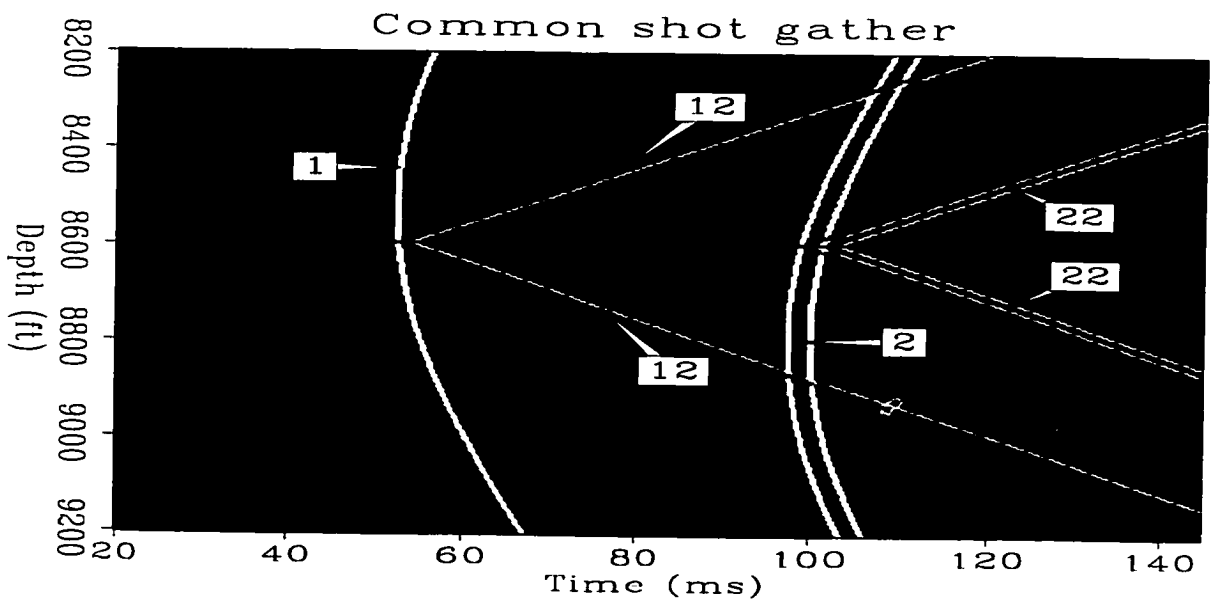


Figure 3.2: A synthetic common shot gather. Events 1, 2, 12, and 22 have the same descriptions as in Figure 3.1(b).

Common Receiver Gather

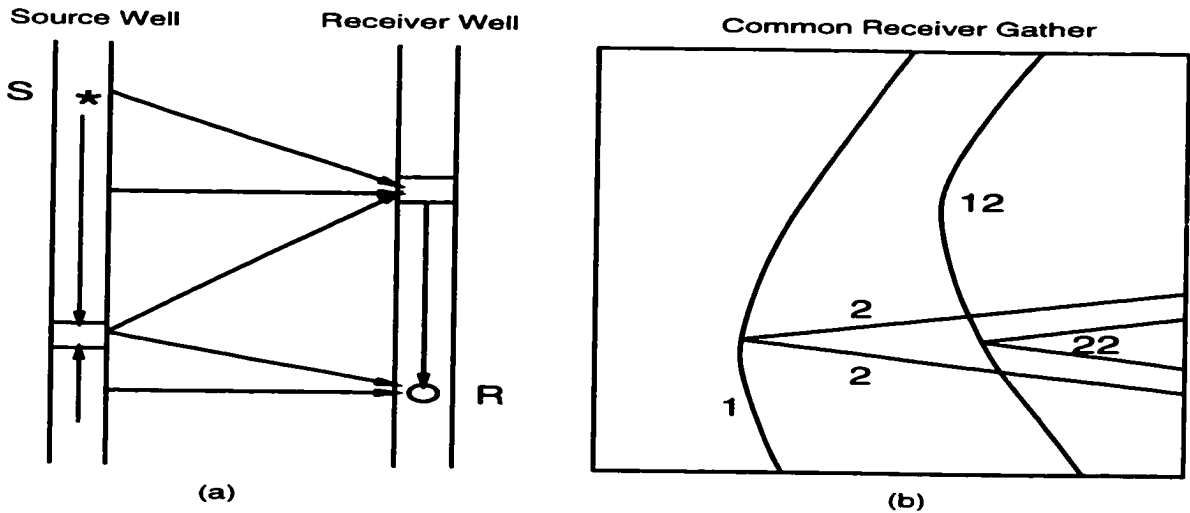


Figure 3.3: (a) is the crosswell experiment setup. (b) is the travel time trajectory of a common receiver gather. In (b), 1 is the direct arrival, 2 is the body wave excited by the source well tube wave, 12 (22) is the receiver well tube wave excited by 1 (2), as in Figure 3.1. By the principle of reciprocity, 1 can be considered as the first arrival excited by the receiver, 12 is the body wave excited by tube wave in the receiver well, 2 (22) is the source well tube wave excited by 1 (12). And these waves are "recorded" by the sources.

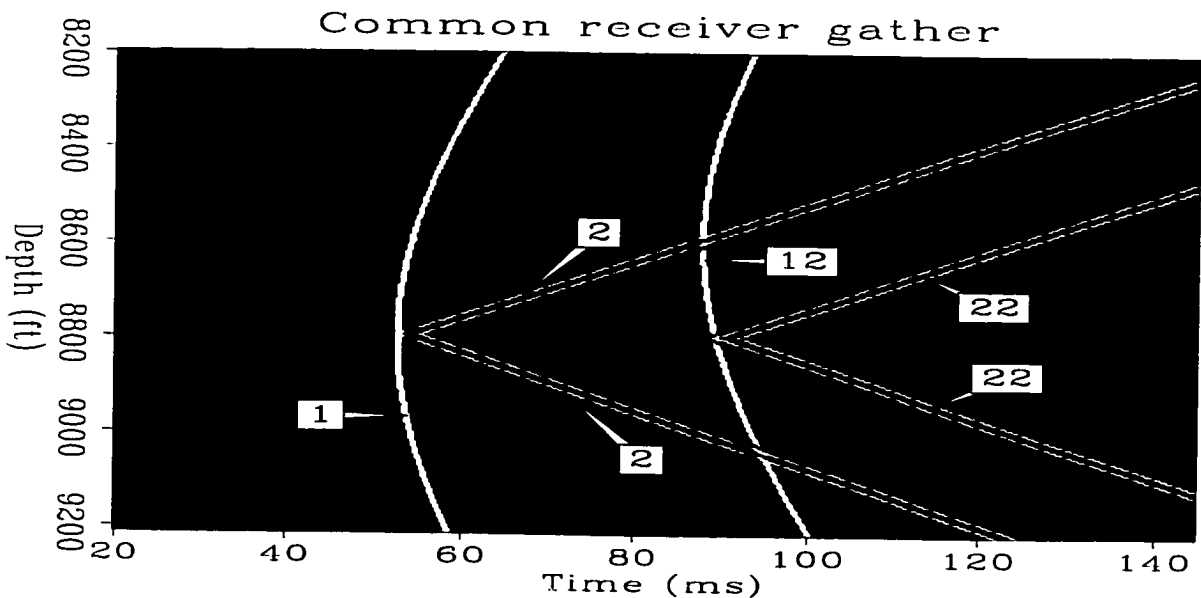


Figure 3.4: A synthetic common receiver gather. Events 1, 2, 12, and 22 have the same descriptions as in Figure 3.3. Polarities help to identify the corresponding events between Figure 3.2 and Figure 3.4. Notice how the aliasing and dealiasing of the tube wave events vary between Figure 3.2 and this figure.

at the location S in Figure 3.5. I pick the direct arrival travel time trajectory of this CSG (I call it TT). For a source located away from the location that excites source well tube wave, there is a time delay that the tube wave takes to propagate from the source location to the source well tube wave excitation point (I call it delay); this is demonstrated as the sources at the locations S_{-1} , S_i and S_{+1} in Figure 3.5. This tube wave travel time delay can be computed from the wireline separation distance between sources in the borehole and the tube wave velocity in the fluid. Thus the travel time trajectory of the source well tube waves in these CSGs is TT + delay. Since one can predict the travel time trajectory of source well tube wave in CSG's, one can use the relationship between neighboring CSG's to estimate the source well tube wave. When the estimated source well tube wave is subtracted from the original CSG's data, source well tube wave is then attenuated.

A CSG data can be modeled as

$$D_i = S_i + T(t - t_0), \quad (3.1)$$

where i is the index of the CSG, D_i is the whole CSG data, T is source well tube wave (events 2 and 22 in Figure 3.1 and Figure 3.2), t is recording time, t_0 is the first arrival time trajectory of the tube wave as explained in the previous paragraph, S_i is the portion of the data other than T . A neighboring CSG around the i -th CSG can be modeled as

$$D_j = S_j + T(t - t_0 + \delta t_{ij}), \quad (3.2)$$

where T is the same as in equation (3.1) except for a time shift δt_{ij} (the time delay the tube wave travels between the source locations i and j , the time delay t_{BC} or t_{CD} in Figure 3.5). Cross-correlating D_i with D_j around t_0 and picking the time lag of the maximum correlation value can determine the time shift δt_{ij} . Cross-correlation can be carried out for the whole CSG, or for individual traces. The tube wave time delay δt_{ij} can also be computed from the wireline separation distance between the sources and the tube wave velocity in the fluid.

Neighboring CSG's are shifted to place the source well tube waves in phase and are stacked to estimate the source well tube waves for the i -th CSG.

$$\hat{T}_i = \frac{1}{2n + 1} \sum_{j=-n}^n D_{i+j}(t - \delta t_{ij}), \quad (3.3)$$

where n is the number of chosen CSG's on each side of the designated i -th CSG. In the following field data example, I choose n to be 5 so that the events other than the tube

waves to be estimated are attenuated by an order of magnitude in the stacking. The estimated source well tube wave \hat{T}_i is then subtracted from the CSG data D_i .

In practice, source well tube waves are excited at an identifiable finite number of points of impedance discontinuities. Source well tube waves excited at these points are individually estimated and attenuated. Finally, the data are sorted into CRG's, and estimation and attenuation of receiver well tube waves (events 12 and 22 in Figure 3 and Figure 3) are carried out by the same method as outlined above, using the principle of reciprocity. In order to apply this method, one must identify the locations where source (receiver) well tube waves are excited and pick the first arrival travel time trajectories of these particular CSGs (CRGs). These time picks are almost always ready from the shelf as they are part of the travel time picks routinely used for transmission travel time tomography. The locations in the receiver well where tube waves are excited can be easily identified in the CSGs as the junction points of the upward and downward slopes of the steeply dipping tube wave events, Figures 3.1 and 3.2. Whereas the locations in the source well where tube waves are excited can be easily identified in the CRGs, Figures 3.3 and 3.4. The tube wave velocity in the fluid can be measured from the slope of the steeply dipping tube wave events in either CSG or CRG.

3.4 Data examples

I apply the above method to a field crosswell data set, recorded in the Permian Basin, West Texas. The data set has 201 CSG's and 203 CRG's. Figure 3.6 is an unprocessed CSG, Figure 3.7 an unprocessed CRG. The borehole source excites both compressional (P -) and shear (S -) waves, as does the source well tube wave. In this data set, both the source and receiver well tube waves are much stronger than the body waves. The source (receiver) well has a perforation at the depth of 9000 ft (8930 ft) that excites source (receiver) well tube waves. First arrival time trajectory of this particular CSG (CRG) is picked and applied for the estimation of the source (receiver) well tube wave. Figure 3.8 is the estimated source well tube wave for the CSG data in Figure 3.6. Figure 3.9 is the result after subtracting the source well tube wave in Figure 3.8 from Figure 3.6. The direct arrival and reflections stand out much more clearly in Figure 3.9 than in Figure 3.6. After all the CSG's are processed, the data are sorted into CRG's.

Figure 3.10 is the new CRG of the CRG in Figure 3.7. Figure 3.11 is the estimated

Common Shot Gather

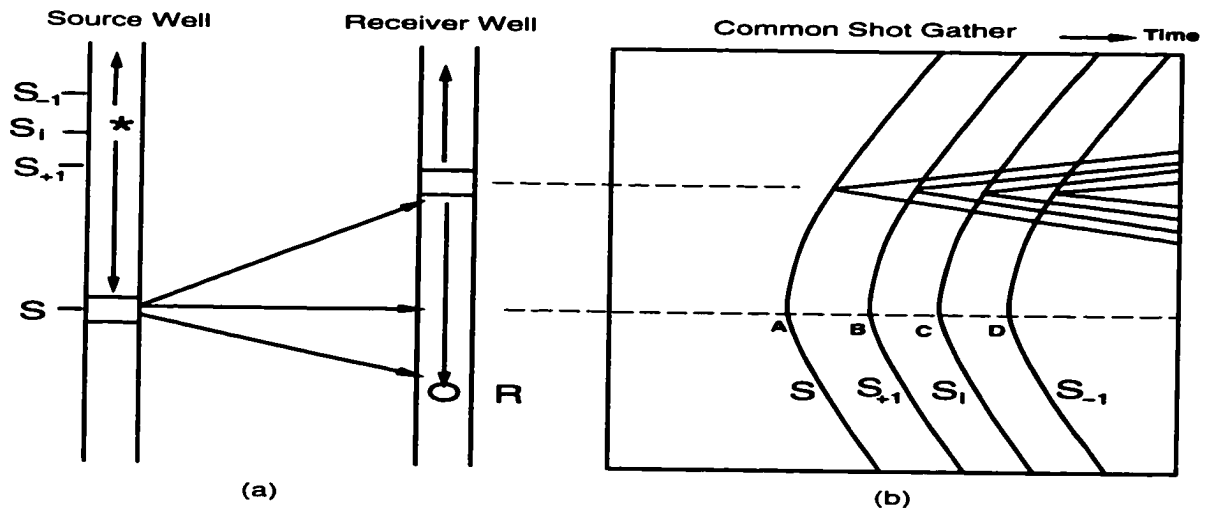


Figure 3.5: (a) is the crosswell experiment, sources at several locations are shown. Source S is at the location that excites source well tube waves. (b) Tube waves in several common shot gathers are overlaid. SA is where the source well tube wave and body wave are time coincident. S_iC is the tube wave corresponding to the source S_i . The time delay AC can be calculated from the distance S_iS and the tube wave velocity in the fluid. The time delay BC and CD can be similarly calculated.

receiver tube wave for the CRG data in Figure 3.10. Figure 3.12 is the result after subtracting the receiver well tube wave in Figure 3.11 from Figure 3.10. After all the CRG's have been processed, Figure 3.13 is the new CSG of the CSG in Figure 3.9. Comparing data in Figure 3.6 and Figure 3.7 to the processed data in Figure 3.12 and Figure 3.13, it is obvious that after attenuation of crosswell tube waves, the direct arrival and reflection of body waves stand out much more clearly.

3.5 Conclusions

The travel time delay relationship of tube waves excited in neighboring data gathers has been used for estimation and attenuation of tube waves. I predict and attenuate source well tube waves in common shot gathers, and then predict and attenuate receiver well tube waves in common receiver gathers. Neighboring CSGs (CRGs) are aligned and stacked to estimate source (receiver) well tube wave and the estimated source (receiver) well tube wave is subtracted from the CSG (CRG) data. Application of the method in a field data set has shown that it is effective. After attenuation of tube waves, body waves direct arrivals and reflections stand out clear, otherwise difficult to identify in the raw data.

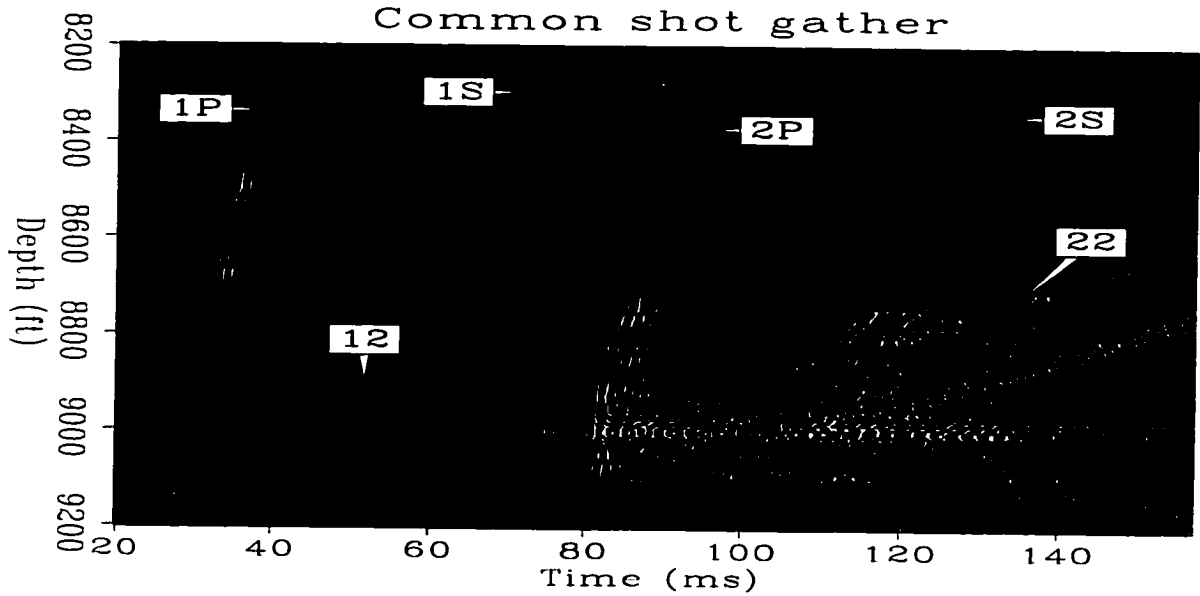


Figure 3.6: An unprocessed common-shot gather. Events 1, 2, 12, and 22 have the same descriptions as in Figure 3.1 and Figure 3.2. *P* (*S*) stands for *P*-wave (*S*-wave). Strong source well tube waves (events 2 and 22) are excited at the depth of 9000 ft.

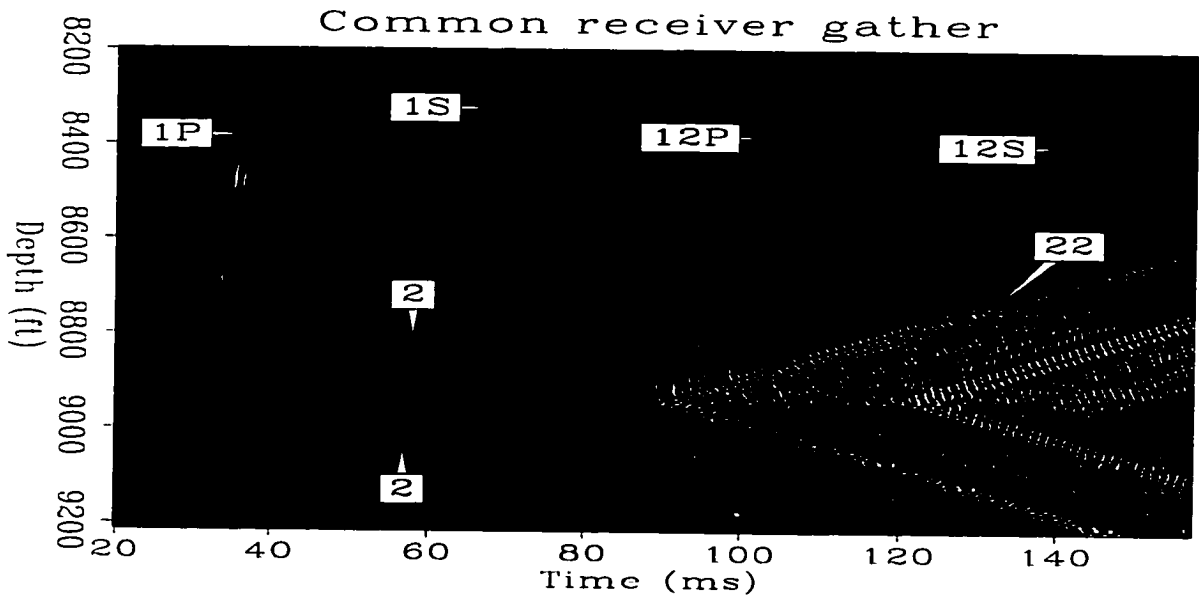


Figure 3.7: An unprocessed common-receiver gather. Events 1, 2, 12, and 22 have the same descriptions as in Figure 3.3 and Figure 3.4. *P* (*S*) stands for *P*-wave (*S*-wave). Strong receiver well tube waves (events 12 and 22) are excited at the depth of 8930 ft.

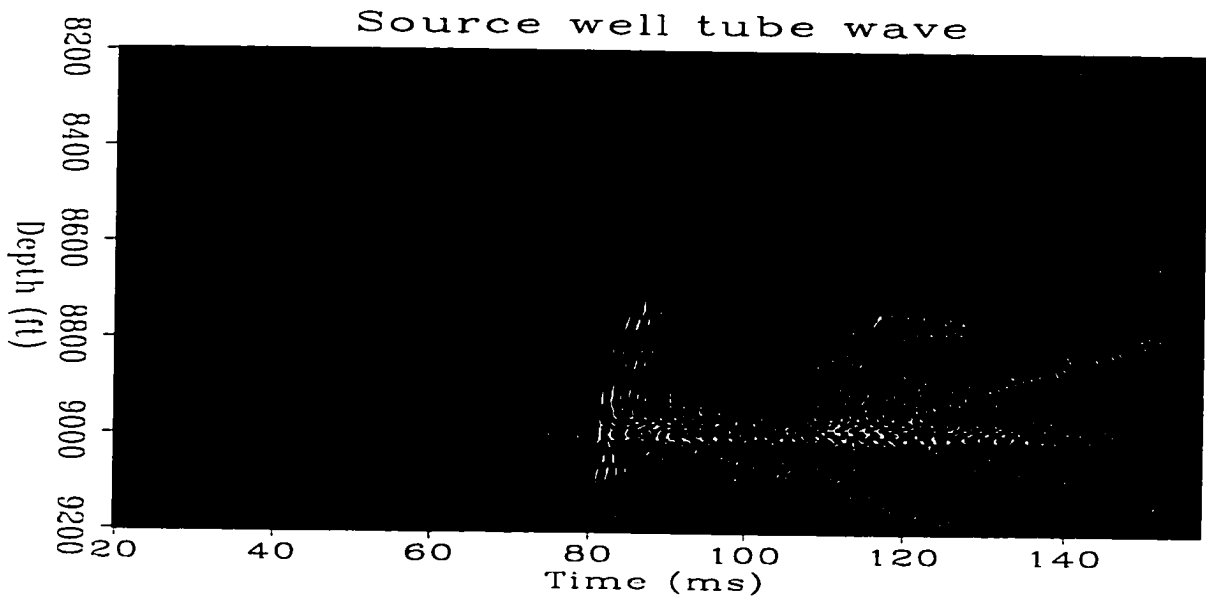


Figure 3.8: Estimated source well tube wave on the CSG data of Figure 3.6.

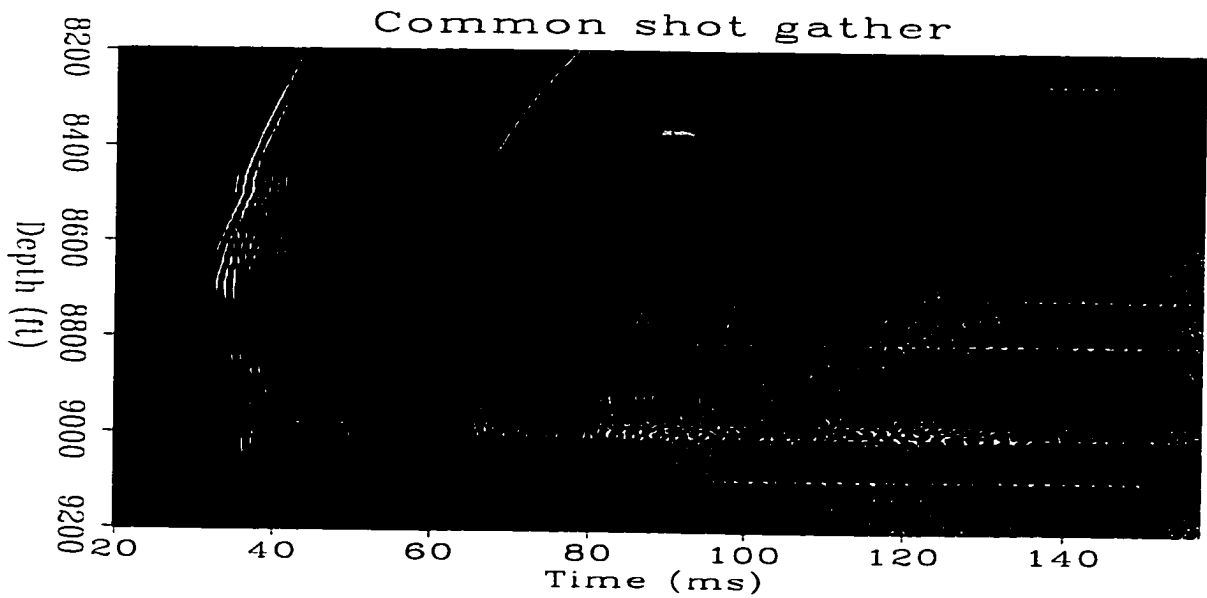


Figure 3.9: Common-shot gather of Figure 3.6. Source well tube waves have been attenuated.

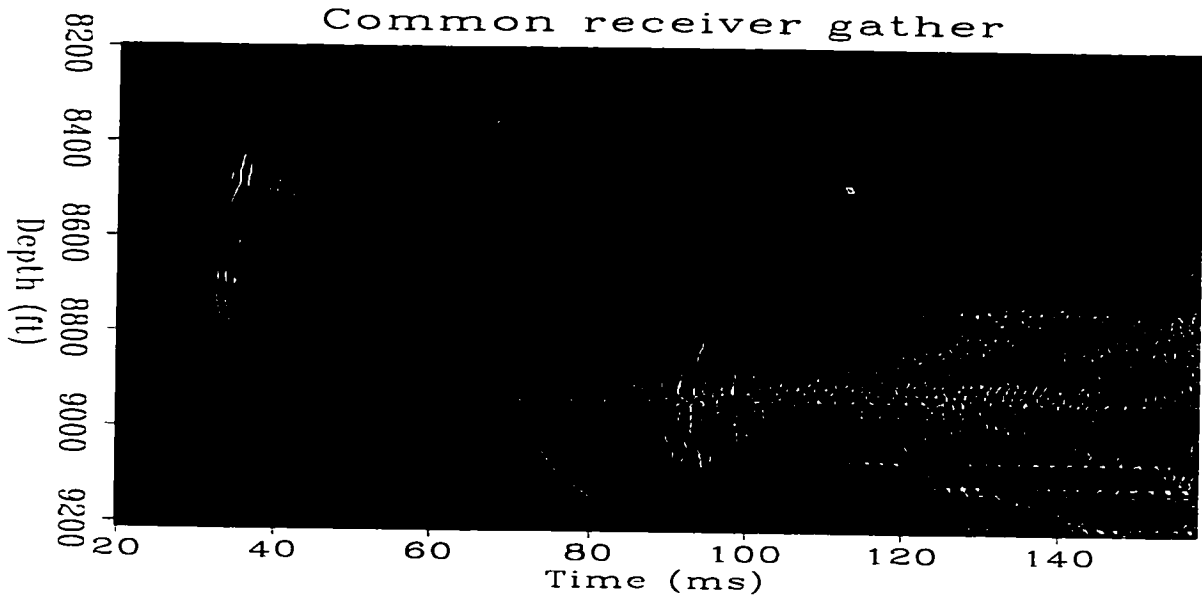


Figure 3.10: Common-receiver gather of Figure 3.7. Source well tube waves have been attenuated.

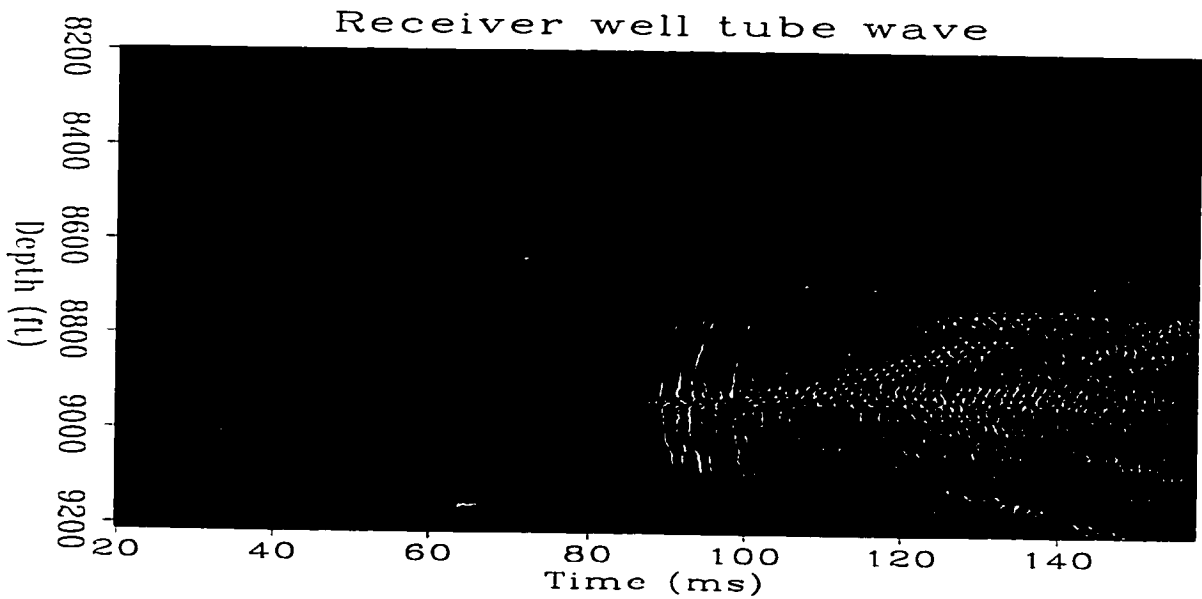


Figure 3.11: Estimated receiver well tube wave on the CRG data of Figure 3.10.

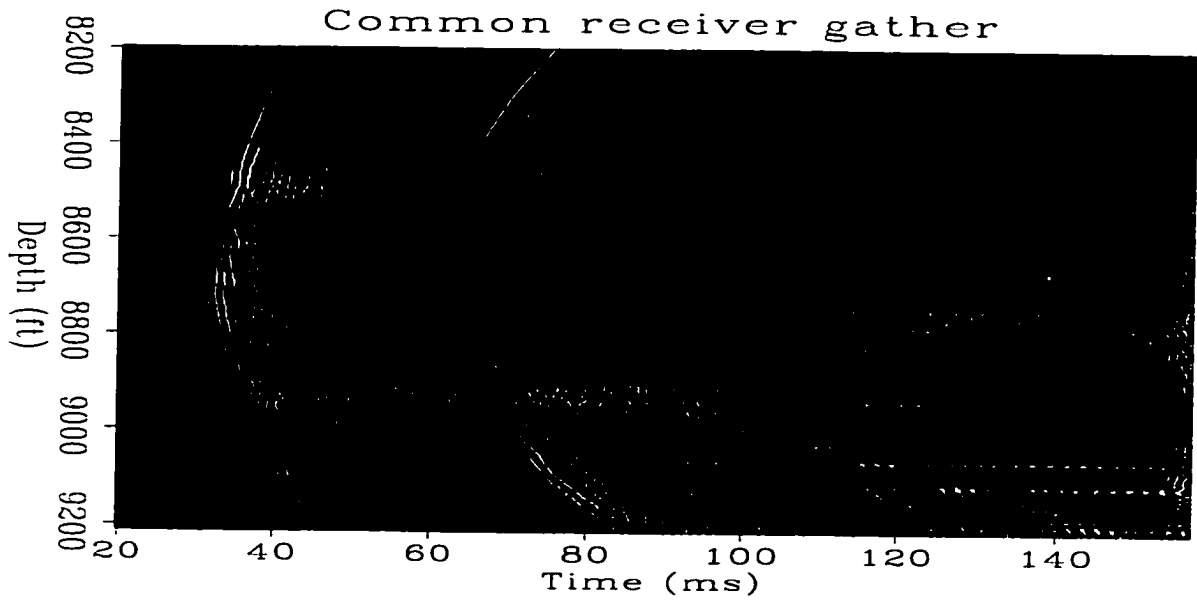


Figure 3.12: Common-receiver gather of Figure 3.10. Receiver well tube waves have been attenuated.

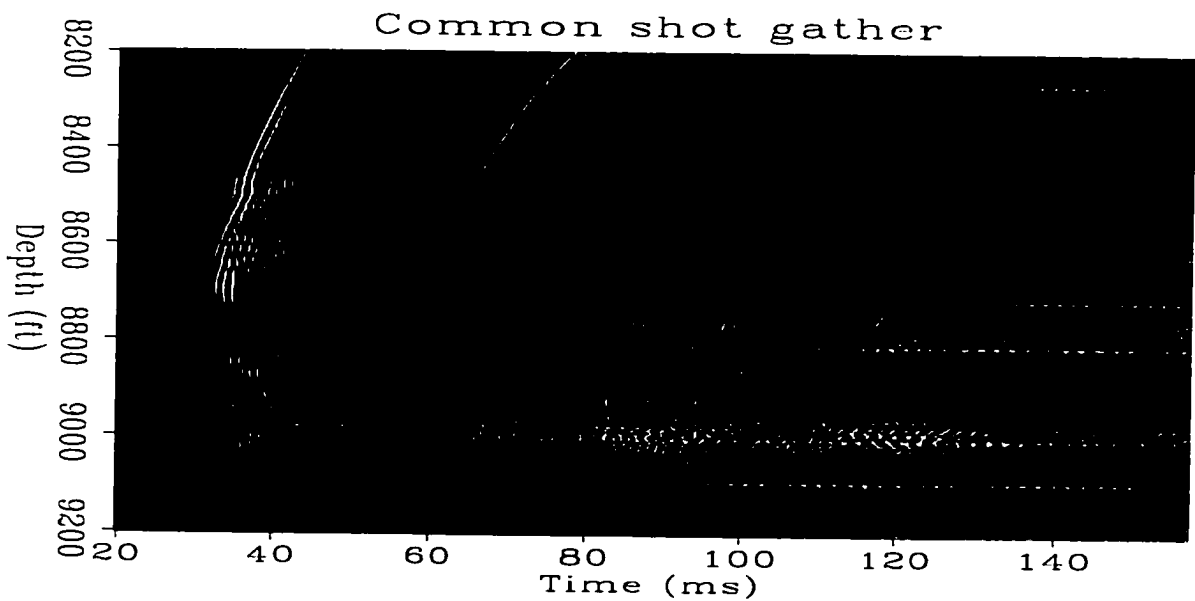


Figure 3.13: Common-shot gather of Figure 3.9. Receiver well tube waves have been attenuated. The direct arrival and reflections stand out much more clearly.

Chapter 4

Finite-difference reverse-time migration of cross-well data

In this chapter, I describe the application of prestack finite-difference reverse-time migration to a field crosswell dataset recorded with a piezoelectric source and hydrophones. The data contain a rich variety of elastic wavemodes, compressional P -, shear S -, and converted waves, with a bandwidth of 2000 Hertz. Data preprocessing consists of interpolation of missing traces, amplitude correction, and attenuation of the direct P - and S -waves.

In the prestack common shot gather migration, I apply a high-order finite-difference scheme to perform wavefield back-propagation from the receivers. Imaging conditions are the traveltimes and amplitude of the direct arrival from the source. Reflectivity is calculated by dividing the focused back-propagated wavefield by the amplitude of the direct arrival from the source. The velocity tomogram obtained from transmission travel time tomography is used as the background velocity model for migration. Prestack single-fold images reveal geological structures depending on illumination from the source. After migration of all the common shot gathers, an image volume is generated. Image gathers at common surface locations sliced from the image volume show that the events are in good alignment, suggesting that the velocity model used in migration is correct. The stacked P - P , S - S , P - S and S - P images clearly show the structure around a 100 ft (30 m) thick reservoir and other geological features such as unconformity. Geological structures suggested by the migration images are consistent with each other, and are consistent with images produced by VSP-CDP mapping.

4.1 Introduction

Crosswell seismic profiling places sources and receivers in the subsurface close to the target. Its distinct difference over other survey configurations, e.g., surface reflection seismic and vertical seismic profiling (VSP), is that wavefields do not propagate through the severely attenuating weathered surface layer before being recorded. The result is that it permits the recording of seismic data with frequencies up to a few thousand Hertz (Harris, 1988). This frequency is an order of magnitude higher than recorded by surface reflection seismic or VSP surveys. The limit on spatial resolution (several feet) is thus an order of magnitude higher than achieved by the surface reflection seismic or VSP surveys. Despite its potential for high resolution, the limitations imposed by current downhole sources dictate that the area that can be effectively surveyed is limited, perhaps no more than 1500 ft (460 m) in lateral dimension. Thus crosswell profiling fills in a gap between large scale, low resolution surface reflection survey and small scale, high resolution log and core measurements. It is mainly used as a tool for reservoir development and monitoring.

An important geophysical parameter of the Earth is velocity. Velocity variation can be decomposed into low and high wavenumber components (Berkhout, 1985). The low wavenumber component of the velocity spectrum is extracted by transmission travel-time tomography using the traveltimes of the direct waves (McMechan, 1983a; Lines and LaFehr, 1989). Crosswell transmission traveltime tomography constrains velocities much better than surface reflection seismology methods, because with precisely located downhole sources and receivers the problem of velocity/depth ambiguity is avoided. Thus the low wavenumber component of the velocity spectrum is usually recovered sufficiently well by crosswell transmission traveltime tomography. Migration imaging operates on the scattered events of the seismic records to recover reflectivity (Berkhout, 1985), which is principally described by the high wavenumber component of the velocity spectrum. In the migration process, the cross-section of tomographic velocities between the two wells is used as the propagation medium.

Several researchers (Stewart, 1992; Lazaratos, 1993) have applied VSP-CDP mapping (Wyatt and Wyatt, 1984) to perform imaging of crosswell seismic data. In this chapter, I apply a more general imaging method, prestack migration, to process crosswell seismic data. Prestack migration, as demonstrated by many previous authors in surface reflection seismic data that it images arbitrary 2-D dipping structures correctly and enhances lateral

resolution by collapsing the Fresnel zones, can also be used to image cross-well seismic data. In the previous publications, Hu et al. (1988) by reverse-time migration and Gray and Lines (1992) by double Kirchhoff VSP depth migration, have demonstrated migration of synthetic and water-tank modeled crosswell seismic data. Qin and Schuster (1993) demonstrated constrained Kirchhoff migration on field crosswell seismic data, in that they reject high dip image events in the migration process. Yet the applications of migration to field crosswell seismic data are still rare. The reasons might be lack of well-sampled crosswell field data and difficulties in processing these field data which are generally very complex.

The crosswell field data used in this study were recorded in a west Texas carbonate reservoir. The field data contain a rich variety of elastic wavemodes, compressional P -, shear S -, and converted waves, with a bandwidth of 2000 Hertz. These complex seismic data present difficulties in processing, but also opportunities to extract various types of geological information.

This chapter is divided into two parts, theory and application in field data. In the first part, I discuss the conjugation of modeling and migration and devise an imaging method that recovers reflectivity by prestack reverse-time migration; then I describe the implementation of the method. In the second part, I present procedures of preprocessing cross-well field records for migration, and describe prestack finite-difference reverse-time migration on the field data, obtaining P - P , S - S , P - S , S - P wave images. The P - P and S - S images generally are in agreement with independent information, such as well logs and VSP-CDP images.

4.2 Theory

4.2.1 Conjugate modeling and migration

To describe modeling, let us consider the 2-D model shown in Figure 4.1 (a). There is a point diffractor D and a reflector. The crosswell profiling geometry includes a source S located at the left well and a series of receivers R located at the right well. Figure 4.1 (b) shows the traveltimes trajectories of the recorded wave events. During the modeling process, the direct wave emitted from the source S excites the diffractor D . The equivalent diffraction source can be expressed as

$$d(x, z, t_{SD}) = r(x, z)s(x, z, t_{SD}), \quad (4.1)$$

written as

$$\hat{d}(x, z, t_{SD}) = \mathcal{L}'[seis(z, t)], \quad (4.3)$$

where \mathcal{L}' is the operator of wave propagation backward in time, i.e., reverse-time. The seismograms $seis(z, t)$, are applied as boundary values at the receiver locations (McMechan, 1983b). Wave propagation backward in time, i.e., phase removal, results in focusing of the wavefront and amplification of the amplitude. The diffraction wavefront focuses at the location of the diffractor at time t_{SD} (Chang and McMechan, 1986). $\hat{d}(x, z, t_{SD})$ is the focused diffraction wavefield and thus the estimated diffraction source. The source wavefield in equation (4.1) is unknown, but it can be approximated as an impulse wave for the purpose of imaging. Thus from equations (4.1) and (4.3) the reflectivity $r(x, z)$ can be estimated as

$$r(x, z) = \frac{\hat{d}(x, z, t_{SD})}{|s(x, z, t_{SD})| + \epsilon}, \quad (4.4)$$

where t_{SD} is the excitation imaging time computed from the eikonal equation, $|s(x, z, t_{SD})|$ is the amplitude of the direct shot arrival computed from the traveltimes map by approximating the transport equation (Vidale, 1991), and ϵ is a small stability factor. It can be shown that the transmission coefficient is always positive for scalar waves (Berkhout, 1985). Direct source wavefields preserve polarity during propagation. Thus, reflectivities estimated by this equation have the correct relative polarity. Each point in the medium is treated as a point diffractor and is imaged accordingly. And in particular, the point of physical source is imaged by the direct wave at time $t_{SD} = 0$.

Figure 4.1 (b) shows that the traveltimes trajectories of the direct arrival and diffraction coincide at certain places, that means by Kirchhoff diffraction stack migration the direct arrival will also affect the imaging of geological structures, creating low-wavenumber background noise in the image. Kinematically, reverse-time migration and Kirchhoff migration are equivalent. Thus the direct arrival should be attenuated before the data are input to migration. The result of reverse-time migration is an image of the high-wavenumber velocity heterogeneity, that is, the locations and strengths of the diffractors.

The common-shot gather data that are input for migration wavefield back-propagation are without divergence corrections because of the reversibility of the wavefield in time and thus the conjugation of modeling and migration (Claerbout, 1991). Geometrical spreading from the source to a diffractor is compensated for by the above imaging operation, and

geometrical spreading from the diffractor to the receivers is compensated for by reverse-time wavefield back-propagation from the receivers. However, if the data is recorded in 3-D world and migration processing is done in 2-D, the data must be corrected for the difference of divergence between 3-D and 2-D.

4.2.2 Implementation of reverse-time migration

The constant density 2-D acoustic wave equation is applied to perform the wavefield back-propagation from the receivers. The seismograms are applied as boundary conditions at the receiver locations. The wave equation is run backward in time stepping from the maximum recording time down to zero. In my implementation, the numerical scheme is a second-order-in-time, tenth-order-in-space finite-differencing (Dablain, 1986), with the absorbing boundary conditions of Cerjan et al. (1985). Imaging conditions are the traveltimes and amplitude of the direct shot arrival computed from the eikonal equation (Chapter 2 of this thesis) and transport equation (Vidale, 1991) by the finite-difference method. Reflectivity is calculated by dividing the focused back-propagated wavefield by the amplitude of the direct shot arrival, as implemented by equation (4.4). In processing hydrophone data that contain elastic wave modes, two images of different wave modes can be produced in one backpropagation of the receiver wavefield. Migration processing of P - P and S - P waves can be coupled, the P -wave velocity model is used for the wavefield backpropagation and two imaging conditions corresponding to P - and S -waves are applied simultaneously to produce the P - P and S - P waves images. Migration processing of P - S and S - S waves can be coupled, the S -wave velocity model is used for the wavefield backpropagation and two imaging conditions corresponding to P - and S -wave are applied simultaneously to produce the P - S and S - S waves images.

The shortest wavelength in the wavefield backpropagation equals the ratio of the slowest velocity and the highest frequency. The shortest wavelength must be sampled by at least three points to avoid numerical dispersion. And the Courant's stability condition must be satisfied, which states that

$$\frac{v_{max} \delta t}{h} < 0.5 \quad (4.5)$$

where v_{max} is the fastest velocity value, δt is the temporal sampling interval and h is the spatial sampling interval. In order to satisfy these two conditions, the data are efficiently interpolated in their Fourier domains.

4.2.3 Stacking images of upgoing/downgoing source wavefields

In the cross-well seismic data used in this study, the temporal wavelet is zero-phase. This transforms into zero-phase spatial wavelet in the migration image, that is, the spatial wavelet centers at the location of a reflection interface.

Two different images are produced in cross-well seismic survey, one has upgoing source wavefield and the other has downgoing source wavefield. According to Aki and Richards (1980), the reflection coefficient for a wave incident on an interface from below has the same value as the reflection coefficient for incidence from above, but an opposite sign. I multiply the image that has upgoing source wavefield by the value -1 to reverse polarity, and stack the resulting image to the image that has downgoing source wavefield. When the two images are stacked, the signs are consistent and the wavelets are aligned at the locations of the reflection interfaces. Of course, this is the idealized solution to the problem of stacking upgoing and downgoing images.

4.3 Application in field data

4.3.1 Description of field data

The crosswell field data were recorded in a west Texas reservoir between two wells 184 ft (56 m) apart and over a depth interval of 500 ft (150 m). The two wells are roughly vertical. Data were acquired using a piezoelectric source and a hydrophone array. Field operations were carried out using the acquisition method of recording on-the-fly, where the source is continuously moving while being fired. By this fast recording technique, over 36 000 seismic traces were recorded in about two days. Firing on-the-fly guarantees that the source depth is accurately controlled, and the dense spatial sampling provided by this fast recording technique allows the wavefield to be recorded without aliasing. The survey consists of 178 receivers scanning in depth from 2687.5 ft (820 m) to 3130 ft (955 m), and 201 shots, scanning in depth from 2650 ft (808 m) to 3150 ft (960 m) (shown in Figure 4.5). A linear up-sweep of 250-2000 Hz was used at the source. The source and receiver depth intervals are both 2.5 ft (0.8 m), and the temporal sampling interval is 0.2 ms. The target of the survey is the reservoir pay zone at a depth interval from about 2850 ft (869 m) to 2950 ft (900 m). A more detailed description of the geology and the data acquisition was given in Harris et al. (1995). By this acquisition technique, the data are recorded as

common receiver gathers (CRG) and the wavelets in the data are zero-phase.

By recording on-the-fly, each data trace is recorded from a different shot. Common receiver gather (CRG) traces share the same receiver and receiver location. Common shot gather (CSG) traces share only the same shot location. As a result, data are more consistent in CRG than in CSG. I will perform all of the data processing in CRG domain. And I treat each CRG as a CSG by the principle of reciprocity.

Figure 4.2 (a) is a unprocessed common receiver gather with the receiver located at a depth of 2900 ft (885 m) (the center of the reservoir pay zone). Even though these are hydrophone data, they contain a rich variety of elastic wave modes, P - P , S - P , P - S , and S - S , and their frequency content ranges from 250 up to 2000 Hertz. The P - S wavemode is weaker in this data. Figure 4.3 shows a sketch of the radiation patterns of the down-hole source (Healan, 1953) for P - and S -waves. The P -wave is strongest along the horizontal direction. The S -wave is strongest along the directions 45 degrees from the horizontal. There is a notch in the horizontal direction for the S -wave. That explains why the direct S -wave is weak in the near offset traces. The concavity of the travel time trajectory of the direct arrival P -wave at near offset suggests that the P -wave velocity is slower in the reservoir zone. The generation of these elastic wavemodes is explained by the following. In a fluid-filled borehole, variations in the fluid pressure produced by the expansion and contraction of the piezoelectric source are coupled at the borehole wall to radiate P - and S -waves. These source-generated P - and S -waves are reflected, diffracted, and converted in the formations. The resulting P - P , S - P , P - S , and S - S modes are coupled at the receiver borehole wall into pressure variations to be recorded by the hydrophones. In this chapter, I demonstrate migration imaging of the P - P , S - P , P - S , and S - S data.

4.3.2 Preprocessing of field data

Because of occasional malperformance of the sources and receivers, there are blank traces in the dataset. The procedure to interpolate blank traces is described as follows. The CSGs and CRGs are alternatively searched for blank traces of the current minimum gap. Linear spatial interpolation is used to fill in blank traces across the current minimum gap. During each iteration, gaps in CSGs (CRGs) are reduced by interpolation in CRGs (CSGs).

Differences in source strengths, and source and receiver radiation patterns result in abnormal amplitude variation among traces. Some other factors that cause amplitude

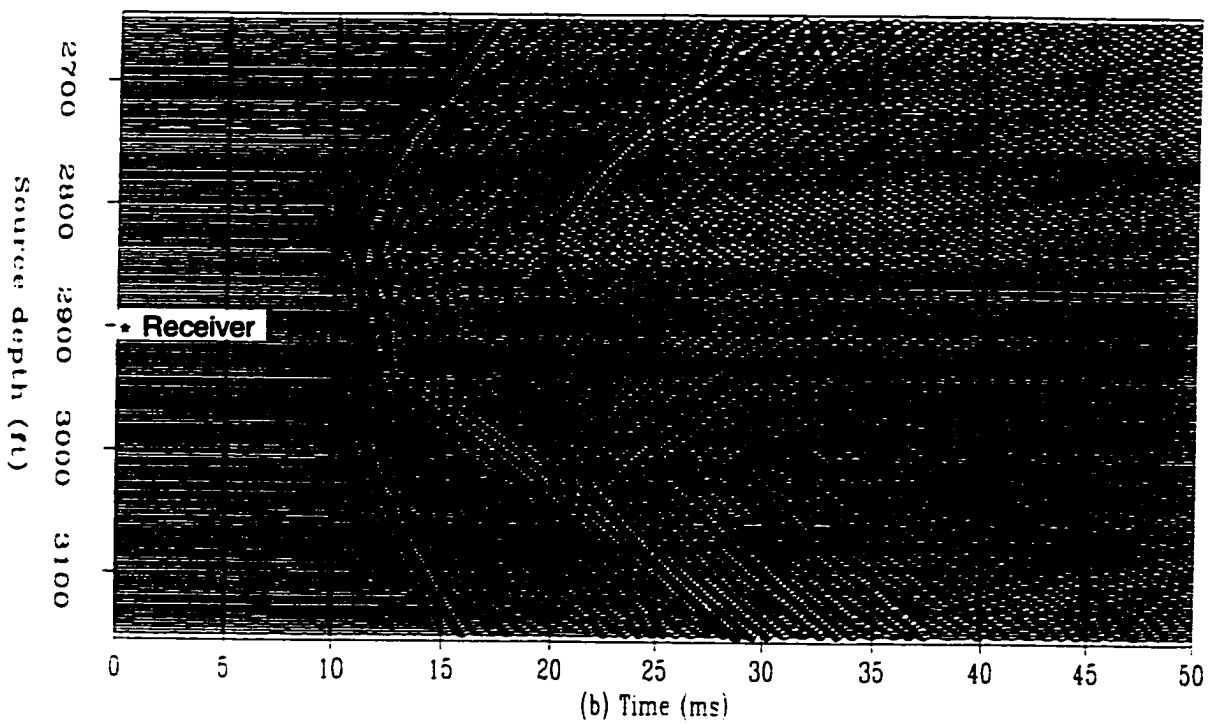
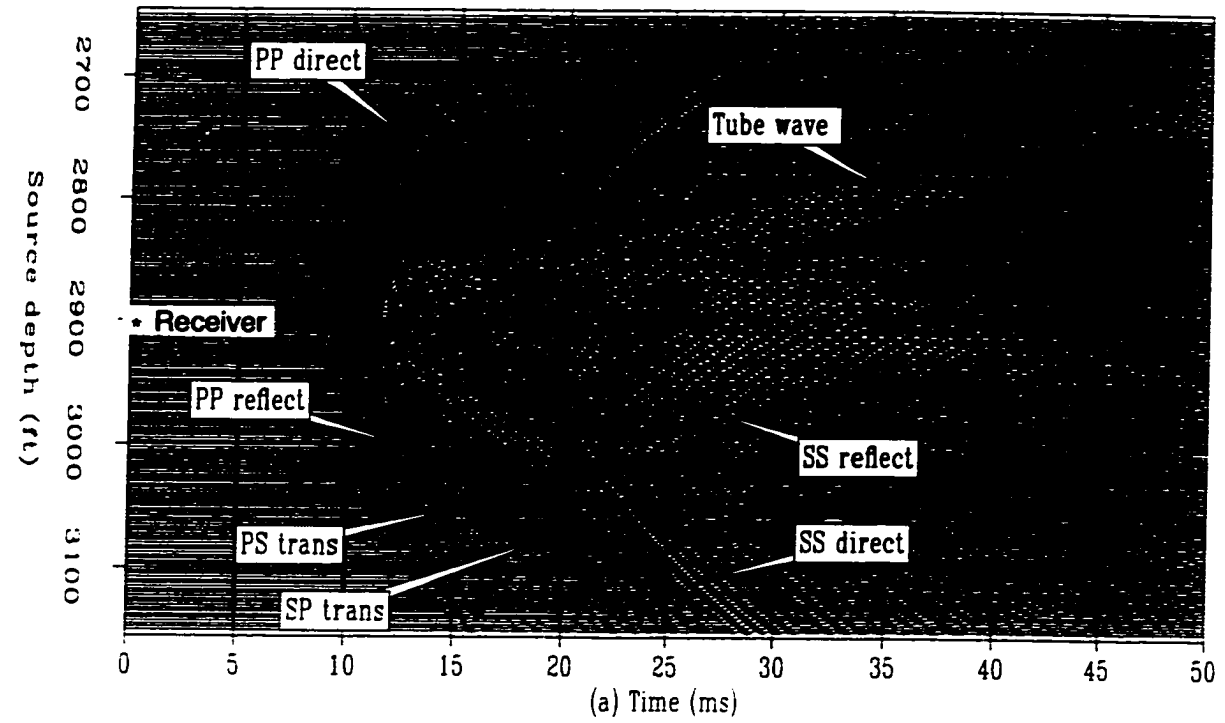


Figure 4.2: (a) is a common receiver gather, the depth of the receiver is 2900 ft, the elastic wave modes are labeled; (b) common receiver gather after amplitude corrections for the P-wave.

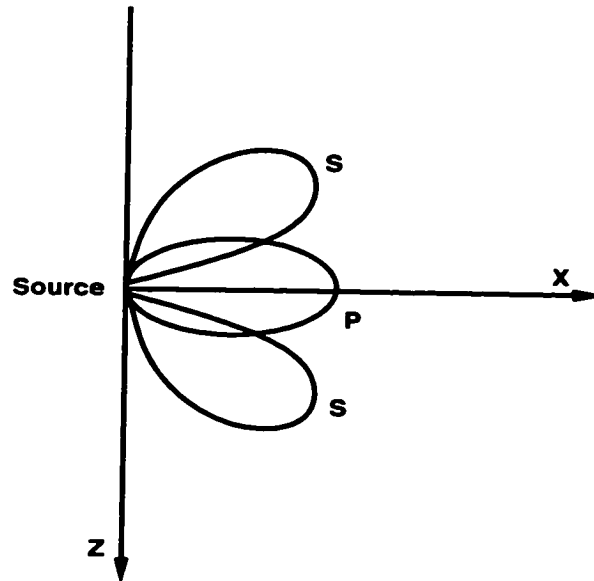


Figure 4.3: Radiation patterns for P - and S -waves of the piezoelectric down-hole source.

variations are borehole coupling, spherical divergence, transmission losses, scattering, and absorption. To approximate point source data in a 3-D homogeneous medium, I normalize the data of each trace to the root-mean-square amplitude of the direct P -wave, and divide the data by the distance from the source to the receiver.

Crosswell migration operates in a 2-D plane. However, the field data were recorded in 3-D space. 2-D geometrical spreading in a constant velocity medium differs by \sqrt{t} from 3-D spreading (Claerbout, 1985), where t is travelttime. Thus, I made the 3-D to 2-D amplitude adjustment by applying a time scaling of \sqrt{t} . Figure 4.2(b) is the resulting common receiver gather after these preprocessings.

The next step in preprocessing is to attenuate the direct arrivals. The operation is performed in common receiver gathers. The direct P -wave is attenuated along its travel-time trajectory by tapered muting. The direct S -wave is attenuated by averaging over five aligned adjacent traces and subtraction along the hand-picked travelttime trajectory in a window covering the direct arrival S -wave wavelet. However, the requirement of preserving reflection events dictates that the attenuation of direct arrivals not be radical. Figure 4.4 is the resulting common receiver gather data that are input to migration processing for P - P , S - S , P - S and S - P waves.

The data are then interpolated by Fourier transform to half of the original sampling

interval in depth, i.e., 1.25 ft (0.4 m). Migration reflectivity images are computed at this interval for depth and offset, that is, half the sampling intervals of the source and receiver, which is analogous to the conventional surface seismic reflection CDP processing.

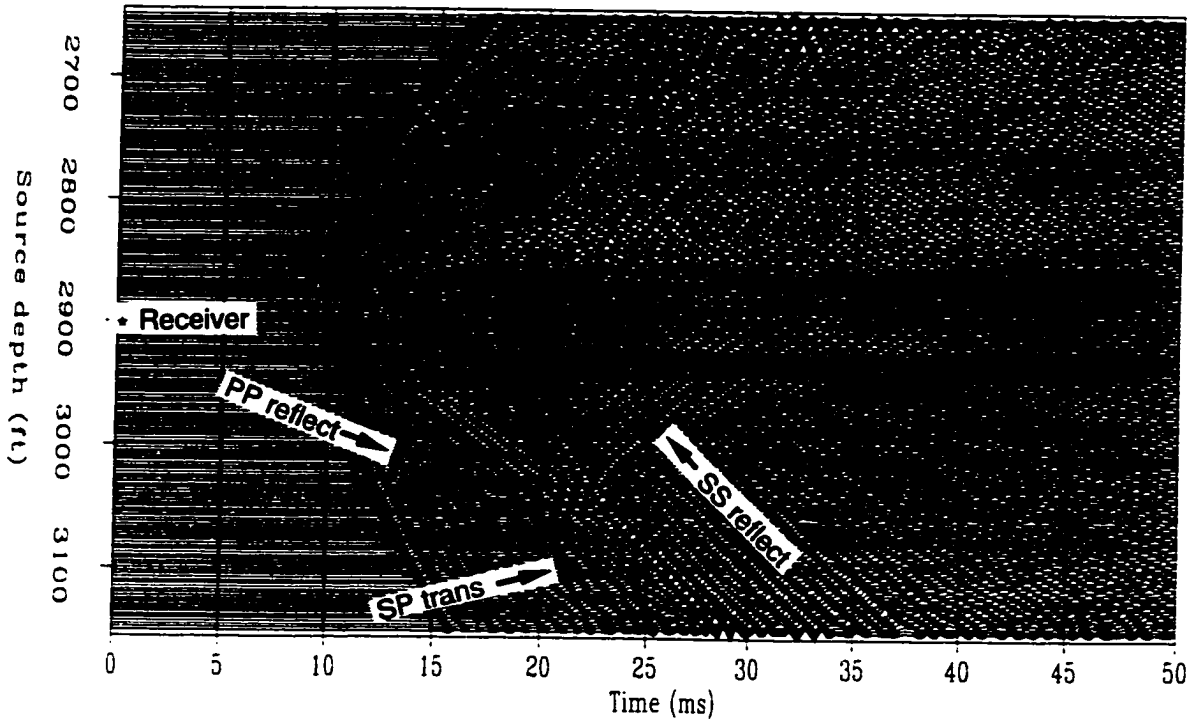


Figure 4.4: Common receiver gather after tapered muting of the *P*-wave direct arrival and attenuation of the *S*-wave direct arrival. The receiver is at the depth of 2900 ft. Notice the strong *P-P* and *S-S* reflections, and *S-P* transmissions at the depth of 3050 ft.

4.3.3 Background velocity model

Figure 4.5 shows a background velocity model for the *P*-wave. The overlay on it is the direct arrival traveltimes from the receiver at 2900 ft (885 m). The velocity ranges from 16 kft/s (4.9 km/s) to 21 kft/s (6.4 km/s). The grid size is 480 nodes in depth and 148 nodes in offset. The sampling intervals are 1.25 ft (0.4 m) in both vertical and lateral directions. This model is the result of transmission traveltimes tomography (Harris et al., 1995) after some smoothing to remove obvious artifacts. In the data of Figure 4.2(a), the traveltimes of the direct *S*-wave are about 1.83 times that of the *P*-wave, so I derive the *S*-wave velocity as a factor 1/1.83 of the *P*-wave tomogram velocity. These *P*- and *S*-wave

velocity models are used as the background models for migration. The central frequency in the field data is 1000 Hertz, thus the dominant wavelength is about 20 ft (6 m) for the *P*-wave and 10 ft (3 m) for the *S*-wave.

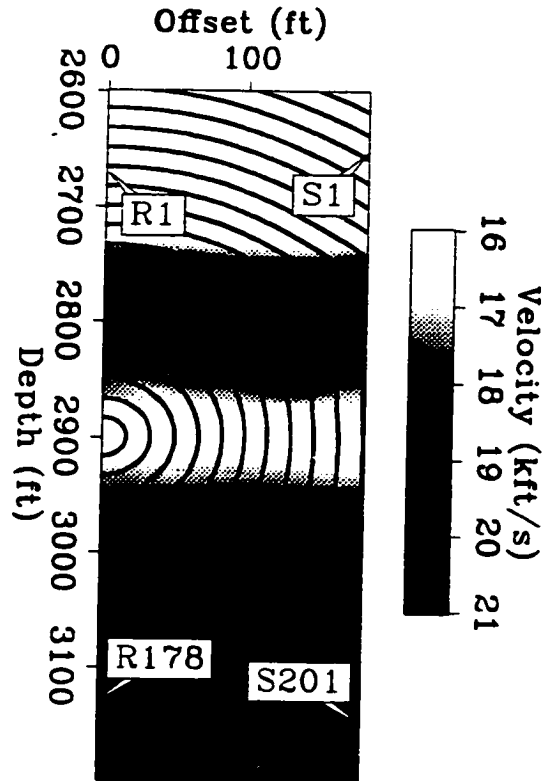


Figure 4.5: *P*-wave velocity used as the background model of migration. Overlay on it is the direct arrival traveltime from the receiver at 2900 ft (885 m) used as the imaging condition.

4.3.4 *P-P* wave migration

By applying the principle of reciprocity, I process the CRG data as common shot gathers (CSG). The *P*-wave velocity tomogram is used for the wavefield back-propagation, and it is also used to calculate the imaging conditions. Figure 4.6 shows the resulting *P-P* wave image for the common receiver gather shown in Figure 4.4. In this single-fold image, flat reflectors at the depths from 2700 ft to 2750 ft, flat reflector at the depth of 3040 ft, and right to left dipping reflectors at the depths from 3050 ft to 3100 ft can be identified. The remnant direct arrival images the migration source at the depth of 2900 ft, this is considered as noise in imaging geological structures. But this implies that the

transmission traveltimes tomogram predicts the direct arrival traveltimes pretty well. The elliptical events in this *P-P* image are produced by noises – the *S*- and converted waves.

Figure 4.7 shows the *P-P* wave image for the CRG whose receiver is located at the depth of 2750 ft. The top of the reservoir at the depth of 2850 ft is imaged. Figure 4.8 shows the *P-P* wave image for the CRG whose receiver is located at the depth of 2850 ft. The flat reflectors at the depths from 2700 ft to 2750 ft, the bottom of the reservoir at the depth of 2950 ft, flat reflector at the depth of 3040 ft and dipping reflectors at the depths from 3050 ft to 3100 ft are imaged. Notice in the single-fold images of Figures 4.6, 4.7, and 4.8, the reflectors on the right half are more continuous. That is because the specular reflections from the right half of the image are received at the right well and used in migration.

After migration of all the common receiver gathers, an image volume is generated, Figure 4.9. Image gathers at common surface locations (CSL) can be sliced from the image volume to demonstrate the correctness of the velocity model. If the velocity model is correct, the images produced by migration of different common shot gathers should be consistent, and thus the image events in the CSLs should be flat. Figure 4.10 shows the CSL at the lateral location of 50 ft from the left well. The upper-left to lower-right diagonal region contains artifacts resulted from imaging the migration sources. These artifacts must be muted before the images are stacked. The image events at the lower-left and upper-right triangular regions are flatly aligned, suggesting that the velocity model used in migration is correct. The image at the upper-right triangular region which is made by upgoing source wavefield is multiplied by the value of -1 to reverse polarity. Finally, the traces in this CSL image are stacked to produce the single image trace 50 ft from the left well. Figure 4.11 shows the CSL at the lateral location of 150 ft from the left well. Similar observations and data processings are made as in Figure 4.10.

Figure 4.12 shows the final stacked *P-P* wave image, compared with the sonic logs and the synthetic seismograms at the two wells. The synthetic seismograms are made using the following procedures. The vertical incidence reflection coefficient series is calculated from the sonic log. Then a zero-phase Ricker wavelet of similar frequency band as in the migration image is convolved to the reflection coefficient series. The making of the synthetic seismograms is very rough, as the cross-well image is not produced by vertical incidence source wave field and the wavelet in the image is not Ricker. The synthetic seismograms are only for purpose of qualitative comparison with the migration image.

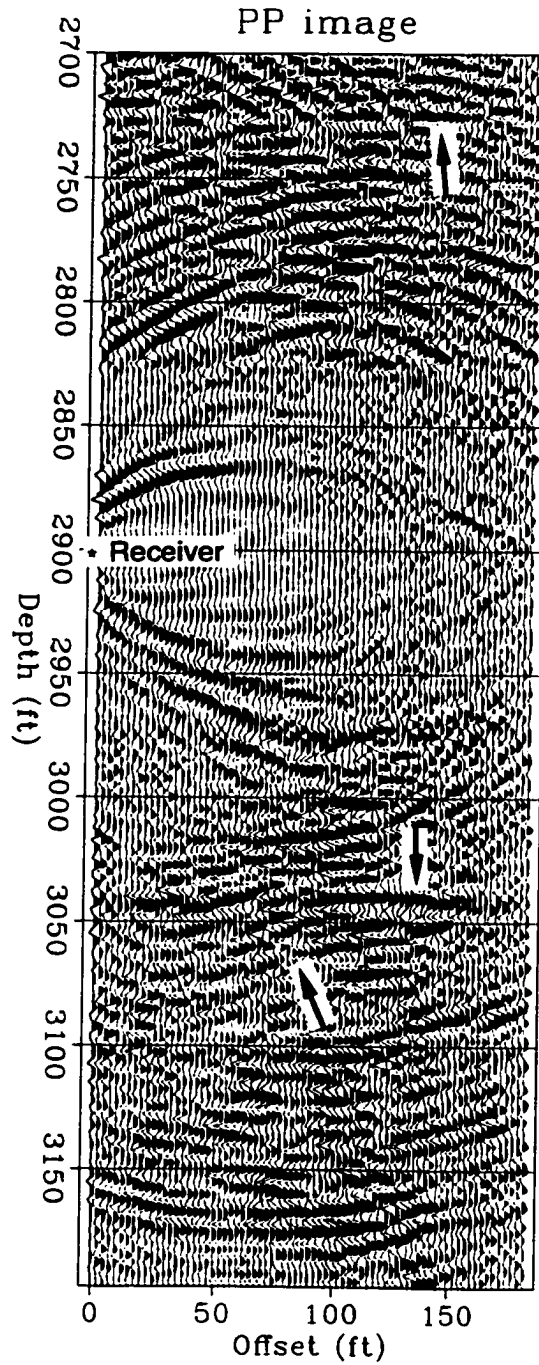


Figure 4.6: *P-P* wave image for the CRG, the depth of the receiver is 2900 ft. Notice the flat reflectors at the depths of 2725 ft and 3040 ft, and right to left dipping reflectors at the depths from 3050 ft to 3100 ft.

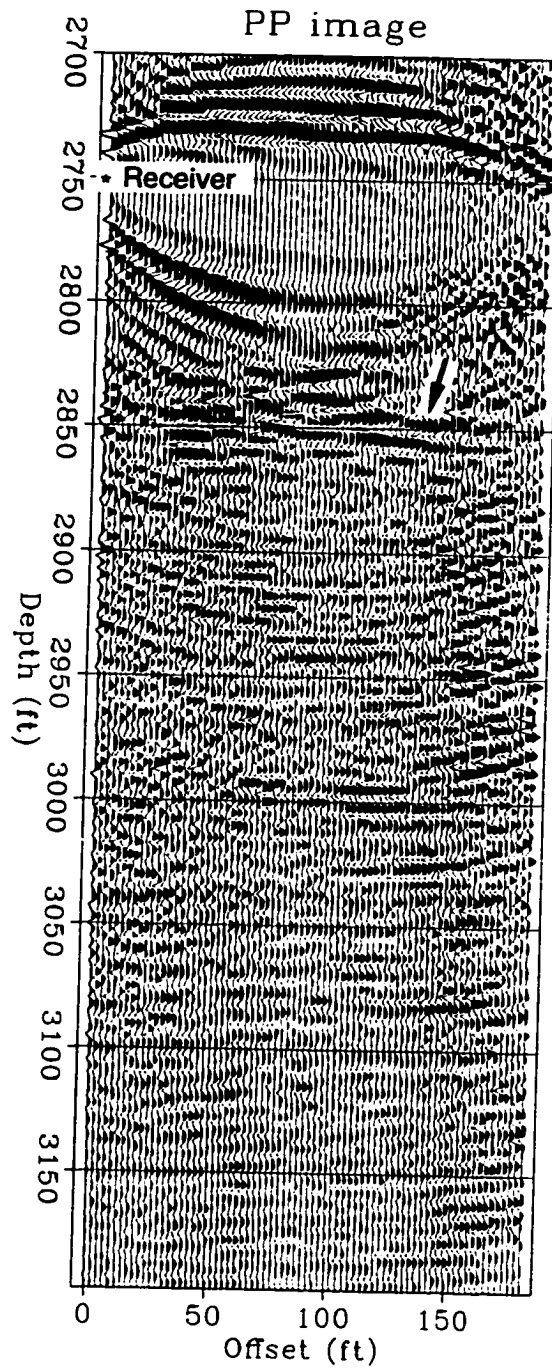


Figure 4.7: *P-P* wave image for the CRG, the depth of the receiver is 2750 ft. The strong event at the depth of 2850 ft is the top of the reservoir.

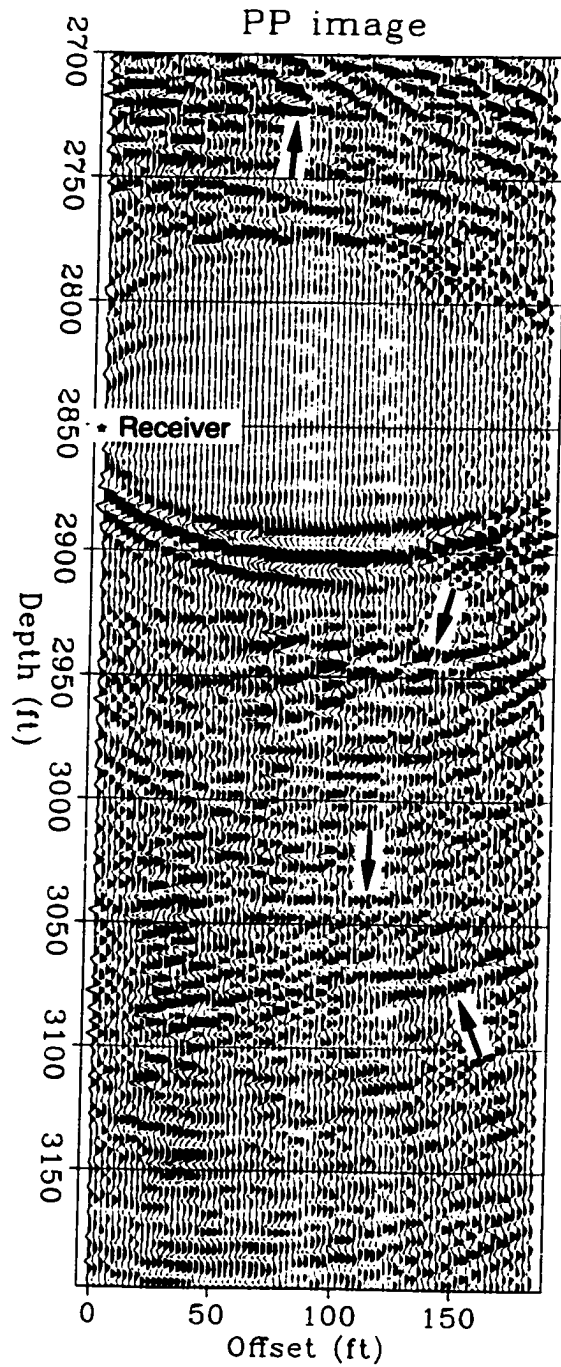


Figure 4.8: *P-P* wave image for the CRG, the depth of the receiver is 2850 ft. The strong event at the depth of 2950 ft is the bottom of the reservoir. Notice the flat reflector at the depth of 3040 ft and right to left dipping reflectors at the depths from 3050 ft to 3100 ft.

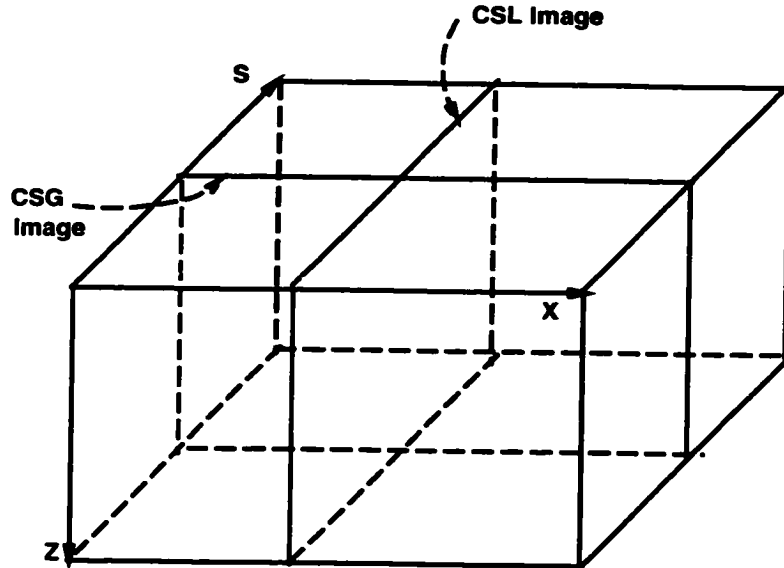


Figure 4.9: After migration of all the common shot gathers, a volume of images is generated. From this volume, CSG image planes and common surface location (CSL) image planes can be sliced.

The formations from depths of 2700 ft to 2775 ft are nearly flat, as suggested by the two sonic logs in this interval. The migration image clearly shows what the sonic logs only suggest that below depth of 3050 ft there is an unconformity, the dip of which is about 5 degrees. As described in Harris et al. (1995), the reservoir pay zone is dolomitized carbonate from depth of 2850 ft (870 m) to 2950 ft (900 m) and is within the Permian-aged Grayburg formation.

Figure 4.13 compares the *P-P* wave migration image and the image produced by VSP-CDP mapping (Larazatos, 1993). The geological structures as suggested in these two images are mostly consistent, the flat reflectors at the depth of 2750 ft and the unconformity at the depth of 3050 ft.

4.3.5 *S-S* wave migration

The migration for *S-S* wave is carried out in a similar procedure as for *P-P* wave. The *S*-wave velocity is used for the wavefield back-propagation, and it is also used to calculate the imaging conditions. Figure 4.14 shows the resulting *S-S* wave image for the common receiver gather shown in Figure 4.4. In this single-fold image, flat reflectors at the depths from 2700 ft to 2750 ft, flat reflector at the depth of 3040 ft and dipping reflectors at the

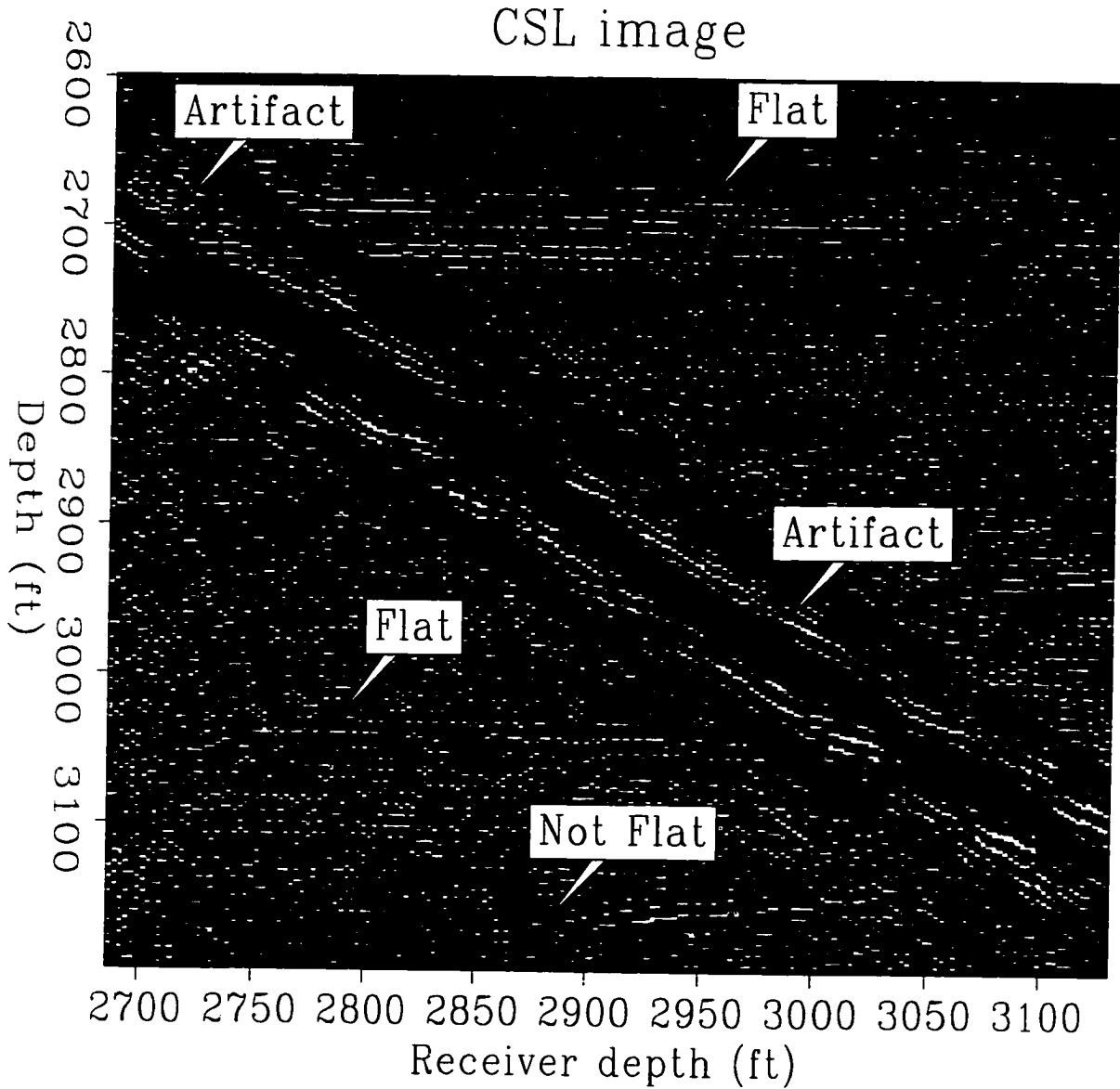


Figure 4.10: *P-P* wave common surface location (CSL) image plane 50 ft from the left well. The upper-left to lower-right diagonal region contains artifacts resulted from imaging the migration sources. The image events at the middle depths are flatly aligned, suggesting that the velocity model used in migration is correct. At the edges of the survey, in depths 2600 ft to 2700 ft and 3100 ft to 3200 ft where the accuracy of the tomogram is poor the image events are not very well flatly aligned.

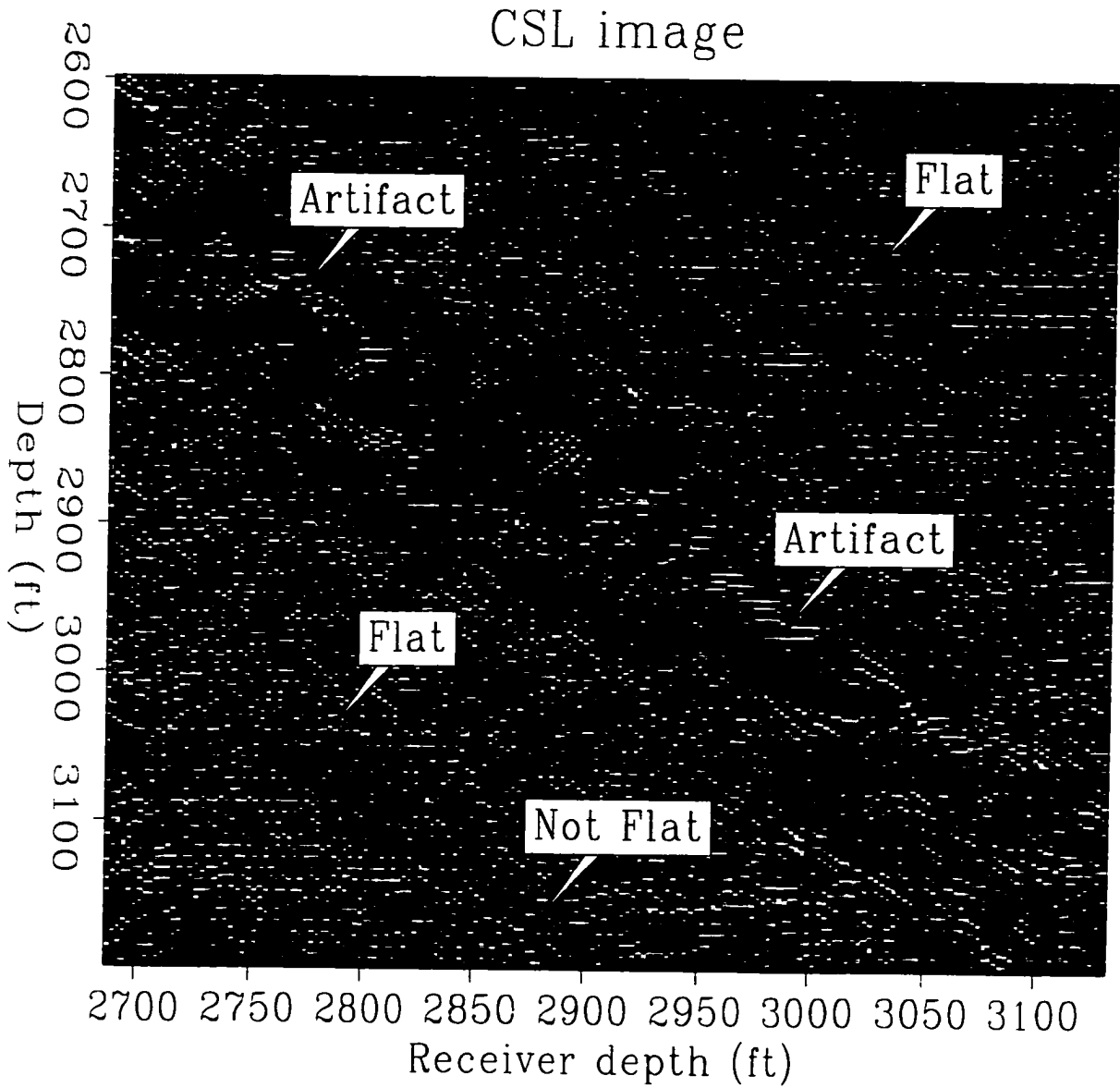


Figure 4.11: *P-P* wave common surface location (CSL) image plane 150 ft from the left well. The upper-left to lower-right diagonal region contains artifacts resulted from imaging the migration sources. The image events away from the diagonal region are flatly aligned.

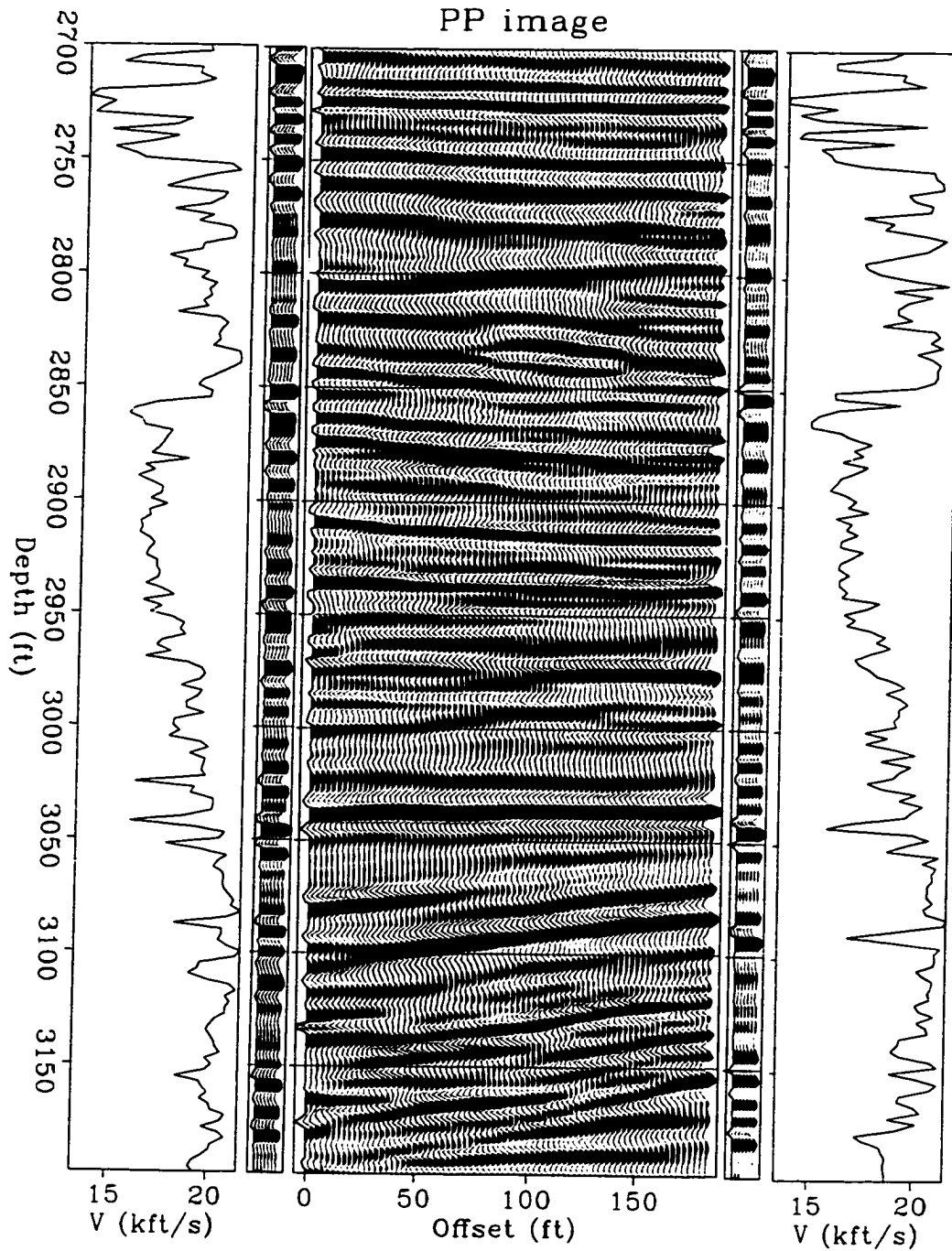


Figure 4.12: *P-P* wave image, sonic logs, and synthetic seismograms. Flat reflectors at the depths from 2700 ft to 2750 ft and unconformity at the depths from 3040 ft to 3100 ft can be identified. Reservoir pay zone is from the depth of 2850 ft to 2950 ft.

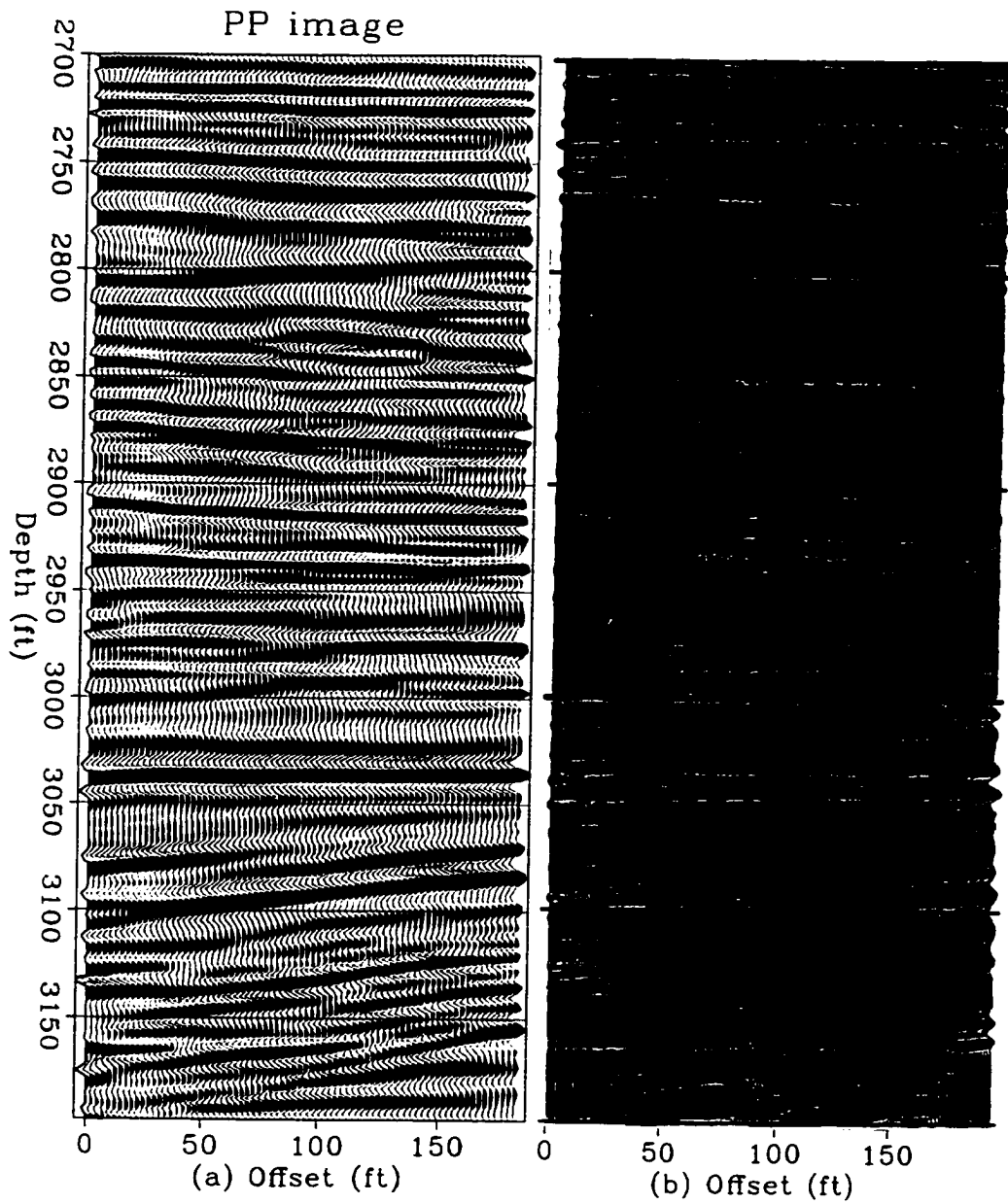


Figure 4.13: (a) *P-P* wave migration image, (b) *P-P* wave VSP-CDP mapping image (Larazatos, 1993). The geological structures as suggested in these two images are mostly consistent.

depths from 3050 ft to 3100 ft can be identified. These features are consistent with those in the *P-P* wave image. The elliptical events at the depth of 2900 ft in this *S-S* image are produced by noises.

After migration of all the common receiver gathers, an image volume is generated, as in *P-P* wave, Figure 4.8. Figure 4.15 shows the CSL at the lateral location of 150 ft from the left well. The upper-left to lower-right diagonal region contains artifacts resulted from imaging the migration sources. These artifacts must be muted before the images are stacked. The image events at the lower-left and upper-right triangular regions are flatly aligned, suggesting that the velocity model used in migration is correct. Then the image at the upper-right triangular region is multiplied by the value of -1. Finally, the traces in this CSL image are stacked to produce the single image trace 150 ft from the left well.

Figure 4.16(a) shows the final stacked *S-S* wave migration image. The formations from depths of 2700 ft to 2800 ft are nearly flat. Below the depth of 3050 ft is an unconformity, the dip of which is 5 degrees. Figure 4.16(b) shows the *S-S* wave image produced by VSP-CDP mapping (Larazatos, 1993). The geological structures as suggested in these two images are mostly consistent, the flat reflectors at the depth of 2750 ft and the unconformity at the depth of 3050 ft.

4.3.6 *P-S* wave migration

The migration for *P-S* wave is carried out in a similar procedure as for *P-P* wave. The *S*-wave velocity is used for the wavefield back-propagation, and *P*-wave velocity is used to calculate the imaging conditions. Figure 4.17 shows the resulting *P-S* wave image for the common receiver gather shown in Figure 4.4. In this single-fold image, reflectors around the depth of 2900 ft can be identified. Figure 4.18 shows the resulting *P-S* wave image for the common receiver gather, the depth of the receiver is 3000 ft. In this single-fold image, reflectors at the depths from 3000 ft to 3050 ft can be identified.

After migration of all the common receiver gathers, an image volume is generated, as in *P-P* wave, Figure 4.8. Figure 4.19 shows the CSL at the lateral location of 150 ft from the left well. The image events at the middle depths are flatly aligned, suggesting that the velocity model used in migration is correct. However, at the bottom of the survey below 3100 ft, the image events are not well flatly aligned.

Figure 4.20 shows the final stacked *P-S* wave migration image. The formations from depths of 2700 ft to 2800 ft are nearly flat. Below the depth of 3050 ft is an unconformity,

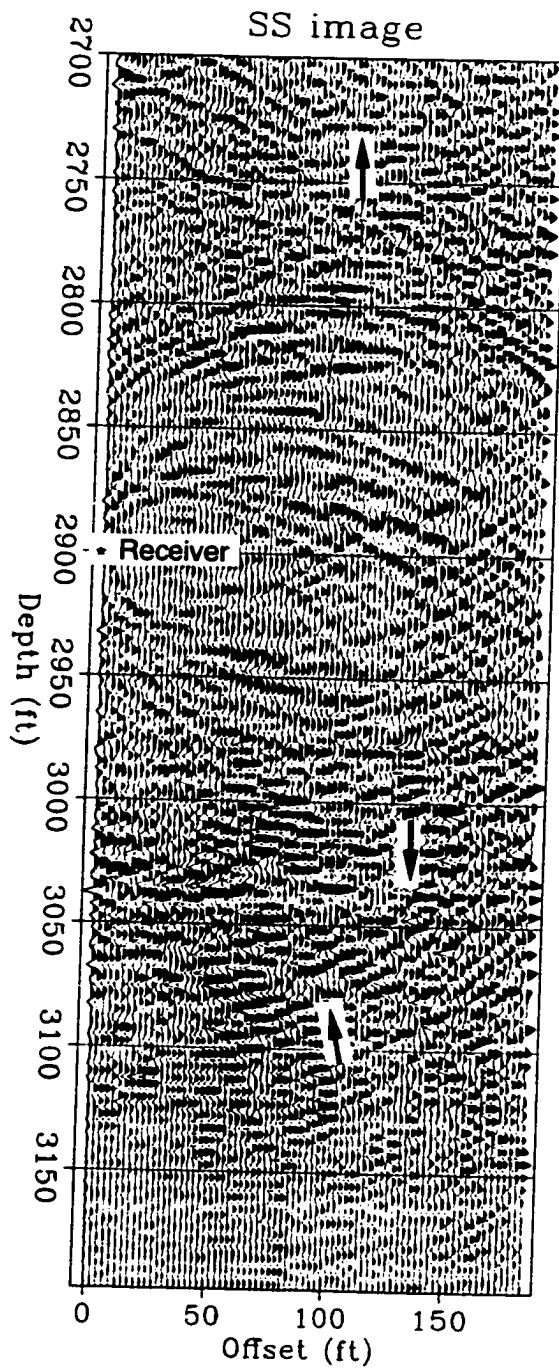


Figure 4.14: *S-S* wave image for the CRG, the depth of the receiver is 2900 ft. Notice the flat reflectors at the depth of 2725 ft, flat reflector at the depth of 3040 ft and dipping reflectors at the depths from 3050 ft to 3100 ft.

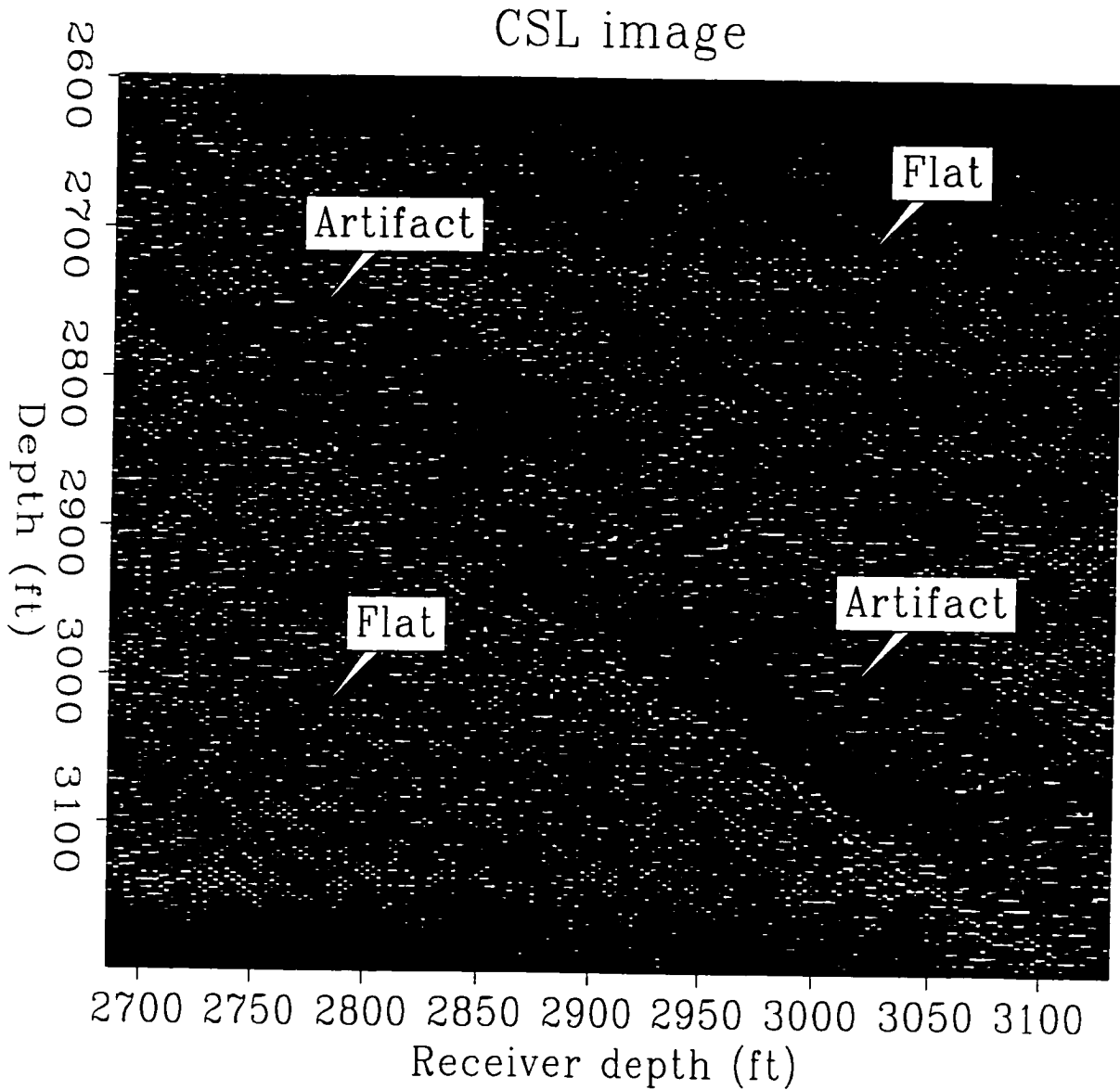


Figure 4.15: *S-S* wave common surface location (CSL) image plane 150 ft from the left well. Except for the upper-left to lower-right diagonal region of artifacts resulted from imaging the migration sources, the image events are flatly aligned, suggesting that the velocity model used in migration is correct.

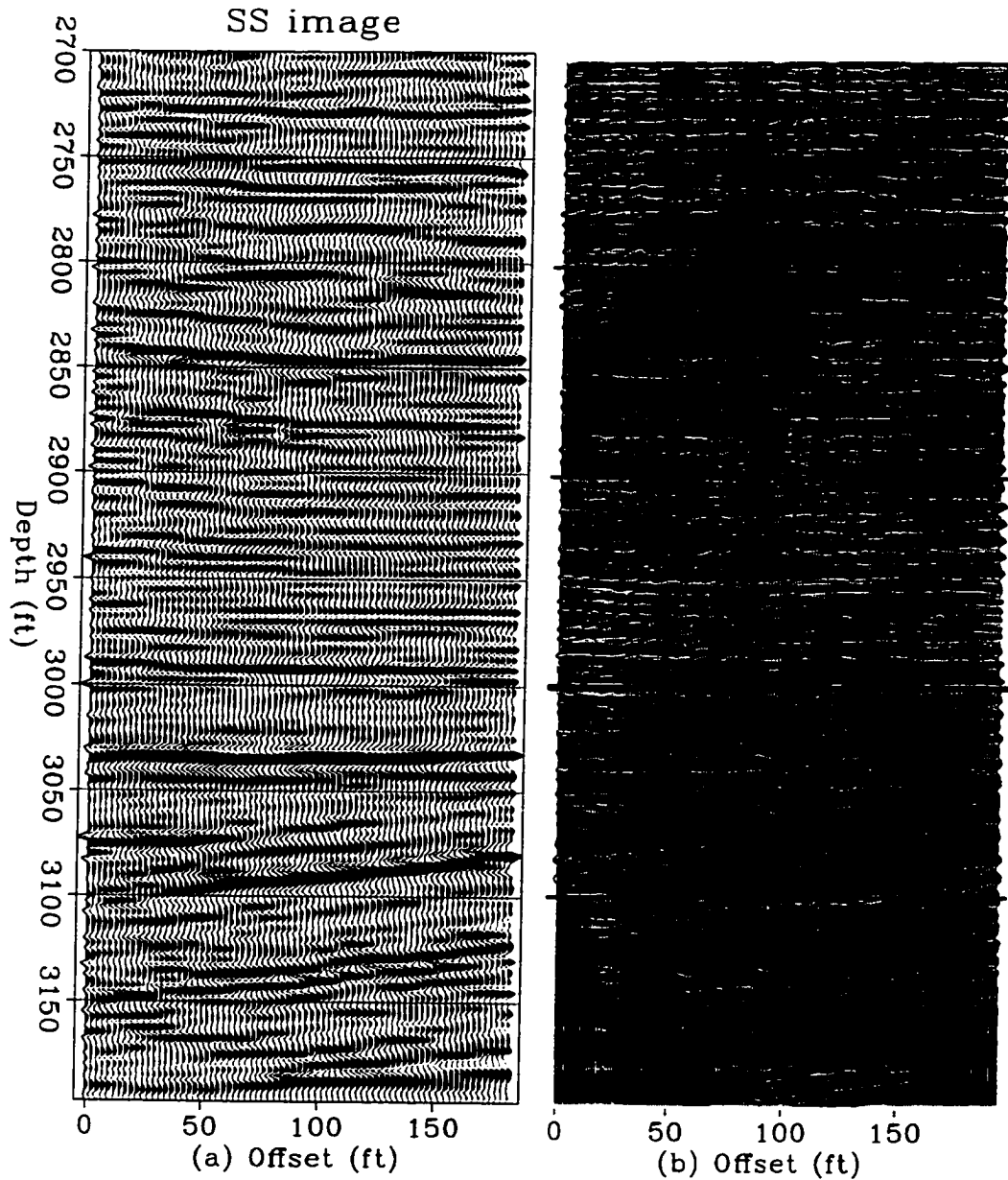


Figure 4.16: (a) *S-S* wave migration image, (b) *S-S* wave VSP-CDP mapping image (Larazatos, 1993). The geological structures as suggested in these two images are mostly consistent. Flat reflectors at the depths from 2700 ft to 2750 ft and unconformity at the depths from 3050 ft to 3100 ft can be identified. Reservoir pay zone is from the depth of 2850 ft to 2950 ft.

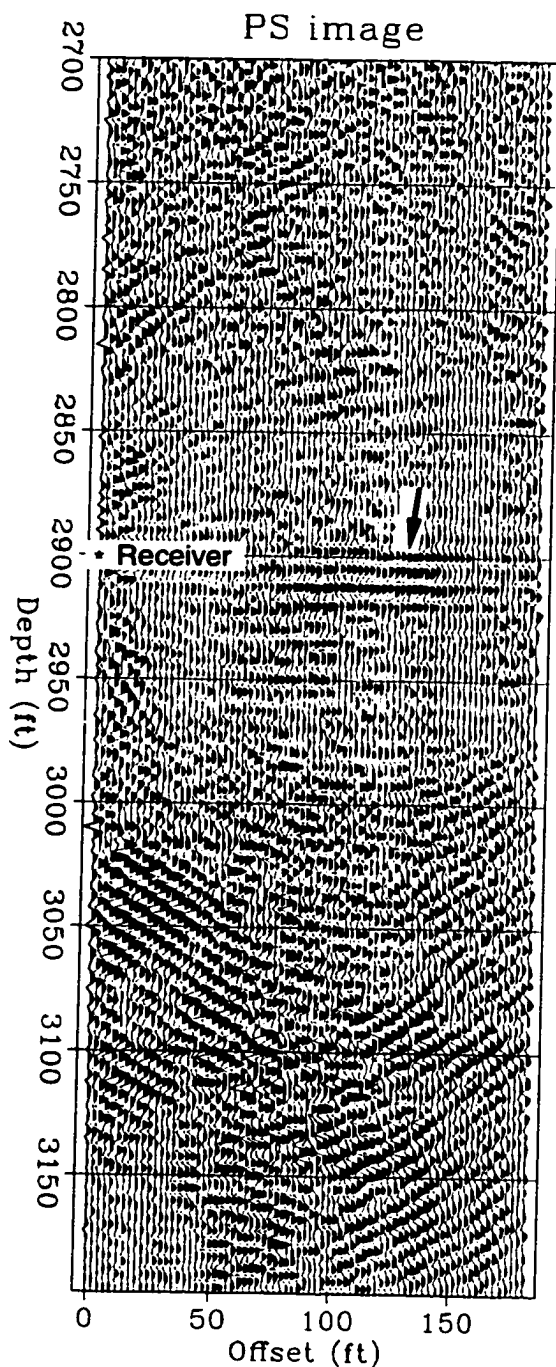


Figure 4.17: *P-S* wave image for the CRG, the depth of the receiver is 2900 ft. Notice the reflectors at the depth of 2900 ft inside the reservoir.

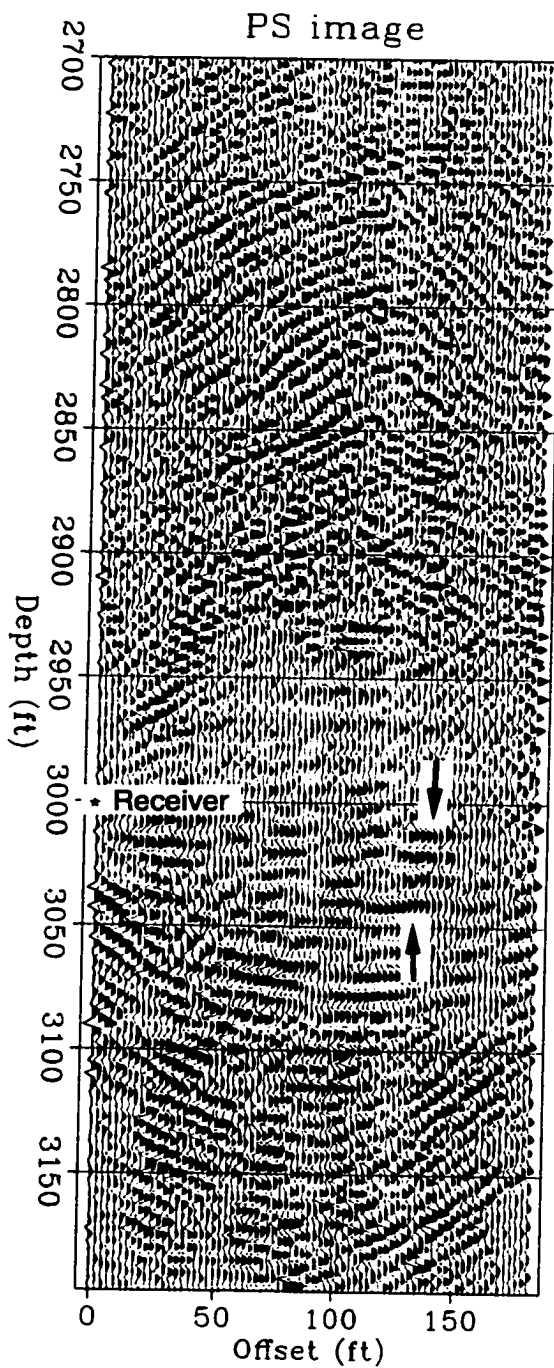


Figure 4.18: *P-S* wave image for the CRG, the depth of the receiver is 3000 ft. Notice the flat reflectors at the depth of 3000 ft to 3050 ft.

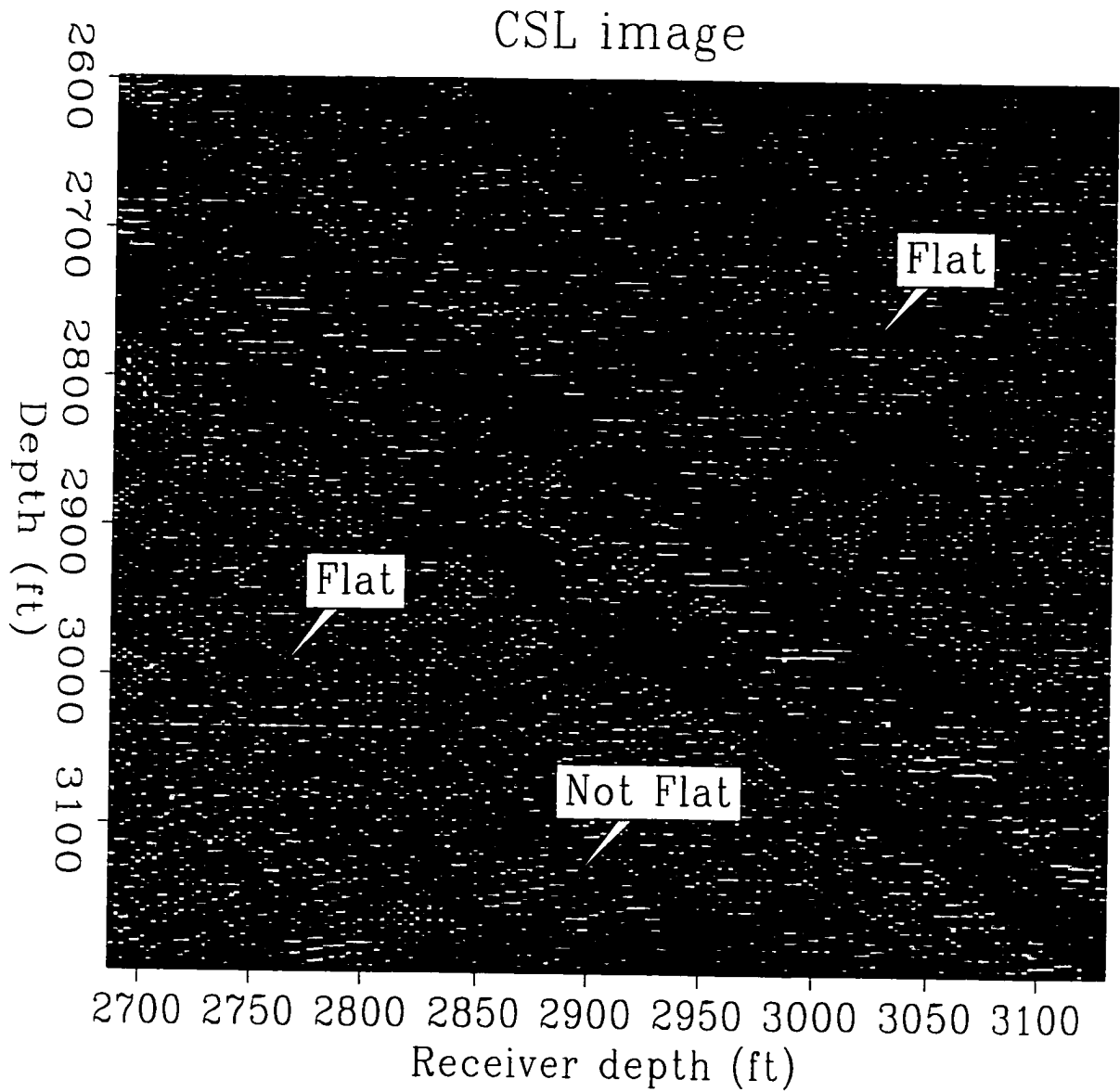


Figure 4.19: *P-S* wave common surface location (CSL) image plane 150 ft from the left well. The upper-left to lower-right diagonal region contains artifacts resulted from imaging the migration sources. The image events at the middle depths are flatly aligned. At the bottom of the survey, in depths from 3100 ft to 3200 ft, the image events are not well flatly aligned.

the dip of which is 5 degrees. The reservoir pay zone is dolomitized carbonate from depth of 2850 ft (870 m) to 2950 ft (900 m).

4.3.7 *S-P* wave migration

The migration for *S-P* wave is carried out in a similar procedure as for *P-P* wave. The *P*-wave velocity is used for the wavefield back-propagation, and *S*-wave velocity is used to calculate the imaging conditions. Figure 4.21 shows the resulting *S-P* wave image for the common receiver gather shown in Figure 4.4. In this single-fold image, flat reflectors at the depths from 2700 ft to 2750 ft can be identified. These features are consistent with those in the *P-P* wave image. The elliptical events at the depth of 2900 ft in this *S-P* image are produced by noises. The low amplitude and absence of interpretable reflectors around the depth of 2900 ft in this *S-P* wave image are explained by the radiation pattern of the source – there is a notch in the *S*-wave at the horizontal direction.

After migration of all the common receiver gathers, an image volume is generated, as in *P-P* wave, Figure 4.8. Figure 4.22 shows the CSL at the lateral location of 150 ft from the left well. The upper-left to lower-right diagonal region contains artifacts resulted from imaging the migration sources. These artifacts must be muted before the images are stacked. The image events at the lower-left and upper-right triangular regions are flatly aligned.

Figure 4.23 shows the final stacked *S-P* wave migration image. The formations from depths of 2700 ft to 2800 ft are nearly flat. Below the depth of 3050 ft is an unconformity, the dip of which is 5 degrees. The reservoir pay zone is dolomitized carbonate from depth of 2850 ft (870 m) to 2950 ft (900 m).

4.4 Conclusions

Prestack finite-difference reverse-time migration has been successfully applied on a field crosswell dataset recorded with the piezoelectric source and hydrophones. High-quality reflectivity images of the *P-P*, *S-S*, *P-S*, *S-P* elastic wavemodes are obtained. Geological structures suggested by these four images are consistent with each other, and are consistent with images produced by VSP-CDP mapping. The structures around a 100 ft (30 m) thick reservoir are clearly imaged. Other geological features imaged include flat beds and unconformity.

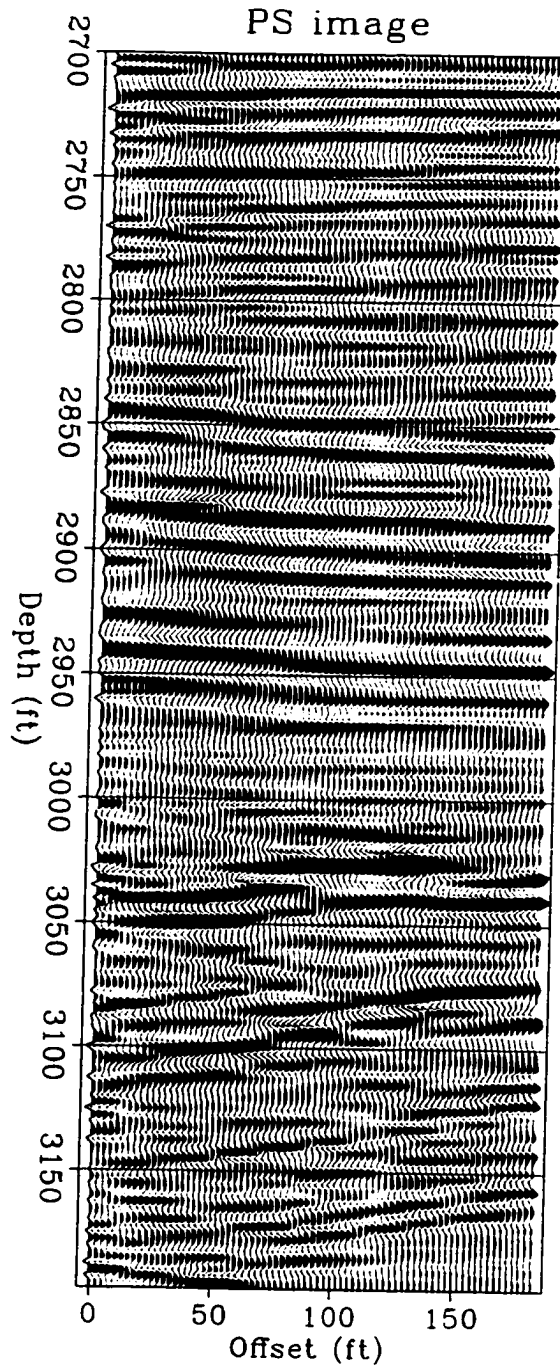


Figure 4.20: *P-S* wave migration image. The principal features are the flat reflectors at the depths from 2700 ft to 2750 ft and unconformity at the depths from 3040 ft to 3100 ft. Reservoir pay zone is from the depth of 2850 ft to 2950 ft.

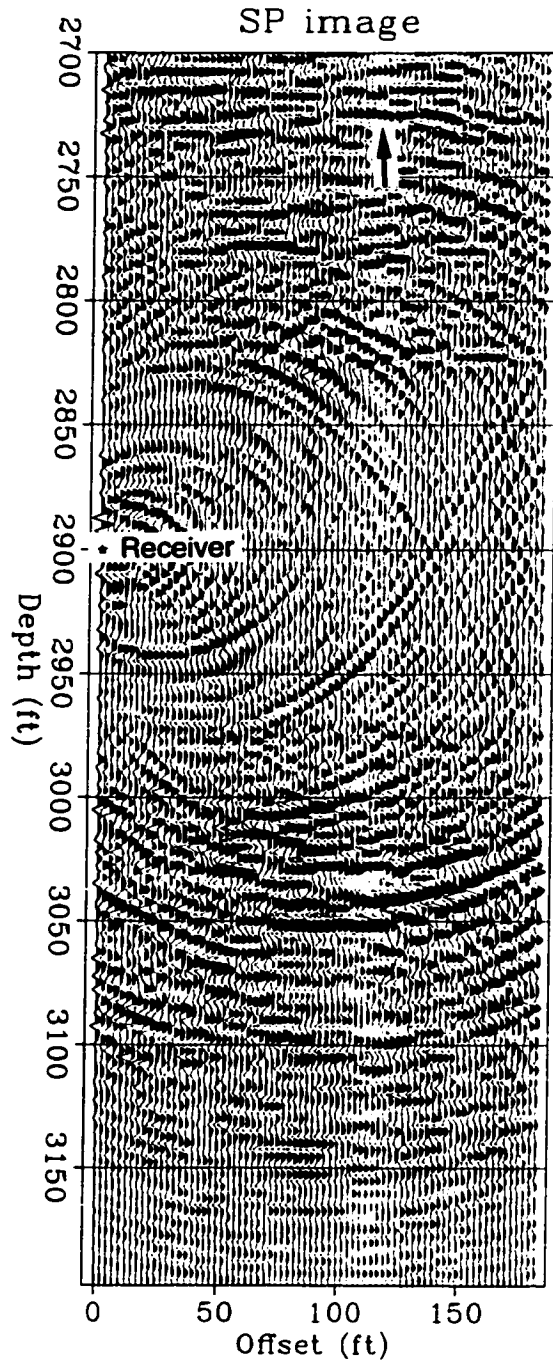


Figure 4.21: *S-P* wave image for the CRG, the depth of the receiver is 2900 ft. Notice the flat reflectors at the depth of 2725 ft.

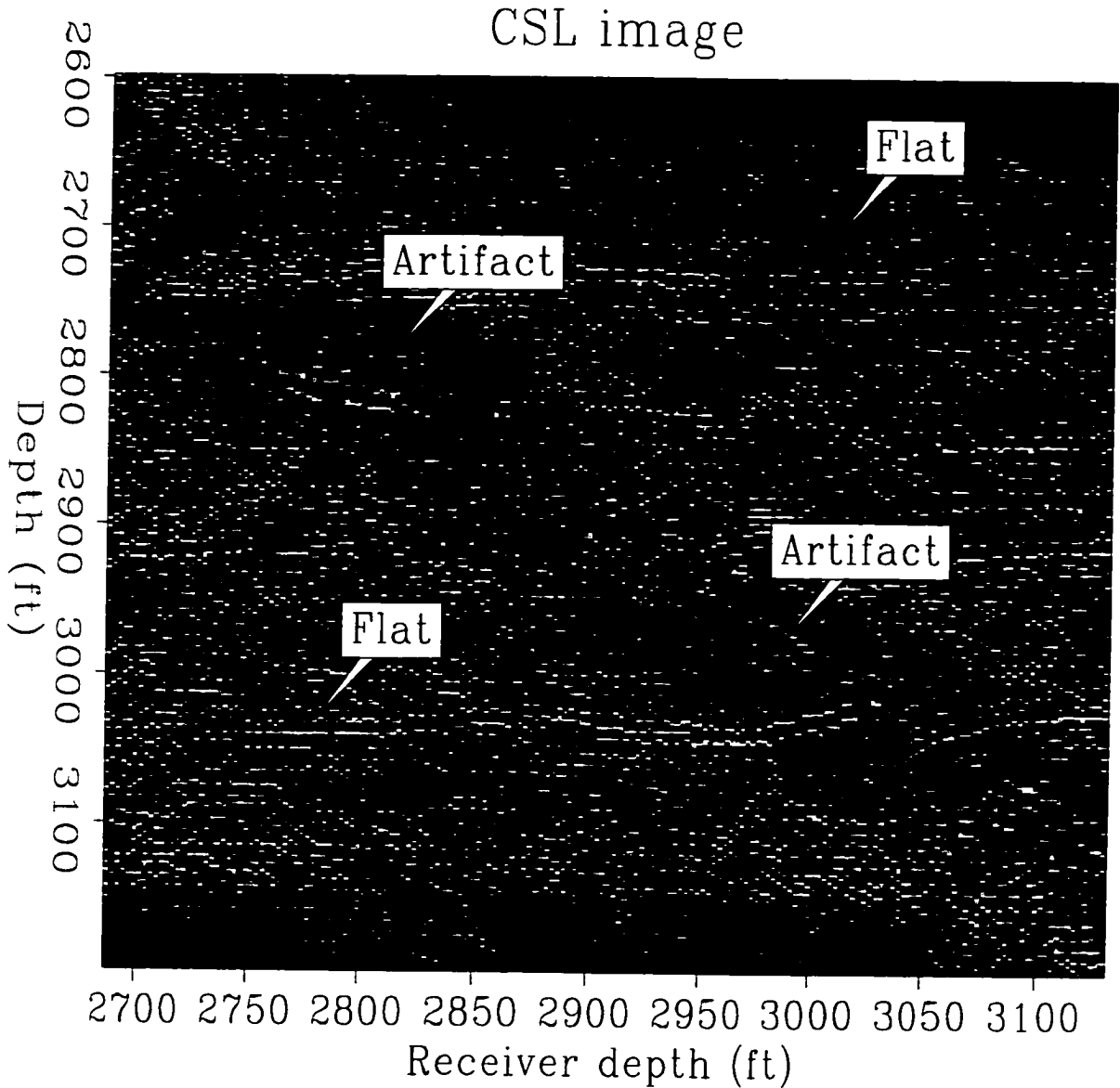


Figure 4.22: *S-P* wave common surface location (CSL) image plane 150 ft from the left well. Except for the upper-left to lower-right diagonal region of artifacts resulted from imaging the migration sources, the image events are flatly aligned, suggesting that the velocity model used in migration is correct.

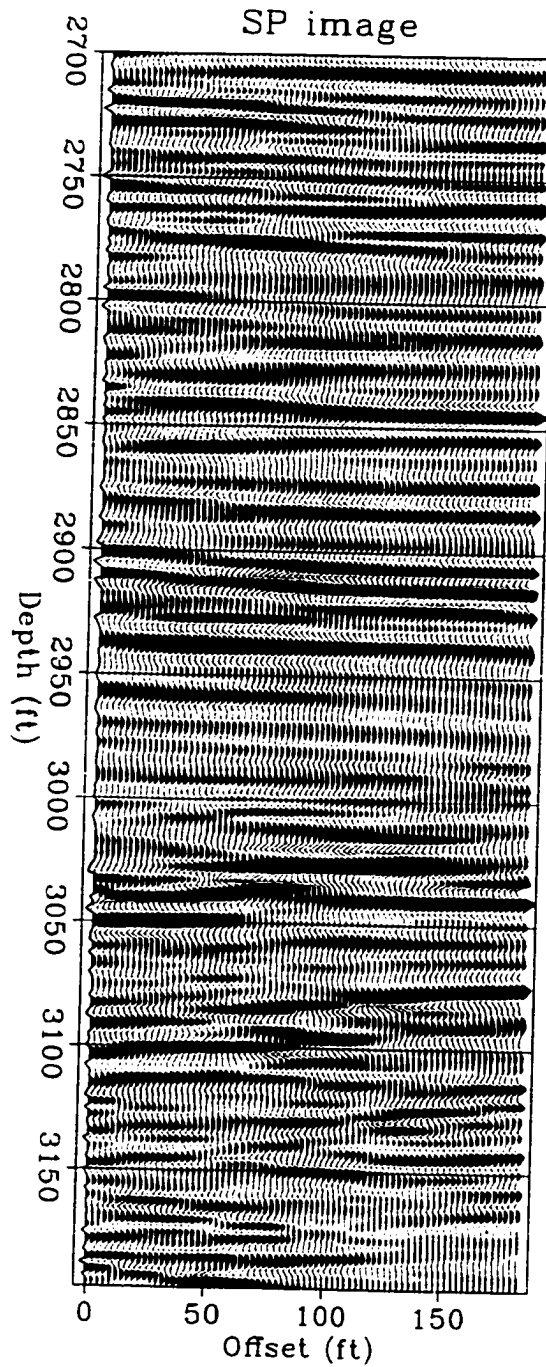


Figure 4.23: *S-P* wave migration image, The principal features are the flat reflectors at the depths from 2700 ft to 2750 ft and unconformity at the depths from 3040 ft to 3100 ft. Reservoir pay zone is from the depth of 2850 ft to 2950 ft.

The field data are effectively conditioned for migration by interpolation of missing traces, correction of amplitude, and attenuation of the direct arrivals. A high-order finite-difference scheme is applied to perform the wavefield back-propagation. The imaging conditions – traveltimes and amplitudes are calculated by solving the Eikonal equation and the transport equation. Reflectivity is calculated by dividing the focused back-propagated wavefield by the amplitude of the direct arrival from the source. The velocity tomogram obtained from transmission travel time tomography is an accurate background velocity model for migration, as is demonstrated by the flatness of the image events in the common surface location image gathers. Because of the radiation patterns of the source and the presence of noises in the data, a single-fold CSG migration image can only image a limited portion of the interwell region sufficiently well. A complete interwell image can be obtained by stacking the individual CSG migration images.

Chapter 5

Kirchhoff migration of cross-well data

In this chapter, I describe the application of prestack Kirchhoff migration to a field cross-well dataset recorded with a piezoelectric source and hydrophones. The data contain a rich variety of elastic wavemodes, compressional P -, shear S -, and converted waves, with a bandwidth of 2000 Hertz. Data preprocessing consists of interpolation of missing traces, amplitude correction, and attenuation of the direct P - and S -waves.

In the prestack common shot gather migration, wavefield back-propagation from the receivers is performed by using the Kirchhoff integral. Imaging conditions are the traveltime and amplitude of the direct arrival from the source. Reflectivity is calculated by dividing the estimated diffraction source by the direct arrival from the source. The velocity tomogram obtained from transmission travel time tomography is used as the background velocity model for migration. Prestack single-fold images reveal geological structures depending on illumination from the source. After migration of all the common shot gathers, an image volume is generated. Image gathers at common surface locations sliced from the image volume show that the events are in good alignment, suggesting that the velocity model used in migration is correct. The stacked P - P , S - S , P - S and S - P images clearly show the structure around a 100 ft (30 m) thick reservoir and other geological features such as unconformity. The results are consistent with those obtained by finite-difference reverse-time migration and VSP-CDP mapping.

5.1 Introduction

In the previous chapter, I have demonstrated the application of finite-difference reverse-time migration to a field cross-well seismic data set. Migration is achieved through wave field extrapolation, subject to an imaging procedure. Wave field extrapolation is based upon the scalar wave equation. In the wave field backpropagation of finite-difference reverse-time migration, the scalar wave equation is explicitly solved in space and time. The recorded seismograms are applied as boundary conditions on the recording surface. This requires the seismograms be regularly sampled in space to fit in the finite-difference mesh. But sometimes this can not be satisfied in practice as the wells are crooked and deviated from vertical, so that the sources and receivers are not evenly spaced in depth. Data processing in the borehole environments require methodologies that can handle irregular recording geometry elegantly. Kirchhoff integral migration can handle virtually any configuration of sources and receivers, can be compensated for irregular spatial sampling of the receivers, and can handle dips up to 90 degrees as in reverse-time migration. In addition, Kirchhoff migration more readily lends itself to external control; flexible weighting schemes can be incorporated in the integral to combat seismic noise not comprehended by the wave equation.

In the previous publications, Hu et al. (1988) by reverse-time migration and Gray and Lines (1992) by double Kirchhoff VSP depth migration, have demonstrated migration of synthetic and water-tank modeled crosswell seismic data. Qin and Schuster (1993) demonstrated constrained Kirchhoff migration on field crosswell seismic data, in that they reject high dip image events in the migration process. Yet the applications of migration to field crosswell seismic data are still rare. The reasons might be lack of well-sampled crosswell field data and difficulties in processing these field data which are generally very complex.

This chapter is divided into two parts, theory and application in field data. In the first part, I derive the Kirchhoff migration algorithm using the WKBJ Green's function; then I describe the implementation of the method. In the second part, I describe prestack Kirchhoff migration on the field data, obtaining P - P , S - S , P - S , S - P wave images. These four elastic wavemode images are consistent with those obtained by finite-difference reverse-time migration.

5.2 Theory

5.2.1 Kirchhoff migration

In this section, I derive the Kirchhoff migration integral for a medium with arbitrary velocity variations, for prestack migration of common shot multi-channel data. The application is for prestack migration of cross-well seismic data, in particular. First of all, the recorded wavefield needs to be backpropagated from the recording surface back to the medium. Begin with the Helmholtz equation,

$$(\nabla^2 + \omega^2/v^2)G = \delta(\mathbf{r} - \mathbf{r}_1) \quad (5.1)$$

where G is the Green's function that solves equation (5.1) and satisfies the radiation condition (Goodman, 1970); ∇^2 is the Laplacian operator, ω is frequency, $v(x, z)$ is acoustic velocity, and δ is the Dirac delta function. The vectors \mathbf{r} and \mathbf{r}_1 are the position of the receiver and point scatterer, respectively. The wave field $P(\mathbf{r}, \omega)$ satisfies the equation

$$(\nabla^2 + \omega^2/v^2)P(\mathbf{r}, \omega) = 0 \quad (5.2)$$

inside the source-free volume V . To obtain the Kirchhoff integral, I use the Green's second theorem (Goodman, 1970),

$$\int_V (\phi_1 \nabla^2 \phi_2 - \phi_2 \nabla^2 \phi_1) dV = \int_S (\phi_1 \partial_n \phi_2 - \phi_2 \partial_n \phi_1) dS \quad (5.3)$$

where n denotes the outward normal direction to the surface S , and substitute $\phi_1 = P(\mathbf{r}, \omega)$ and $\phi_2 = G$ to obtain

$$P(\mathbf{r}_1, \omega) = \int_S (P(\mathbf{r}, \omega) \partial_n G - G \partial_n P(\mathbf{r}, \omega)) dS \quad (5.4)$$

which is the Kirchhoff integral, Figure 5.1.

In the Kirchhoff integral equation (5.4), both the record of the wave field $P(\mathbf{r}, \omega)$ and its gradient are involved. But in actual seismic profiling, only the wave fields $P(\mathbf{r}, \omega)$ are recorded. French (1975) and Schneider (1978) showed that if the data are collected in a flat plane, the second term in the integrand of the Kirchhoff equation is the negative of the first term. This condition is approximately valid for borehole profiling, since any change of borehole direction must proceed gradually and may be assumed negligible for typical seismic wavelengths. Therefore I replace the second term containing the normal derivative of the data with the negative of the first term. Also, I extend the boundary

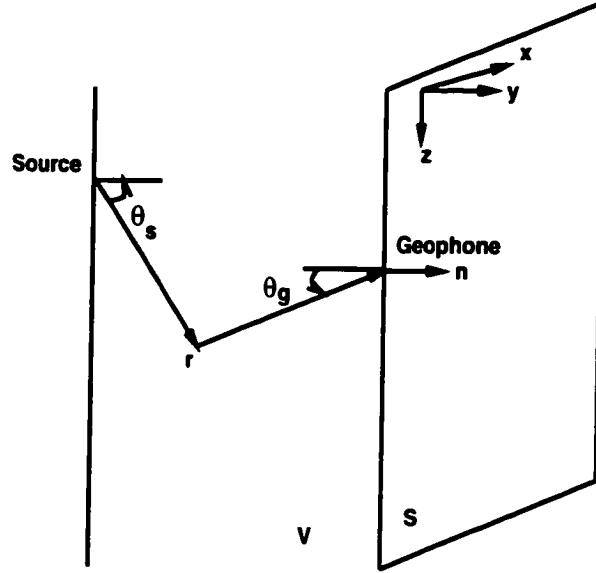


Figure 5.1: Wavefield extrapolation and imaging. The wavefield in the medium is reconstructed by Kirchhoff integration over the recording surface. Imaging is performed by taking the quotient of the reconstructed diffraction wavefield and the source wavefield.

of the integration surface to infinite distance, where there is no back-scattered energy as governed by the radiation condition, so that the only remaining contribution to the integral comes from the recording surface S . Equation (5.4) becomes

$$P(\mathbf{r}, \omega) = 2 \int_S P(\mathbf{r}_g, \omega) \partial_n G dS \quad (5.5)$$

I now write $G = A(\mathbf{r}|\mathbf{r}_g) e^{-i\omega\tau(\mathbf{r}|\mathbf{r}_g)}$ and use the geometrical optics approximation for the amplitude $A(\mathbf{r}|\mathbf{r}_g)$ and phase $\tau(\mathbf{r}|\mathbf{r}_g)$. The negative sign in the phase of G is used because the wave fields are backpropagated from the recording surface. Along a ray path, the variation in $e^{-i\omega\tau}$ is much larger than the variation in A . Thus the first term in the derivative of G

$$\partial_n G = (\partial_n A) e^{-i\omega\tau} - A e^{-i\omega\tau} i\omega (\partial_n \tau) \quad (5.6)$$

is small compared to the second term and is neglected. The Kirchhoff integral (5.5) can now be written in the form

$$P(\mathbf{r}, \omega) = -2 \int_S P(\mathbf{r}_g, \omega) A e^{-i\omega\tau} i\omega (\partial_n \tau) dS \quad (5.7)$$

in which

$$\partial_n \tau = \mathbf{n} \cdot \partial \tau = \mathbf{n} \cdot \mathbf{t} / v_g = \cos \theta_g / v_g \quad (5.8)$$

where \mathbf{t} is the unit tangent vector for the emerging ray, and θ_g is the angle of emergence, and v_g is the acoustic velocity at the receiver. The amplitude term $A(\mathbf{r}|\mathbf{r}_g)$ can be obtained from the transport equation.

The reflectivity function $R(\mathbf{r}, \omega)$ is defined as the ratio of the back-propagated field from the receivers $P(\mathbf{r}, \omega)$ to the incidence field from the source $P_s(\mathbf{r}, \omega)$ (Claerbout, 1970),

$$R(\mathbf{r}, \omega) = \frac{P(\mathbf{r}, \omega)}{P_s(\mathbf{r}, \omega)} \quad (5.9)$$

The incidence source field is approximated by the WKB Green's function

$$P_s(\mathbf{r}, \omega) = A(\mathbf{r}|\mathbf{r}_s)e^{i\omega\tau(\mathbf{r}|\mathbf{r}_s)} \quad (5.10)$$

Combining equations (5.7) through (5.10) gives the holographic (i.e., frequency-domain) form of Kirchhoff migration.

$$R(\mathbf{r}, \omega) = -2 \int_S \frac{A(\mathbf{r}|\mathbf{r}_g)}{A(\mathbf{r}|\mathbf{r}_s)} \frac{\cos \theta_g}{v_g} e^{-i\omega(\tau(\mathbf{r}|\mathbf{r}_s) + \tau(\mathbf{r}|\mathbf{r}_g))} i\omega P(\mathbf{r}_g, \omega) dS \quad (5.11)$$

The time-space domain reflectivity is obtained by an inverse Fourier transform,

$$R(\mathbf{r}) = -2 \int_S \frac{A(\mathbf{r}|\mathbf{r}_g)}{A(\mathbf{r}|\mathbf{r}_s)} \frac{\cos \theta_g}{v_g} \partial_t P(\mathbf{r}_g, \tau(\mathbf{r}|\mathbf{r}_s) + \tau(\mathbf{r}|\mathbf{r}_g)) dS \quad (5.12)$$

This is the conventional full-aperture Kirchhoff migration algorithm. To image a point in the image space, the integral sums contributions from all the traces on the recording surface, ie, it is a full-aperture algorithm. Figure 5.2 shows the redisplay of Figure 4.1. For example, to image point D , the contributions along its diffraction travel time trajectory are summed.

The points in the image where the sum of the travel time from the source and the travel time to the receiver being a constant form an elliptical trajectory. To view it in another way, the Kirchhoff migration spreads a spike in the data along an elliptical trajectory in the image, ie, the algorithm has a full 90-degree impulse response. Figure 5.3 shows contours of travel times calculated for a constant velocity model. Figure 5.3(a) and (b) are the travel times from the source or the receiver to all points in the image space. Figure 5.3(c) is the sum of Figure 5.3(a) and (b), and its contours are called isochrone trajectories. These isochrone trajectories are actually ellipses with the source and the receiver as the foci. In a variable velocity medium, the circular wavefronts in Figure 5.3(a) and (b), and the elliptical isochrone trajectories in Figure 5.3(c) will be distorted. Figure 5.4 shows how

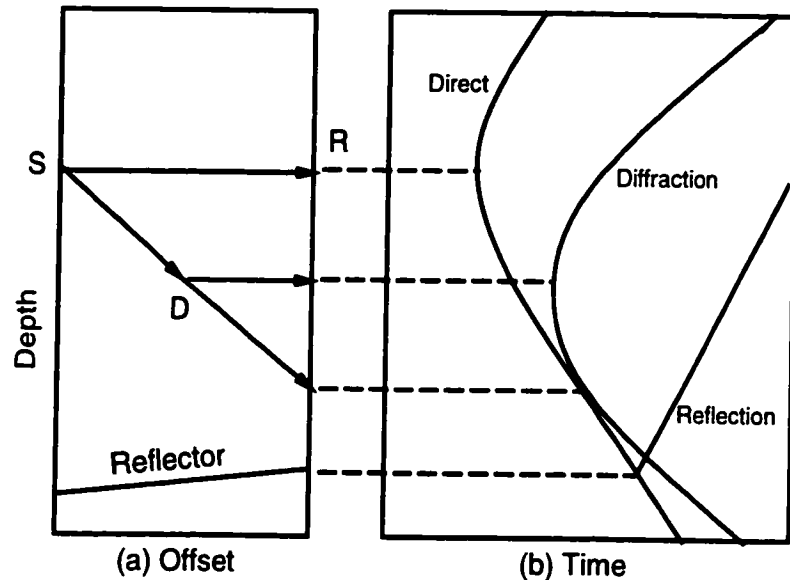


Figure 5.2: (a) Crosswell surveying geometry, S is source, R is receiver, D is a point diffractor; (b) traveltime trajectories of direct arrival, diffraction and reflection. To image point D , the contributions along its diffraction travel time trajectory are summed.

the migration algorithm operates in imaging a single trace containing four wavelet spikes. Figure 5.4 is actually a representation of Figure 5.3(c) in waveforms. The full-aperture 90-degree migration algorithm spreads a wavelet along the whole isochrone trajectory, by doing so it can correctly image all dips up to 90-degrees, focus diffractions and shrink the Fresnel zone to increase lateral resolution.

Each point in the medium is treated as a point diffractor and is imaged accordingly. And in particular, the point of a physical source is imaged by the direct wave at time $\tau(\mathbf{r}|\mathbf{r}_s) = 0$, ie, the direct arrivals are summed to image at the physical source. Figure 5.2(b) shows that the traveltime trajectories of the direct arrival and diffraction coincide at certain place, this means by Kirchhoff diffraction stack migration the direct arrival will also affect the imaging of geological structures, creating low-wavenumber background noise in the image. Thus the direct arrival should be attenuated before the data are input to migration. The result of migration is an image of the high-wavenumber velocity heterogeneity, that is, the locations and strengths of the diffractors.

The common-shot gather data that are input for migration wavefield back-propagation are without divergence corrections. Geometrical spreading from the source to a diffractor and geometrical spreading from the diffractor to the receivers are compensated for by the

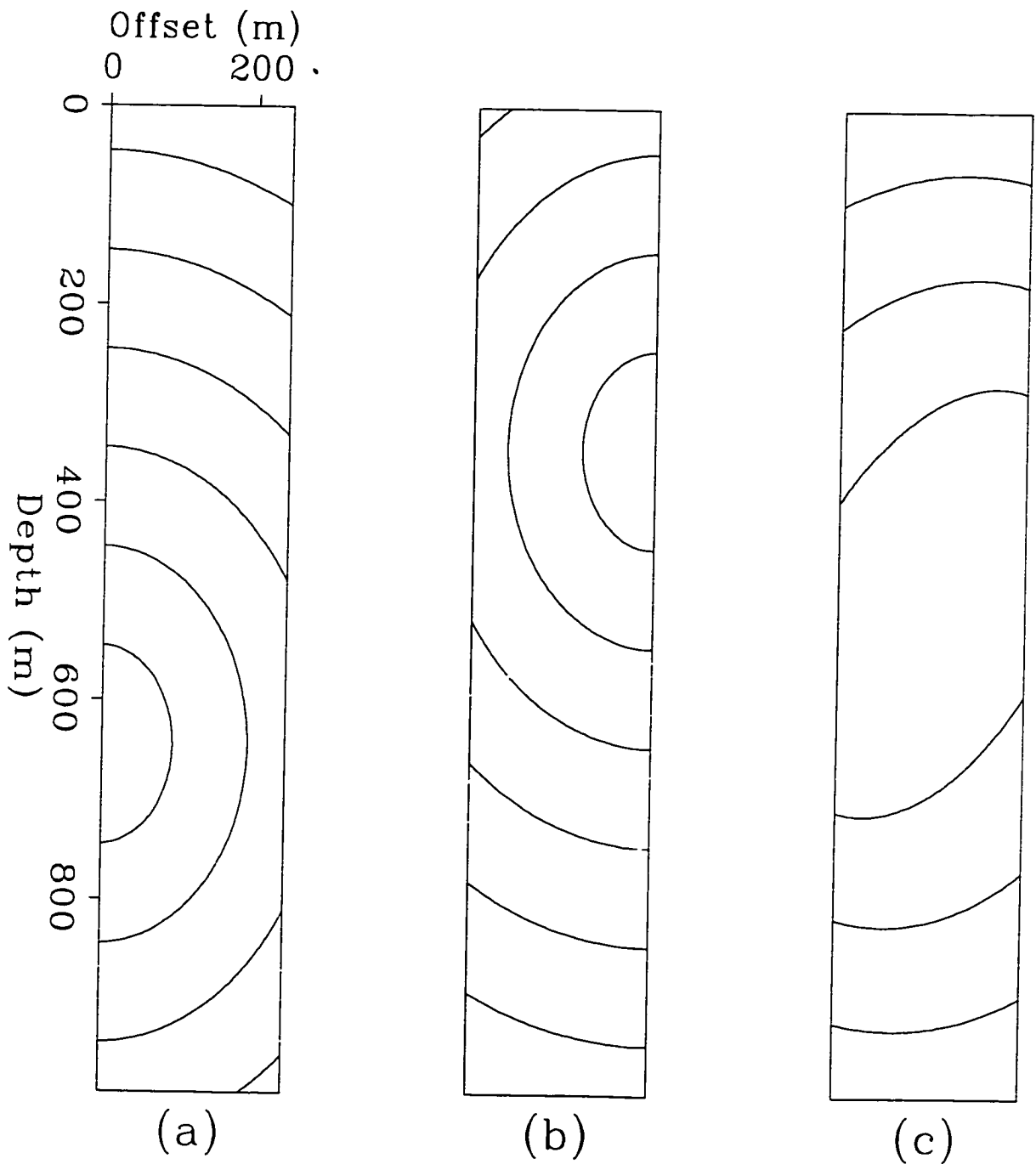


Figure 5.3: (a) The travel time contours of wavefronts from a source. (b) The travel time contours of backpropagation wavefronts from a receiver. (c) Prestack migration spreads a spike in the data along an elliptical trajectory with the source and the receiver as the foci.

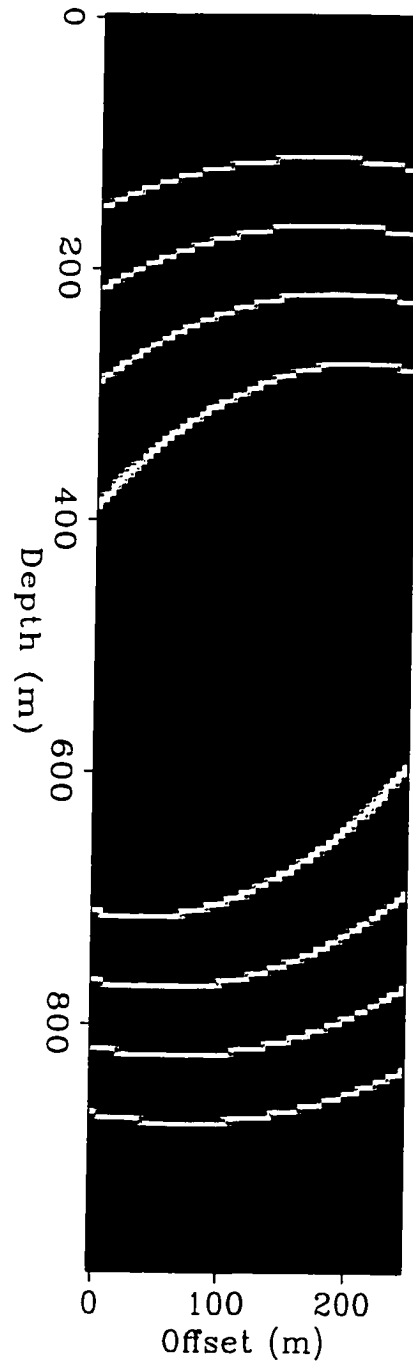


Figure 5.4: Impulse responses of prestack migration. In a full-aperture 90-degree migration algorithm, a spike in the data is spread along an elliptical isochron with the source and the receiver as the foci.

amplitude weighting factors in the Kirchhoff integral. However, if the data is recorded in 3-D world and migration processing is done in 2-D, the data must be corrected for the difference of divergence between 3-D and 2-D.

5.2.2 Implementation of Kirchhoff migration

Prestack common shot gather Kirchhoff migration is realized by implementing equation (5.12). The time derivative of the seismograms is computed by first transforming the data to the frequency domain, multiplying by $i\omega$, and finally doing an inverse Fourier transform back to the time domain. The obliquity factor $\cos \theta_g$ at the receivers are computed by using geometrical ray theory assuming constant velocity model. The most frequently accessed data in the equation (5.12) are the travel time and amplitude tables from the source. Before doing migration of a CSG, these two tables are computed and stored in the computer main memory for fast access. The travel time and amplitude tables from each of the receiver locations are computed and stored as floating-point numbers in two volumes in disk. The combined sizes of these tables are usually too large to fit in computer main memory and they are much less frequently accessed than the tables from the source, so they must be stored in disk. The Unix operating system and the C language environment provide an utility "fseek" that can quickly position the read/write head at a certain position of a data file. Thus the travel time and amplitude tables from each of the receiver locations can also be accessed efficiently.

In processing hydrophone data that contain elastic wave modes, two images of different wave modes can be produced in one backpropagation of the receiver wavefield. Migration processing of P - P and S - P waves can be coupled; the P -wave velocity model is used to compute the travel time and amplitude tables from the receivers for the wavefield backpropagation and two imaging conditions corresponding to P - and S -wave are applied simultaneously to produce the P - P and S - P waves images. Migration processing of P - S and S - S waves can be coupled; the S -wave velocity model is used to compute the travel time and amplitude tables from the receivers for the wavefield backpropagation and two imaging conditions corresponding to P - and S -wave are applied simultaneously to produce the P - S and S - S waves images.

After migration of all the common shot gathers, a volume of images is generated. These single-fold images are stacked as in finite-difference reverse-time migration.

5.3 Application in field data

5.3.1 Description of field data

A description of the data may be found in section 4.3.1 of Chapter 4, "Finite-difference reverse-time migration of cross-well data".

5.3.2 Preprocessing of field data

Data preprocessing consists of interpolation of missing traces, amplitude correction, and attenuation of the direct P - and S -waves. Figure 5.5 is a common receiver gather data that is input to migration processing for P - P , S - S , P - S and S - P waves. It is a redisplay of Figure 4.4.

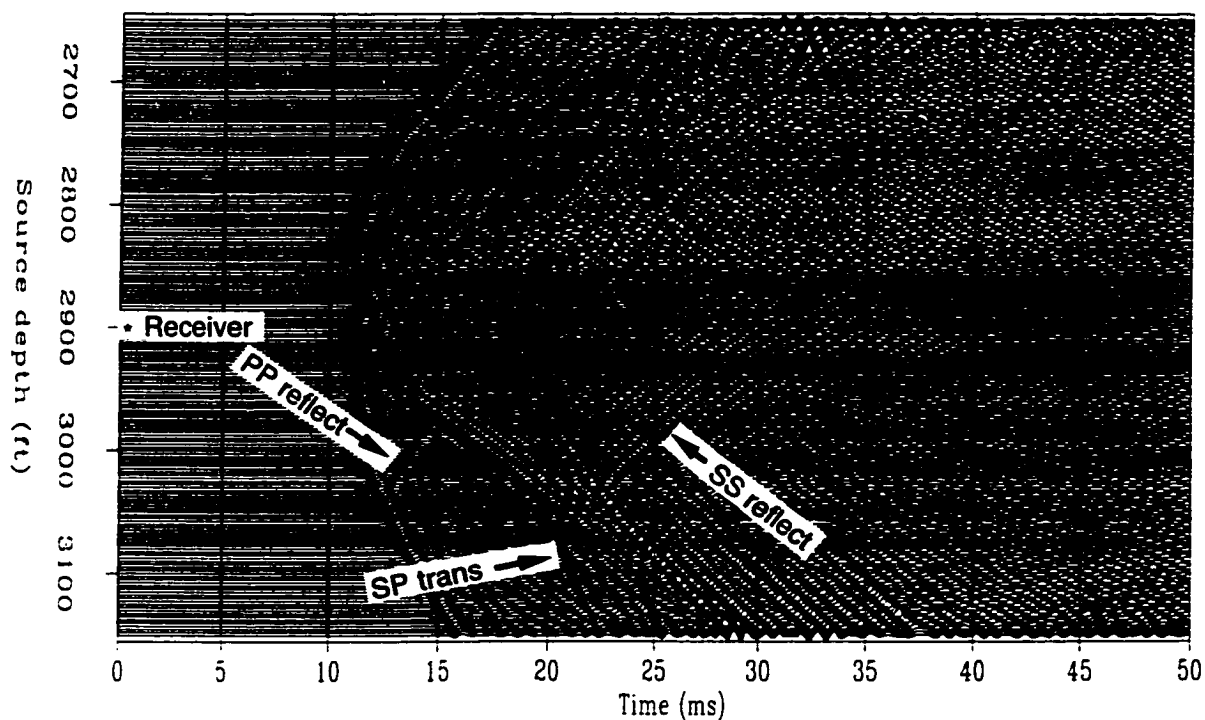


Figure 5.5: Common receiver gather after preprocessing of amplitude corrections, tapered muting of the P -wave direct arrival and attenuation of the S -wave direct arrival. The receiver is at the depth of 2900 ft. Notice the strong P - P and S - S reflections, and S - P transmissions at the depth of 3050 ft. This data is input for migration processings of P - P , S - S , P - S and S - P waves.

5.3.3 Background velocity model

A description of the data may be found in section 4.3.3 of Chapter 4, "Finite-difference reverse-time migration of cross-well data".

5.3.4 *P-P* wave migration

By applying the principle of reciprocity, I process the CRG data as common shot gathers (CSG). The *P*-wave velocity is used for the wavefield back-propagation, and it is also used to calculate the imaging conditions. Figure 5.6 shows the resulting *P-P* wave image for the common receiver gather shown in Figure 5.5. In this single-fold image, flat reflectors at the depths from 2700 ft to 2750 ft, flat reflector at the depth of 3040 ft, and right to left dipping reflectors at the depths from 3050 ft to 3100 ft can be identified. The remnant direct arrival images the migration source at the depth of 2900 ft, this is considered as noise in imaging geological structures. But this also implies that the transmission traveltimes tomogram predicts the direct arrival traveltimes pretty well. The elliptical events in this *P-P* image are produced by noises – the *S*- and converted waves.

After migration of all the common receiver gathers, an image volume is generated, Figure 5.7. Image gathers at common surface locations (CSL) can be sliced from the image volume to demonstrate the correctness of the velocity model. If the velocity model is correct, the images produced by migration of different common shot gathers should be consistent, and thus the image events in the CSLs should be flat. Figure 5.8 shows the CSL at the lateral location of 150 ft from the left well. The upper-left to lower-right diagonal region contains artifacts resulted from imaging the migration sources. These artifacts must be muted before the images are stacked. The image events at the lower-left and upper-right triangular regions are flatly aligned, suggesting that the velocity model used in migration is correct. Then the image at the upper-right triangular region which is made by upgoing source wavefiled is multiplied by the value of -1 to reverse polarity. Finally, the traces in this CSL image are stacked to produce the single image trace 150 ft from the left well.

Figure 5.9 shows the final stacked *P-P* wave image, compared with the sonic logs and the synthetic seismograms at the two wells. The synthetic seismograms are the same that appear in Chapter 4. The synthetic seismograms are made using the following procedures. The vertical incidence reflection coefficient series is calculated from the sonic log. Then a

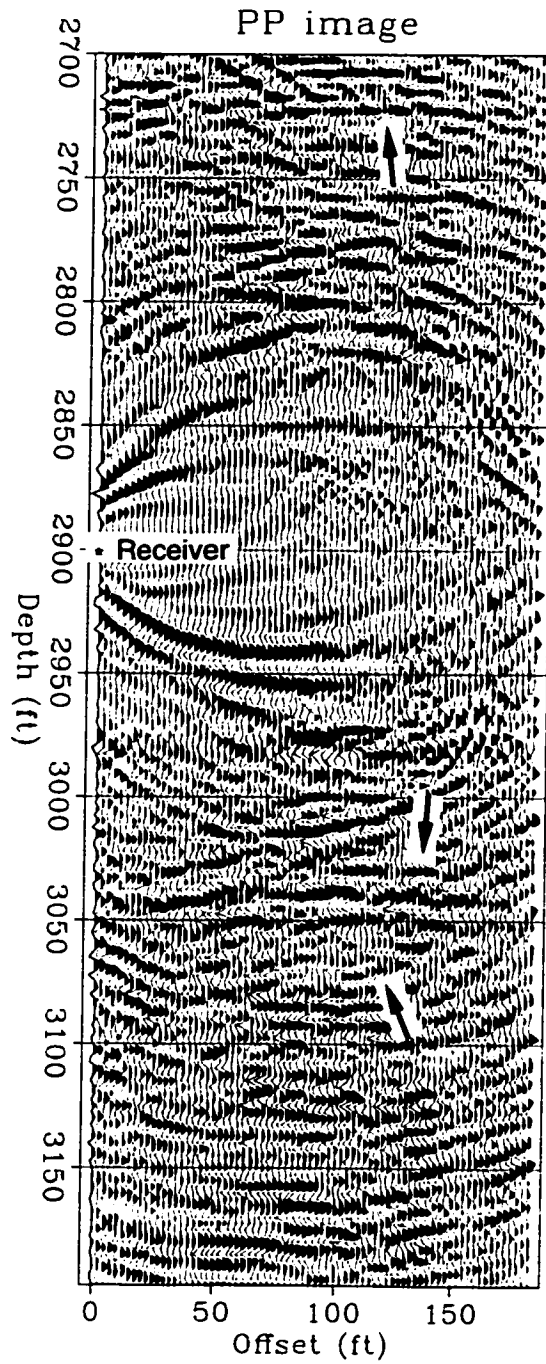


Figure 5.6: P - P wave image for the CRG, the depth of the receiver is 2900 ft. Notice the flat reflectors at the depth of 2725 ft and 3040 ft, and the right to left dipping reflectors at the depths from 3050 ft to 3100 ft.

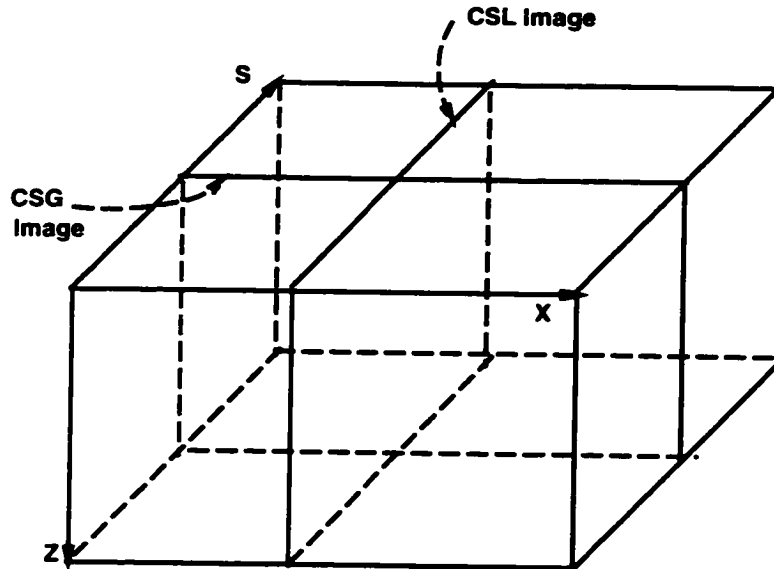


Figure 5.7: After migration of all the common shot gathers, a volume of images is generated. From this volume, CSG image planes and common surface location (CSL) image planes can be sliced.

zero-phase Ricker wavelet of similar frequency band as in the migration image is convolved to the reflection coefficient series. The making of the synthetic seismograms is very rough, as the cross-well image is not produced by vertical incidence source wave field and the wavelet in the image is not Ricker. The synthetic seismograms are only for purpose of qualitative comparison with the migration image. The formations from depths of 2700 ft to 2800 ft are nearly flat, as suggested by the two sonic logs in this interval. The migration image clearly shows what the sonic logs only suggest that at depth of 3050 ft there is an unconformity, the dip of which is 5 degrees. As described in Harris et al. (1995), the reservoir pay zone is dolomitized carbonate from depth of 2850 ft (870 m) to 2950 ft (900 m) and is within the Permian-aged Grayburg formation.

5.3.5 *S-S* wave migration

The migration for *S-S* wave is carried out in a similar procedure as for *P-P* wave. The *S*-wave velocity is used for the wavefield back-propagation, and it is also used to calculate the imaging conditions. Figure 5.10 shows the resulting *S-S* wave image for the common receiver gather shown in Figure 5.5. In this single-fold image, flat reflectors at the depths from 2700 ft to 2750 ft, flat reflector at the depth of 3040 ft, and right to left dipping

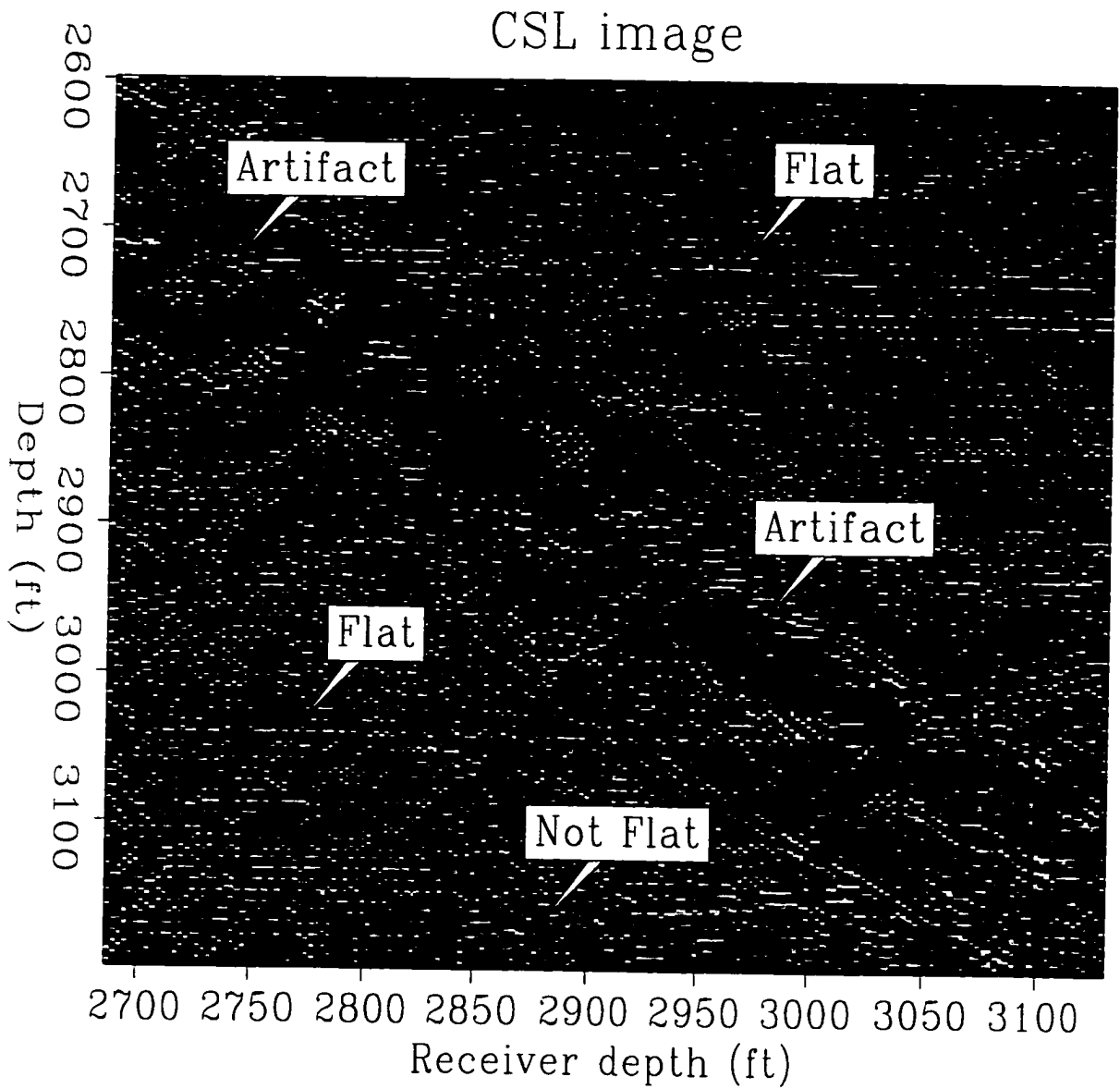


Figure 5.8: *P-P* wave common surface location (CSL) image plane 150 ft from the left well. Except for the upper-left to lower-right diagonal region of artifacts resulted from imaging the migration sources, the image events are flatly aligned, suggesting that the velocity model used in migration is correct.

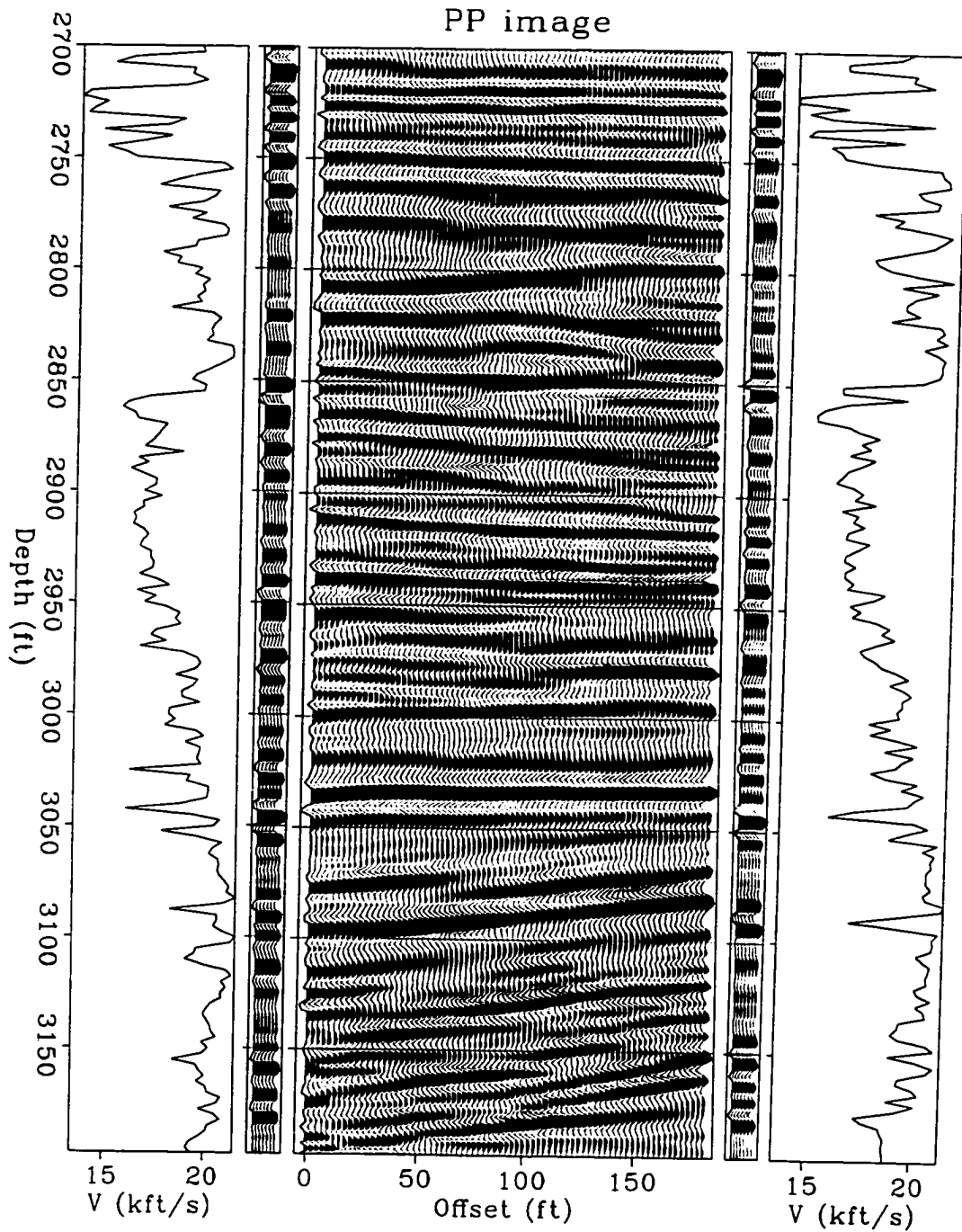


Figure 5.9: *P-P* wave image, sonic logs, and synthetic seismograms. Flat reflectors at the depths from 2700 ft to 2750 ft and unconformity at the depths from 3040 ft to 3100 ft can be identified. Reservoir pay zone is from the depth of 2850 ft to 2950 ft.

reflectors at the depths from 3050 ft to 3100 ft can be identified. These features are consistent with those in the *P-P* wave image. The elliptical events in this *S-S* image are produced by noises.

After migration of all the common receiver gathers, an image volume is generated, as in *P-P* wave, Figure 5.7. Figure 5.11 shows the CSL at the lateral location of 150 ft from the left well. The upper-left to lower-right diagonal region contains artifacts resulted from imaging the migration sources. These artifacts must be muted before the images are stacked. The image events at the lower-left and upper-right triangular regions are flatly aligned, suggesting that the velocity model used in migration is correct.

Figure 5.12 shows the final stacked *S-S* wave migration image. The formations from depths of 2700 ft to 2800 ft are nearly flat. Below the depth of 3050 ft is an unconformity, the dip of which is 5 about degrees. The reservoir pay zone is from depth of 2850 ft (870 m) to 2950 ft (900 m).

5.3.6 *P-S* wave migration

The migration for *P-S* wave is carried out in a similar procedure as for *P-P* wave. The *S*-wave velocity is used for the wavefield back-propagation, and *P*-wave velocity is used to calculate the imaging conditions. Figure 5.13 shows the resulting *P-S* wave image for the common receiver gather shown in Figure 5.5. In this single-fold image, reflectors at the depth of 2900 ft can be identified.

After migration of all the common receiver gathers, an image volume is generated, as in *P-P* wave, Figure 5.7. Figure 5.14 shows the CSL at the lateral location of 150 ft from the left well. The image events at the middle depths are flatly aligned, suggesting that the velocity model used in migration is correct. However, at the bottom of the survey below 3100 ft, the image events are not well flatly aligned.

Figure 5.15 shows the final stacked *P-S* wave migration image. The formations from depths of 2700 ft to 2800 ft are nearly flat. Below the depth of 3050 ft is an unconformity, the dip of which is 5 degrees. The reservoir pay zone is dolomitized carbonate from depth of 2850 ft (870 m) to 2950 ft (900 m).

5.3.7 *S-P* wave migration

The migration for *S-P* wave is carried out in a similar procedure as for *P-P* wave. The *P*-wave velocity is used for the wavefield back-propagation, and *S*-wave velocity is used

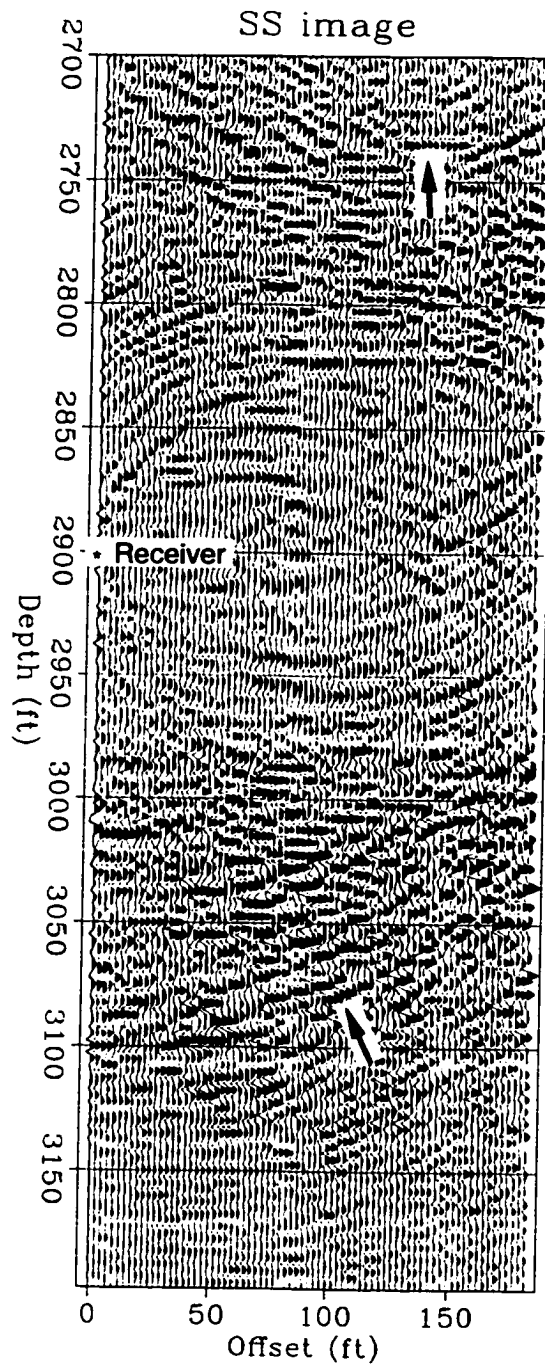


Figure 5.10: *S-S* wave image for the CRG, the depth of the receiver is 2900 ft. Notice the flat reflectors at the depth of 2725 ft and right to left dipping reflectors at the depths from 3050 ft to 3100 ft.

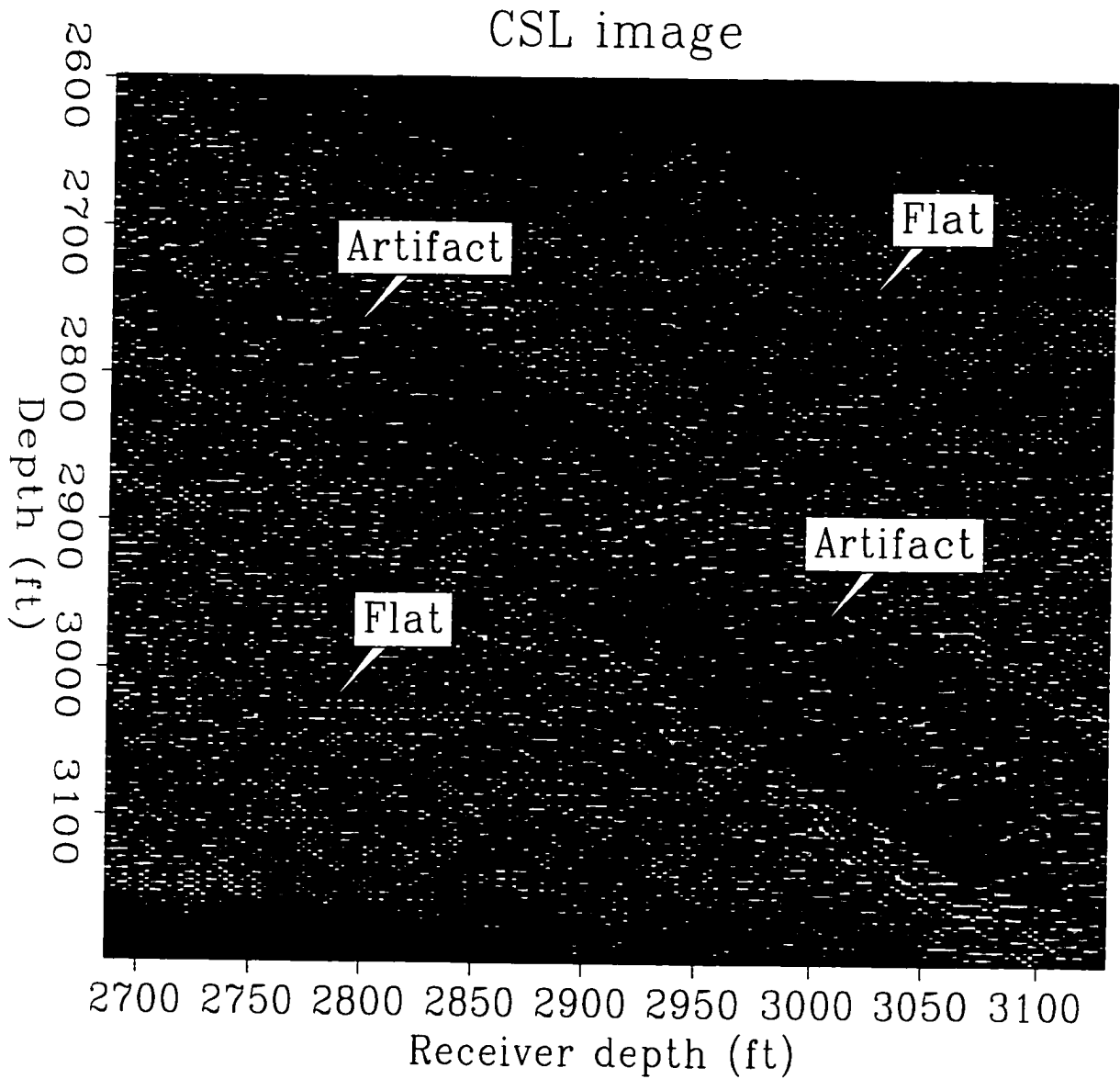


Figure 5.11: *S-S* wave common surface location (CSL) image plane 150 ft from the left well. Except for the upper-left to lower-right diagonal region of artifacts resulted from imaging the migration sources, the image events are flatly aligned, suggesting that the velocity model used in migration is correct.

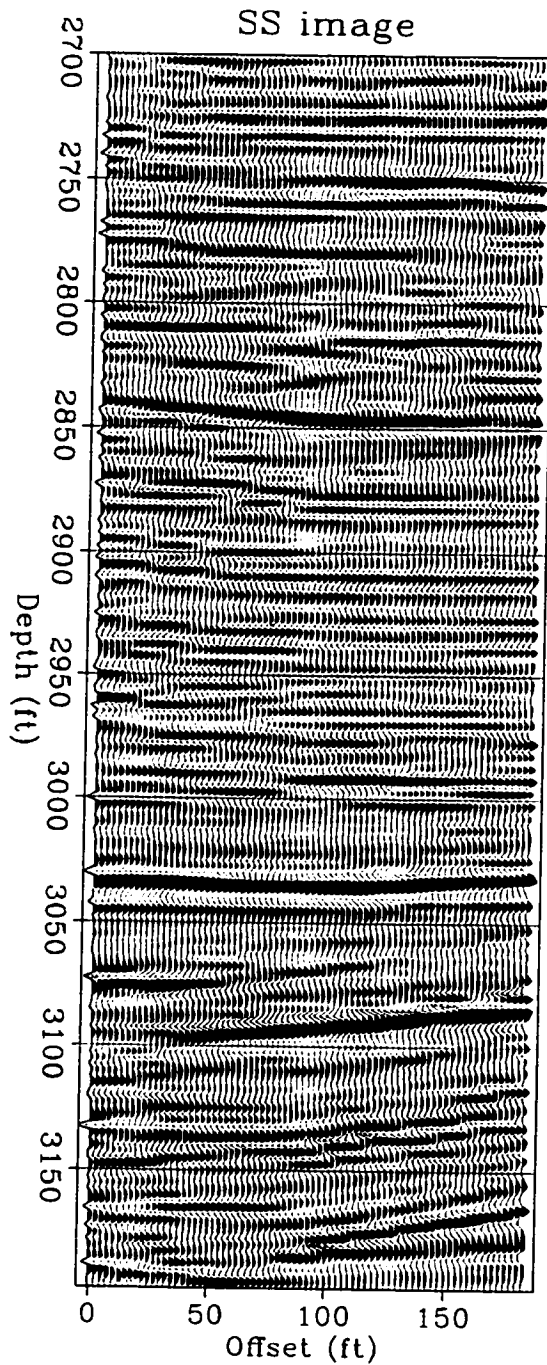


Figure 5.12: *S-S* wave migration image. Flat reflectors at the depths from 2700 ft to 2750 ft and unconformity at the depths from 3040 ft to 3100 ft can be identified. Reservoir pay zone is from the depth of 2850 ft to 2950 ft.

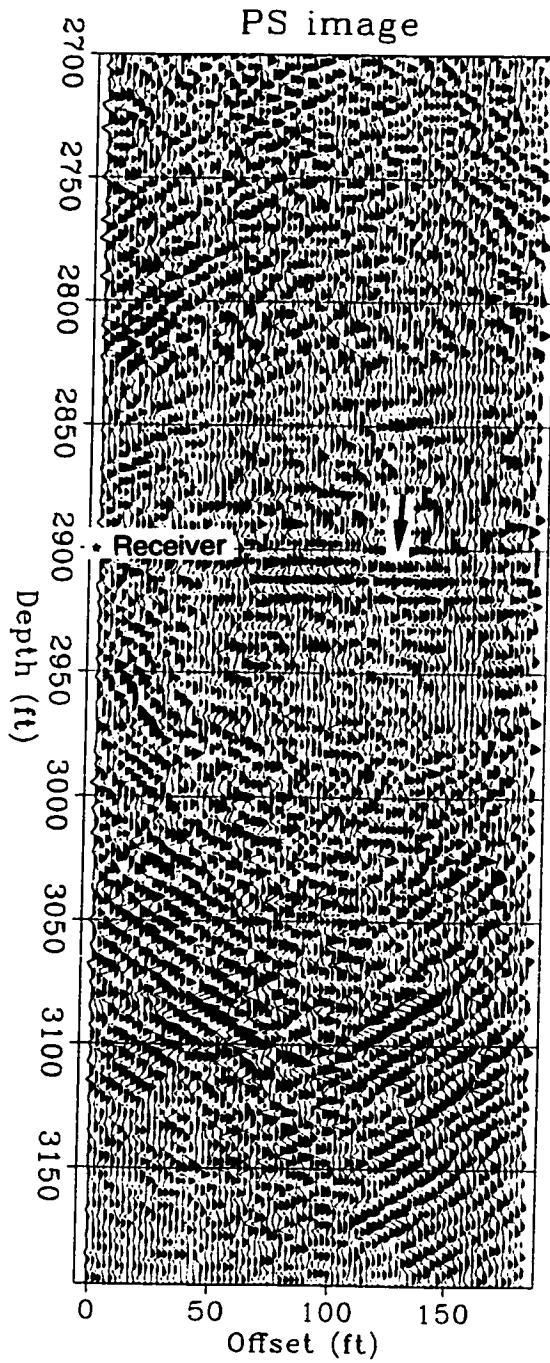


Figure 5.13: *P-S* wave image for the CRG, the depth of the receiver is 2900 ft. Notice the reflectors at the depth of 2900 ft inside the reservoir.

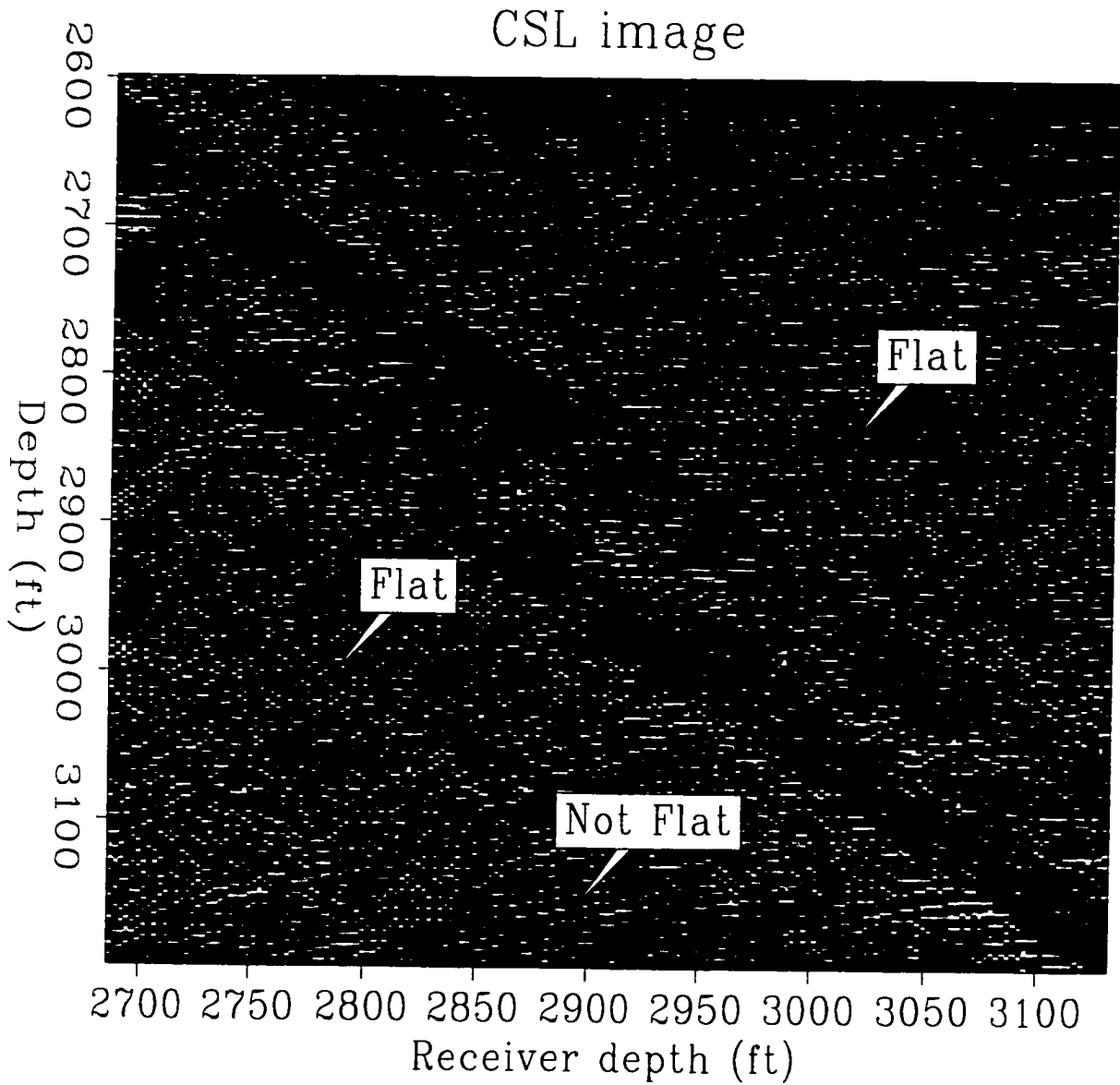


Figure 5.14: *P-S* wave common surface location (CSL) image plane 150 ft from the left well. The image events at the middle depths are flatly aligned. However, at the depths from 3100 ft to 3200 ft, the image events are not well flatly aligned.

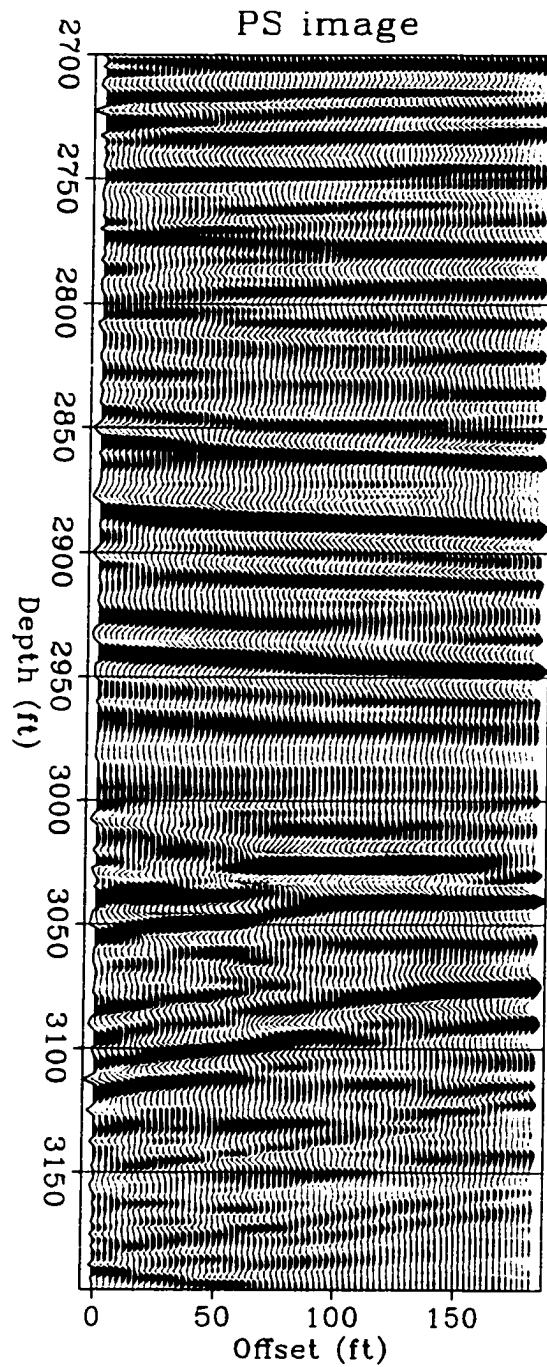


Figure 5.15: *P-S* wave migration image. The principal features are the flat reflectors at the depths from 2700 ft to 2750 ft and unconformity at the depths from 3050 ft to 3100 ft. Reservoir pay zone is from the depth of 2850 ft to 2950 ft.

to calculate the imaging conditions. Figure 5.16 shows the resulting *S-P* wave image for the common receiver gather shown in Figure 5.5. In this single-fold image, flat reflectors at the depths from 2700 ft to 2750 ft can be identified. These features are consistent with those in the *P-P* wave image. The elliptical events around the depth of 2900 ft in this *S-P* image are produced by noises.

After migration of all the common receiver gathers, an image volume is generated, as in *P-P* wave, Figure 5.7. Figure 5.17 shows the CSL at the lateral location of 150 ft from the left well. The upper-left to lower-right diagonal region contains artifacts resulted from imaging the migration sources. These artifacts must be muted before the images are stacked. The image events at the lower-left and upper-right triangular regions are flatly aligned.

Figure 5.18 shows the final stacked *S-P* wave migration image. The formations from depths of 2700 ft to 2800 ft are nearly flat. Below the depth of 3050 ft is an unconformity, the dip of which is 5 degrees. The reservoir pay zone is dolomitized carbonate from depth of 2850 ft (870 m) to 2950 ft (900 m).

5.4 Comparison with finite-difference reverse-time migration

Migration as a general algorithm, is achieved through wave field extrapolation, subject to an imaging procedure. Wave field extrapolation is based upon the scalar wave equation. In the implementations of finite-difference reverse-time migration and Kirchhoff migration presented in Chapters 4 and 5, the imaging conditions and procedure are identical; the only difference is the way the receiver wavefields are backpropagated to estimate the diffraction source. Finite-difference reverse-time migration solves the wave equation explicitly, whereas Kirchhoff migration applies the integral solution to the wave equation. Theoretically, these two approaches of wavefield backpropagation are equivalent. But actual implementation can have differences both in accuracy and efficiency. Finite-difference migration solves the wave equation explicitly. Thus the wavefield extrapolation of finite-difference migration can be considered being exact solution. In complicated velocity model where there are multiple direct arrivals from the source to a diffractor or from a diffractor to the receivers, there will be differences in the migration results of the two algorithms. The velocity model in this field data set is not complicated, one can expect

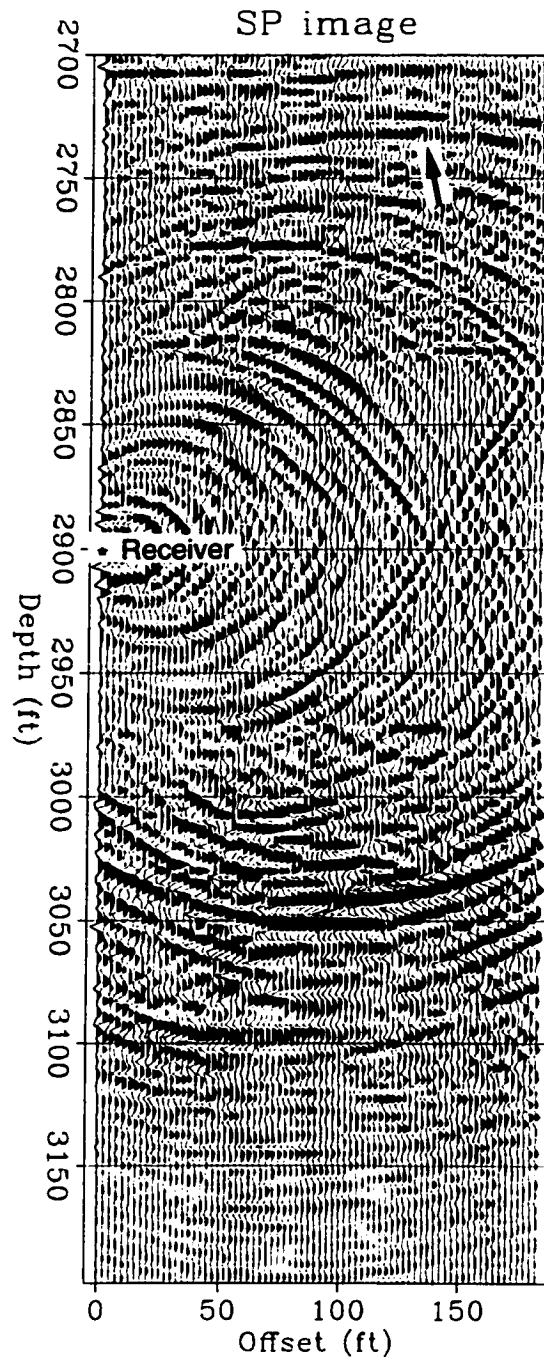


Figure 5.16: *S-P* wave image for the CRG, the depth of the receiver is 2900 ft. Notice the flat reflectors at the depth of 2725 ft.

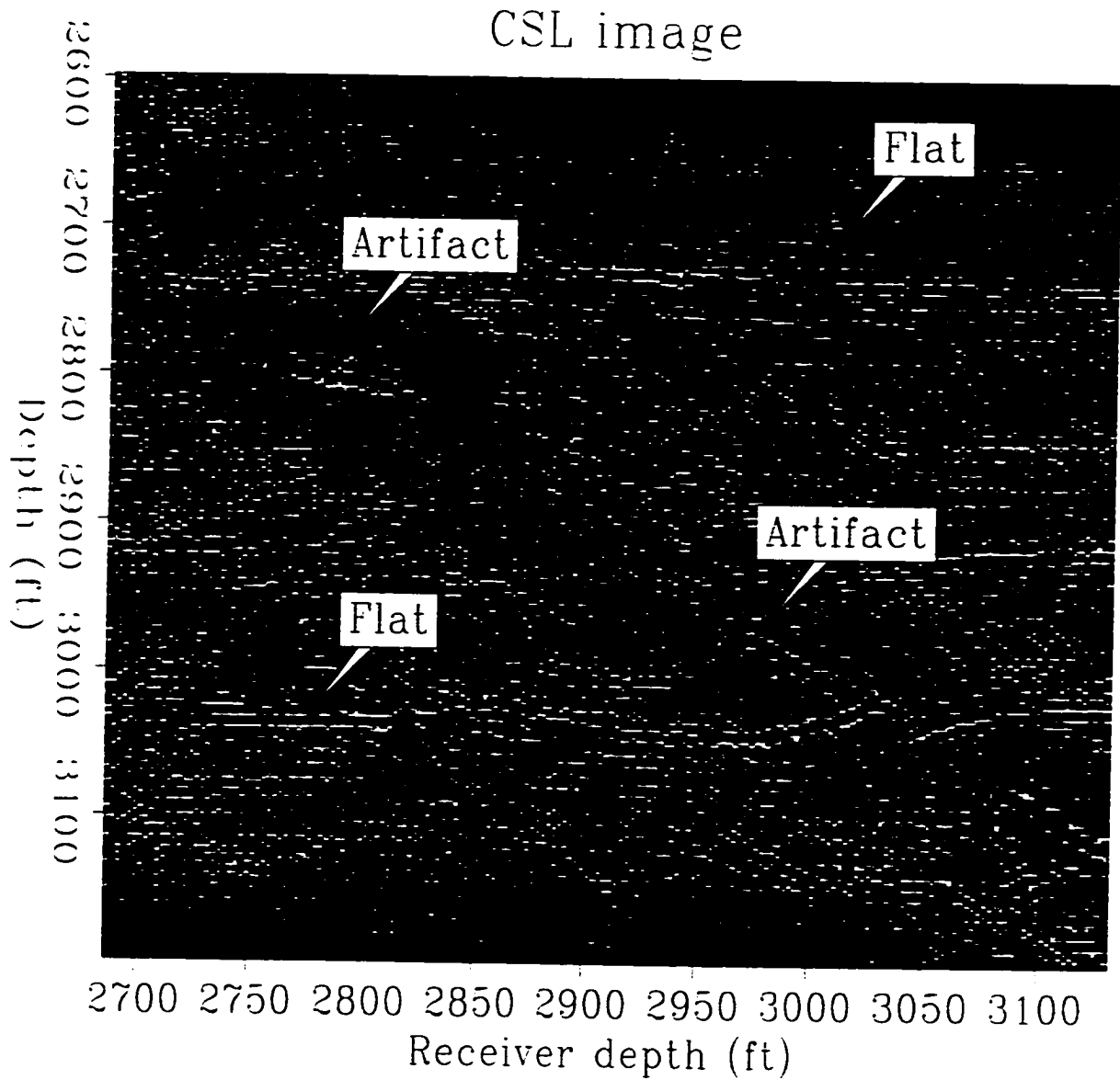


Figure 5.17: *S-P* wave common surface location (CSL) image plane 150 ft from the left well. The upper-left to lower-right diagonal region contains artifacts resulted from imaging the migration sources. The image events away from the diagonal region are flatly aligned.

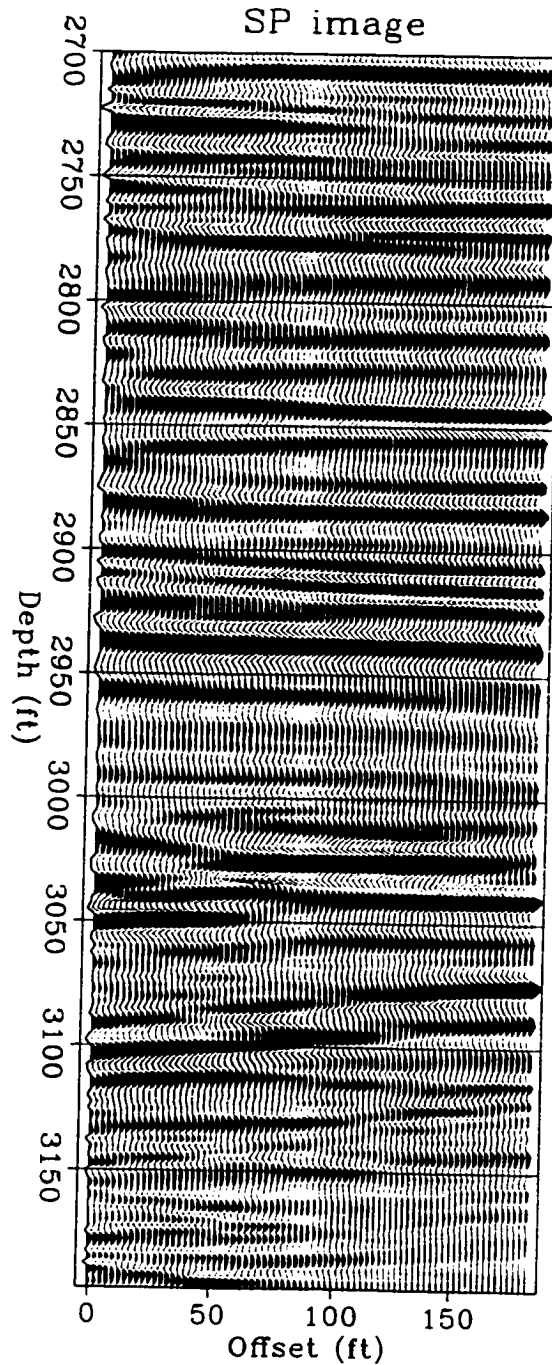


Figure 5.18: *S-P* wave migration image, The principal features are the flat reflectors at the depths from 2700 ft to 2750 ft and unconformity at the depths from 3050 ft to 3100 ft. Reservoir pay zone is from the depth of 2850 ft to 2950 ft.

similar results to be produced by the two algorithms. Actually, the images produced by finite-difference migration and those produced by Kirchhoff migration are almost identical in structures. But on the other hand, the Kirchhoff migration is much more efficient than the finite-difference reverse-time migration. In finite-difference migration, in order to suppress numerical dispersion and satisfy the Courant's stability condition, the spatial and temporal sampling intervals must be interpolated to be very small. As a result, the wave equation must be solved over a large grid for many time steps, making the reverse-time migration costly. The whole process of migration processing 178 common receiver gathers in the previous chapter takes 18 hours CPU time on a DEC alpha 3000 workstation. The Kirchhoff migration is relatively more efficient. Once the travel time and amplitude tables are computed by solving the Eikonal equation and the transport equation, the remaining computation work is to perform the Kirchhoff integral. The travel time tables are efficiently computed by solving the Eikonal equation using a finite-difference method as presented in Chapter 2 of this thesis. The amplitude tables are efficiently computed based on the travel time tables by approximating the transport equation. The whole process of migration processing 178 common receiver gathers in this chapter takes 6 hours CPU time on a DEC alpha 3000 workstation, which is three times faster than finite-difference reverse-time migration.

5.5 Conclusions

Prestack Kirchhoff migration has been successfully applied on a field crosswell dataset recorded with the piezoelectric source and hydrophones. High-quality reflectivity images of the P - P , S - S , P - S , S - P elastic wavemodes are obtained. Geological structures suggested by these four images are consistent with each other, and are consistent with images produced by finite-difference reverse-time migration and VSP-CDP mapping. The structures around a 100 ft (30 m) thick reservoir are clearly imaged. Other geological features imaged include flat beds and unconformity.

The field data are effectively conditioned for migration by interpolation of missing traces, correction of amplitude, and attenuation of the direct arrivals. The Kirchhoff integral is used to perform the wavefield back-propagation. The imaging conditions – traveltimes and amplitude are calculated by solving the Eikonal equation and the transport equation. Reflectivity is calculated by dividing the estimated diffraction source by

the direct arrival from the migration source. The velocity tomogram obtained from transmission travel time tomography is an accurate background velocity model for migration, as is demonstrated by the flatness of the image events in the common surface location image gathers. Because of the radiation patterns of the source and the presence of noises in the data, a single-fold CSG migration image can only image a limited portion of the interwell region sufficiently well. A complete interwell image can be obtained by stacking the individual CSG migration images.

Kirchhoff migration differs from finite-difference reverse-time migration in only the way the receiver wavefields are backpropagated to estimate the diffraction source. The finite-difference reverse-time migration is more accurate. But the Kirchhoff migration is much more efficient and flexible. The Kirchhoff migration as implemented is three times faster than the finite-difference reverse-time migration.

Chapter 6

Noise-tolerant and aperture-limited Kirchhoff migration

In this chapter, I describe a noise-tolerant and aperture-limited Kirchhoff migration algorithm. By limiting the aperture of the Kirchhoff migration integral, noises in the data are not spread to a large area, and the accuracy of imaging is good up to some user-defined dip limits. The aperture of the Kirchhoff integral is governed by the required range of dips that are to be imaged correctly. Trigonometric equation is used to calculate the width of the aperture from the required maximum dip.

6.1 Introduction

Many approaches for processing cross-well full-waveform data have been proposed in recent years. These approaches include ray-based VSP-CDP mapping (Lazaratos, 1993; Smalley, 1997), wave equation migration (Hu et al, 1988), acoustic diffraction tomography (Devaney, 1984; Harris, 1987), elastic migration/inversion (Beydoun et al, 1989) and non-linear inversion (Luo and Schuster, 1990). Theoretically, the wave equation based migration/tomography/inversion approaches are much more accurate and capable than the ray-based VSP-CDP mapping approach. But the VSP-CDP mapping approach is still being used. The reason is that the VSP-CDP mapping approach is a point-to-point transformation like the normal moveout (NMO) in surface seismic data processing and it

does not smear noises in the data. VSP-CDP essentially is a new way of looking at the data, without operating on the data as drastically as the wave-theoretical algorithms do. The VSP-CDP algorithm is more robust in processing noisy field data. The limitations of VSP-CDP approach are that it is only accurate for imaging reflectors of known dip. In this approach, the dip angles must first be estimated before VSP-CDP can be used to produce an image. The estimation of dip angle and VSP-CDP mapping are usually done iteratively and interactively on a graphical workstation (Lazaratos, 1993; Smalley, 1997). Although this can be done, but this approach requires a lot of human interaction and the efficiency is low. VSP-CDP also does not collapse the Fresnel zone, thus limiting the potential lateral resolution that can be achieved from the data. The wave equation based approaches can image geological structures of arbitrary complexity, but their long spatial impulse response makes them sensitive to problems often encountered in real cross-well data applications, like noise, imperfect amplitude, and gaps in the recording aperture.

In this chapter, I will develop an imaging algorithm - limited-aperture Kirchhoff migration, that stands in between VSP-CDP mapping and full-aperture wave equation migration. It is a migration algorithm, but the Kirchhoff integration aperture is limited to a certain width so that it can correctly image dipping reflectors up to the user-defined limits. Because the integration aperture is relatively narrow, it has the feature of VSP-CDP mapping that it does not severely spread noises. I first derive the Kirchhoff migration algorithm using the WKBJ Green's function. Although the concept of Kirchhoff migration algorithm has been fully described in the previous chapter, it is redescribed here to facilitate the presentation of limited-aperture Kirchhoff migration. Then, I describe the theory and implementation of limited-aperture Kirchhoff migration. Finally, I test the algorithm on synthetic data which contain Gaussian noises to demonstrate the usefulness and limitation of this algorithm. A similar algorithm to reduce migration smiles was also reported by Qin et al (1993) in the name of constrained Kirchhoff migration. In Qin's algorithm, for every data spike in the data a corresponding elliptical trajectory in the image must first be calculated, and the data spike was put in the image only if the dip of the migration ellipse at this point was estimated to be less than a certain value. A better approach is to limit the aperture in the Kirchhoff integral. Because the migration aperture is much easier to calculate than the elliptical trajectory and the number of image points is far less than the number of data points, the limited-aperture Kirchhoff algorithm as presented here is more efficient and flexible.

6.2 Theory

6.2.1 Kirchhoff migration

In this section, I derive the Kirchhoff migration integral for a medium with arbitrary velocity variations, for prestack migration of common shot multi-channel data. The application is for prestack migration of cross-well seismic data, in particular. First of all, the recorded wavefiled needs to be backpropagated from the recording surface back to the medium. Begin with the Helmholtz equation,

$$(\nabla^2 + \omega^2/v^2)G = \delta(\mathbf{r} - \mathbf{r}_1) \quad (6.1)$$

G is the Green's function that solves equation (6.1) and satisfies the radiation condition (Goodman, 1970); ∇^2 is the Laplacian operator, ω is frequency, $v(x, z)$ is acoustic velocity, and δ is the Dirac delta function. The vectors \mathbf{r} and \mathbf{r}_1 are the position of the receiver and point scatterer, respectively. The wave field $P(\mathbf{r}, \omega)$ satisfies the equation

$$(\nabla^2 + \omega^2/v^2)P(\mathbf{r}, \omega) = 0 \quad (6.2)$$

inside the source-free volume V . To obtain the Kirchhoff integral, I use the Green's second theorem,

$$\int_V (\phi_1 \nabla^2 \phi_2 - \phi_2 \nabla^2 \phi_1) dV = \int_S (\phi_1 \partial_n \phi_2 - \phi_2 \partial_n \phi_1) dS \quad (6.3)$$

where n denotes the outward normal direction to the surface S , and substitute $\phi_1 = P(\mathbf{r}, \omega)$ and $\phi_2 = G$ to obtain

$$P(\mathbf{r}_1, \omega) = \int_S (P(\mathbf{r}, \omega) \partial_n G - G \partial_n P(\mathbf{r}, \omega)) dS \quad (6.4)$$

which is the Kirchhoff integral, Figure 6.1.

In the Kirchhoff integral equation (6.4), both the record of the wave field $P(\mathbf{r}, \omega)$ and its gradient are involved. But in actual seismic profiling, only the wave fields $P(\mathbf{r}, \omega)$ are recorded. French (1975) and Schneider (1978) showed that if the data are collected in a flat plane, the second term in the integrand of the Kirchhoff equation is the negative of the first term. This condition is approximately valid for borehole profiling, since any change of borehole direction must proceed gradually and may be assumed negligible for typical seismic wavelengths. Therefore I replace the second term containing the normal derivative of the data with the negative of the first term. Also, I extend the boundary

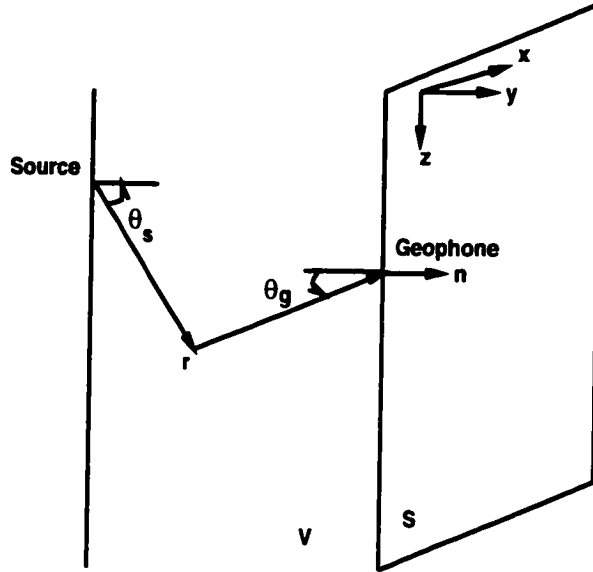


Figure 6.1: Wavefield extrapolation and imaging. The wavefield in the medium is reconstructed by Kirchhoff integration over the recording surface. Imaging is performed by taking the quotient of the reconstructed diffraction wavefield and the source wavefield.

of the integration surface to infinite distance, where there is no back-scattered energy as governed by the radiation condition, so that the only remaining contribution to the integral comes from the recording surface S . Equation (6.4) becomes

$$P(\mathbf{r}, \omega) = 2 \int_S P(\mathbf{r}_g, \omega) \partial_n G dS \quad (6.5)$$

I now write $G = A(\mathbf{r}|\mathbf{r}_g) e^{-i\omega\tau(\mathbf{r}|\mathbf{r}_g)}$ and use the geometrical optics approximation for the amplitude $A(\mathbf{r}|\mathbf{r}_g)$ and phase $\tau(\mathbf{r}|\mathbf{r}_g)$. The negative sign in the phase of G is used because the wave fields shall be extrapolated backward in time. Along a ray path, the variation in $e^{-i\omega\tau}$ is much larger than the variation in A . Thus the first term in the derivative of G

$$\partial_n G = (\partial_n A) e^{-i\omega\tau} - A e^{-i\omega\tau} i\omega (\partial_n \tau) \quad (6.6)$$

is small compared to the second term and is neglected. The Kirchhoff integral (6.5) can now be written in the form

$$P(\mathbf{r}, \omega) = -2 \int_S P(\mathbf{r}_g, \omega) A e^{-i\omega\tau} i\omega (\partial_n \tau) dS \quad (6.7)$$

in which

$$\partial_n \tau = \mathbf{n} \cdot \partial \tau = \mathbf{n} \cdot \mathbf{t} / v_g = \cos \theta_g / v_g \quad (6.8)$$

where \mathbf{t} is the unit tangent vector for the emerging ray, and θ_g is the angle of emergence, and v_g is the acoustic velocity at the receiver. The amplitude term $A(\mathbf{r}|\mathbf{r}_g)$ can be obtained from the transport equation.

The reflectivity function $R(\mathbf{r}, \omega)$ is defined as the ratio of the back-propagated field from the receivers $P(\mathbf{r}, \omega)$ to the incidence field from the source $P_s(\mathbf{r}, \omega)$ (Claerbout, 1970),

$$R(\mathbf{r}, \omega) = \frac{P(\mathbf{r}, \omega)}{P_s(\mathbf{r}, \omega)} \quad (6.9)$$

The incidence source field is approximated by the WKB Green's function

$$P_s(\mathbf{r}, \omega) = A(\mathbf{r}|\mathbf{r}_s)e^{i\omega\tau(\mathbf{r}|\mathbf{r}_s)} \quad (6.10)$$

Combining equations (6.7) through (6.10) gives the holographic (i.e., frequency-domain) form of Kirchhoff migration.

$$R(\mathbf{r}, \omega) = -2 \int_S \frac{A(\mathbf{r}|\mathbf{r}_g) \cos \theta_g}{A(\mathbf{r}|\mathbf{r}_s) v_g} e^{-i\omega(\tau(\mathbf{r}|\mathbf{r}_s) + \tau(\mathbf{r}|\mathbf{r}_g))} i\omega P(\mathbf{r}_g, \omega) dS \quad (6.11)$$

The time-space domain reflectivity is obtained by an inverse Fourier transform,

$$R(\mathbf{r}) = -2 \int_S \frac{A(\mathbf{r}|\mathbf{r}_g) \cos \theta_g}{A(\mathbf{r}|\mathbf{r}_s) v_g} \partial_t P(\mathbf{r}_g, \tau(\mathbf{r}|\mathbf{r}_s) + \tau(\mathbf{r}|\mathbf{r}_g)) dS \quad (6.12)$$

This is the conventional full-aperture Kirchhoff migration algorithm. To image a point in the image space, the integral sums contributions from all the traces on the recording surface, ie, it is a full-aperture algorithm. The points in the image where the sum of the travel time from the source and the travel time to the receiver being a constant form an elliptical trajectory. To view it in another way, the Kirchhoff migration spreads a spike in the data along an elliptical trajectory in the image, ie, the algorithm has a full 90-degree impulse response. Figure 6.2 shows contours of travel times calculated for a constant velocity model. Figure 6.2(a) and (b) are the travel times from the source or the receiver to all points in the image space. Figure 6.2(c) is the sum of Figure 6.2(a) and (b), and its contours are called isochrone trajectories. In a variable velocity medium, the circular wavefronts in Figure 6.2(a) and (b), and the elliptical isochrone trajectories in Figure 6.2(c) will be distorted. Figure 6.3 shows how the migration algorithm operates in imaging a single trace containing four wavelet spikes. The full-aperture 90-degree migration algorithm spreads a wavelet along the whole isochrone trajectory, by doing so it can correctly image all dips up to 90-degrees, focus diffractions and shrink the Fresnel zone to increase lateral resolution.

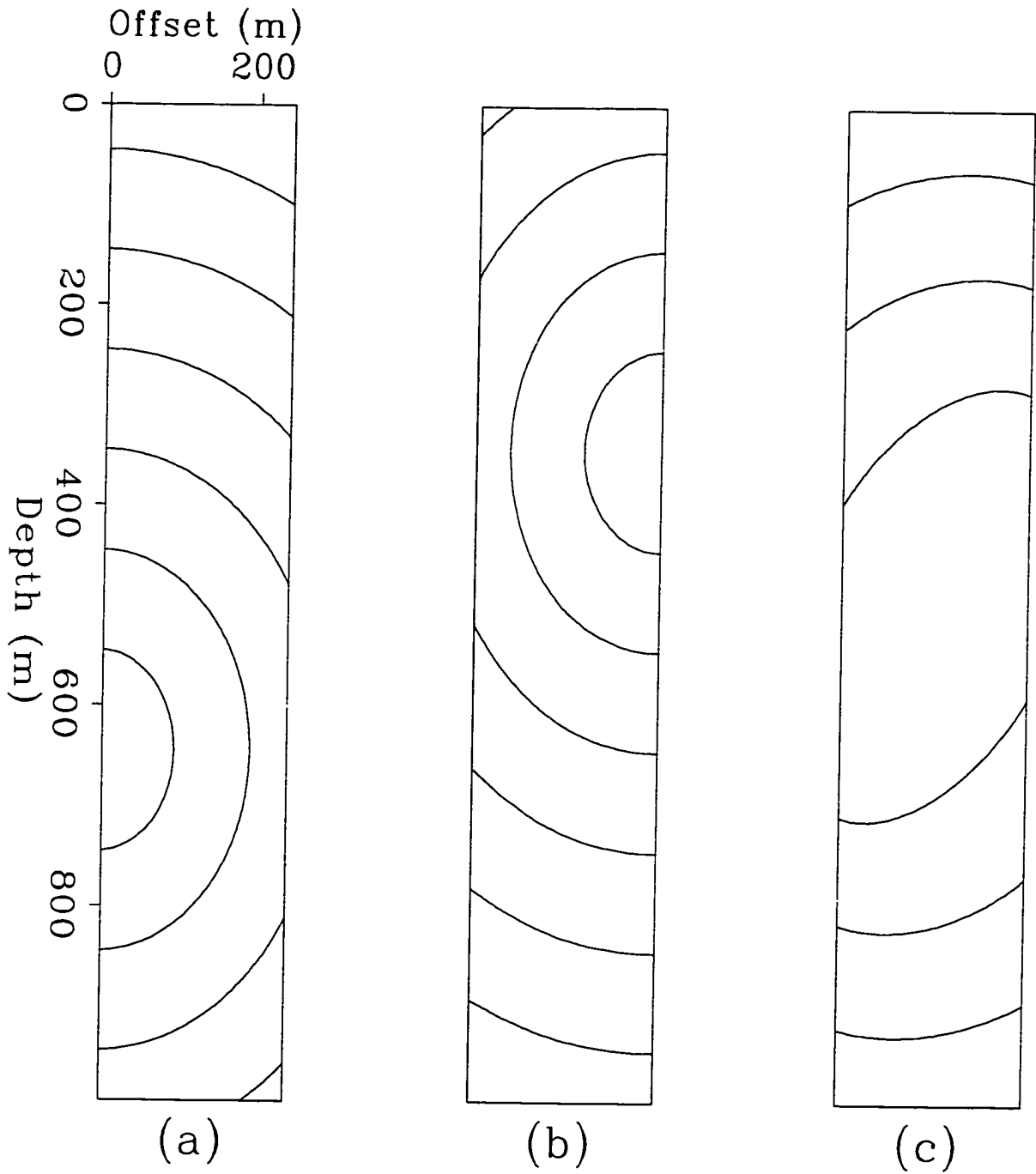


Figure 6.2: (a) The travel time contours of wavefronts from a source. (b) The travel time contours of backpropagation wavefronts from a receiver. (c) Prestack migration spreads a spike in the data along an elliptical trajectory with the source and the receiver as the foci.

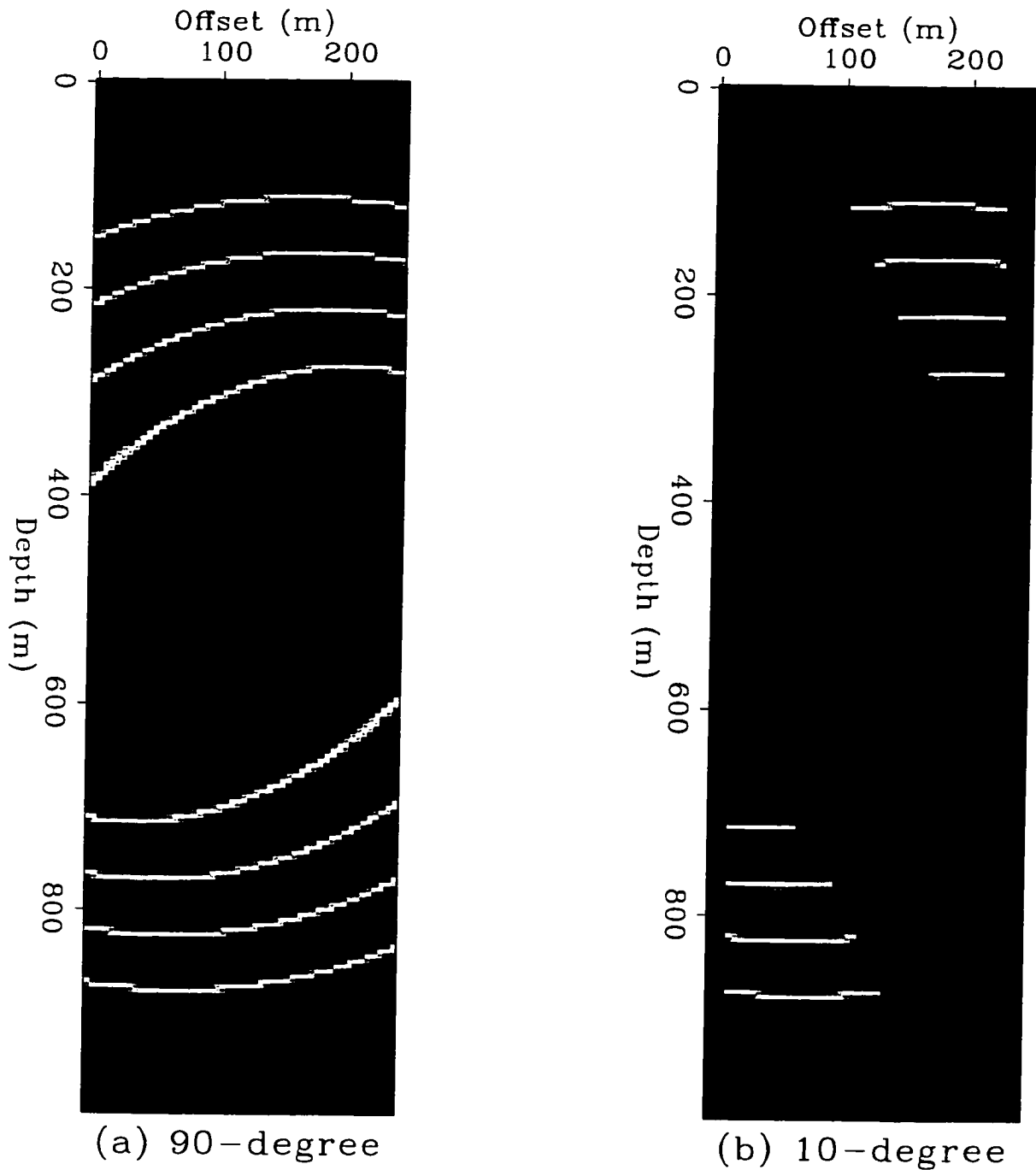


Figure 6.3: Impulse responses of prestack migration. (a) Full-aperture 90-degree migration, a spike in the data is spread along an elliptical isochron with the source and the receiver as the foci; noises in the data are also spread over a large area in the image. (b) Limited-aperture 10-degree migration, a spike in the data is only spread along a portion of the elliptical isochron; noises in the data are thus confined to only a limited area in the image.

6.2.2 Aperture-limited Kirchhoff migration

Notice in Figure 6.3(a), the full-aperture 90-degree migration algorithm spreads a wavelet spike over the whole isochrone ellipse. This algorithm has the theoretical potential of correctly imaging reflectors with all kinds of dips up to 90-degrees. But this potential can hardly be achieved in field data. Field data are usually not noise-free. Noises in the data are spread out in the image as artifacts. Boundaries of recording coverage, gaps and missing traces in the recording aperture and amplitude anomalies in the data also generate strong noise artifacts in the image. The user of migration imaging needs to make a balance between harnessing the theoretical potentials of wave equation migration and controlling the noise effects of this algorithm.

In migration, we could also spread a data spike on only part of the isochrone ellipse, Figure 6.3(b). By doing so, the imaging capability of migration is limited to a certain range of dips. However, the noise tolerance of this algorithm improves because the spreading of noises is limited. When the integration aperture is reduced to zero, migration degenerates to be VSP-CDP mapping. Technically, spreading data over part of the isochrone ellipse can be equivalently and conveniently implemented by limiting the integration aperture in the Kirchhoff migration algorithm.

In the cross-well common shot profile of Figure 6.4, S is the source, R is one of the receivers; AB is a flat reflector and PE is the normal to it; CD is a dipping reflector with dip angle θ and PF is the normal to it; P is the point to be imaged with lateral and depth coordinates of (x, z) ; L is the separation distance between the two wells.

By trigonometry, for the flat reflector AB , source S and receiver R , the incidence angle $\angle SPE$ and reflection angle $\angle EPR$ can be computed by α ,

$$\tan \alpha = \frac{x}{z - z_S} \quad (6.13)$$

and the depth of the receiver R can be computed by

$$z_R = z - \frac{L - x}{\tan \alpha} \quad (6.14)$$

For dipping reflector CD , source S and receiver R' , the incidence angle $\angle SPF$ and reflection angle $\angle FPR'$ are $\alpha + \theta$. The angle $\angle EPR'$ is $\alpha + 2\theta$. The depth of the receiver R' can be computed by the following equation,

$$z_{R'} = z - \frac{L - x}{\tan(\alpha + 2\theta)} \quad (6.15)$$

For reflectors with negative dip angles $-\theta$, the equation to compute the depth of the receiver receiving the reflection is the same as Equation (6.15). Thus, in order to correctly image reflectors with dips from $-\theta$ to θ , limited-aperture Kirchhoff migration can be implemented by integration over the recording aperture with R as the center and RR' as the half-width. When the integration aperture is reduced to zero, ie, when only a data spike of the trace at receiver R is transformed to the image point P , migration degenerates to be VSP-CDP mapping.

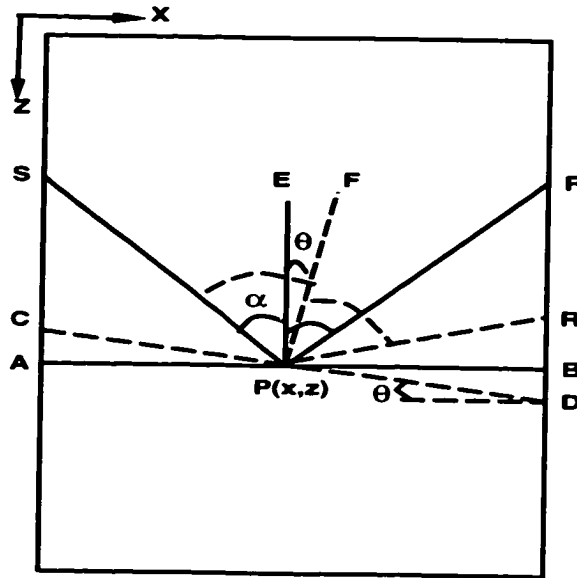


Figure 6.4: In order to correctly image dipping reflectors with dips from $-\theta$ to θ degrees, the Kirchhoff migration integration aperture can be limited to the range that R is the center and RR' is the half width.

6.2.3 Implementation

The implementation of the limited-aperture Kirchhoff migration is almost the same as the full-aperture Kirchhoff migration presented in the previous chapter. The only difference is the additional constraint that a data trace is used to compute the Kirchhoff integral only if the corresponding receiver is located within the imaging aperture for an image point. The aperture is calculated using geometrical ray theory assuming constant velocity.

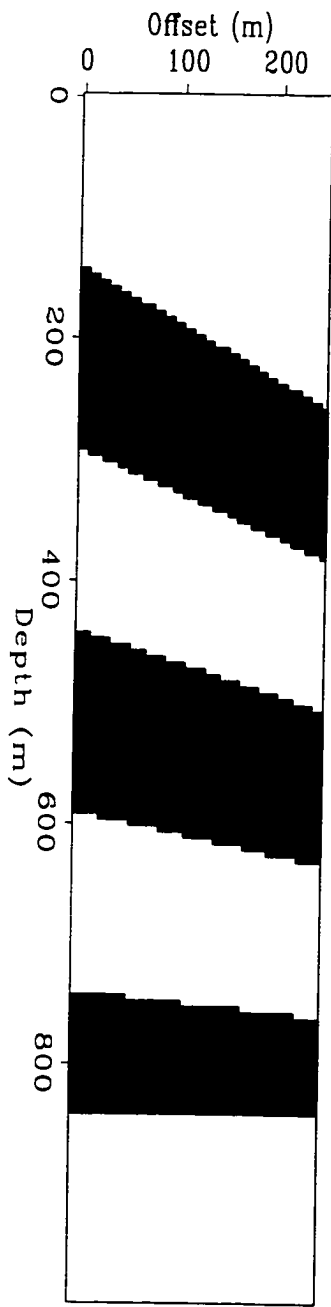
6.3 Synthetic data examples

Figure 6.5(a) shows a velocity model with dipping reflectors whose dip angles increase from 0 to 25 degrees in increments of 5 degrees from bottom to top. A finite-difference wave equation modeling program is used to generate the cross-well seismic survey common shot gather of Figure 6.5(b). The source is located at the depth of 50 m in the left well, and the receivers are located in the right well. Gaussian random noise is added to the data, so that the signal to noise ratio is 1 for the reflections. Blank traces are also made in the data to emulate field recording conditions. Figure 6.6 shows the images obtained by applying the full-aperture 90-degree migration and limited-aperture migration of 15-degree dip-limit to the data of Figure 6.5(b). The image produced by the full-aperture migration algorithm is very noisy, in particular the elliptical signatures of the gaps in the data are quite strong. In contrast, the image produced by the limited-aperture algorithm has better signal to noise ratio, and the migration smiles resulting from the gaps in the data are weaker. Figure 6.7 compares two images obtained by limited-aperture 15-degree migration and the true locations of the reflectors. Reflectors with dip angle less than 15 degrees are correctly positioned, but reflectors with dip angles larger than 15 degrees are mispositioned. The mispositioning of the dipping reflectors varies as the relative positions of the reflectors and the source vary. In Figure 6.7(a), the 20-degree and 25-degree dipping reflectors dip away from the source, their images show larger dip angles. In Figure 6.7(b), the 20-degree and 25-degree dipping reflectors dip toward the source, their images show smaller dip angles. These mispositionings of dipping reflectors are explained in Figure 6.8 and Figure 6.9. S is the source, R is a receiver, PQ is a dipping reflector. The ellipse is the migration image trajectory with the source and receiver as the foci. In limited-aperture migration, reflection from the point B is imaged at portion of the ellipse with B' as the center. At B' , the tangent of the migration ellipse is flat. Image point B' shifts in the down-dip direction relative to the reflection point B . As a result, the image of the dipping reflector has a smaller or larger dip angle if the migration ellipse is not wide enough depending on the relative orientation of the source and the reflector. Thus, in applying migration to process noisy field data, one needs to make a balance between correctly imaging dipping reflectors by using a wide migration aperture and controlling noise spreading by using a small migration aperture. Notice the images of the 20-degree and 25-degree dipping reflectors have opposite polarities between Figure 6.7(a) and Figure 6.7(b), because the

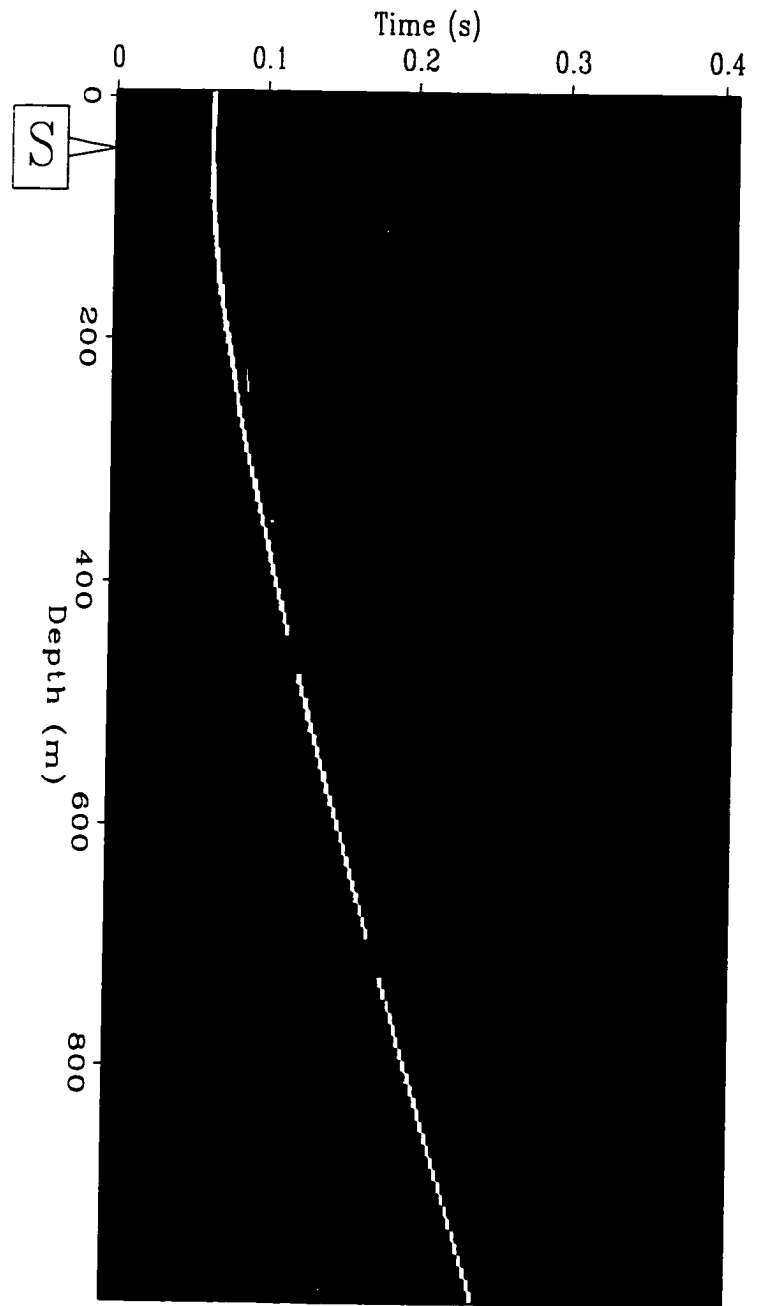
source wavefield illuminates the reflectors from opposite sides. The images show that the direct arrivals image at the physical source, generating strong noises in the vicinity of the physical source. Thus, the direct arrivals should be attenuated before the data are input to migration processing.

6.4 Conclusions

The aperture-limited Kirchhoff migration algorithm as presented stands in between VSP-CDP mapping and full-aperture wave equation migration. The aperture of the Kirchhoff integral is governed by the requirements of the range of dips that are to be imaged correctly. Trigonometric equation is used to relate the width of the aperture and the required maximum dip. By limiting the aperture of the Kirchhoff migration integral, noises in the data are not spread to a large area, and migration smiles of ill-conditioned data are weaker.



(a) Vel model



(b) CSG

Figure 6.5: (a) is the velocity model, six interface reflectors ranging from 0 to 25 degrees in increments of 5 degrees. (b) Cross-well common shot gather data obtained by finite-difference wave equation modeling. Gaussian random noise is added so that the signal to noise ratio is 1 for the reflections, and blank traces are made to emulate field data.

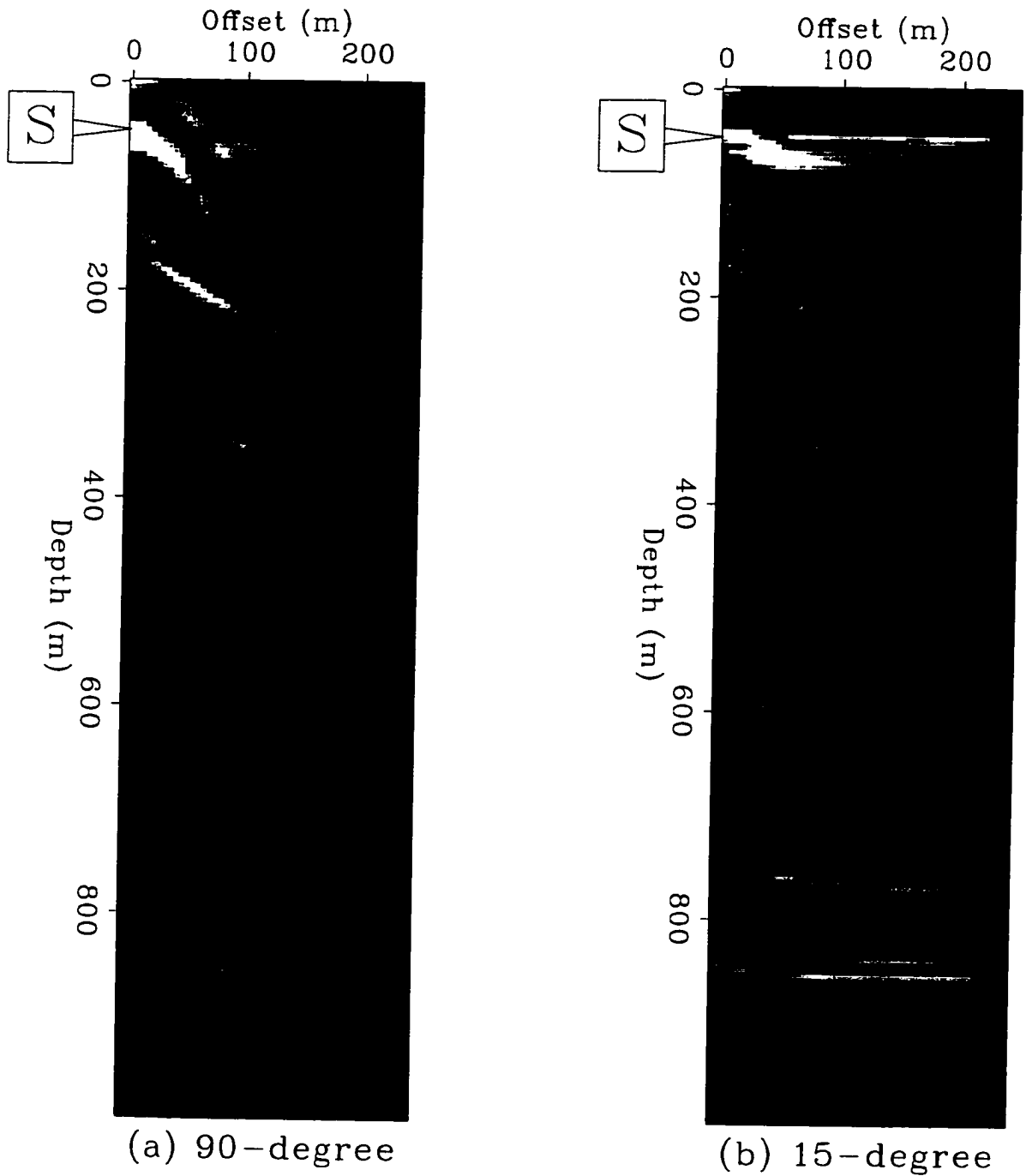


Figure 6.6: Migration images obtained by two different algorithms. (a) The image obtained by the full-aperture 90-degree algorithm is noisier and the smiles from the gaps in the data are stronger. (b) The image obtained by the limited-aperture 15-degree algorithm has better signal to noise ratio.

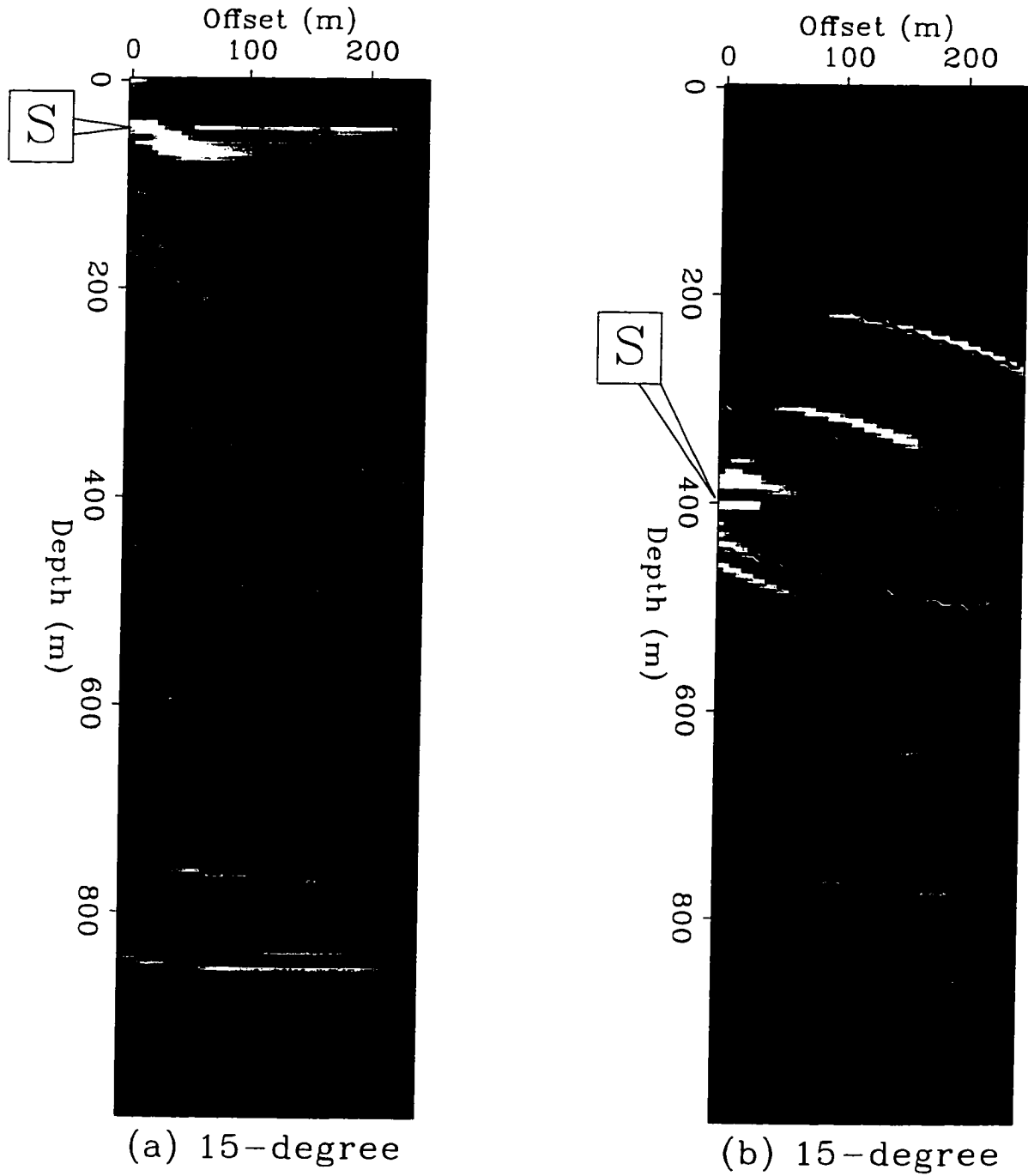


Figure 6.7: The two images are obtained by the limited-aperture migration of 15-degree dip-limit. Overlain on the images are the true locations of the reflectors. Reflectors with dips less than 15-degrees are correctly positioned. (a) The source is located at the depth of 50 ft; the two reflectors of 20-degree and 25-degree dip are positioned at a slightly larger dips. (b) The source is located at the depth of 400 ft; the two reflectors of 20-degree and 25-degree dip are positioned at a slightly smaller dips.

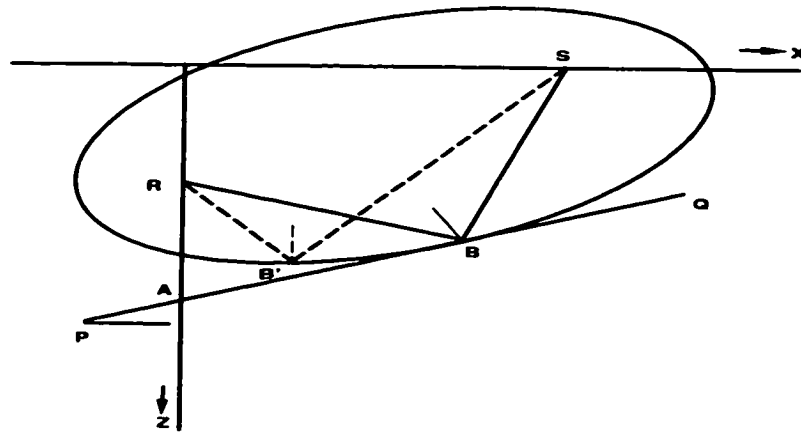


Figure 6.8: S is the source, R is a receiver, PQ is a dipping reflector. In limited-aperture migration, reflection from the point B is imaged at portion of the ellipse with B' as the center. At B' , the tangent of the migration ellipse is flat. Image point B' shifts in the down-dip direction relative to the reflection point B . As a result, the image of this dipping reflector has a larger dip angle if the migration ellipse is not wide enough.

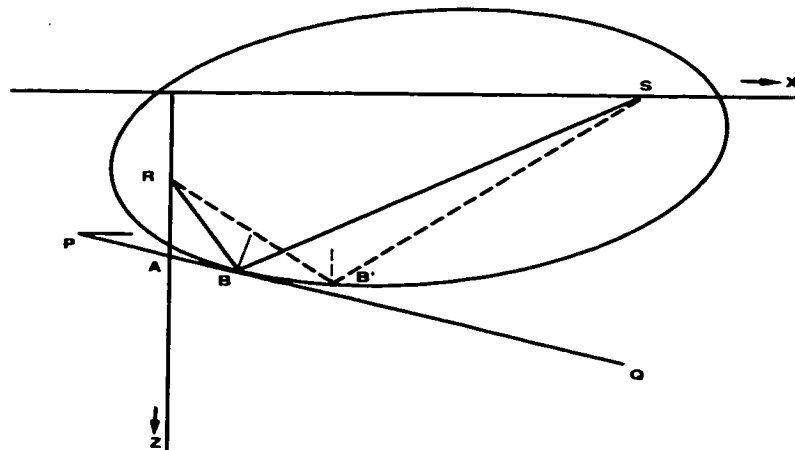


Figure 6.9: S is the source, R is a receiver, PQ is a dipping reflector. In limited-aperture migration, reflection from the point B is imaged at portion of the ellipse with B' as the center. Image point B' shifts in the down-dip direction relative to the reflection point B . As a result, the image of this dipping reflector has a smaller dip angle if the migration ellipse is not wide enough.

Chapter 7

Prestack migration of cross-well field data in bigger doses

In this chapter, I apply the techniques presented in this thesis to perform prestack Kirchhoff depth migration of the King Mountain cross-well field data set, recorded in the Permian Basin, West Texas. The data preprocessing consists of tube wave attenuation, amplitude correction, and attenuation of the direct arrivals. The velocity model used in migration is the tomogram obtained from transmission travel time tomography. Two elastic wave modes, namely $P - P$ and $S - S$ are each used in migration. Migration is performed in the domains of both common shot gather (CSG) and common receiver gather (CRG). The two images of CSG and CRG migration where the source and receiver share the same depth are stacked to create a single-fold image. After migration of all the CSGs and CRGs, a volume of images is produced. Image events at common surface location gathers sliced from the volume show generally good alignment suggesting the velocity model used in migration is correct. Geological structures, dipping beds, unconformity and reef of thickness less than 200 ft are clearly imaged.

Two versions of migration are performed, 45-degree limited-aperture and 90-degree full-aperture migrations. The image produced by the 90-degree migration has stronger artifacts of migration ellipses as also shown in synthetic data test. The maximum dip of about 40 degrees in the geology supports the choice of 45-degree aperture in the migration.

7.1 The processing sequence

The processing sequence is illustrated by the flow chart of Figure 7.1. The first step in processing cross-well seismic data is to pick the traveltimes of the direct arrivals. These traveltimes are used in transmission traveltome tomography to invert for the velocity tomogram. These traveltimes are also used in the later steps of preprocessing the data before migration. After prestack migration, a volume consisting of image slices is generated. The final step is to stack the images in the volume to produce the final image.

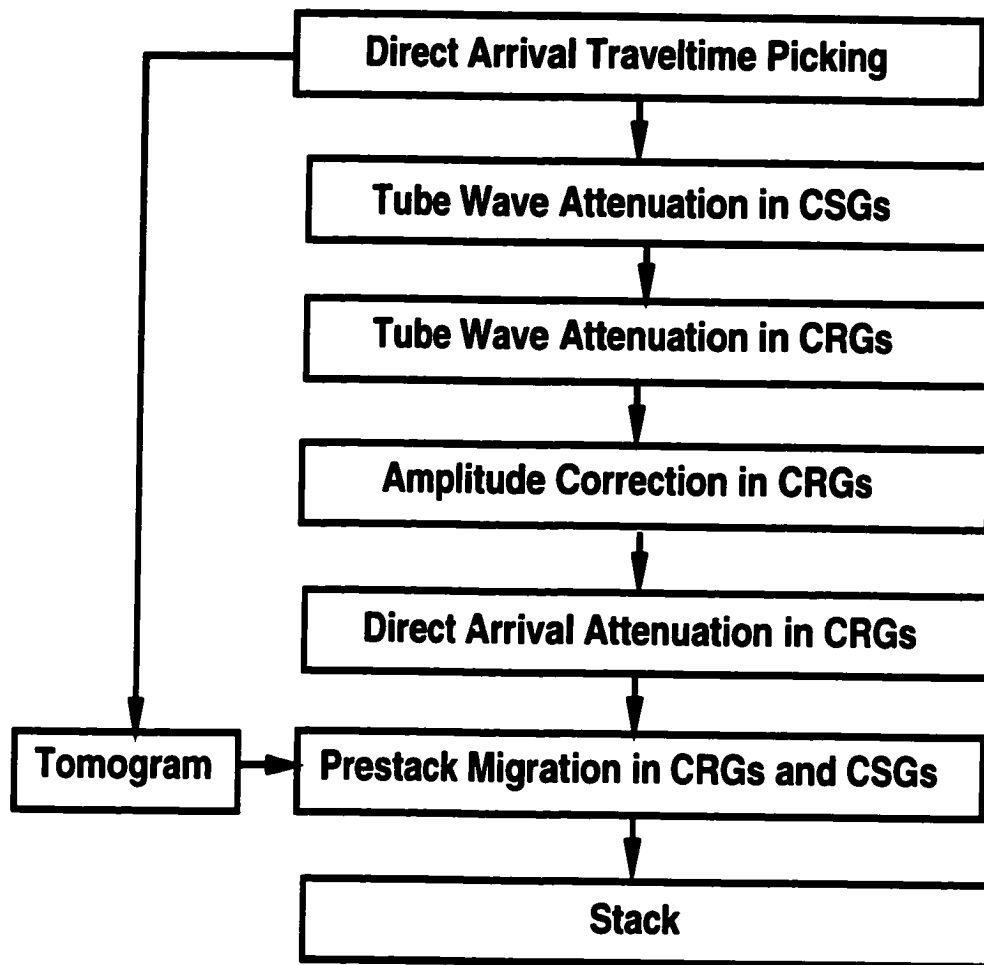


Figure 7.1: Processing sequence flow chart.

7.2 The field data

The cross-well seismic data was recorded in the Permian Basin, West Texas. The data set has 201 common shot gathers and 203 common receiver gathers. The depth of the sources ranges from 8200 ft to 9200 ft, and the depth of the receivers ranges from 8190 ft to 9200 ft. The source and receiver sampling intervals are both 5 ft. The record length is 180 ms, and the time sampling interval is 0.25 ms. The usable frequencies in the data are from 400 Hertz to 1200 Hertz. The interwell separation distance is 640 ft.

7.3 Preprocessing

Preprocessing of the data before migration consists of the following major steps in sequence. There are other data processing techniques, such as bandpass filtering and deconvolution, but they are minor for the purpose of this thesis and therefore are not discussed.

7.3.1 Attenuation of tube waves

Because both the source and receiver wells have a perforation in the depth range of the survey, these perforations excite strong tube waves in both the source and receiver wells. Intensive preprocessing is needed to attenuate the tube waves (Chapter 3 of this thesis). The tube wave attenuation method applies the kinematic wave propagation process of the source and receiver well tube waves. The source well tube waves are well sampled in the common shot gathers. I align and stack the source well tube waves in CSGs to estimate the source well tube waves. The estimated source well tube waves are then subtracted from the CSG data. The data are resorted into common receiver gathers. Then, I apply the same method to attenuate the receiver well tube waves in common receiver gathers. Figure 7.2 shows a common receiver gather after attenuation of both source and receiver well tube waves. On the figure, both P - P and S - S wave reflection events can be easily identified and some are pointed by arrows.

7.3.2 Amplitude corrections

To correct the instrument amplitude inconsistency between different traces, I pick the amplitude of the direct P -wave arrivals in each trace, and normalize the whole trace by

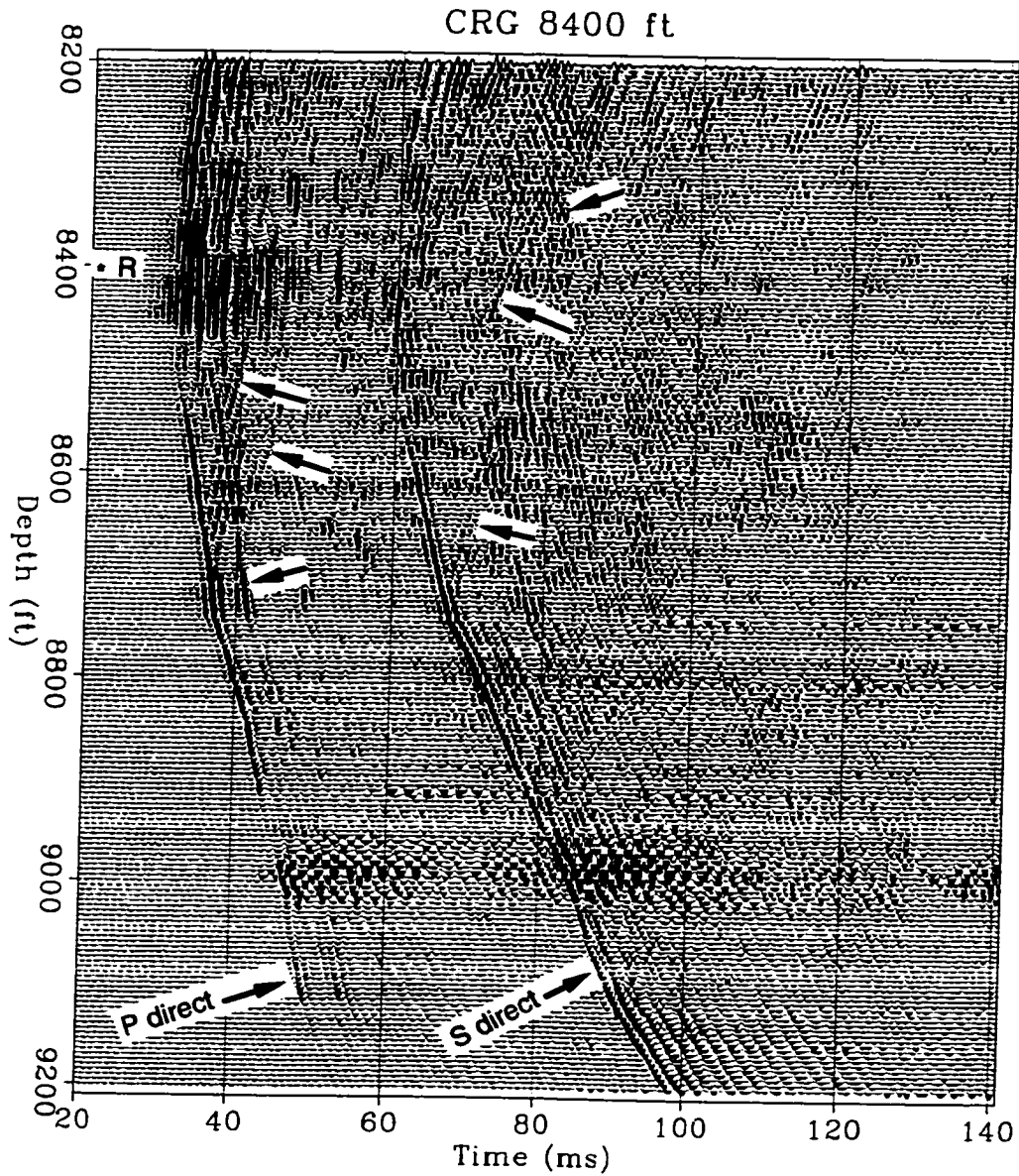


Figure 7.2: Common receiver gather, the depth of the receiver is 8400 ft. The direct *P*- and *S*-waves are pointed out by arrows. Some of the reflection events for *P*-wave (before 60 ms) and for *S*-wave (after 60 ms) are also pointed out.

the direct arrival amplitude. Then, I divide the data by the straight line distance from the source to the receiver. This results in data recorded in 3-D from an ideal point source.

Because cross-well migration method operates in 2-D, but the field data are actually recorded in 3-D, the geometrical spreading amplitude difference is \sqrt{r} , where r is the propagation distance proportional to the travel time in a constant velocity medium. I multiply each trace by the square root of the travel time to correct for the 2-D to 3-D geometrical spreading difference (Claerbout, 1985). Figure 7.3 shows the common receiver gather after amplitude corrections. Compared to the same CRG data in Figure 7.2, the amplitude at later time has been boosted up and the amplitude variation across the traces is smoother.

7.3.3 Attenuation of direct arrivals

The last step in preprocessing is to attenuate the direct arrivals. The operation is performed in common receiver gathers. The direct P -wave is attenuated along its travelttime trajectory by tapered muting. The direct S -wave is attenuated by averaging over five aligned adjacent traces and subtraction along the hand-picked travelttime trajectory in a window covering the direct arrival S -wave wavelet. Figure 7.4 is the resulting common receiver gather data that are input to migration processing for P - P and S - S waves in the domain of common receiver gathers. After attenuation of the direct arrivals in CRGs, the direct arrivals in CSGs are also attenuated. Figure 7.5 is the resulting common source gather data (the depth of the source is 8400 ft) that are input to migration processing for P - P and S - S waves in the domain of common source gathers.

7.4 Velocity model used in migration

Figure 7.6 shows the background velocity model used in $P - P$ wave migration. The left edge of the tomogram is the location of the receiver well, and the right edge the source well. Velocities range from 14 kft/s to 20 kft/s. The grid size is 203 nodes in depth and 130 nodes in offset with sampling intervals of 5 ft in both vertical and lateral directions. This velocity model was obtained from transmission travel time tomography (M. Van Schaack). Since the usable frequencies in the data range from 400 Hertz to 1200 Hertz, the monochromatic wavelength for P -wave is calculated to range from 20 ft to 50 ft. I expect the imaging resolution of the $P - P$ wave to be about 30 ft, that is half of the

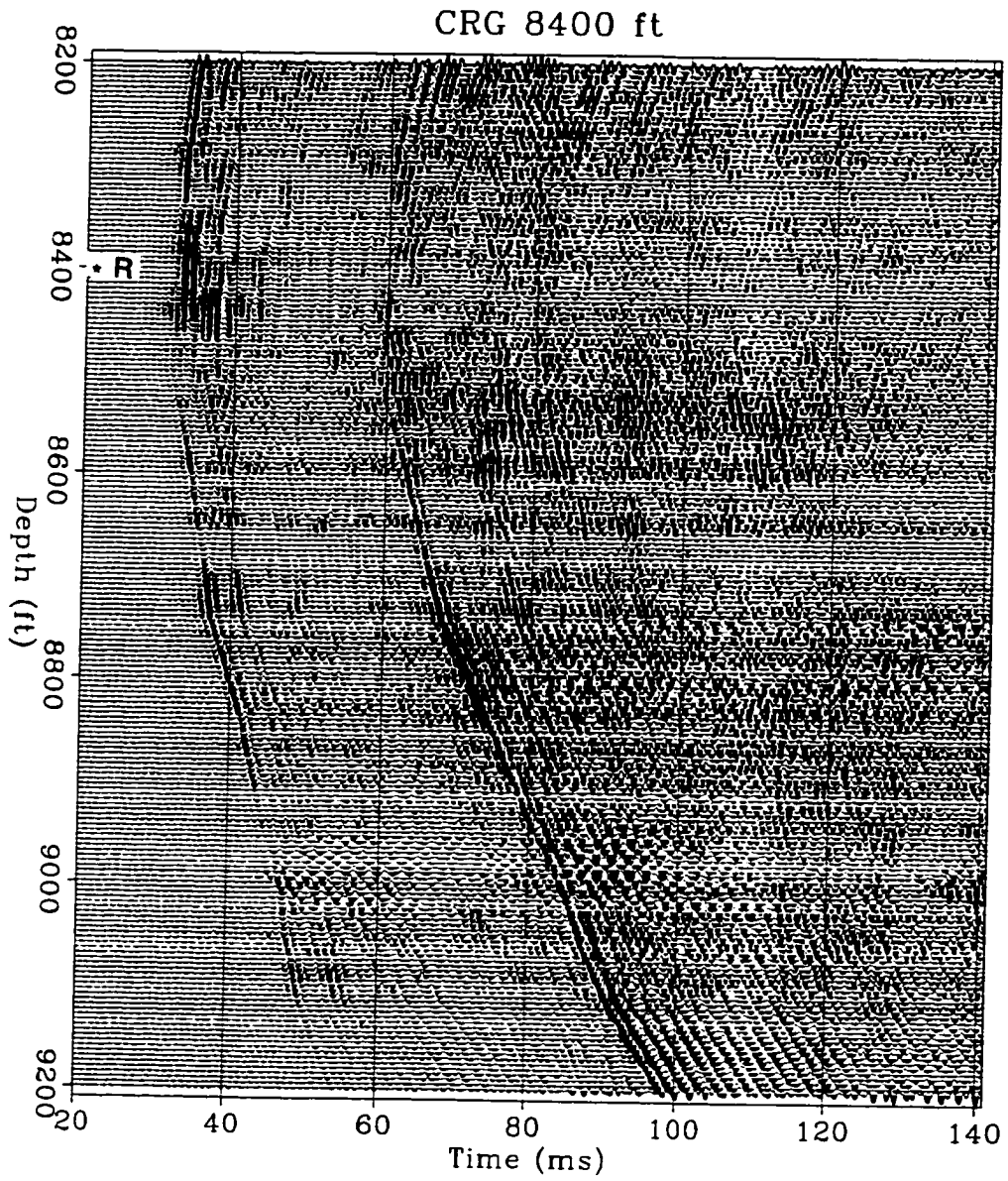


Figure 7.3: Common receiver gather, the depth of the receiver is 8400 ft. The amplitudes of later events in time have been boosted up.

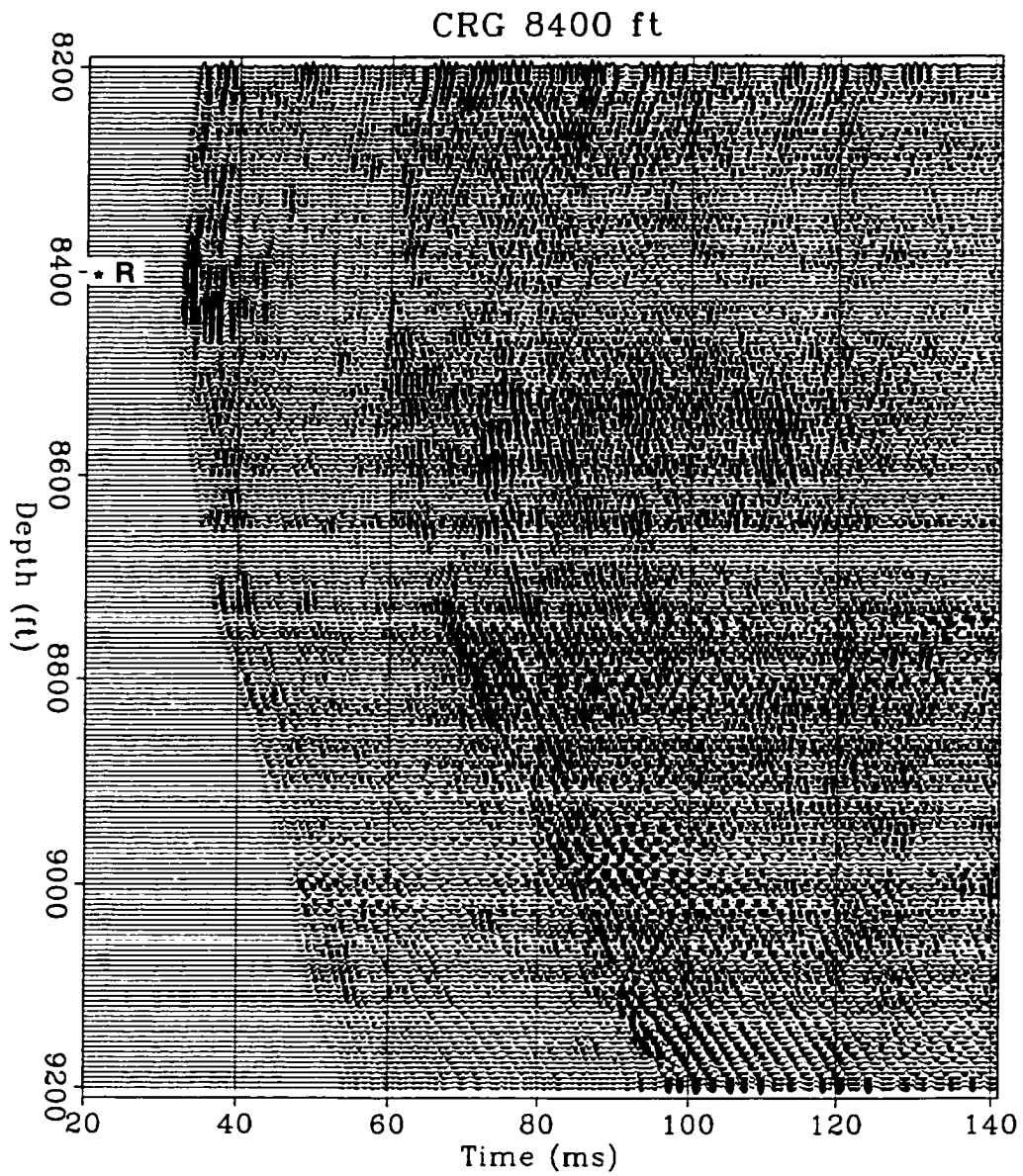


Figure 7.4: Preprocessed common receiver gather, the depth of the receiver is 8400 ft.

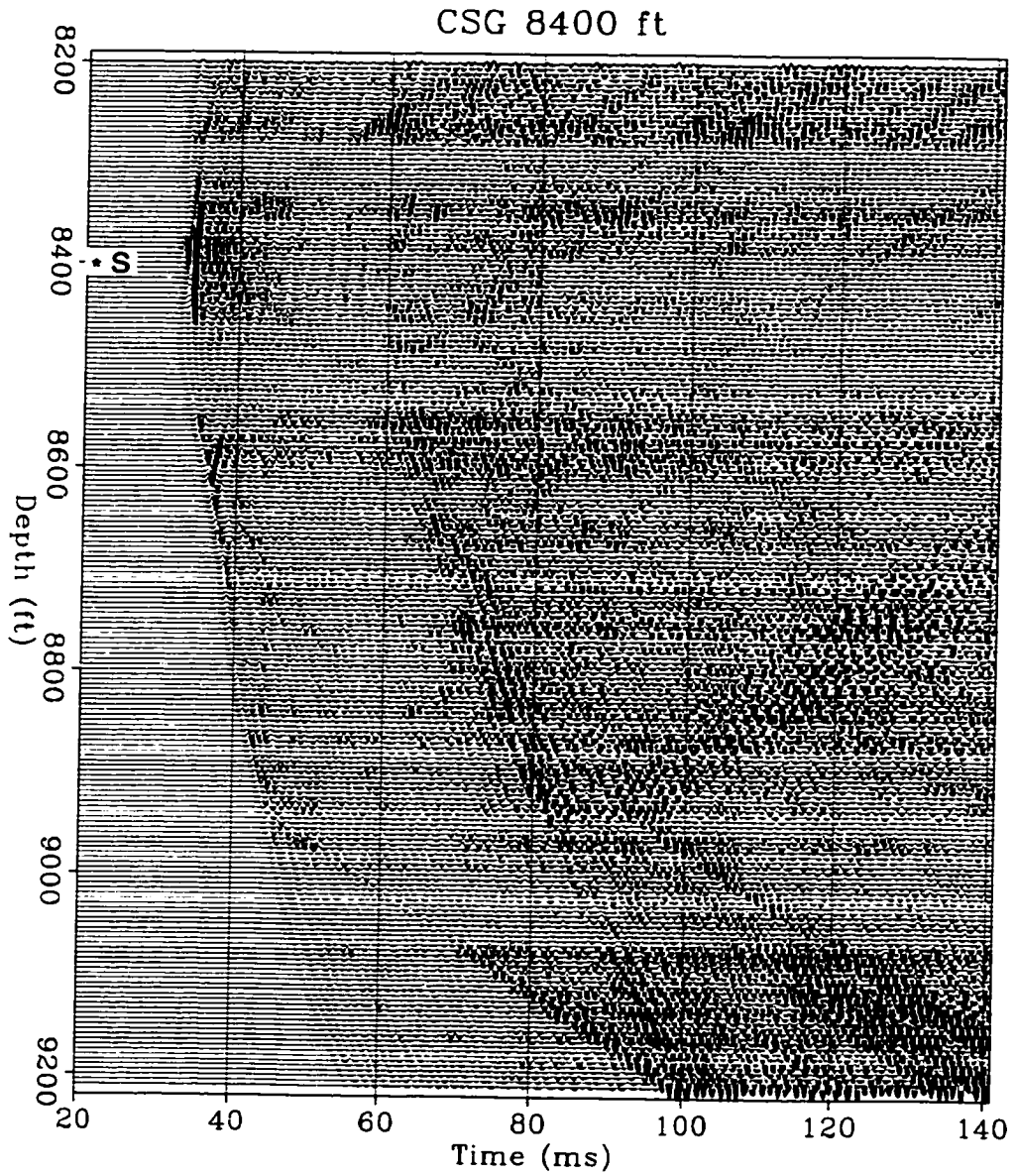


Figure 7.5: Preprocessed common source gather, the depth of the source is 8400 ft.

longest wavelength. In the raw data, the travel times of the direct S -wave are about 1.83 times those of the direct P -wave, so I derive the S -wave velocity as a factor $1/1.83$ of the P -wave tomogram velocity. Usable frequencies of the S -wave are about the same as those of the P -wave, so I expect the imaging resolution of the $S - S$ wave to be about 20 ft.

7.5 Kirchhoff migration

Two observations from data tests in the last three chapters are integrated in the present Kirchhoff migration of cross-well data. One observation is that the single-fold migration images in Chapter 4 and Chapter 5 show that the half of the image space away from the migration source where specular reflections are recorded is imaged better, showing more continuous reflectors and having higher signal to noise ratio. In order to image both halves of the interwell region more effectively and compensate for the narrow recording apertures in both CSG and CRG migration, two passes of migration will be performed, one pass using common shot gathers and the other pass using common receiver gathers. The two images of CSG and CRG migration where the source and receiver share the same depth are stacked to create a single-fold image. The other observation is that in either CSG and CRG migration, the direct arrivals image at the migration source as strong artifacts, thus the horizontal strip around the migration source will be muted. After migration of all the CSGs and CRGs, a volume of images is produced.

In the implementation of the Kirchhoff migration, I use the finite-difference Eikonal solver in Chapter 3 to compute travel time maps from the sources and the receivers. The limited-aperture Kirchhoff migration algorithm in Chapter 6 is applied to process this data set.

7.5.1 90-degree full-aperture P - P wave migration

For the CRG data in Figure 7.4 and CSG data in Figure 7.5, the 90-degree full-aperture P - P wave migration image is shown in Figure 7.7. In this image, flat reflectors at the depths from 8600 ft to 8700 ft, and right to left dipping reflectors at the depths from 8800 ft to 9000 ft can be identified. But this image is noisy, it contains strong artifacts of migration ellipses. Figure 7.7 also shows the artifacts around the migration source at the depth of 8400 ft, suggesting the data processing of muting this strip of the image. Similar

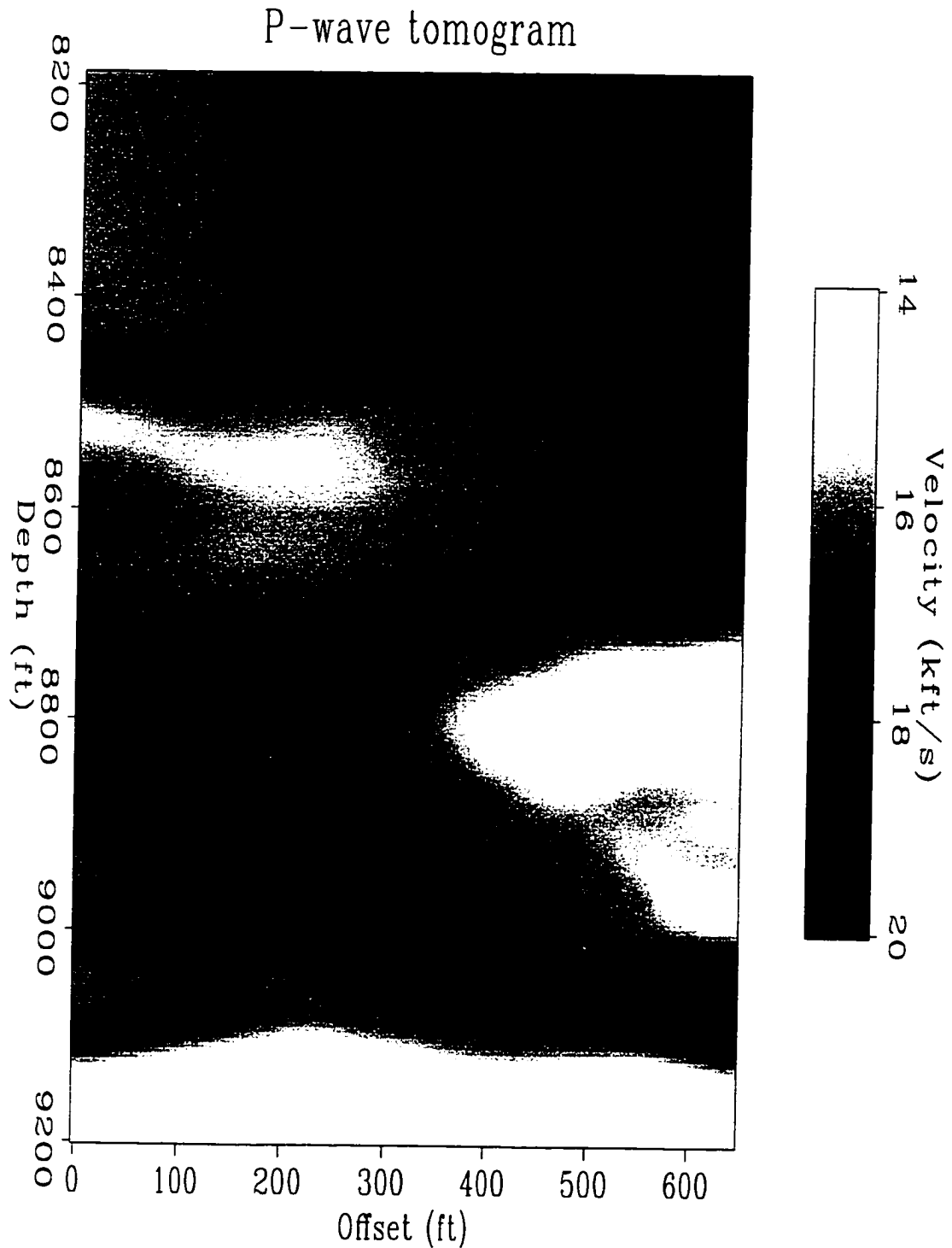


Figure 7.6: *P*-wave velocity tomogram obtained from transmission travel time tomography. This is the velocity model used in *P* - *P* wave migration. The velocity model used in *S* - *S* wave migration is obtained by dividing the *P*-wave velocity by 1.83.

observations can be made in the synthetic data test in Figure 6.6.

Figure 7.8 shows the final stacked *P-P* wave migration image. In this stacked migration image, right to left dipping reflectors at the depths from 8400 ft to 8600 ft can be identified. The target of the cross-well survey is a reef structure near the right well at depths from 8700 ft to 8900 ft. The highest dip at the reef is about 40 degrees, suggesting that the data should be processed in migration using an aperture of about 40 degrees.

7.5.2 45-degree limited-aperture *P-P* wave migration

For the CRG data in Figure 7.4 and CSG data in Figure 7.5, the 45-degree limited-aperture *P-P* wave migration image is shown in Figure 7.9. In this image, flat reflectors at the depths from 8600 ft to 8700 ft, right to left dipping reflectors at the depths from 8800 ft to 9000 ft and in lateral extent 0 to 200 ft from the left well can be identified. The curving events at the depths from 8200 ft to 8300 ft, from 8500 ft to 8600 ft are probably noises. The image below the depth of 9000 ft is quite noisy. Comparing this image to its counterpart of 90-degree full-aperture migration in Figure 7.7, one can see that the interpretable geological features remain the same, namely flat reflectors at the depths from 8600 ft to 8700 ft and dipping reflectors around the depth of 8900 ft. But the image in Figure 7.9 has higher signal to noise ratio, and in particular the high dip noises are not present in Figure 7.9.

Figure 7.10 shows the migration image for the CSG and CRG where the depth of the migration source is 8900 ft. In this image, continuous reflector at the depth of 8470 ft can be identified. The curving events at the depths from 8700 ft to 8800 ft, from 9000 ft to 9100 ft are probably noises. The image above the depth of 8300 ft is quite noisy. Figure 7.9 and Figure 7.10 show that in single-fold migration images good quality reflection events can only be obtained in depth offset 200 ft to 600 ft from the migration source.

After migration of the 201 common shot gathers and 203 common receiver gathers, a volume consisting of 201 images is produced. Image gathers at common surface locations (CSL) can be sliced from the image volume to demonstrate the correctness of the velocity model. Figure 7.11 shows the CSL at the lateral location of 100 ft from the left well. Figure 7.12 shows the CSL at the lateral location of 500 ft from the left well. Image events in these CSL profiles are generally in good horizontal alignments, suggesting that the tomogram velocity model used in the migration is correct. The reasons cross-well tomography can accurately estimate velocity model are that in this survey geometry the

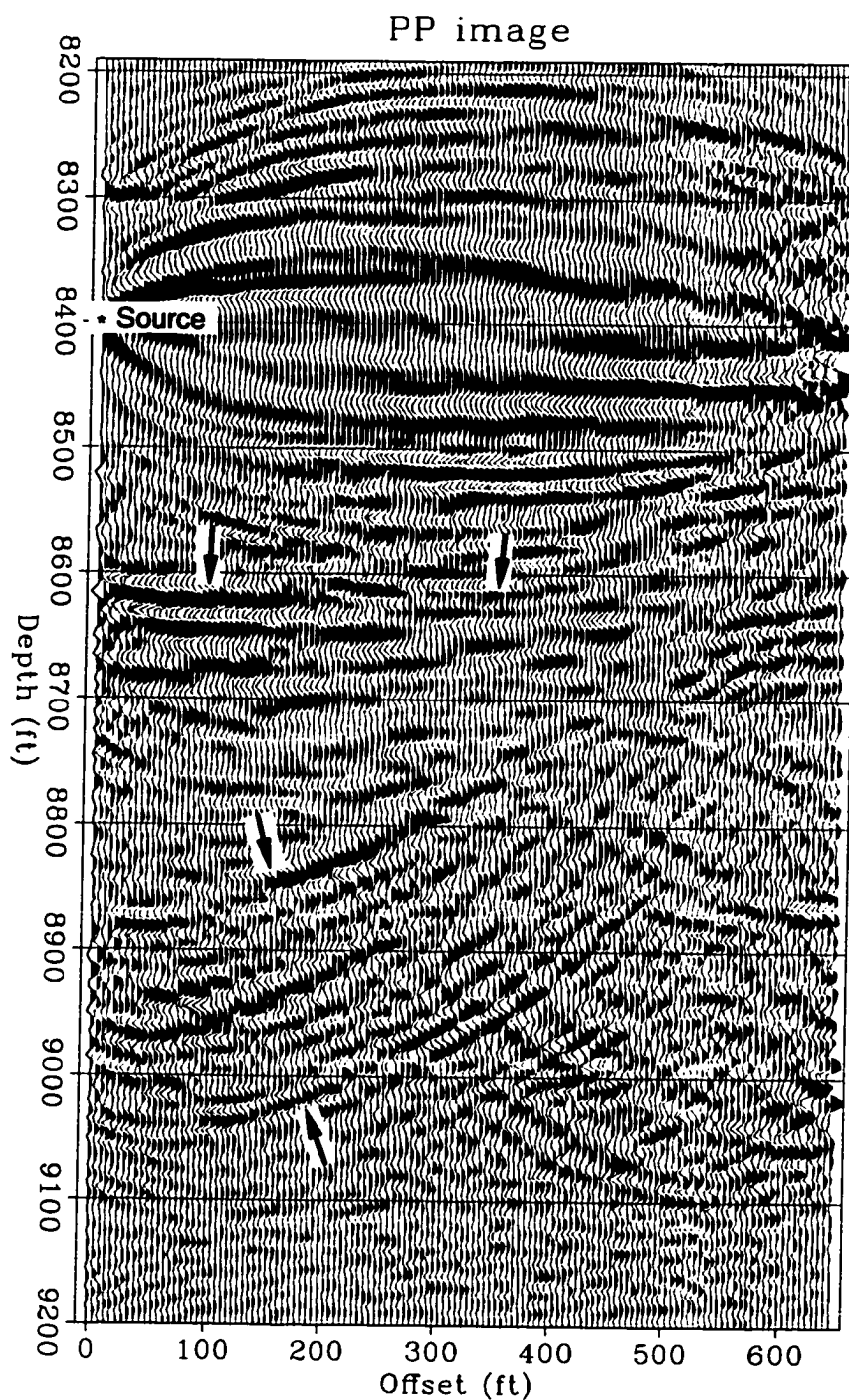


Figure 7.7: Full-aperture *P-P* wave migration image, the depth of migration source is 8400 ft. Notice the flat reflectors at the depths from 8600 ft to 8700 ft, right to left dipping reflectors around the depth of 8900 ft. Also notice the artifacts of migration ellipses.

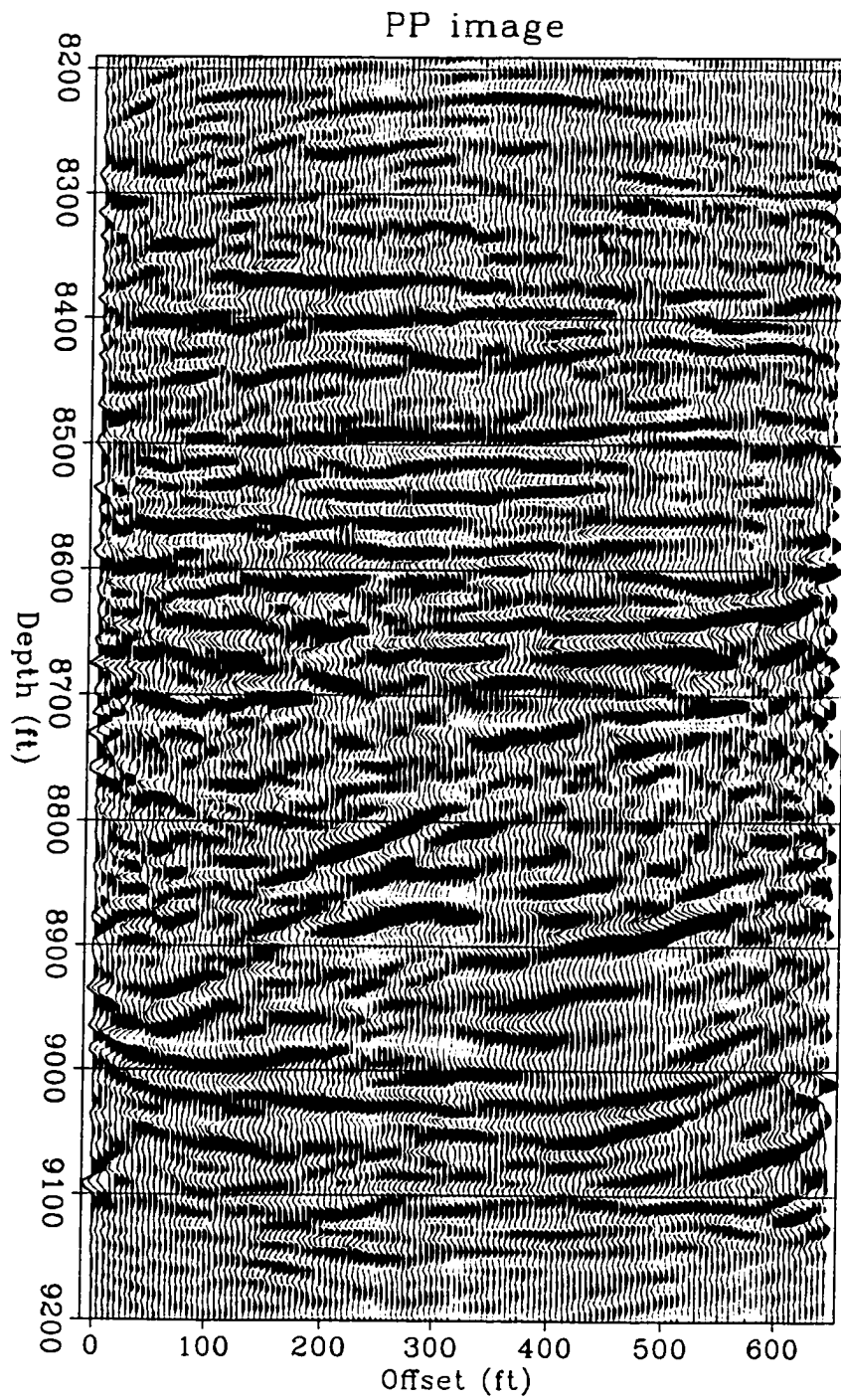


Figure 7.8: Final stacked *P-P* wave image of 90-degree full-aperture migration.

locations of the sources and receivers are known accurately and there is no depth/velocity uncertainty involved in the tomography velocity inversion.

Figure 7.13 shows the final stacked P - P wave migration image.

7.5.3 45-degree limited-aperture S - S wave migration

For the CRG data in Figure 7.4 and CSG data in Figure 7.5, the 45-degree limited-aperture S - S wave migration image is shown in Figure 7.14. In this image, right to left dipping reflectors at the depths from 8750 ft to 9000 ft and in lateral extent 0 to 200 ft from the left well can be identified.

Figure 7.15 shows the migration image from the CSG and CRG where the depth of the migration source is 8900 ft. In this image, right to left dipping reflectors at the depth of 8450 ft can be identified.

Figure 7.16 shows the CSL at the lateral location of 100 ft from the left well. Figure 7.17 shows the CSL at the lateral location of 500 ft from the left well. Image events in these profiles are generally in good horizontal alignments.

Figure 7.18 shows the final stacked S - S wave migration image.

7.6 Interpretation of results

For the final stack $P - P$ wave migration image (Figure 7.13) and the final stack $S - S$ wave migration image (Figure 7.18), I make some tentative interpretations. The most obvious is that the $S - S$ wave image has higher resolution than the $P - P$ wave image. The $P - P$ wave image is more noisy than the $S - S$ image, because the processing of the $P - P$ wave is contaminated by the $S - S$ wave acting as noises.

The geological structures as suggested by these two images are consistent. The formations from the depths 8200 ft to 8400 ft are flat. The formations from the depths 8400 ft to 8600 ft are slightly dipping from the right to left. The formations from the depths 8600 ft to 8700 ft are flat. The target of this cross-well survey is a reef structure near the right well. The reef structure extends in depth from 8700 ft to 8900 ft and in lateral from the right well to about mid-way between the two wells. The formations left of the reef structure are dipping right to left and contact the reef as an unconformity. The formations below the depth of 9000 ft are flat.

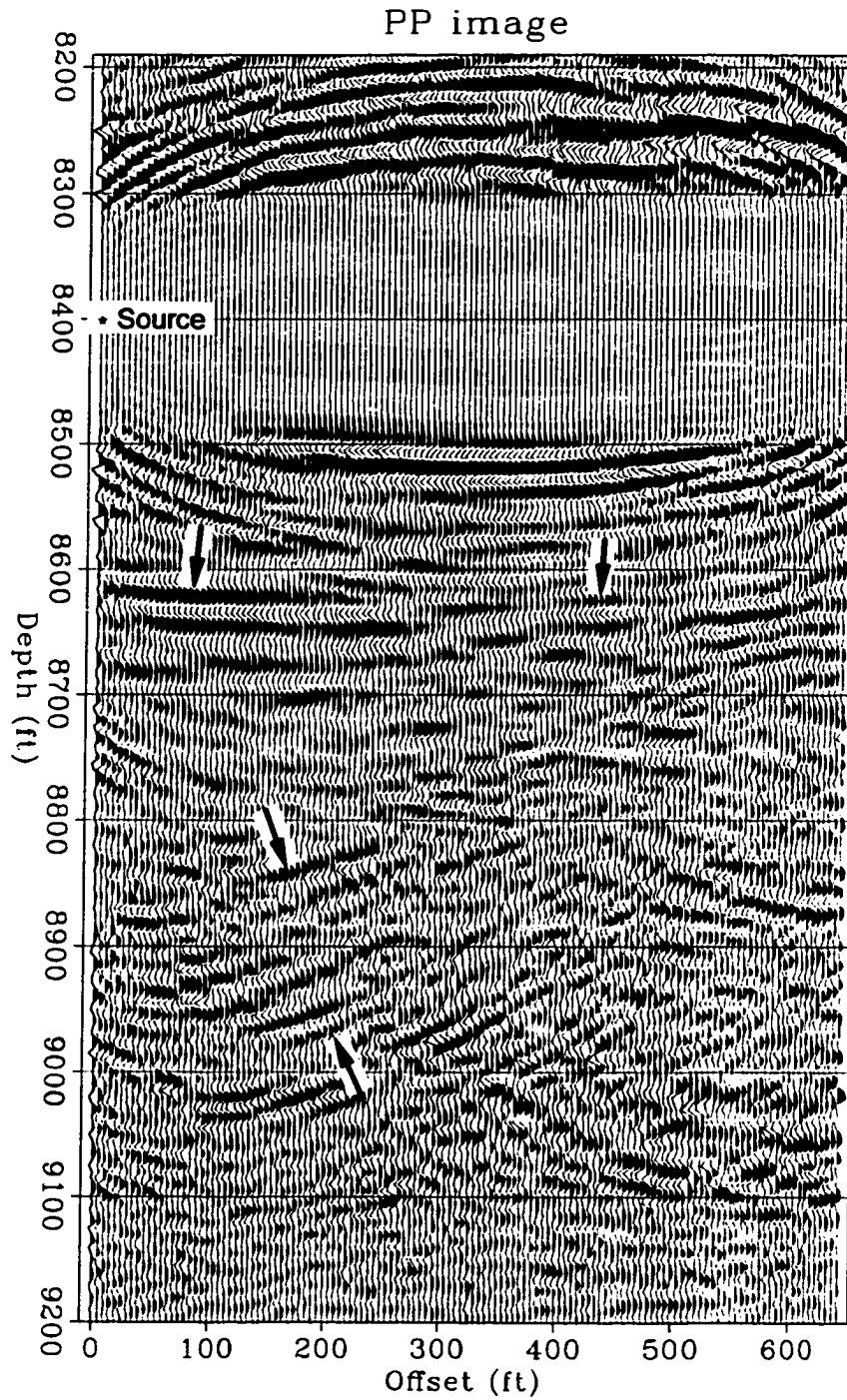


Figure 7.9: 45-degree aperture *P-P* wave migration image, the depth of migration source is 8400 ft. Notice the flat reflectors at the depths from 8600 ft to 8700 ft, right to left dipping reflectors around the depth of 8900 ft.

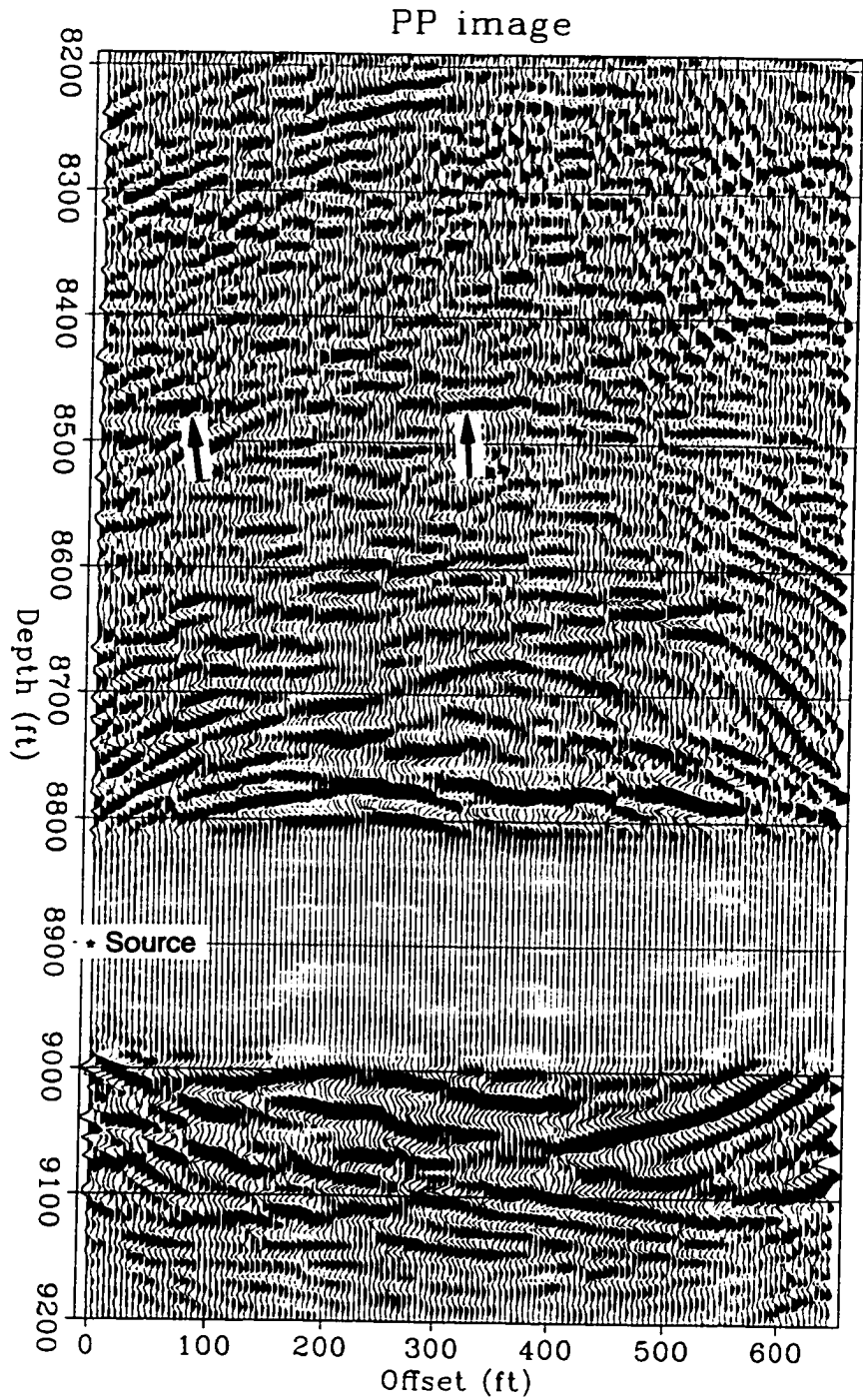


Figure 7.10: 45-degree aperture *P-P* wave migration image, the depth of migration source is 8900 ft. Notice the continuous reflector at the depth of 8470 ft.

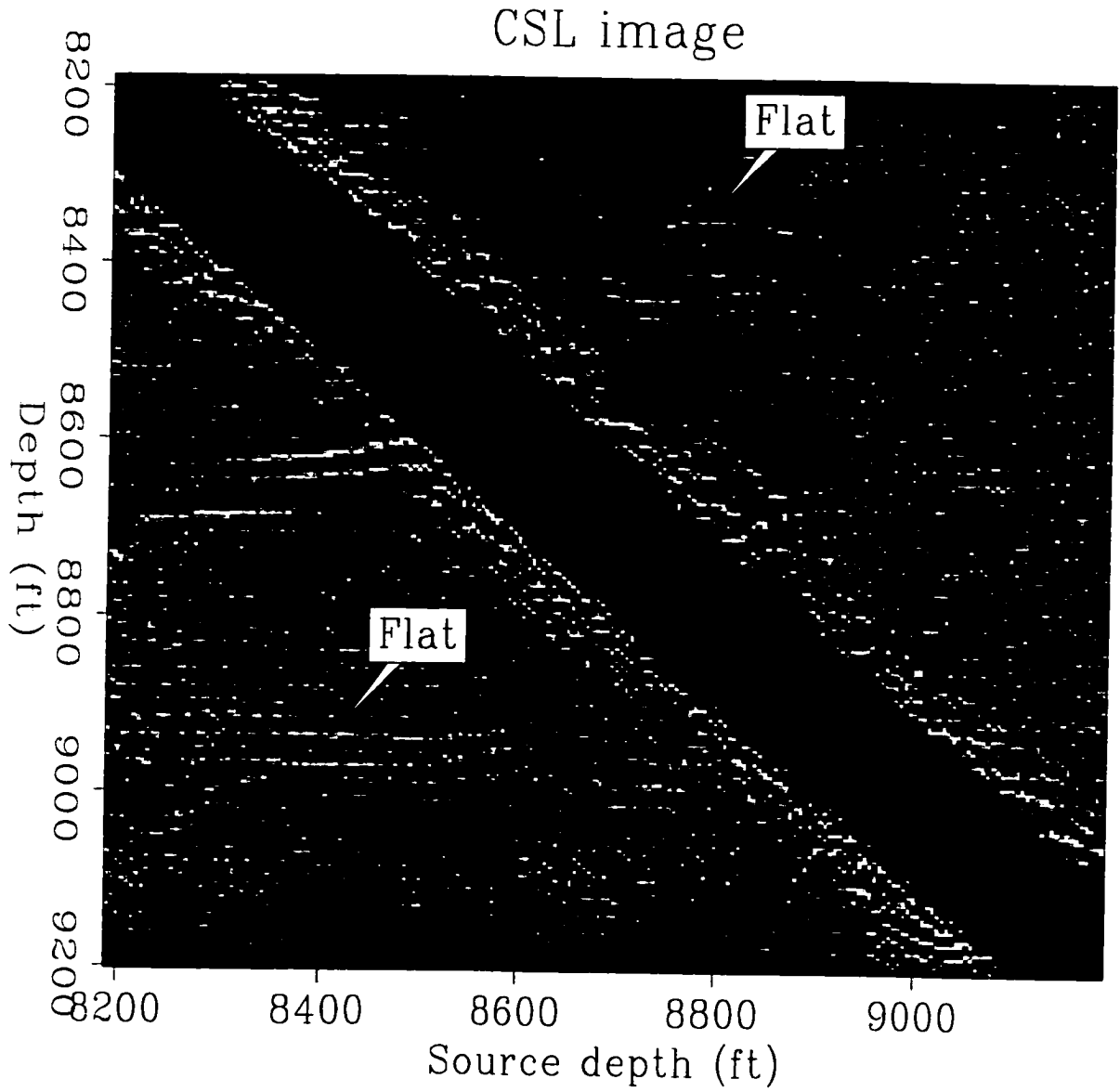


Figure 7.11: *P-P* wave common surface lateral location image profile, 100 ft from the left well.

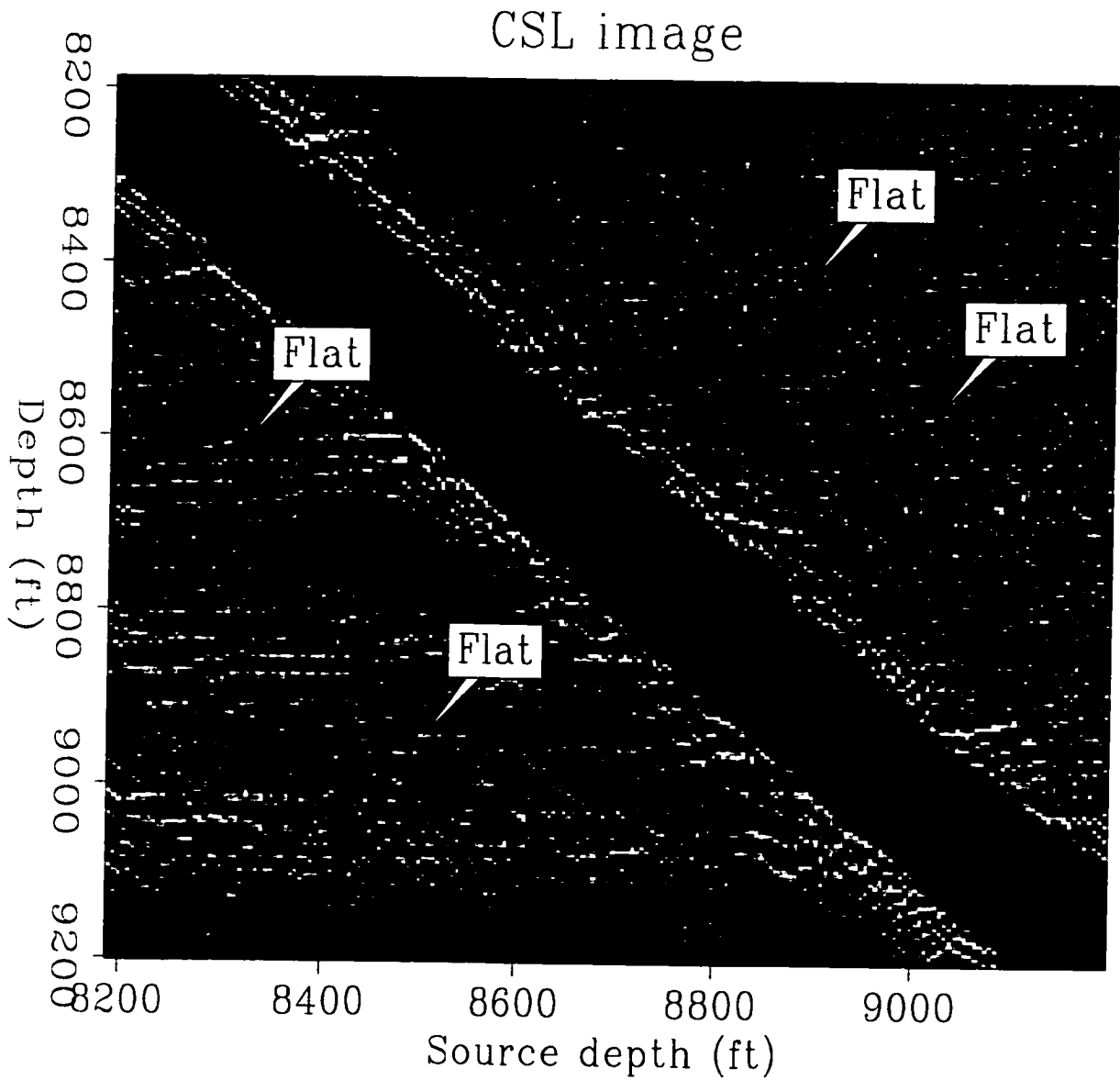


Figure 7.12: *P-P* wave common surface lateral location image profile, 500 ft from the left well.

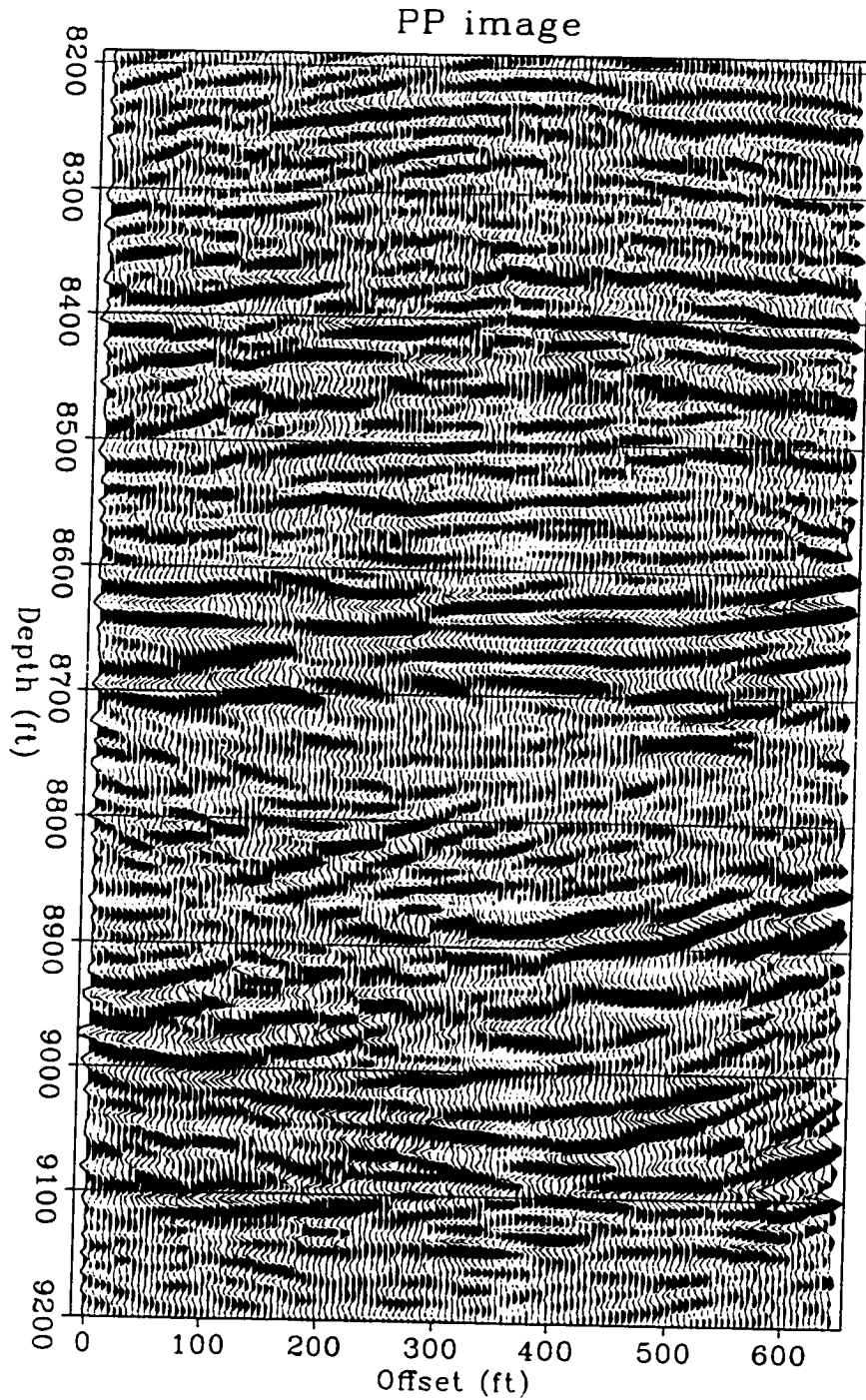


Figure 7.13: Final stacked *P-P* wave image of 45-degree aperture migration.

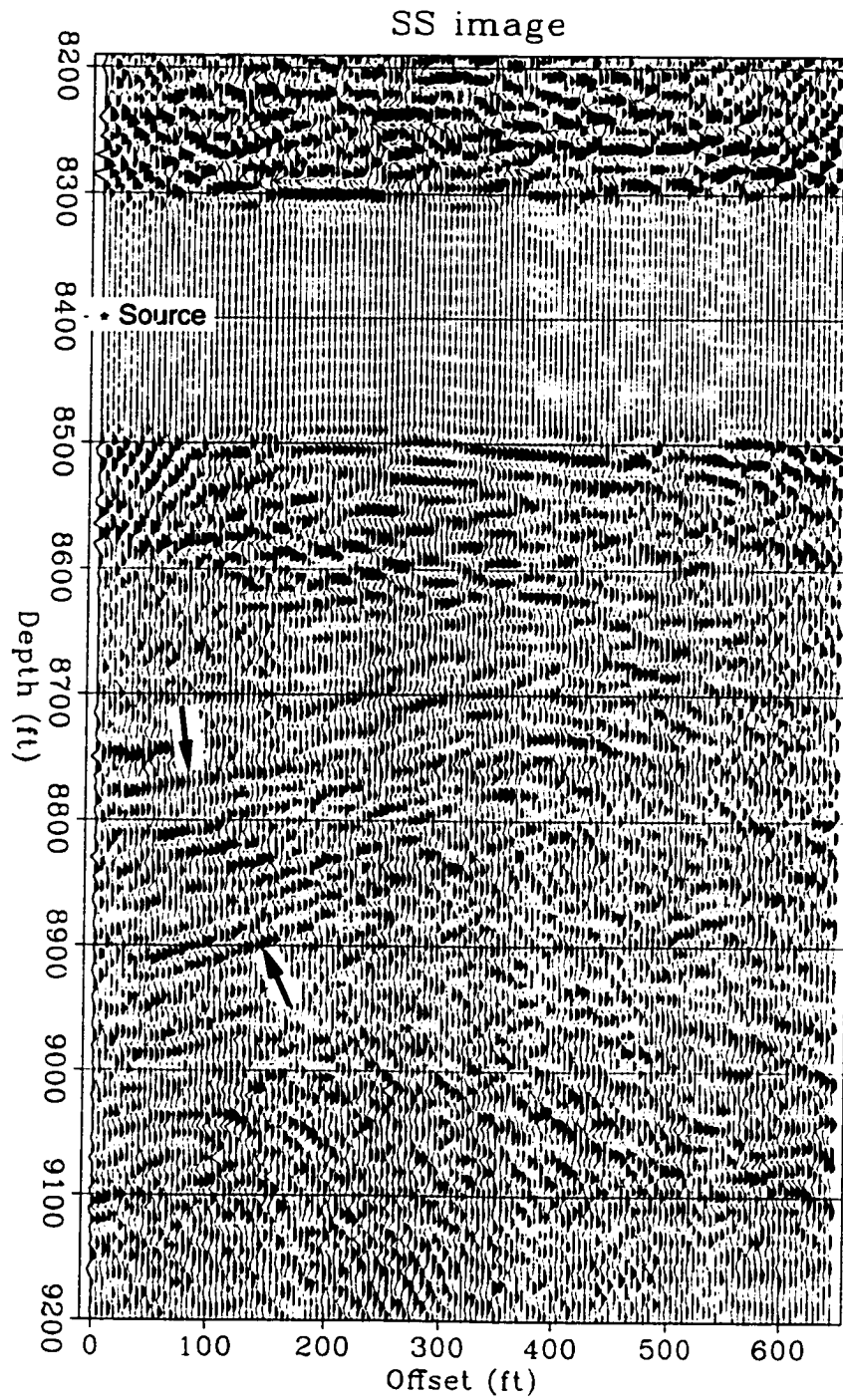


Figure 7.14: 45-degree aperture *S-S* wave migration image, the depth of migration source is 8400 ft. Notice the right to left dipping reflectors around the depth of 8900 ft.

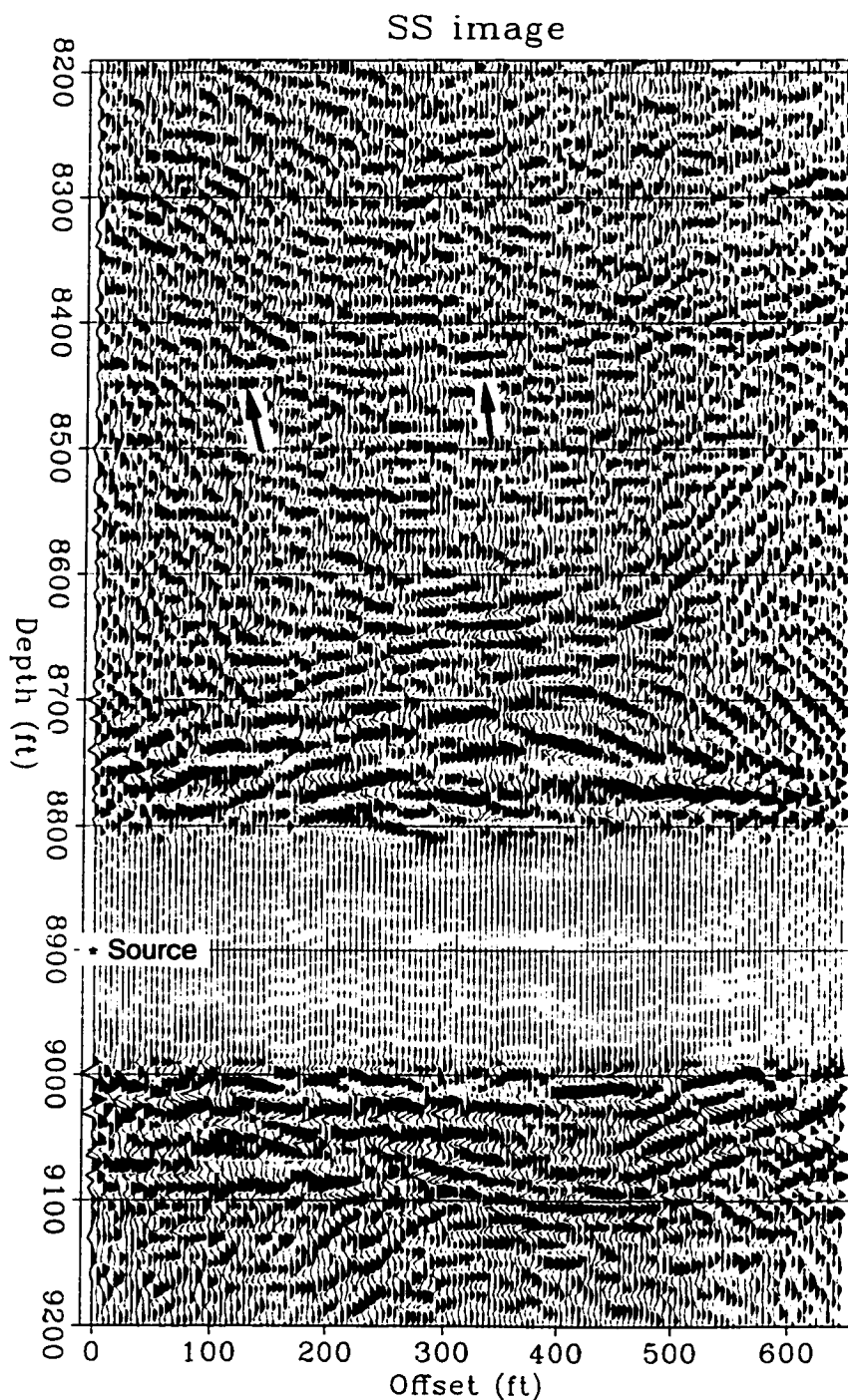


Figure 7.15: 45-degree aperture *S-S* wave migration image, the depth of migration source is 8900 ft. Notice the right to left dipping reflector at the depth of 8450 ft.

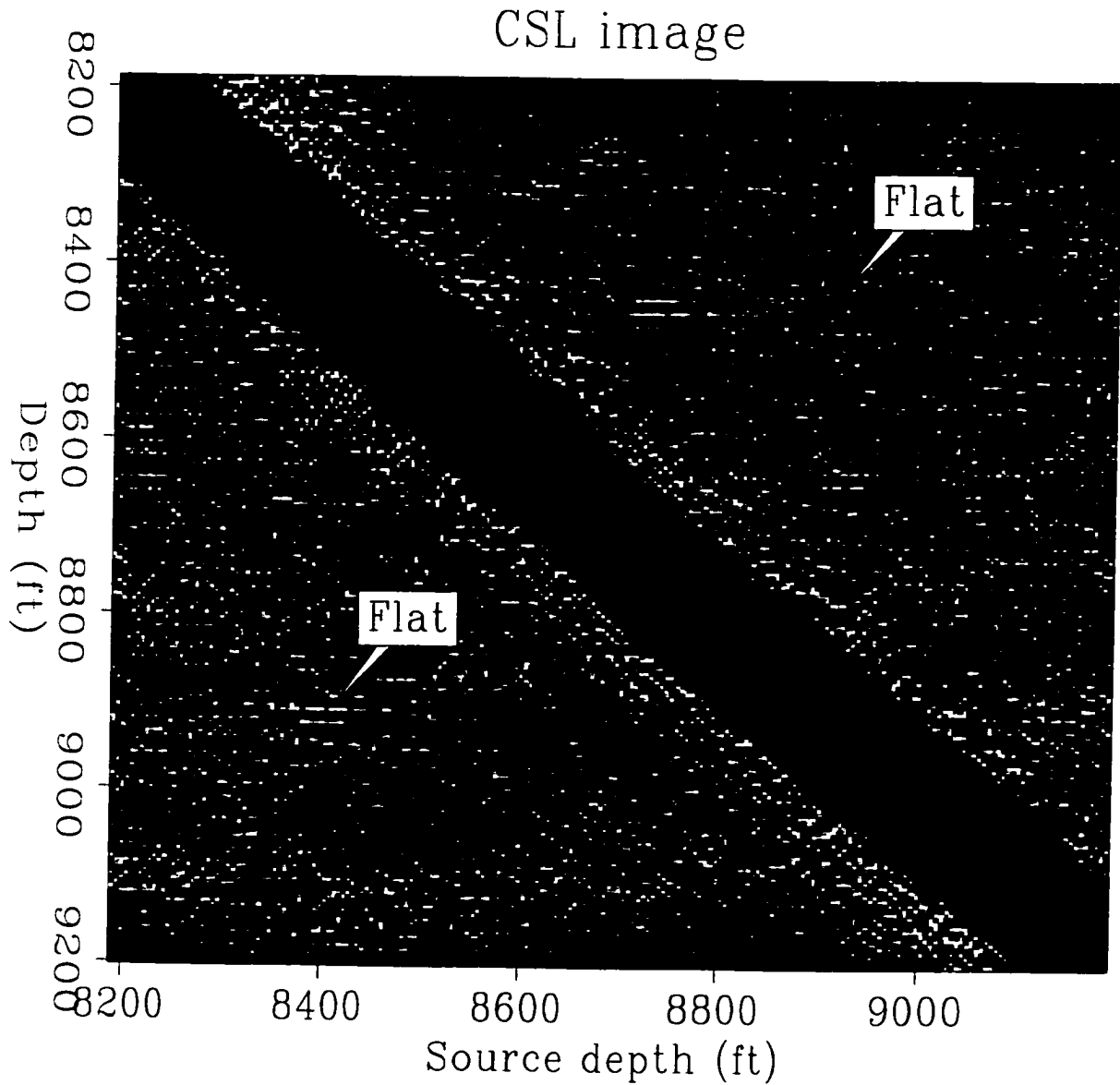


Figure 7.16: *S-S* wave common surface lateral location image profile, 100 ft from the left well.

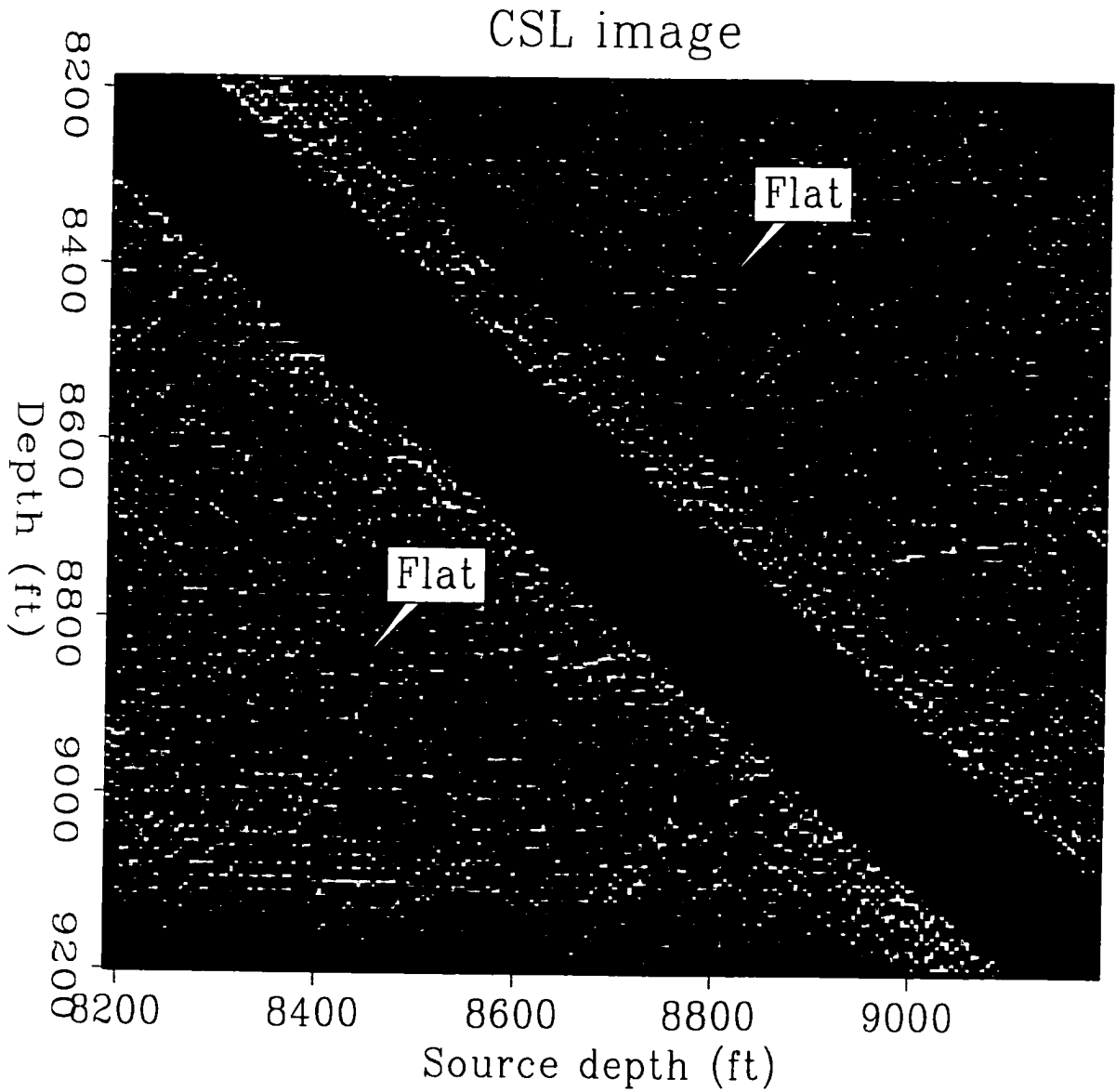


Figure 7.17: *S-S* wave common surface lateral location image profile, 500 ft from the left well.

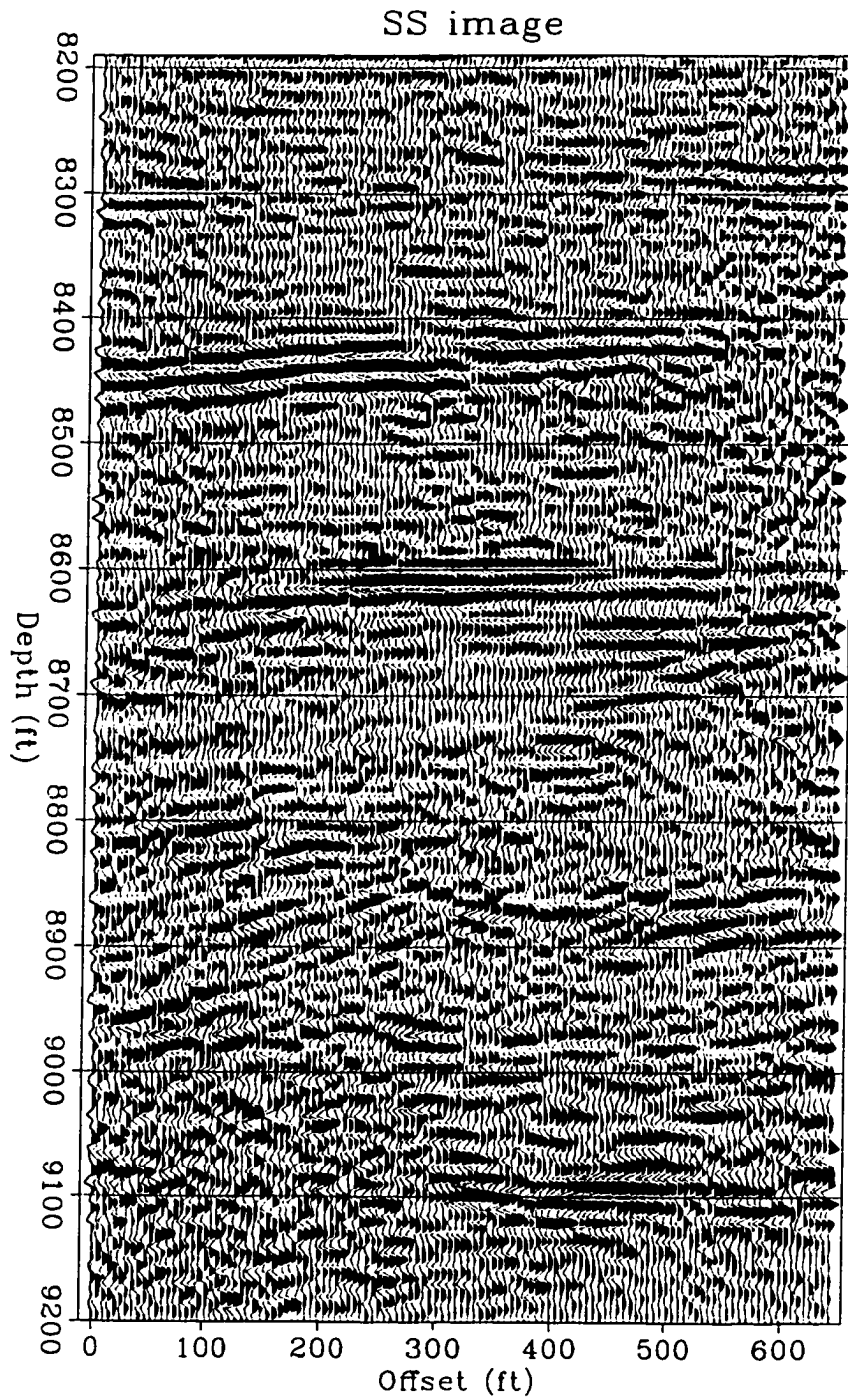


Figure 7.18: Final stacked *S-S* wave image of 45-degree aperture migration.

7.7 Conclusions

I have demonstrated the limited-aperture Kirchhoff depth migration in the King Mountain cross-well data set. Preprocessing, which consists of tube wave attenuation, amplitude correction, and attenuation of the direct arrivals, is applied to condition the data for migration. The transmission travel time tomogram is an accurate background velocity model for migration. The resulting $P - P$ and $S - S$ wave images clearly show geological structures, dipping beds, unconformity and reef of thickness less than 200 ft.

By limiting the aperture used in migration, noises in the data are not spread to a large area in the image and the resulting images have higher signal to noise ratio. The maximum dip in the geology dictates the choice of migration aperture to balance the correct imaging of geological features and spreading of noises.

Chapter 8

Post-CDP-mapped migration in vertical seismic profile

VSP-CDP maps reflection from a dipping reflector into a third-order polynomial in unmigrated VSP-CDP image (offset-depth) space. A point in the $\tau - p$ space of the migrated image is obtained by stacking the VSP-CDP image along the image trajectory calculated by modeling the VSP-CDP mapping process. Inverse transformation on the resulting $\tau - p$ data gives the migration image. Curves are migrated by operation on lines as a curve is the envelope of lines of various dips. The VSP-CDP migration algorithm assumes a constant velocity medium.

8.1 Introduction

In vertical seismic profiling (VSP), a source is located on the Earth surface and a string of receivers are placed in the borehole to record both the downgoing direct arrival and the upgoing reflections, Figure 8.1. The advantages of vertical seismic profiling over the conventional surface seismic reflection surveys are many. Since the receivers are buried in the borehole within the earth rather than on the earth surface, the source excited seismic waves propagate only once through the severe attenuating near-surface weathered zone. The frequency contents of the seismic waves as recorded are richer. As VSP data are recorded inside the earth during the wave propagation process, VSP data are in-situ recorded data. VSP data has been used for correlating surface reflection data and well log data, for identifying multiple reflections, for analyzing source signature effects,

and for studying the effects of attenuation. As in surface seismic reflection survey, VSP data can also provide structural information of the earth subsurface, in particular near the borehole. Since the receivers are placed within the earth and the resulting recorded frequency bandwidth is wide, VSP data can provide high resolution structural image in the vicinity of the borehole, revealing small features otherwise unseen in conventional surface seismic reflection survey images. High resolution structural images near the boreholes are very useful in reservoir characterizations. It has been reported that VSP can detect water flooding and CO₂ injection fluid fronts. However, the VSP can only provide high resolution information in the vicinity of the boreholes, it is a complementary survey method to the conventional surface seismic method which provide low resolution information but over a large area.

The method of structural imaging in VSP has largely been influenced by surface seismic reflection data processing. For example, in migration imaging, many authors (Chang and McMechan, 1986; Wiggins et al, 1986; Dillon, 1988) have reported applying pre-stack depth profile migration methods. These pre-stack migration methods, e.g., Kirchhoff integration, reverse-time, phase-shift plus interpolation, are equivalent, they only differ in the way wave fields are extrapolated. In surface seismic reflection surveys, pre-stack depth migration has been applied to all survey areas, and it has enjoyed many successes in subsurface structural imaging. The success of pre-stack depth migration in surface seismic survey lies in the wide recording aperture and the dense survey coverage (there are many shots and receivers in a survey). In VSP, there is usually only one shot gather data or in a better situation there are a few shot gathers; and in each shot gather there are usually less than 100 receiver traces. This means the surveying aperture in VSP is very narrow, and there are not enough pre-stack profile migration images in stacking to attenuate the edge diffractions and noises. Thus, even though pre-stack depth profile migration is a powerful imaging method, when applied to VSP where the conditions for its utilization are not satisfied, the results might not be satisfactory. In surface seismic survey, a less sophisticated structural imaging method is the sequence of CDP stack and post-stack migration, which has a better noise tolerance even though suffering in somewhat lower accuracy than the pre-stack depth migration.

Wyatt et al (1981) introduced the CDP technique of surface seismic reflection survey into VSP data processing. People know that the VSP-CDP images of dipping reflectors are mispositioned owing to the assumption of flat reflector in CDP data processing. Interactive

data processing techniques (Lazaratos, 1993; Smalley, 1997) have been developed to correct the mispositioning in the VSP-CDP images. These techniques work by mapping the data using an assumed known dip angle of the reflector. By trial and error in fitting the data, the final dip angle of the reflector is selected. These interactive methods are flexible but time consuming. In this chapter, I develop an automatic method of post-CDP-mapped migration to VSP data structural imaging. Like surface seismic data processing, the VSP data are first CDP mapped into the image space under the assumption of flat reflector, then the CDP image is corrected for dip errors by a migration process. First, I derive the travel time equation for reflection from a dipping reflector. Then I analyse the mispositioning of dipping reflector in VSP-CDP imaging. Then I describe the algorithm of post-CDP-mapped migration. Finally, I apply the algorithm on both synthetic and field data.

8.2 VSP reflection travel time from a dipping interface

The VSP survey geometry for a single dipping interface of an angle θ is shown in Figure 8.1 (Wyatt et al, 1981). In this survey geometry, L is the well-to-shot offset; d is the depth to the geophone receiving the reflected ray; and h is the depth to the point where the dipping interface intercepts the well.

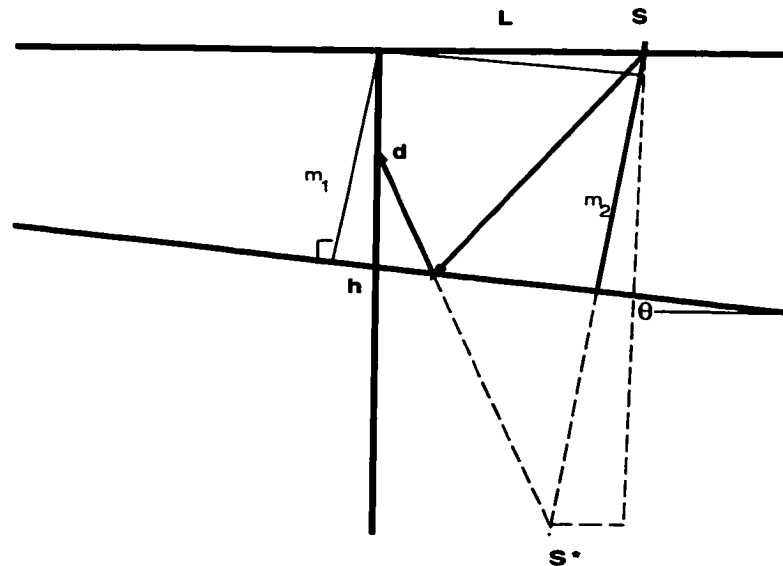


Figure 8.1: Layout of VSP survey. Travel time of reflection from a reflector can be equivalently computed from the image source S^* .

In deriving travel time equation for the reflected ray, let us assume, m_1 is the perpendicular distance from the top of the well to the interface, m_2 is the perpendicular distance from the shot to the interface. The following relationships follow from this figure:

$$m_1 = h \cos \theta \quad (8.1)$$

$$\begin{aligned} m_2 &= m_1 + L \sin \theta \\ &= h \cos \theta + L \sin \theta \end{aligned} \quad (8.2)$$

The Cartesian coordinates at the image source S^* are:

$$\begin{aligned} x_{S^*} &= L - 2m_2 \sin \theta \\ &= L - 2(h \cos \theta + L \sin \theta) \sin \theta \end{aligned} \quad (8.3)$$

$$z_{S^*} = 2(h \cos \theta + L \sin \theta) \cos \theta \quad (8.4)$$

Let the layer velocity above the reflector be v . The reflection travel time from the source to the receiver is t ,

$$\begin{aligned} v^2 t^2 &= x_{S^*}^2 + [z_{S^*} - d]^2 \\ &= [L - 2(h \cos \theta + L \sin \theta) \sin \theta]^2 + [2(h \cos \theta + L \sin \theta) \cos \theta - d]^2 \end{aligned} \quad (8.5)$$

After some algebraic simplifications, I arrive at:

$$v^2 t^2 - L^2 = 4(h - d)(h \cos^2 \theta + L \cos \theta \sin \theta) + d^2 \quad (8.6)$$

When $d = 0$ and $\theta = 0$, it reduces to the NMO travel time equation for surface seismic reflection survey.

8.3 VSP reflection CDP depth mapping

The CDP mapping algorithm assumes flat reflectors, Figure 8.2. The coordinates of the reflection image point are related by

$$\frac{x}{z - d} = \frac{L - x}{z} \quad (8.7)$$

From this equation I obtain

$$x = \frac{z - d}{2z - d} L \quad (8.8)$$

and

$$d = z - \frac{xz}{L - x} \quad (8.9)$$

The CDP mapping travel time equation is

$$v^2 t^2 = L^2 + (2z - d)^2 \quad (8.10)$$

From this equation and equation (8.8), I obtain the coordinates of the image point,

$$x = \frac{1}{2} \frac{\sqrt{v^2 t^2 - L^2} - d}{\sqrt{v^2 t^2 - L^2}} L \quad (8.11)$$

$$z = \frac{\sqrt{v^2 t^2 - L^2} + d}{2} \quad (8.12)$$

VSP-CDP maps a point in the data space (t, d) (travel time t and receiver depth d) into a point in the image space (x, z) .

To see the effect of VSP-CDP mapping on the reflection of a dipping reflector, I substitute the travel time equation (8.6) in the above two equations (8.11) and (8.12) to obtain

$$x = \frac{1}{2} \frac{\sqrt{4(h-d)(h \cos^2 \theta + L \sin \theta \cos \theta) + d^2} - d}{\sqrt{4(h-d)(h \cos^2 \theta + L \sin \theta \cos \theta) + d^2}} L \quad (8.13)$$

$$z = \frac{\sqrt{4(h-d)(h \cos^2 \theta + L \sin \theta \cos \theta) + d^2} + d}{2} \quad (8.14)$$

In these two equations when the depth of the receiver is the same as the depth of the dipping reflector intersecting the well $d = h$, $x = 0$ and $z = h$, that is, the image of a reflector is pinned at the location intersecting the well. Finally, I substitute the CDP mapping relation for d in equation (8.9) (depth of the receiver) into the above equation for z -coordinate to obtain

$$xz^2 = [(L - x)h + (2x - L)z](h \cos^2 \theta + L \sin \theta \cos \theta) \quad (8.15)$$

This is a third-order nonlinear equation. Let $\delta = h \cos^2 \theta + L \sin \theta \cos \theta$, and fix x , it becomes a second-order equation for z where z can be directly solved for,

$$z = \frac{(2x - L)\delta + \sqrt{(2x - L)^2 \delta^2 + 4x(L - x)h\delta}}{2x} \quad (8.16)$$

that is, a linear line in the model space is mapped into a curve in the image space. However, for the special case of reflectors being flat $\theta = 0$, equation (8.16) gives the solution $z = h$ for arbitrary lateral coordinate x where h is the depth of the reflector, ie, flat reflectors are correctly imaged by VSP-CDP mapping.

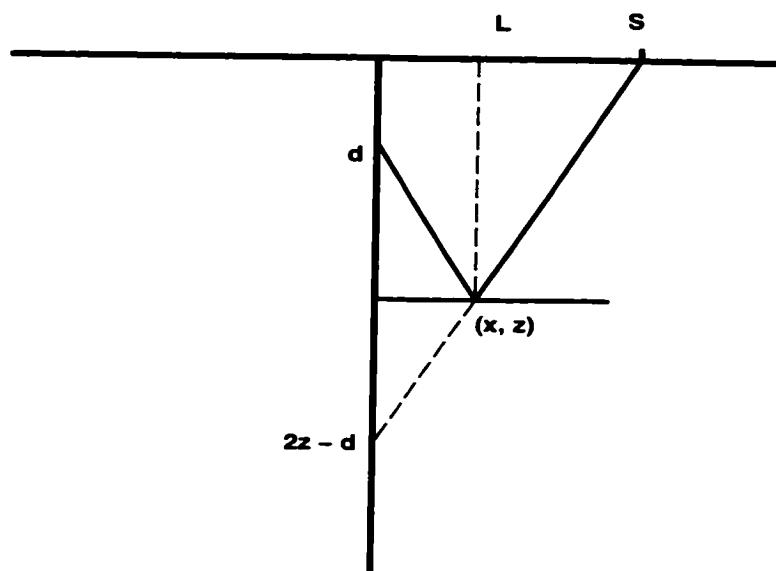


Figure 8.2: VSP-CDP mapping assumes the reflectors are flat. S is the source, L is the offset, d is the depth of a receiver.

8.4 Analysis of VSP-CDP mispositioning caused by dip

From the beginning of VSP-CDP imaging data processing, people noticed that dipping reflectors are mispositioned owing to the assumption of flat reflector in CDP data processing. Analyses of VSP-CDP mispositioning errors were given by Lazaratos (1993). In this section, I present a detailed analysis of VSP-CDP mispositioning errors from a different perspective, for the purpose of post VSP-CDP migration. Figure 8.3 and Figure 8.4 show how the VSP-CDP mispositions a dipping reflector PQ whose dip angle is θ . The equation describing this dipping reflector is

$$z = x \tan \theta + h. \quad (8.17)$$

The coordinates of the image source S^* are given in equations (8.3) and (8.4). The equation describing the ray RS^* from the image source to the receiver is

$$\frac{z-d}{x} = \frac{z_{S^*}-d}{x_{S^*}} \quad (8.18)$$

Point B is the reflection point, it is the intersection of the line PQ and RS^* . The coordinates of point B can be calculated by solving the system of linear equations for lines PQ and RS^* . From the equations (8.17) and (8.18), I can solve for the coordinates of the reflection point B

$$\begin{aligned} x_B &= -\frac{(h-d)x_{S^*}}{x_{S^*}\tan\theta - z_{S^*} + d} \\ &= -\frac{(h-d)[L - 2(h\cos\theta + L\sin\theta)\sin\theta]}{[L - 2(h\cos\theta + L\sin\theta)\sin\theta]\tan\theta - 2(h\cos\theta + L\sin\theta)\cos\theta + d}, \end{aligned} \quad (8.19)$$

$$z_B = x_B \tan\theta + h. \quad (8.20)$$

Point B' is the point in the image space where the VSP-CDP maps the reflection point B to under the assumption of flat reflector. From equations (8.13) and (8.14), I have

$$x_{B'} = \frac{1}{2} \frac{\sqrt{4(h-d)(h\cos^2\theta + L\sin\theta\cos\theta) + d^2} - d}{\sqrt{4(h-d)(h\cos^2\theta + L\sin\theta\cos\theta) + d^2}} L \quad (8.21)$$

$$z_{B'} = \frac{\sqrt{4(h-d)(h\cos^2\theta + L\sin\theta\cos\theta) + d^2} + d}{2} \quad (8.22)$$

In equation (8.15), when the horizontal coordinate is set $x = 0$ in the VSP-CDP mapped image space, then $z = h$, ie, the depth of the point where the reflector intercepts the well. The same is true in equation (8.22) when the depth of the receiver is the same as that of the reflector intersecting the well. A reflector intercepting the well is imaged by VSP-CDP at the exact depth at the well location. The image of dipping reflector is only distorted away from the well.

Figures 8.3 and 8.4 show that the image point shifts from the reflection point in the down-dip direction. From the above analysis, I know that the depth of the reflector is imaged exactly at the well location. As a result, when the dip angle of the reflector is negative as in Figure 8.3, the dip angle of the image is larger in magnitude than the actual dip angle of the reflector; whereas when the dip angle of the reflector is positive as in Figure 8.4, the dip angle of the image is smaller in magnitude.

Equations (8.19) versus (8.21), and equations (8.20) versus (8.22) are fairly complex. The values of these equations are best compared numerically in a graph. I use the following

survey parameters for comparison study, the offset $L = 600$, the depth of the reflector intersecting the well $h = 400$, the depth of the receiver $d = 0$, in the above equations to make Figures 8.5 and 8.6. Figure 8.5 shows that the lateral coordinate of the image points are half-way between the receiver and the source when both the source and the receiver are on the earth surface under the imaging assumption of flat reflector. The lateral coordinate of the image point is smaller (larger) than that of the corresponding reflection point when the dip angle of the reflector is negative (positive), as shown in Figure 8.3 (Figure 8.4). Figure 8.6 shows that the depth of the image point is larger than that of the corresponding reflection point when the reflector is dipping. The coordinates of the image point agree with those of the reflection point in the case the reflector is flat, that is when the assumption of flat reflector in VSP-CDP mapping is satisfied. In another comparison of coordinates between reflection point and image point, I choose the following parameters which are particular to vertical seismic profile, the offset $L = 600$, the depth of the reflector intersecting the well $h = 400$, the depth of the receiver $d = 100$. Figure 8.7 compares the lateral coordinates, and Figure 8.8 compares the vertical coordinates. Figures 8.7 and 8.8 are consistent with Figures 8.5 and 8.6. I conclude that the lateral coordinate of the image point is smaller (larger) than that of the corresponding reflection point when the dip angle of the reflector is negative (positive); and the depth of the image point is larger than that of the corresponding reflection point when the reflector is dipping; the coordinates of the image point agree with those of the reflection point in the case the reflector is flat.

Figure 8.9 shows the true location of a -10° dipping reflector (equations (8.19) and (8.20)) and its VSP-CDP image (equations (8.21) and (8.22)). Figure 8.10 shows the true location of a 10° dipping reflector and its VSP-CDP image. In these two figures, the VSP-CDP images of dipping straight reflectors are actually curves, but for small source-receiver offset, they can be approximated as straight dipping lines.

8.5 Analysis of VSP-CDP mispositioning caused by velocity inaccuracy

In the above section of describing VSP reflection CDP depth mapping, I show that VSP-CDP maps a point in the data space (t, d) (travel time t and receiver depth d) into a point in the image space (x, z) . In order to analyze positioning errors, let me assume the

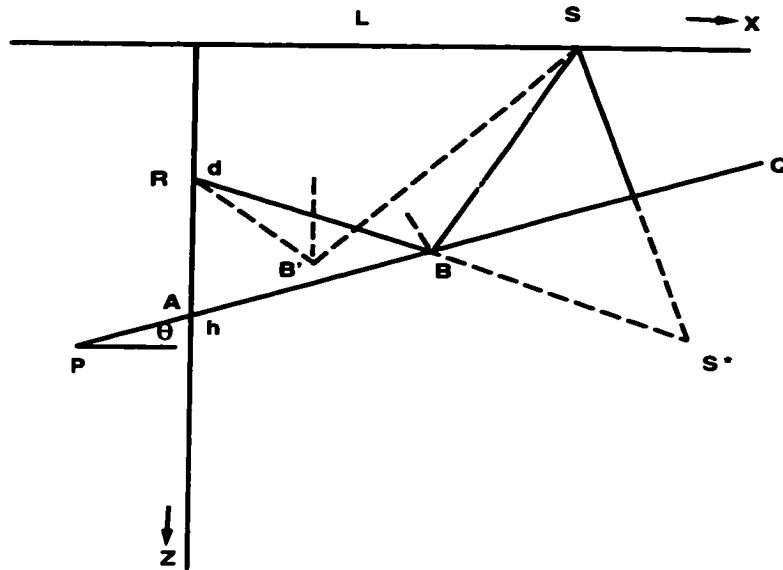


Figure 8.3: The point of the reflector intersecting the well (point A) is imaged exactly at the well location. Image point B' shifts in the down-dip direction relative to the reflection point B . As a result, the image of this dipping reflector has a larger dip angle.

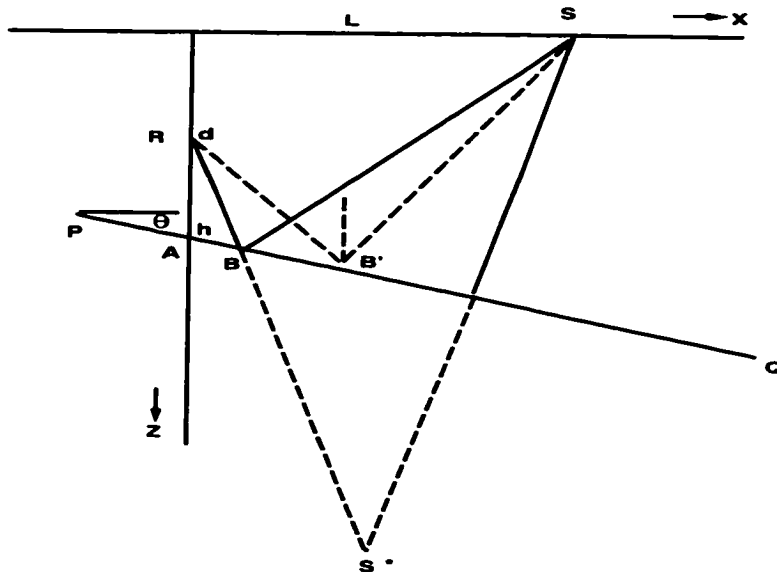


Figure 8.4: The point of the reflector intersecting the well (point A) is imaged exactly at the well location. Image point B' shifts in the down-dip direction relative to the reflection point B . As a result, the image of this dipping reflector has a smaller dip angle.

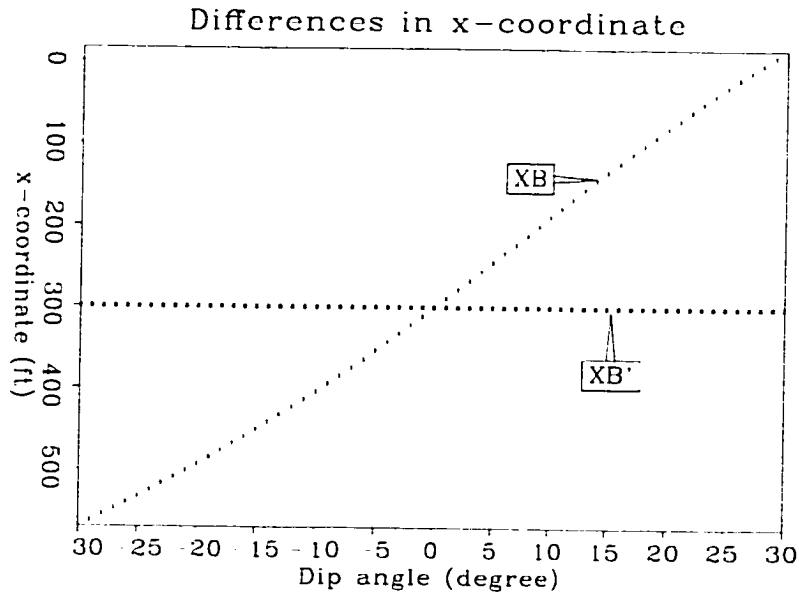


Figure 8.5: Curve labeled 1 (XB) shows the lateral coordinate of the reflection point as a function of the dip angle of the reflector; curve labeled 2 (XB') shows the lateral coordinate of the corresponding image point. In this figure, both the receiver and the source are located on the surface, the offset is 600 ft. And the depth of the reflector intersecting the well is 400 ft.

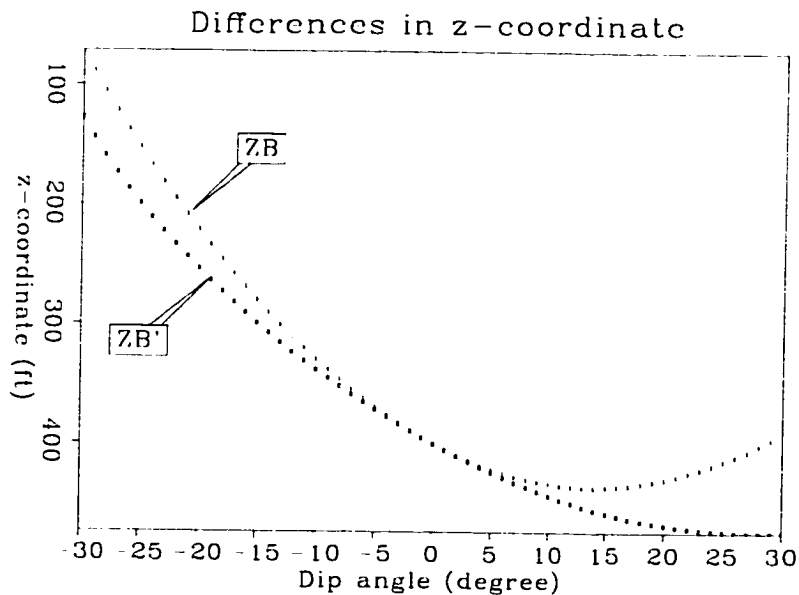


Figure 8.6: Curve labeled 1 (ZB) shows the depth coordinate of the reflection point as a function of the dip angle of the reflector; curve labeled 2 (ZB') shows the depth coordinate of the corresponding image point. In this figure, both the receiver and the source are located on the surface, the offset is 600 ft. And the depth of the reflector intersecting the well is 400 ft.

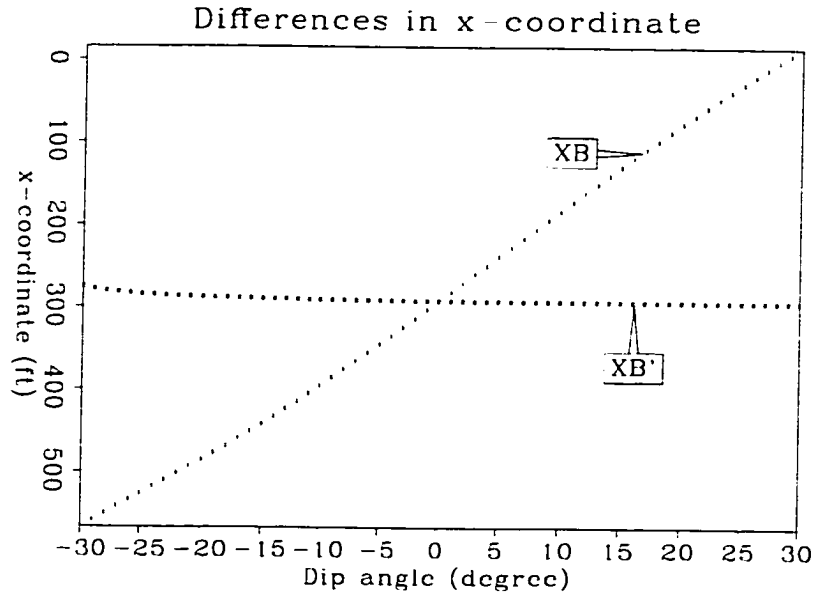


Figure 8.7: Curve labeled 1 (XB) shows the lateral coordinate of the reflection point as a function of the dip angle of the reflector; curve labeled 2 (XB') shows the lateral coordinate of the corresponding image point. In this figure, the source is on the surface, the receiver is positioned at depth of 100 ft in the well, the offset is 600 ft. And the depth of the reflector intersecting the well is 400 ft.

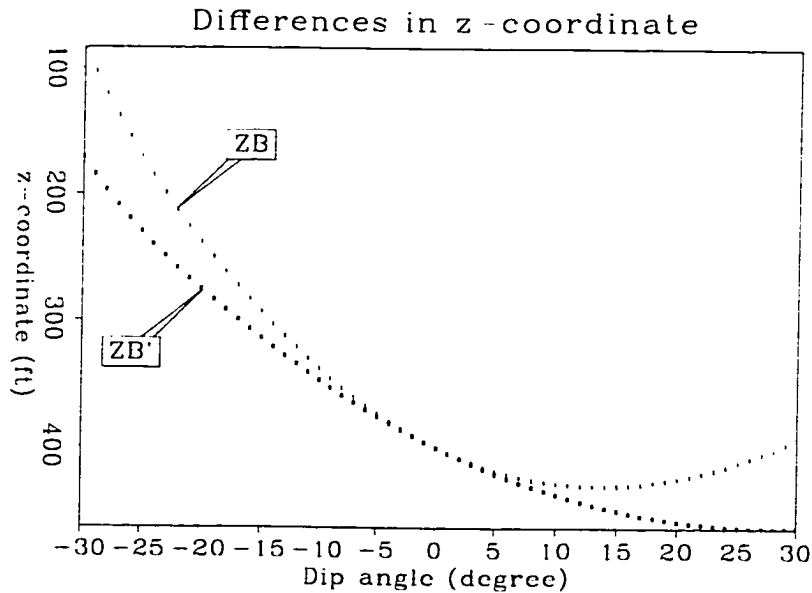


Figure 8.8: Curve labeled 1 (ZB) shows the depth coordinate of the reflection point as a function of the dip angle of the reflector; curve labeled 2 (ZB') shows the depth coordinate of the corresponding image point. In this figure, the source is on the surface, the receiver is positioned at depth of 100 ft in the well, the offset is 600 ft. And the depth of the reflector intersecting the well is 400 ft.

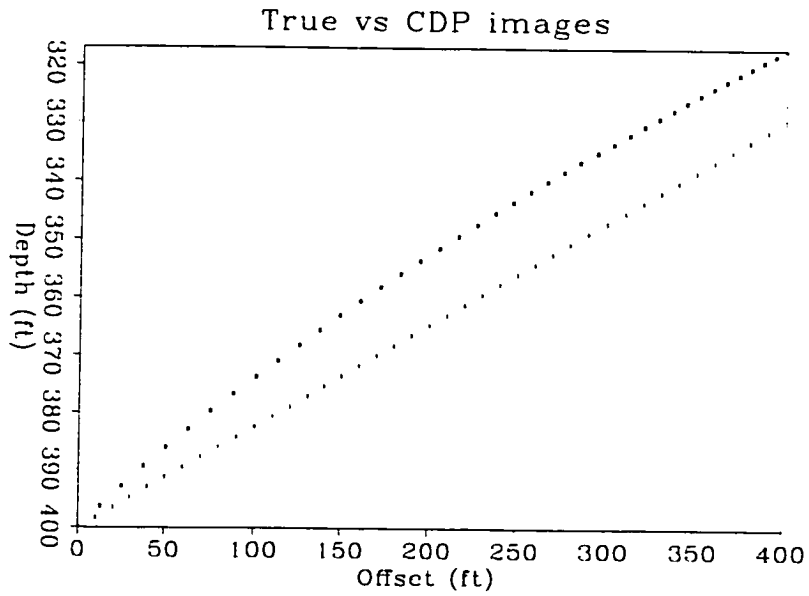


Figure 8.9: Line labeled 1 is a reflector dipping at -10° intersecting the well at the depth of 400 ft. Curve labeled 2 is the VSP-CDP image of the dipping reflector.

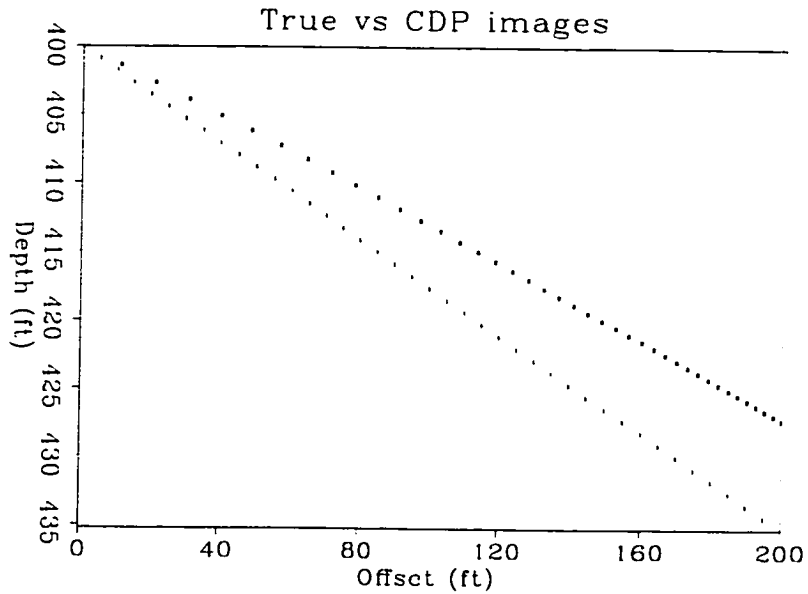


Figure 8.10: Line labeled 1 is a reflector dipping at 10° intersecting the well at the depth of 400 ft. Curve labeled 2 is the VSP-CDP image of the dipping reflector.

true velocity is v_0 and the velocity used in the mapping processing is v_1 . By equating the forward modeling travel time in equation (8.6) and the mapping travel time in equations (8.11) and (8.12), I arrive at the following equations for the coordinates of the image point,

$$x = \frac{1}{2} \frac{\sqrt{\left(\frac{v_1}{v_0}\right)^2 [4(h-d)(h \cos^2 \theta + L \sin \theta \cos \theta) + d^2 + L^2] - L^2 - d}}{\sqrt{\left(\frac{v_1}{v_0}\right)^2 [4(h-d)(h \cos^2 \theta + L \sin \theta \cos \theta) + d^2 + L^2] - L^2}} L \quad (8.23)$$

$$z = \frac{\sqrt{\left(\frac{v_1}{v_0}\right)^2 [4(h-d)(h \cos^2 \theta + L \sin \theta \cos \theta) + d^2 + L^2] - L^2 + d}}{2} \quad (8.24)$$

In analyzing the equations (8.23) and (8.24), let me consider the special case $d = h$, ie, the receiver is located at the depth of the reflector intersecting the well. I get the following two equations for this special case.

$$x = \left(1 - \frac{v_0}{v_1}\right) L \quad (8.25)$$

$$z = \frac{1}{2} \left(1 + \frac{v_1}{v_0}\right) d \quad (8.26)$$

These two equations are independent of reflector dip angle. When the velocity used in mapping is lower than the true velocity ($v_1 < v_0$), the lateral coordinate of the image point is negative (on the opposite side of the well from the source) and the depth is less than the true depth of the reflector at the well. When the velocity used in mapping is higher than the true velocity ($v_1 > v_0$), the lateral coordinate of the image point is positive and the depth is larger than the true depth of the reflector at the well. Only when the velocity used in mapping is the same as the true velocity will the first break reflection data of a receiver map to the well location and at the same depth as the receiver. These observations are guidelines in determining velocity for VSP-CDP reflection mapping. The VSP survey is usually conducted at a small scale in the vicinity of the well, thus a one-dimensional velocity field is sufficient for VSP-CDP mapping. Also, the first break reflection data are time-coincident with the first break direct arrivals. One can use the direct arrival travel times to invert for a one-dimensional velocity field, and use that for VSP-CDP mapping.

8.6 Post-CDP-mapped migration

Equation (8.16) describes how a dipping reflector with dip angle θ and depth h at the point intersecting the well is represented in the image space after data processing by the VSP-CDP mapping, where L is the source to well offset. The dipping reflector is distorted in

the image space. I perform a correction to the VSP-CDP image to remove the distortion, that is post-CDP-mapped migration. I start from the $\tau - p$ space of the true image. Each point in the $\tau - p$ space is calculated by summing the VSP-CDP image along the image trajectory predicted by equation (8.16)

$$P(h, p) = \sum_x CDPIImage(z(x, h, p, L), x) dx \quad (8.27)$$

Finally, the true reflector image is reconstructed by an inverse $\tau - p$ transform on the above $\tau - p$ data.

$$MIGImage(z, x) = \rho(z) * \sum_p P(z - px, p) dp \quad (8.28)$$

In this case τ is the depth coordinate h , p is the tangent of the dip angle θ and $\rho(z)$ is the ρ filter (Claerbout, 1985). Note, this migration algorithm is velocity independent, because the VSP-CDP image is already in spatial (x, z) domain and this migration algorithm performs a correction on the image where the source and target domains are the same.

Figure 8.11 shows the processing flow. The first step is to perform VSP-CDP mapping on the up-going wave fields of the data to obtain VSP-CDP image. The second step is to do migration on the distorted VSP-CDP image mapping to the $\tau - p$ space of the true reflector image. The third step is to perform inverse $\tau - p$ transform on the $\tau - p$ data to obtain the correctly positioned reflector image.

8.7 Synthetic data

8.7.1 Dipping reflectors

Figure 8.12 shows a common shot gather of vertical seismic profile obtained by ray tracing. The background velocity is 5000 ft/s. The source to well offset is 500 ft. The receiver depth interval in the well is 5 ft. There are 200 receiver traces. Two dipping reflectors, -20° and 20° are simulated by ray tracing on a constant velocity background of 5000 ft/s. Figure 8.13 shows the image produced by VSP-CDP mapping. Figure 8.14 shows the migrated image, in which the two dipping reflectors are correctly positioned.

8.7.2 Curvilinear reflectors

Figure 8.15 shows the VSP common shot gather data obtained by finite-difference wave equation modeling. The source to well offset is 500 ft. The receiver depth interval in

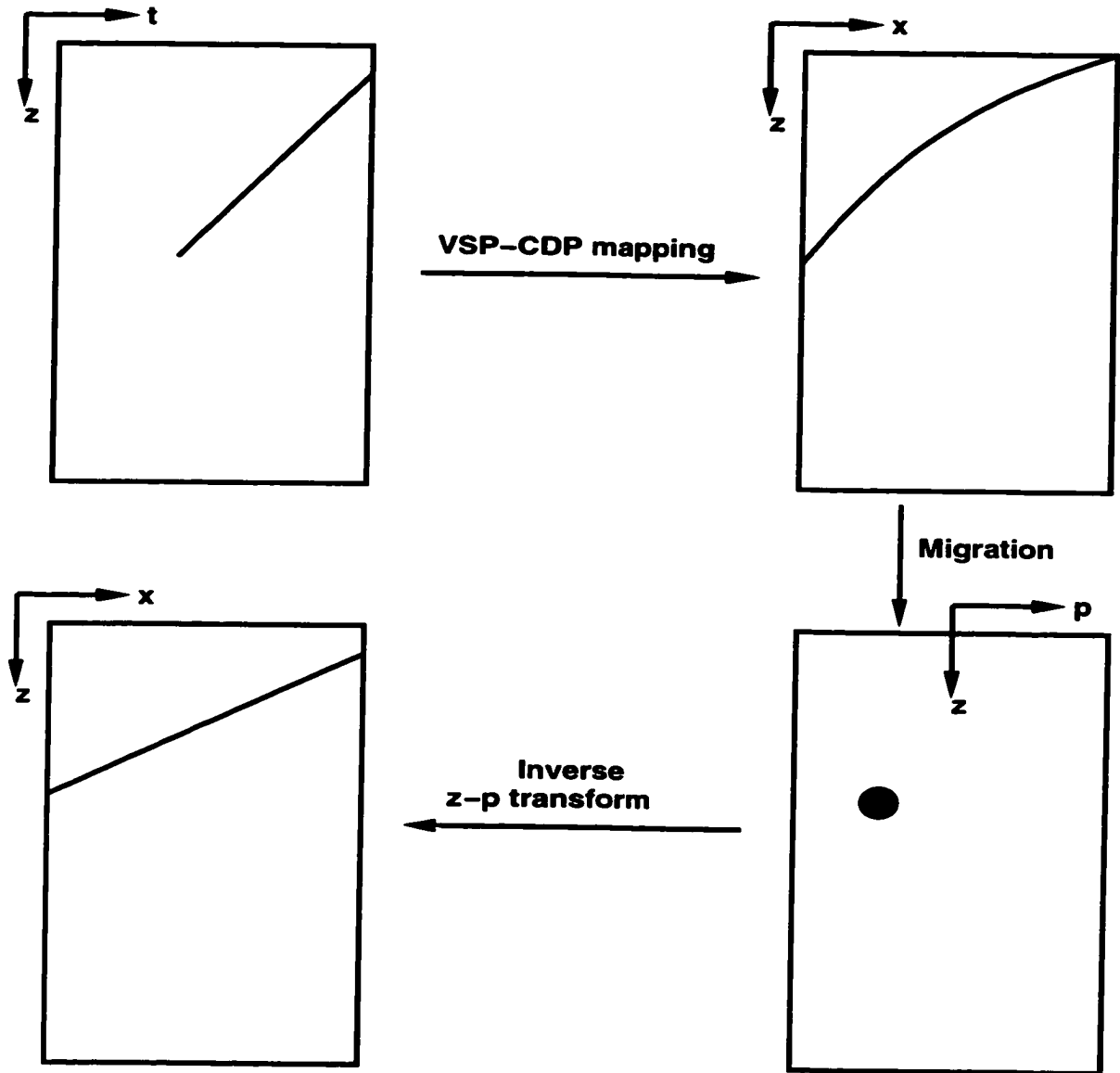


Figure 8.11: Three steps are involved to process VSP data to obtain correctly positioned reflector image. The first step is the conventional VSP-CDP mapping. The second step constructs the $\tau - p$ space representation of the correctly positioned reflector from the VSP-CDP image using an algorithm described in the text. The third step is to perform an inverse $\tau - p$ transform to obtain the correctly positioned reflector image.

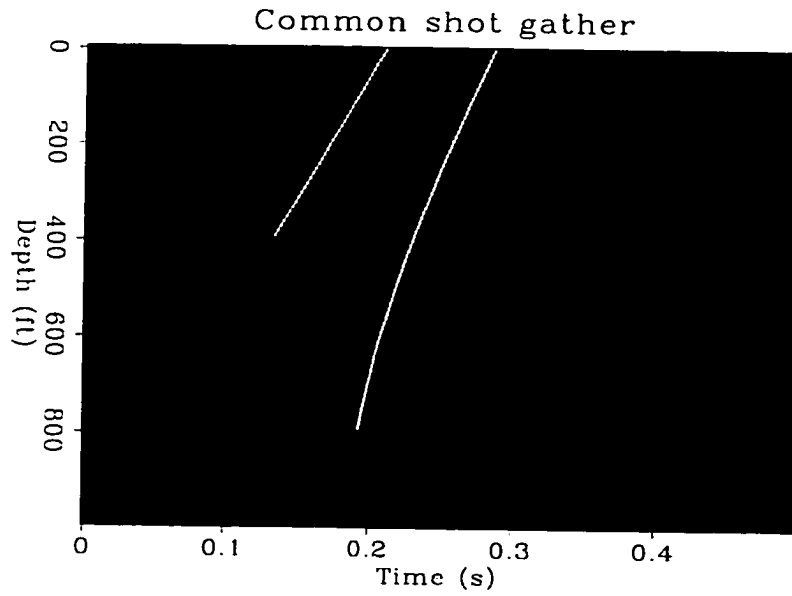


Figure 8.12: A VSP common shot gather data.

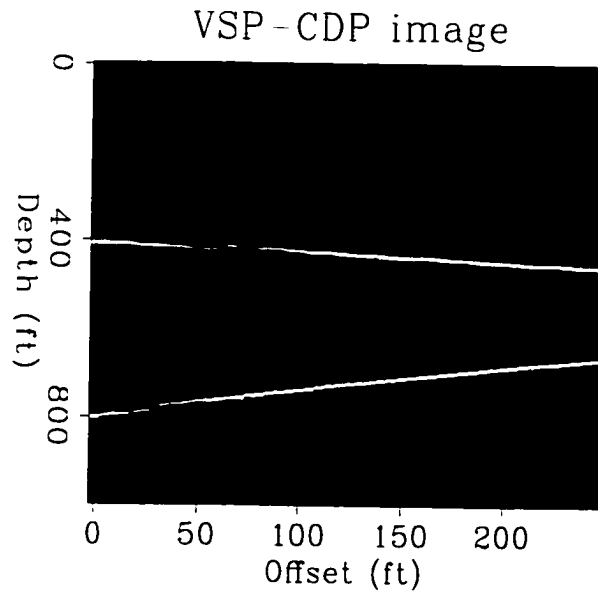


Figure 8.13: Image produced by the conventional VSP-CDP mapping. Overlaid lines show the true location of the reflectors.

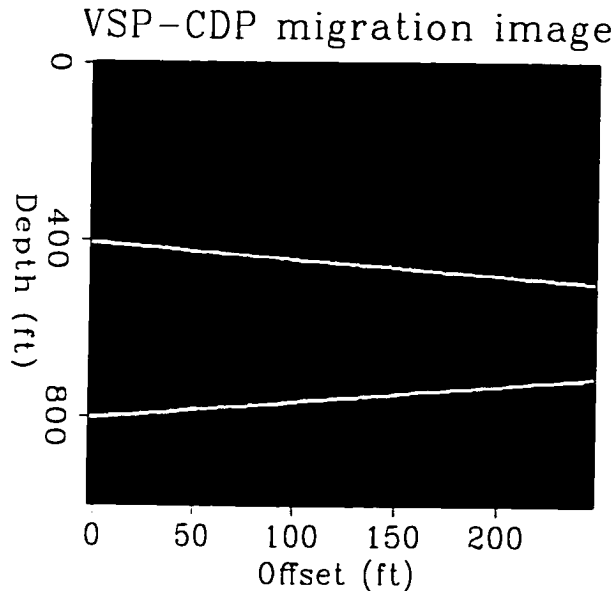


Figure 8.14: Migration image, in which the dipping reflectors are correctly positioned. Overlaid lines show the true location of the reflectors.

the well is 5 ft. There are 200 receiver traces. Two circular reflectors are modeled, the background velocity is 5000 ft/s. Figure 8.16 shows the up-going wave field data obtained by f-k filtering. Figure 8.17 shows the VSP-CDP mapping image. Figure 8.18 is the image after VSP-CDP migration. These two circular reflectors have zero dip at the left hand side of the figures (the well location), and their dip angles increase to the right. Notable differences between the reflector images in Figures 8.17 and 8.18 are at the parts where the reflectors have large dips.

8.8 Field data – Exxon Friendswood

Figure 8.19 shows the common shot gather data of a vertical seismic profiling survey. This data is taken from a reverse vertical seismic profiling survey carried out at Friendswood, Texas (Chen et al., 1990). The source to well offset is 500 ft. There are 98 receiver traces ranging from depths 30 ft to 1000 ft in the well, with a depth interval of 10 ft. The time sampling interval is 0.25 ms. Processing of the data consists of the following steps. A bandpass filter is applied to the data to filter out the low- and high-frequency noises. Only frequencies between 30 Hz and 500 Hz are retained. In order to have a better sampling in the VSP-CDP image, the data is interpolated in depth so that the depth interval is 5

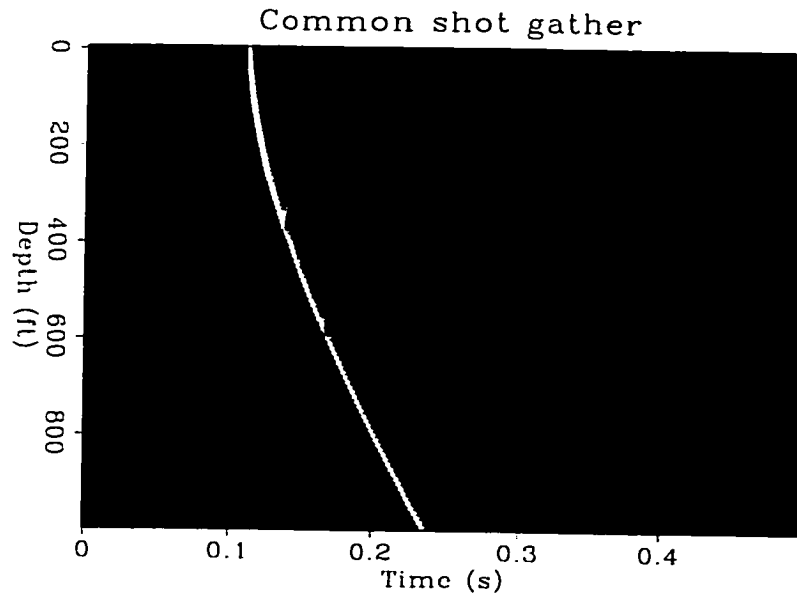


Figure 8.15: A VSP common shot gather data.

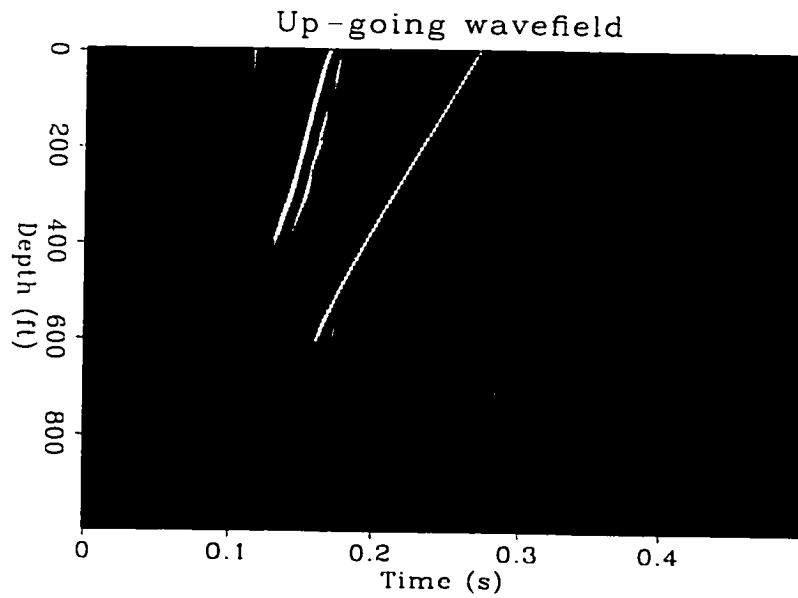


Figure 8.16: Up-going reflection data obtained by f-k filtering.

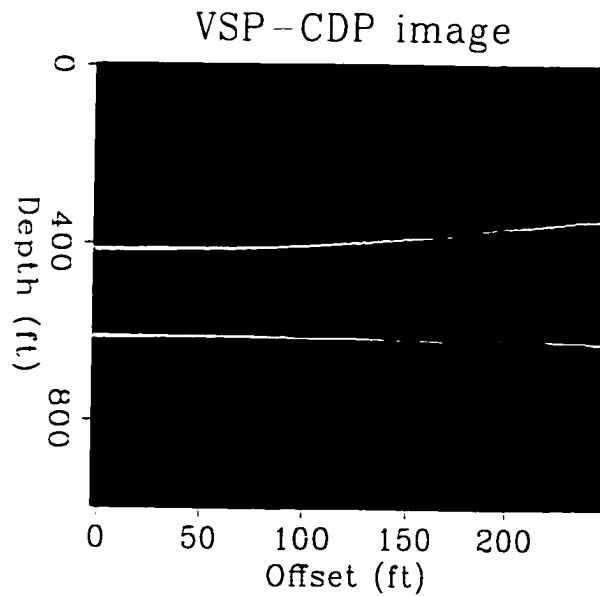


Figure 8.17: Image produced by the conventional VSP-CDP mapping. Overlaid curves show the true location of the reflectors.

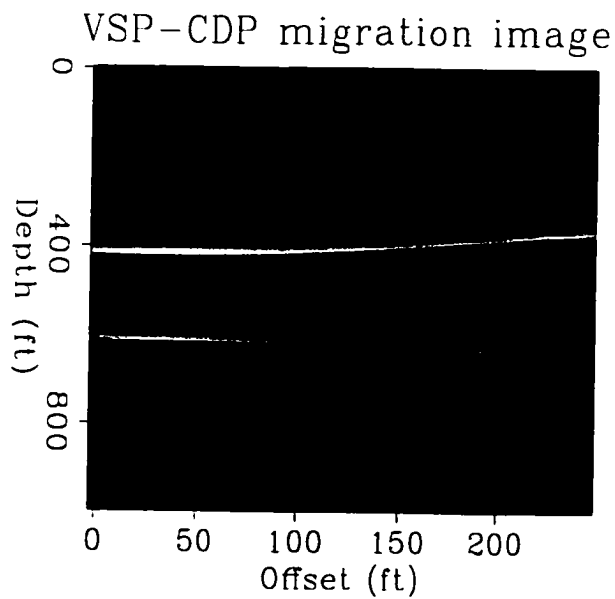


Figure 8.18: Migration image, in which the curvilinear reflectors are correctly positioned. Overlaid curves show the true location of the reflectors.

ft. Figure 8.20 shows the result data after these initial data processings. A frequency-wavenumber (f - k) filter is applied to the data to remove the unwanted down-going direct arrivals and multiples. Figure 8.21 shows the up-going components of the common shot gather data. The upgoing wavefield data are input to a VSP-CDP mapping module in ProMax to produce the image in Figure 8.22. Results of surface seismic reflection survey (Chen et al., 1990) show that the reflectors in the image have only gentle dips. Thus, the dips of the reflectors at the lower part of the image (Figure 8.22) are too high. Figure 8.23 shows the $\tau - p$ image obtained by scanning the VSP-CDP image using equation (8.27). Figure 8.24 shows the VSP-CDP migration image obtained by inverse $\tau - p$ transform on the $\tau - p$ image. The dip errors in the image have been corrected.

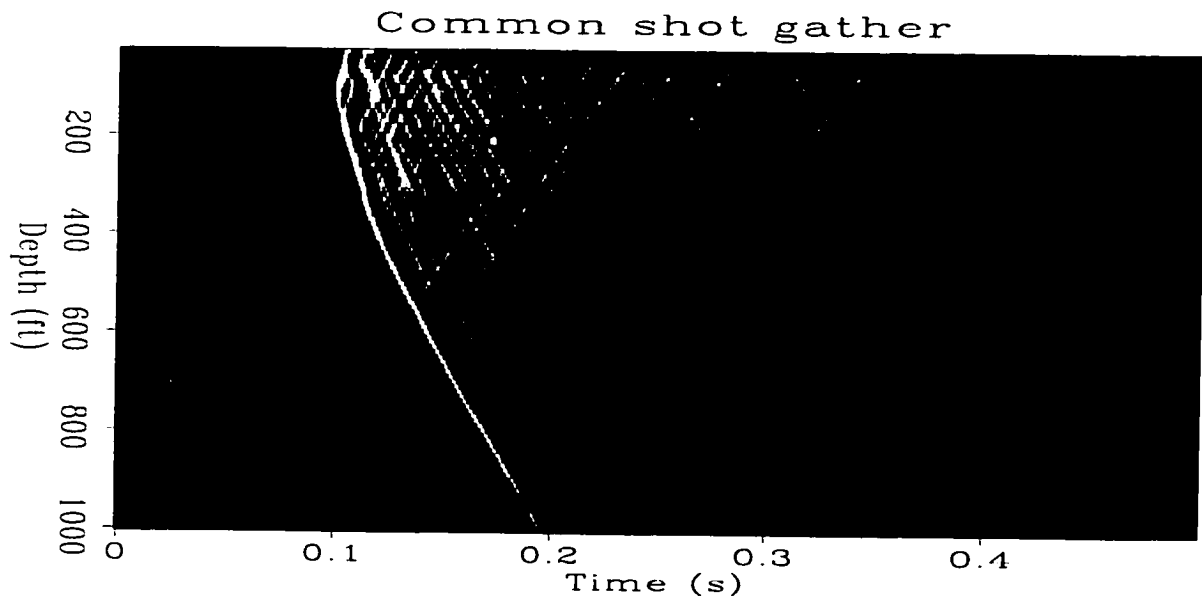


Figure 8.19: Original common shot gather VSP data.

8.9 Conclusions

VSP-CDP maps reflection from a dipping reflector into a third-order polynomial in unmigrated VSP-CDP image (offset-depth) space. When the dip of the reflector is not large, the image polynomial does not deviate significantly from the true position of the reflector, then the VSP-CDP image is accurate. When the dip of the reflector is large, migration should be applied. A point in the $\tau - p$ space of the migrated image is obtained by stacking the VSP-CDP image along the image trajectory calculated by modeling the VSP-CDP

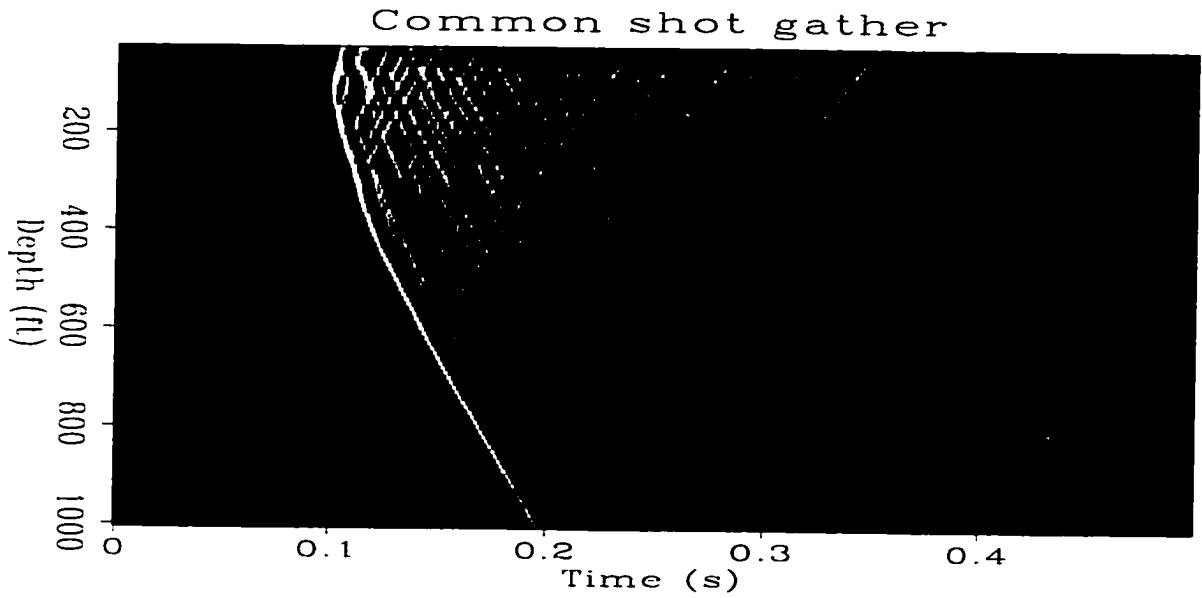


Figure 8.20: Common shot gather VSP data after bandpass filtering to remove noises.

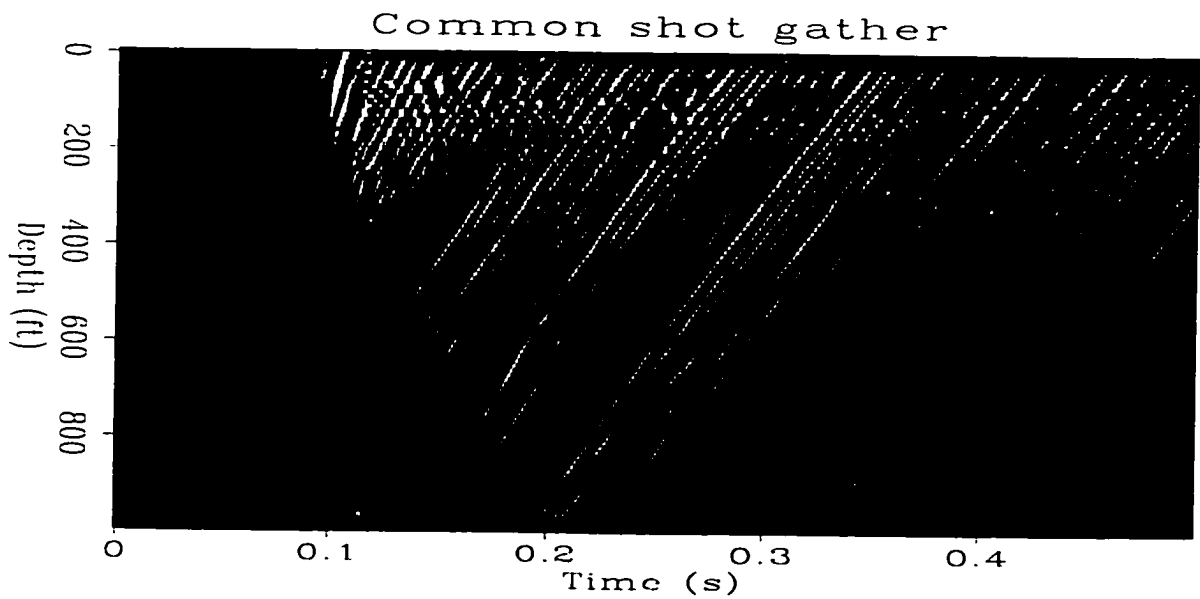


Figure 8.21: Upgoing wavefield obtained by f-k filtering.

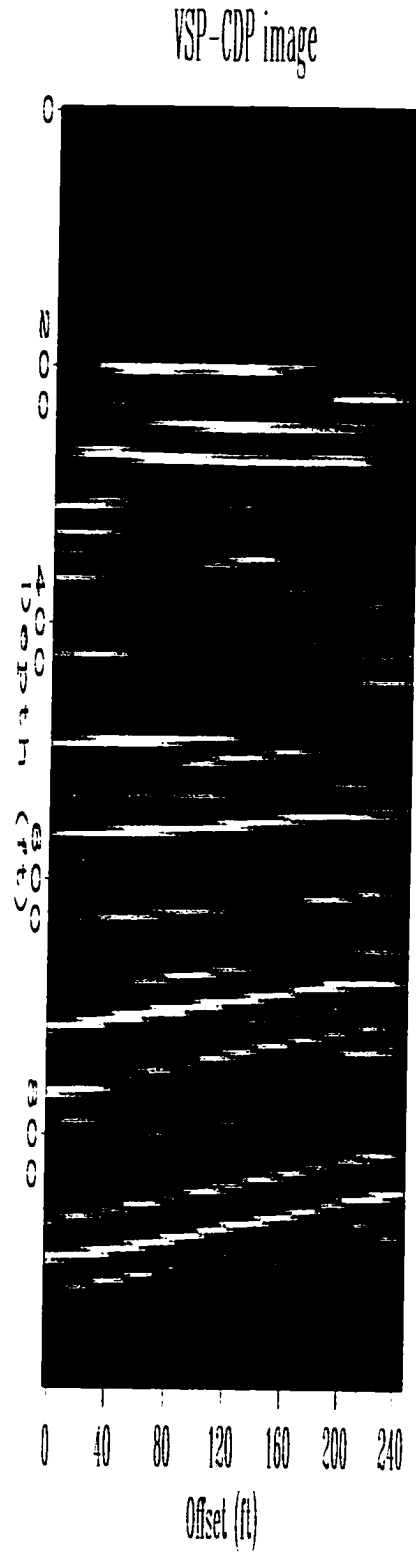


Figure 8.22: VSP-CDP image. The dips of the reflectors at the lower part of the image are too high.

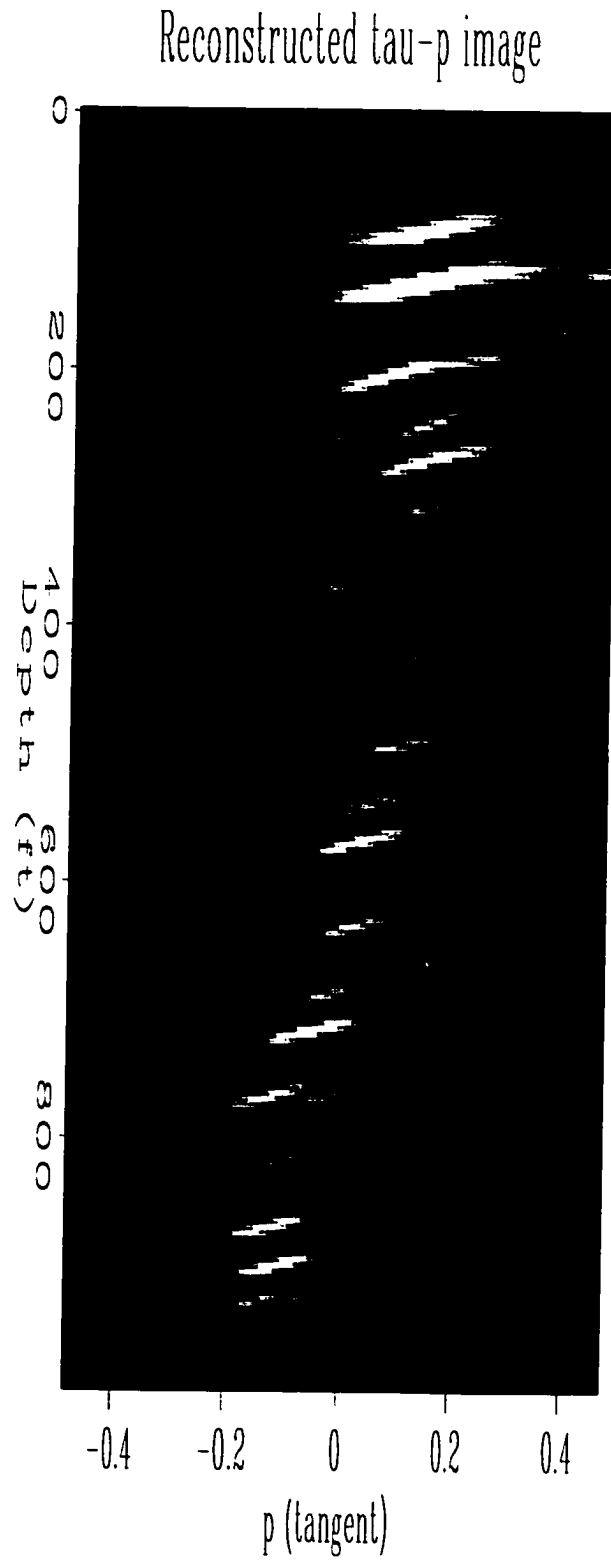


Figure 8.23: Constructed $\tau - p$ image obtained by scanning the VSP-CDP image.

VSP-CDP migration image

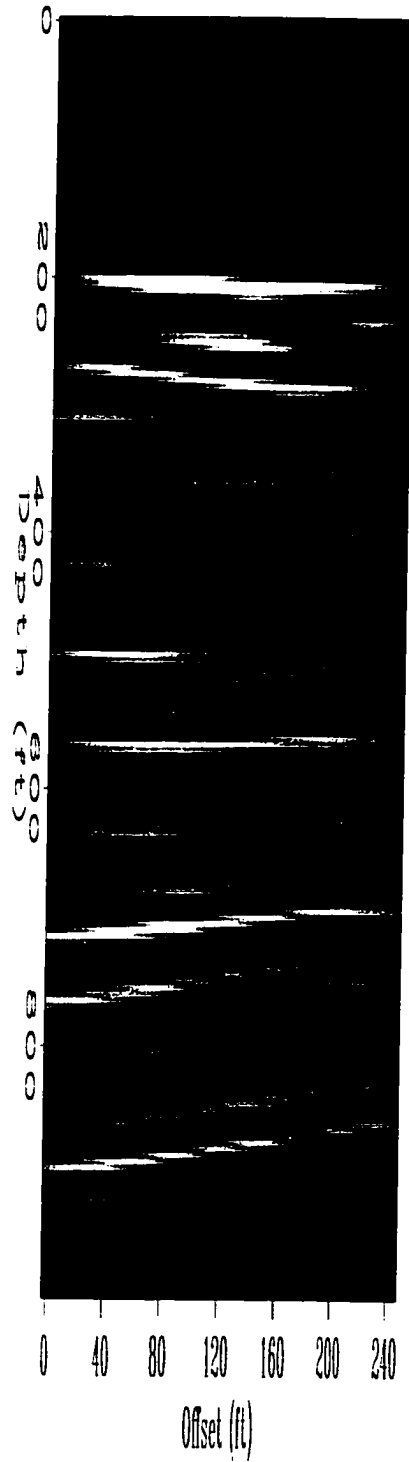


Figure 8.24: VSP-CDP migration image.

mapping process. Inverse transformation on the resulting $\tau - p$ data gives the migration image. Curves are migrated by operation on lines as a curve is the envelope of lines of various dips. The migration algorithm assumes the medium has a constant velocity. But the correct velocity model should be used in VSP-CDP mapping. Imaging of the direct arrivals to the well and at the same depths as the receivers is a good criterion in determining velocity model for VSP-CDP mapping. Because of the discrepancy between the velocity models that can be handled in VSP-CDP mapping and post-mapping migration, this algorithm should only be used where the velocity of the medium is constant or where the variation of velocity is very mild and the dips of the reflectors are large to necessitate migration. This algorithm can perhaps best be used to help estimating the dip of the reflector in interactive VSP-CDP mapping (Lazaratos, 1993; Smalley, 1997).

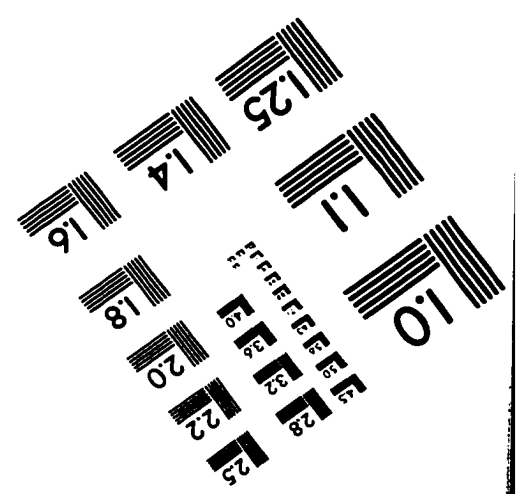
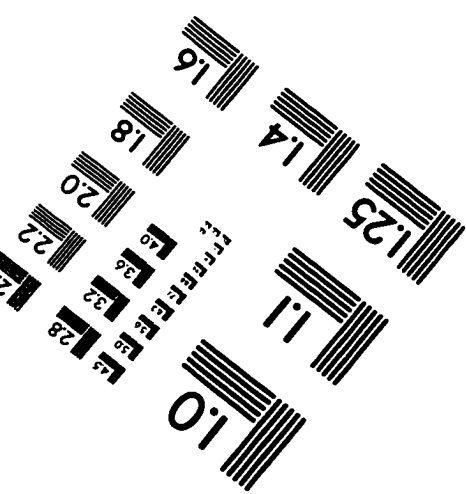
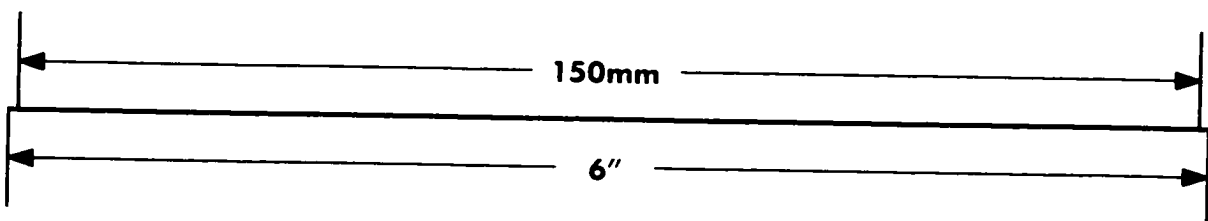
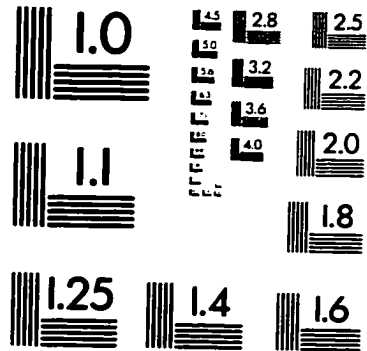
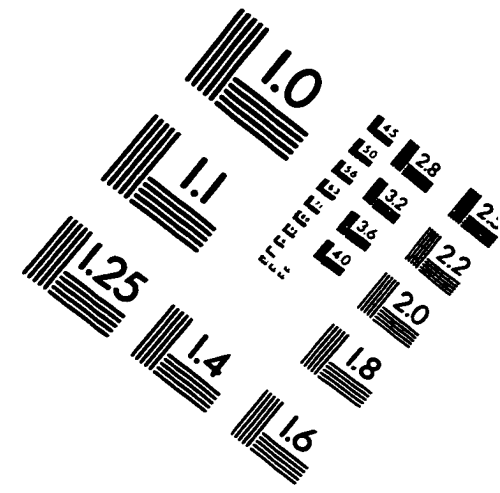
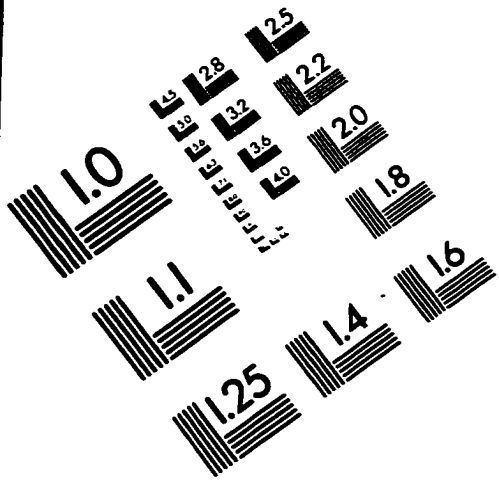
Bibliography

- Aki, K., and Richards, P. G., 1980, Quantitative seismology, volume 1: W. H. Freeman Co.
- Aldridge, D. F., and Oldenburg, D. W., 1993, Two-dimensional tomographic inversion with finite-difference travel times: *Journal of Seismic Exploration*, **2**, 257-274.
- Avasthi, J. M., Nolen-Hoeksema, R. J., and El Rabaa, A. W. M., 1991, In-situ stress evaluation of the McElroy field, west Texas: *SPE Formation Eval.*, September issue, 301-309.
- Balch, A. H., and Lee, M. W., 1984, Vertical seismic profiling: techniques, application, and case histories: International Human Resources Development Corporation.
- Berkhout, A. J., 1985, Seismic migration – Imaging of acoustic energy by wave field extrapolation. A: Theoretical aspects, Elsevier Science Publishers.
- Beydoun, W. B., and Mendes, M., 1989, Elastic ray-Born l2-migration/inversions: *Geophys. J.*, **97**, 151-160.
- Cai, W., and Schuster, G. T., 1993, Processing Friendswood cross-well seismic data for reflection imaging: 63rd Ann. Internat. Mig., Soc. Expl. Geophys., Expanded Abstracts, 92-94.
- Cerjan, C., Kosloff, D., Kosloff, R., and Reshef, M., 1985, A nonreflecting boundary condition for discrete acoustic and elastic wave equations: *Geophysics*, **50**, 705-708.
- Cerveny, V., Molotkov, I. A., and Psencik, I., 1977, Ray method in seismology: Karlova Univerzita, Prague.
- Chang, W. F., and McMechan, G. A., 1986, Reverse-time migration of offset vertical seismic profiling data using the excitation-time imaging conditions: *Geophysics*, **51**, 67-84.
- Chen, S. T., Zimmerman, L. J., and Tugnait, J. K., 1990, Subsurface imaging using reversed vertical seismic profiling and crosshole tomographic methods: *Geophysics*, **55**, 1478-1487.
- Claerbout, J. F., 1985, *Imaging the Earth's Interior*: Blackwell Scientific.
- Claerbout, J. F., 1991, *Earth Soundings Analysis: Processing versus Inversion*: Blackwell Scientific.
- Dablain, M., 1986, The application of high-order differencing to the scalar wave equation: *Geophysics*, **51**, 54-66.
- Devaney, A. J., 1984, Geophysical diffraction tomography: *IEEE Trans. Geosci. Remote Sensing*, **GE 22**, 3-13.

- Dillon, P. B., 1988, Vertical seismic profile migration using the Kirchhoff integral: *Geophysics*, **53**, 786-799.
- Dillon, P. B., and Thomson, R. C., 1984, Offset source VSP surveys and their image reconstruction: *Geophysical Prospecting*, **32**, 790-811.
- Goodman, J., 1970, *Introduction to Fourier Optics*.
- Gray, S., and Lines, L., 1992, Cross-borehole tomographic migration: *Journal of Seismic Exploration*, **1**, 315-324.
- Hardage, B. A., 1983, *Vertical seismic profiling part A - principles*: Geophysical Press.
- Harris, J. M., 1987, Diffraction tomography with arrays of discrete sources and receivers: *IEEE Trans. Geosci. Remote Sensing*, **GE 25**, 448-455.
- Harris, J. M., Nolen-Hoeksema, R. C., Langan, R. T., Van Schaack, M. A., Lazaratos, S. K., and Rector, J. W., 1995, High-resolution crosswell imaging a west Texas carbonate reservoir: Part 1-Project summary and interpretation, *Geophysics*, **60**, 667-681.
- Healan, P., 1953, Radiation from a cylindrical source of finite-length, *Geophysics*, **18**, 685-696.
- Hu, L. Z., McMechan, G. A., and Harris, J. M., 1988, Acoustic pre-stack migration of cross-hole data: *Geophysics*, **53**, 1015-1023.
- Langan, R. T., Harris, J. M., Lazaratos, S. K., and Jensen, T. L., 1995, Crosswell seismic imaging in the Permian Basin: *Seismic Tomography Project*, Vol. 6, No. 1, Paper U.
- Lazaratos, S., 1993, *Crosswell reflection imaging*: Ph.D. thesis, Stanford University.
- Lines, L. R., and LaFehr, E. D., 1989, Tomographic modeling of a cross borehole data set: *Geophysics*, **54**, 1249-1257.
- Luo, Y., and Schuster, G. T., 1990, Wave-equation traveltime + waveform inversions: *60th Ann. Internat. Mig., Soc. Expl. Geophys., Expanded Abstracts*, 947-956.
- McMechan, G. A., 1983a, Seismic tomography in boreholes: *Geophys. J. Roy. Astr. Soc.*, **74**, 601-612.
- McMechan, G. A., 1983b, Migration by extrapolation of time-dependent boundary values: *Geophys. Prosp.*, **31**, 413-420.
- Nemeth, T., 1994, Migration and coherency stacking of the Friendswood reverse VSP data: *64th Ann. Internat. Mig., Soc. Expl. Geophys., Expanded Abstracts*, 97-100.
- Pham, L. D., Krohn, C. E., Murray, T. J., and Chen, S. T., 1993, A tube wave suppression devices for cross-well application: *63rd Ann. Internat. Mig., Soc. Expl. Geophys., Expanded Abstracts*, 17-20.
- Podvin, P., and Lecomte, I., 1991, Finite difference computation of traveltimes in very contrasted velocity models: a massively parallel approach and its associated tools: *Geophys. J. Int.*, **105**, 271-284.
- Qin, F., and Schuster, G. T., 1993, Constrained Kirchhoff migration of cross-well seismic data: *63rd Ann. Internat. Mig., Soc. Expl. Geophys., Expanded Abstracts*, 99-102.
- Qin, F., Luo, Y., Oslon, K. B., Cai, W., and Schuster, G. T., 1992, Finite-difference solution of the eikonal equation along expanding wavefronts: *Geophysics*, **57**, 478-487.
- Reshef, M., and Kosloff, D., 1986, Migration of common-shot gathers: *Geophysics*, **51**, 324-331.
- Smalley, N., 1997, *A new CDP coordinate system for the sorting, velocity analysis, and imaging of Crosswell reflection data*: Ph.D. thesis, Stanford University.

- Stewart, R. R., 1992, Exploration seismic tomography – fundamentals: SEG Cont. Ed. Course Notes, No. 3.
- Van Trier, J., and Symes, W. W., 1991, Upwind finite-difference calculation of traveltimes: Geophysics, **56**, 812-821.
- Vidale, J., 1988, Finite-difference calculation of travel times: Bull. Seism. Soc. Am., **78**, no. 6, 2062-2076.
- Vidale, J., 1990, Finite-difference calculation of travel times in 3-D: Geophysics, **55**, 521-526.
- Vidale, J., 1991, Rapid calculation of amplitude: Geophysics, **56**, 880-884.
- Wyatt, K. D., and Wyatt, S. B., 1981, Determinating subsurface structure using the vertical seismic profiling: 51st Ann. Internat. Mig., Soc. Expl. Geophys., Expanded Abstracts, 99-102.
- Wiggins, J. W., Ng, P., and Manzur, A., 1986, The relation between the VSP-CDP transformation and VSP migration: 56st Ann. Internat. Mig., Soc. Expl. Geophys., Expanded Abstracts, 564-568.
- Zauderer, R., 1989, Partial Differential Equations of Applied Mathematics: John Wiley and Sons.
- Zhang, L., 1993, Imaging by the wavefront propagation method: Ph.D. thesis, Stanford University.

IMAGE EVALUATION TEST TARGET (QA-3)



APPLIED IMAGE . Inc
 1653 East Main Street
 Rochester, NY 14609 USA
 Phone: 716/482-0300
 Fax: 716/288-5989

© 1993, Applied Image, Inc., All Rights Reserved